THE UNIVERSITY OF HULL

3D and 4D Printing of Metal-Organic Frameworks

being a Thesis submitted for the degree of
PhD Chemistry

in the University of Hull

by

Ellis Scott Marshall, MChem

October 2019

Abstract

This thesis describes the development of new composite materials by the 3D printing of metal-organic frameworks. The application of these composites in various settings is described.

Chapter 1 contains a review of the area of additive manufacturing with a focus on 3D printing and 4D printing. This introduces applications of 3D printing within the chemistry field and wider fields and gives a review of metal-organic frameworks. The application of metal-organic frameworks as catalysts and in 3D printing are described.

Chapter 2 describes the experimental work undertaken and the design of the experimental rig for the printing of UV-curable polymer matrices under an inert atmosphere. This chapter contains detailed synthetic methods and procedures used for characterisation equipment used for this work and any characterisation limitations.

Chapter 3 contains the work related to the use of magnetically aligned MOFs by the addition of iron. A method for the alignment of iron-rich MOF particles and adsorbed iron oxide nanoparticles in solution by the application of a magnetic field is presented. The alignment of MOF particles with up to 10wt.% iron oxide nanoparticles in a photo-curable polymer resin is demonstrated and the anisotropic optical response of the same is described. The 4D printing of magnetically aligned MOFs in a polymer resin is described.

Chapter 4 contains works related to the ability of UiO-66 to catalyse and degrade nerve agent simulant as a novel 4D printed polymer composite. This demonstrates that a macroscopic MOF composite can be used to degrade a nerve agent simulation. A new technique is trialled for the partial calcination of the polymer composite resulting in a micro and meso porous structure with a high specific surface area (633 m^2g^{-1}). This technique and the physical properties investigated of the resulting monolith are described.

Chapter 5 presents results of metal-organic framework gels as potential additives for 3D printing and a novel direct-write ink. Metal-organic framework gels of UiO-66, UiO-66-NH_2

and ZIF-8 are fabricated and their ability to act as a rheology modifiers are investigated. Trials are described for the novel 3D printing of metal-organic framework gels and adsorption properties investigated.

Acknowledgements

To my parents, brother, grandparents and family who have supported me through this PhD a massive thank you for helping me through.

To Polly Sanders, Dr. Rhiannon Lee, Mark Sammons, Lloyd Glanville, Alex Goodhand, Adam Young and Aimie Rendle I would like to say a massive thank you for all your assistance and their willingness to go for coffee, cake and a chat when it got tough.

Massive thanks to the Aura team who have taken me under their wing and especially to Emma Platt-Lowe and her wonderful family for all the love and support.

I am grateful to the University of Hull for the funding of this PhD. I would like to thank all the technicians at the University of Hull for all their unwavering support and a special mention to Garry Robinson for training and tutoring me on the use of the SEM and always being on hand to help out. Thanks also go to Bob Knight for ICP-OES and ICP-MS analysis and Carol Kennedy for elemental analysis.

I would like to thank the whole Chin-Reithofer group for all their help, support and motivation throughout the PhD. Thanks go to Dr. Timothy J. Prior for seeing me through my final year of the PhD and expertise in crystallography.

Finally, to my partner Theo for the love, support, motivation and food parcels. A special mention to our new puppy- Baymax, who has given extensive help and distraction by walking over the keyboard, sleeping underfoot and snoring while I write.

Publications

Magnetic Control of MOF Crystal Orientation and Alignment

F. Cheng, E. S. Marshall, A. J. Young, P. J. Robinson, J. S. G. Bouillard, A. M. Adawi, N. A. Vermeulen, O. K. Farha, M. R. Reithofer and J. M. Chin, *Chem. - A Eur. J.*, 2017, **23**, 15578–15582.

I am grateful for the help of Dr. Fei Cheng for his assistance throughout and for carrying out TEM and BET analysis. Also thanks to Adam Young and Peter Robinson for carrying out experiments with polarised light and the creation of the azimuthal plot. I am grateful to everyone involved for their help and support towards this publication.

Direct ink writing of catalytically active UiO-66 polymer composites

A. J. Young, E. S. Marshall, F. Kleitz, A. J. Goodhand, L. B. L. Glanville, M. R. Reithofer and J. M. Chin,. *Chem. Comm.,* 2019, 2190-2193.

I am grateful for the help of Adam Young in this publication for carrying out NMR experiments and to Dr. Freddy Kleitz from the University of Vienna for running BET analysis.

Abbreviations

3DP	3D printing
4DP	4D printing
BDC	Benzene-1,4-dicarboxylic acid or terephthalic acid
DMF	*N,N*-Dimethylformamide
DIW	Direct ink write
EtOH	Ethanol
FDM	Fused deposition modelling
FTIR	Fourier transform infrared
HKUST	Hong Kong University of Science and Technology
ICP-OES	Inductively coupled plasma – optical emission spectrometry
MIL	Materials Institute Lavoisier
MOF	Metal-organic framework
MOF-gel	Metal-organic framework-gel
NMR	Nuclear magnetic resonance
NU	Northwestern University
OM	Optical microscopy
Pa	Pascals
PDMS	Polydimethylsiloxane or Sylgard® 184
PI	Photoinitiator
PXRD	Powder x-ray diffractometer
SEM	Scanning electron microscopy
SLA	Stereolithography
TEM	Transmission electron microscopy
TGA	Thermogravimetric analysis
TMPPTA	Trimethylolpropane propoxylate triacrylate
UiO	Universität i Oslo
UV	Ultraviolet
ZIF	Zeolitic imidazole framework

Table of Contents

1. Introduction

Motivation

The start of the 21st century has seen mankind face many challenging issues but none more so than climate change and chemical warfare. Recent protests by the Extinction Rebellion have brought environmental issues such as climate change, air quality and polluted oceans to the forefront of the public's attention.[1,2] There is growing public demand for governments to provide solutions to these problems. A well-known problem is the increased output of CO_2 from factories causing changes in our environment, which contributes towards global warming and ocean acidification. The impacts are widespread with more extreme weather patterns,[3,4] and reductions of healthy coral reefs in the world, amongst others.[5] In order to reduce damage or even stop further damage a reduction in CO_2 is needed.

In 2017, the world passed a CO_2 threshold of 400 ppm, at the current rate of growth in CO_2, levels will hit 500 ppm within 50 years, impacting temperature by 3 °C or more.[6] Above 3 °C is deemed the 'tipping point' whereby global warning could run out of control: sea levels could rise 25 metres, plants could grow in once inhospitable mountainous environments, the Amazon rainforest may turn to savannah and the northern hemisphere could be free of glaciers and ice sheets.[7] The current CO_2 level at the time of writing was 418 ppm.[8] The UK has committed to reducing carbon emissions by 80% by 2050 with institutions and businesses leading the way. To tackle the rise in CO_2 levels the Committee on Climate Change (CCC) suggest that energy is used more efficiently – by saving energy through insulation, more efficient appliances and heating and lighting controls. The CCC also suggest switching to low carbon fuels by moving away from coal and gas towards nuclear power, renewable sources and new technologies such as carbon capture and storage.[8]

While the UK and the rest of the world switches to renewable energy and nuclear power, newer technologies such as carbon capture and storage are not so readily being taken up and are less

well known. Carbon capture and storage technologies can capture up to 90% of CO_2 emissions produced from fossil fuels in industrial processes, preventing CO_2 entering the atmosphere.[8] The use of such technology can also go one step further and be carbon negative. By taking CO_2 out of the atmosphere, allowing it to be transported and stored under the ocean in geological rock formations, that once held oil, the carbon content is being reduced.

Carbon capture devices aimed to reduce CO_2 levels in the environment frequently use calcium oxide,[9] or aluminosilicate zeolites.[10] Calcium oxide is a good sorbent for CO_2 as it reacts with CO_2 to produce calcium carbonate, which can be reversed by calcination. Aluminosilicate zeolites are also good sorbents for CO_2 due to their porosity but were first discovered by their ability to store water. In 1756, Swedish mineralogist Axel Fredrik Cronstedt discovered that by heating a zeolite (formed as a result of volcanic activity) steam was released, this gave rise to the name zeolite or boiling stone formed from two Greek words *zeo* meaning boil and *lithos* meaning stone. A zeolite, consists of inorganic molecules of tetrahedral $[SiO_4]^{4-}$ and tetrahedral $[AlO_4]^{5-}$, Figure 1.1, creating voids in their structure, ideal for their adsorbent properties.

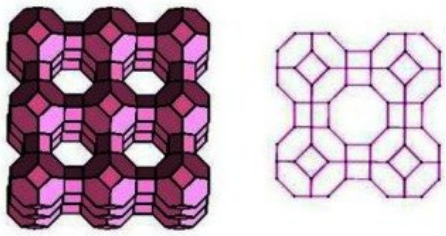

Figure 1.1: Zeolite A (Linde Type A) consisting of tetrahedral $[SiO_4]^{4-}$ and tetrahedral $[AlO_4]^{5-}$. Reproduced from an open access journal- Sensors.[11]

A zeolites structure is not flexible, making them great at separation and storage. A successor to zeolite minerals, with a flexible architecture, are metal-organic frameworks (MOFs). MOFs consist of organic based linker groups, such as terephthalic acid, co-ordinately bound to metal nodes to create either 1D, 2D or 3D structure of a highly porous architecture. The ability to use different metal nodes and long organic linkers, allows a large library of MOFs to be formed, each with unique structural features. MOFs have a much higher surface area, have a greater range of

functionality and can be more mechanically and chemically stable than some zeolites. MOFs have a large range of applications including CO_2 capture,[12] but can also be used in the degradation of dangerous poisonous pollutants.

There are many different pollutants in our environment including, plastics, heavy metals, ozone, pesticides and aromatic hydrocarbons all of which contribute - directly or indirectly towards climate change. The chemical structure of some pesticides are very similar to a more deadly chemical which has received a lot of public attention over recent years - nerve agents. Nerve agents have become more well known in the public domain after the use of nerve agent VX on the assassination of Kim Jong-nam, half-brother of Kim Jong-un in 2017, and in 2018 with the use of Novichok in Salisbury on the Skripal family. While MOFs have been tested and proven to tackle nerve agents their use in real-word applications is hindered by their lack of processability.

MOFs typically are synthesised as powders but can be fabricated into thin-films, 2D membranes and compressed discs with relative ease. However, testing of these MOF-based materials show a drop in efficiency for MOF films and membranes,[13–15] but also monolithic shapes that are also brittle and bulky,[16,17] this is down to the fabrication technique blocking the highly prized porous architecture of the MOF.

A new fabrication method is needed for MOFs to be processable whereby the active surface area of the MOF is still relatively high. A current MOF fabrication technique incorporated clay-based composites and 3D printed.[18] The 3D printer can then be employed to extrude and control the material deposition layer-by-layer to create a bespoke, intricate and 3D structure. However, the clay has potential to block the pores of the MOF rendering it less efficient. An innovative solution and arguably the next generation of multi-dimensional fabrication methods is 4D printing (4DP). 4DP combines 3D printing (3DP) with the 4th dimension of time to create a functional 3D device that can tackle such events as climate change and chemical warfare.

MOFs societal challenges facing the world and decreasing CO_2 output and cleaning up pollutants is achievable.

1.1. Outline of Additive Manufacturing

Additive manufacturing is the name of the group of technologies that build physical 3D objects by adding material layer-by-layer. The material can be plastic,[19] metal,[20] composites,[21] concrete,[22,23] or even biological tissues.[24] The technique is incredibly versatile and offers many benefits above traditional engineering processes. Traditional techniques such as wood turning and computer numerical control (CNC) contrast with additive manufacturing and are termed destructive manufacturing, as they simply work by carving a block of material into the desired shape. These processes are typically time-intensive and create a lot of waste material. Additive manufacturing, on the other hand, allows the precise deposition/addition of a material layer-by-layer with minimal waste and while the manufacturing method is fundamentally synonymous with 3DP it is often confused. Additive manufacturing is the family of processes that encompasses both 3DP and sheet lamination. But sheet lamination is commonly unacknowledged as an additive manufacturing technique although it does provide access to incredibly useful materials such as plywood, floor laminate, hardboard and laminate paper.

There are currently seven categories, Figure 1.2, of additive manufacturing defined by ISO 52900.[25]

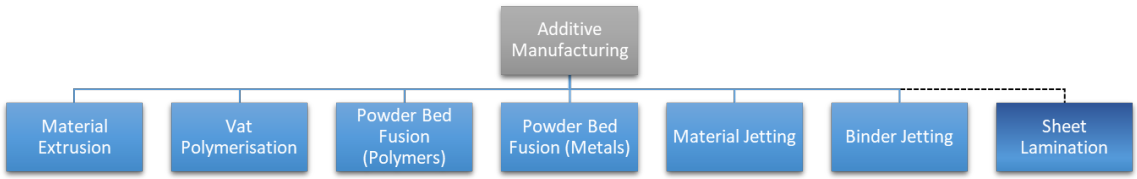

Figure 1.2: Additive Manufacturing has seven categories, 3DP covers all except sheet lamination.

1.1.1. 3D Printing Techniques

Additive manufacturing technologies rely on the use of a computer and 3D modelling software – Computer Aided Design (CAD) to construct a virtual sketch. This sketch is then translated into a .STL file type. STL here stands for stereolithography and is a legacy acronym referring to the first 3D printer invented by Chuck Hull in California in 1987.[26] However, a more useful and descriptive acronym to describe a .STL file is "Standard Triangle Language" or "Standard Tessellation Language". The file type works by tessellating the surface of the CAD drawn design and does not consider colour, textures or other model features. Each triangle has information on the coordinates of the vertices and direction of the normal vector (pointing out of the model). The precision of the printing depends in part on the size and quantity of the triangles when producing an .STL file, illustrated below (Figure 1.3).

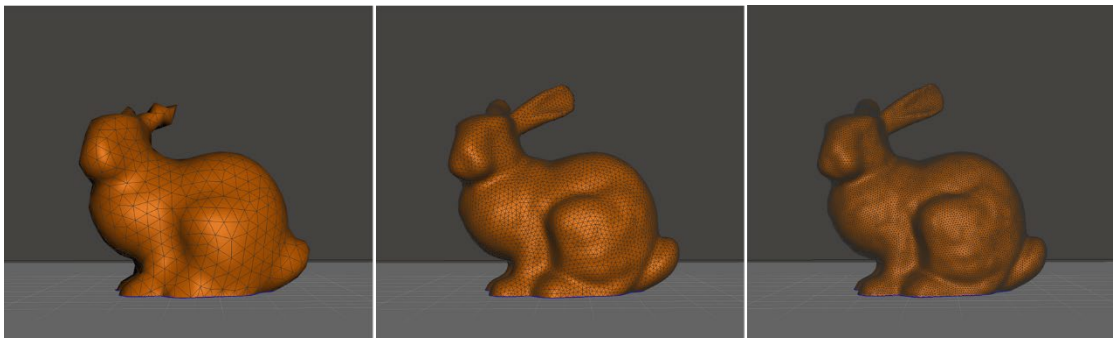

Figure 1.3: Tessellated rabbit model (created from Meshmixer v.3.5.474 software) to demonstrate resolution dependent on the amount of tessellation; visible features are simplified and detail is lost as tessellation decreases.

Once the .STL is formed, a further computer aided function is required. A process called slicing is undertaken where the software 'slices' the model into horizontal layers dependent on the resolution required. The data is then fed into the 3D printer for it to successfully build up a 3D model. There are other file types available, especially for more completed additive manufacturing techniques such as .OBJ, .AMF, .VRML and .3MF which consider more model attributes but are not so commonly used.

1.1.1.1. Material Extrusion

Material extrusion is the most widely used form of 3DP, and the cheapest technology within that sector is fused deposition modelling (FDM) or fused filament fabrication (FFF).

Fused Deposition Modelling (FDM)

FDM works by loading a spool of thermoplastic filament into the 3D printer (as shown in Figure 1.4). The printer nozzle is heated to the desired temperature, whereupon a motor feeds the filament through the heated nozzle, causing the filament to melt. The printer then moves the nozzle along programmed X and Y coordinates, laying down the molten material onto a build plate, whereby cool air is forced onto the material to aid solidification. Once that layer is complete the printer is raised on the Z axis and continues to build the model layer-by-layer. The product of FDM is ideal for the rapid prototyping of engineering and architectural designs. However, limitations of FDM revolve around the elevated temperatures that do not allow for the use of heat-sensitive materials such as clays, biological substances, and polymers. A technique that limits the heat is required and instead uses UV light or other means to construct a 3D object.

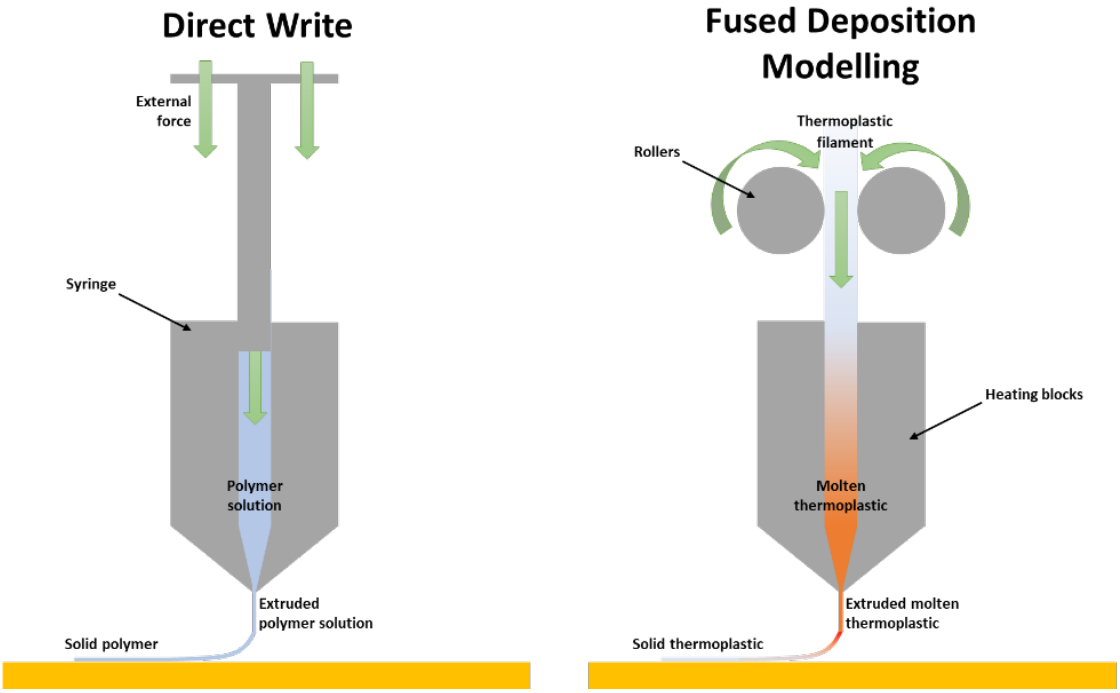

Figure 1.4: Diagram of direct write and fused deposition modelling.

Direct Write (DW) Printing

Two extrusion-based techniques, Robocasting and Direct Write (DW) printing have expanded the field of 3DP for the processing of heat-sensitive materials. For example, inorganic particles inside biocompatible hydrogels have been explored for the fabrication of advanced scaffolds used for tissue regeneration.[27,28] Bio-inspired materials are also being printed displaying flexible and protective properties taken from their inspiration of fish scales.[29] Particulates dispersed in photoactive polymers, also inspired by biological materials, demonstrate the control of particle orientation by application of low strength magnetic fields.[30] Features of viscoelasticity, namely shear-thinning, are key to the room temperature extrusion-based techniques. Work completed by Lewis *et al.* showed the importance of shear thinning on extrusion through micro nozzles, under ambient conditions without the need for high pressures.[31]

1.1.1.2. Vat polymerisation

Vat polymerisation is a 3D printing process whereby a photopolymer resin in a vat is selectively cured by a light source. The two most common are with SLA, it being the pioneering technology for 3D printing and boasts high resolutions of 25 μm, as oppose to 200 μm for FDM techniques.

Stereolithography (SLA) and Digital Light Processing (DLP)

The fundamental principle behind the SLA and DLP technologies is that the light source is used to initiate free radical polymerisation to cure the resin in a single layer. DLP uses projects an image per layer, while SLA uses a point laser to sketch the image. A diagram is shown in Figure 1.5 to illustrate the SLA technique. SLA and DLP 3DP require the laser to penetrate a non-oxygen permeable glass window holding a silicon-based oxygen permeable membrane-polydimethylsiloxane (PDMS) layer and photopolymer resin in place before the laser interacts with the resin. This then requires the build plate to lift and allow resin to flow underneath the build plate after each layer.

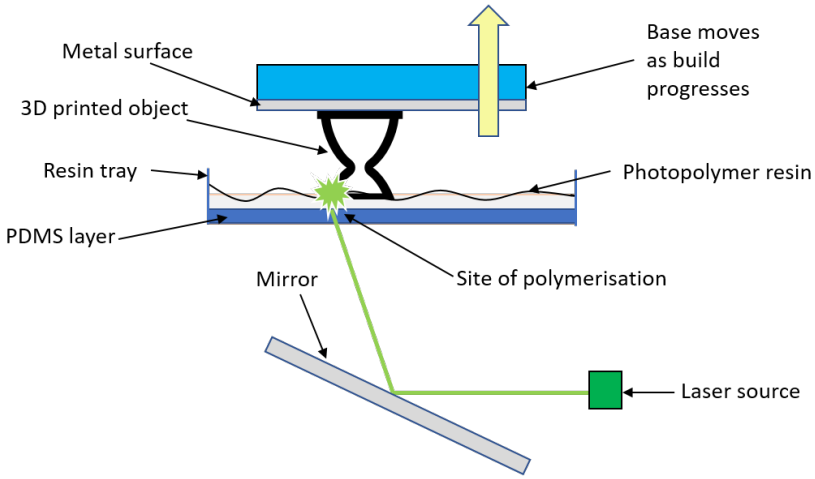

Figure 1.5: Diagram of stereolithography

Photopolymers, photoinhibitors and photoinitiators

SLA and DLP applications utilise photoactive polymers to achieve the desired 3D printed product. Table 1.1 outlines some common photocurable polymers. Photocurable polymers are activated by free radical polymerisation pathways, initiated by photoinitiators on the absorption of UV light. A photoinhibitor may also be added to the mixture to stop over curing of the photopolymers too. In summary, a tuned ratio of photopolymer, photoinitiator and photoinhibitor are formulated to give a viscous photocurable resin.

Table 1.1: Examples of common methacrylate groups that may be used in 3D printing, with relevant abbreviation and molecular structure.

Name	Abbreviation	Structure
Poly(ethylene glycol) diacrylate	PEGDA	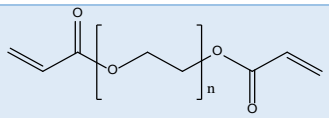
Tetra(ethylene glycol) diacrylate	TEGDA	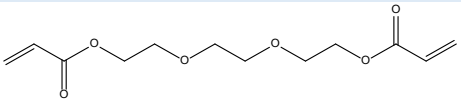

Trimethylolpropane triacrylate	TMPTA	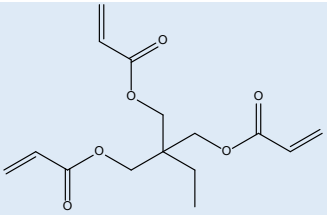
Trimethylolpropane propoxylate triacrylate	TMPPTA	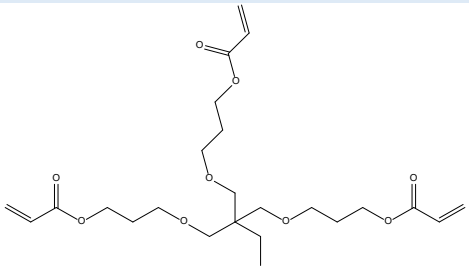

The choice of all three can make a 3D printed product flexible, tough, pliable or rigid. Not only can photopolymers be used in SLA or DLP, they may also be used in in direct write ink,[32] for example Kokkinis *et al.* utilises a formulation of photoinitiators and photocurable polymers characterised by their multiple acrylate groups, to direct-write print a composite material.[33]

Continuous liquid interface production (CLIP) is another technique that along with SLA and DLP uses a UV source and oxygen permeable membrane to inhibit polymerisation at the surface. However, unlike SLA and DLP, CLIP does not need a slow peel and re-coat step every layer, it can continuously produce a 3D printed object in less time and with similar resolution.

1.1.1.3. Powder Bed Fusion

Powder bed fusion methods use either a laser or electron beam to melt, sinter or fuse metal powder together. The powder bed fusion process covers a wide range of techniques including: direct metal laser sintering, electron beam melting, selective heat sintering, selective laser melting and selective laser sintering.[34] The materials used range from common engineering metals such as copper, titanium, aluminium and stainless steel to polymers such as nylon.[34]

The principle behind this technique is that a heat source is used to bind powder, layered onto the build plate 100 - 150 μm thick. The powder is levelled with a roller and selected regions of powder are fused, as outlines by the .STL file. The platform is lowered, new powder is added, and the

layer-by-layer process continues. The benefit of powder bed fusion is that it requires no support material to print, since all parts are supported by unused powder material. This allows for more complex geometries; it does however have limits as unfused powder can be trapped in enclosed pores or fine channels of a component. Powder bed fusion is not as readily available or a cheap process and remains in dedicated additive manufacturing factories due to the use of loose powders and stringent clean room conditions.

1.1.1.4. Material Jetting

Material jetting creates objects in a method similar to ink jet printers used to print ink on paper. Material is jetted onto the build platform, where it is cured by UV light and the model is built up layer-by-layer. The technique gives a product with a great finish in likeness to a manufactured component wich can be temperature resistant, biocompatible, stiff or flexible. It is however limited to a small build volume and is a time intensive process with a few post-processing steps, but can have incredible resolution of 16 μm.[35] Material jetting technology can also print multi-material and multi-colour parts, because, as with a normal inkjet printer, there are multiple cartridges or print heads allowing different materials and colours to be processed.

1.1.1.5. Binder Jetting

Binder jetting uses two materials; a solid powder-based material and an aqueous binder. The powder is spread over the build platform, the binder acts as the adhesive and is deposited from the print head. The process is continuous in layer-by-layer stages and the result is a material of a range of colours made from a range of materials – metals, ceramic and polymers.[36] However, the process is not good for structural components, as the layer adhesion is not great enough. There are also additional post processing steps that add significant time.

1.1.2. Applications of 3DP in Chemistry

As the field of 3DP has grown, accelerated by the ability to generate complex 3D geometries, Chemists, chemical engineers and those in other fields have begun to exploit 3DP to develop their

own research. These new objects have been designed to be used in analytical, biological and pharmaceutical applications. An interesting take on 3DP is the generation of reactionware.

1.1.2.1. 3DP reactors

The principle of reactionware is to 3D print a modular reactor design. The practise of bespoke reactor design is typically seen in large-scale chemical engineering. The whole process is completed by coupling CAD and 3DP software. This brings a large-scale manufacturing process onto the laboratory bench. Reactionware's innovators Cronin *et al.*, generated a connected network of containers that facilitated the synthesis of a muscle relaxant, Baclofen.[37,38] Their 3DP container facilitated three reactions with several extraction, filtration and isolation steps required for synthetic intermediates and the final product. This type of compartmentalised flow reactors is designed to exhibit specific reaction kinetics and produce a high yield with high repeatability. The benefit of reactionware is the low cost of components that are usually, expensive, bespoke and fragile. The processes can be finely tuned by small variations in each print allowing the process to be fully optimised.

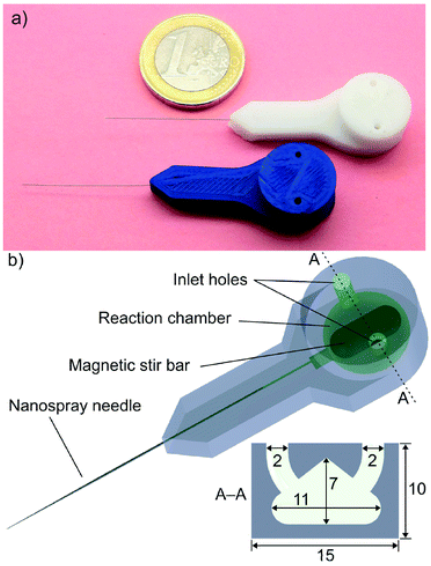

Figure 1.6: 3D printed miniaturised microreactor which can be coupled to mass spectrometer. Reproduced under the creative commons, BY-NC 3.0, Royal Society of Chemistry, 2017.[40]

The practise of continuous flow reactors traditionally use glass columns, however with 3DP these can be replaced with cheaper material and tailored design alternatives.[39] While typically PLA and

ABS are the common 3DP plastics, they are not solvent resistant and dissolve in a wide range of solvents. Polypropylene (PP) can be used instead which has higher solvent resistance but does produce less well resolved objects as it is prone to warping and has poor layer adhesion. 3DP in the chemical field typically is quicker, cheaper and more precise than traditional methods and with resolutions down to the micron scale 3DP lends itself to fabrication of lab on a chip devices.

1.1.2.1. Lab on a Chip and Microfluidic Devices

Lab on a chip technology aims to shrink down the chemistry laboratory onto a single integrated circuit to perform single or multiple laboratory functions. The field is primed for 3DP, as use of a 3D printer replaces the need for time intensive glass laser sintering and expensive cleanrooms. But the correct technique must be selected to reach fine resolutions of < 100 μm. Current techniques use SLA to print lab on a chip devices, with applications ranging from mass spectrometry,[41,42] microfluidic probes,[43] and bio-sensing.[44–46] There are many examples of 3D printed microfluidic reactors for studying chemical reactions which include fabricating a 3D printed reactor combined with IR and UV-vis spectroscopy.[47–49] The miniaturisation of a reaction vessel coupled onto a mass spectrometer allows the reaction to be followed nearly instantaneously.[50] The fabrication technique utilises 3D printing by printing the device, the print is paused to allow the addition of a stirrer bar, which is then sealed in, reactants are then added and connected to the mass spectrometer, Figure 1.6.

Not only can the reactor vessel be 3D printed but the magnetic stirrer bar can be 3D printed to good effect. Typically, magnetic stirrer bars are capsule shaped and are so as they are quick to manufacture. However, the design of the bar can be altered to maximise their efficiency.[51] This can be developed further to have impregnated catalyst into the 3D printed stirrer bar which may improve the reaction time further.[52]

1.1.2.2. 3DP Pharmaceuticals

The field of 3DP has been able to personalise many objects, by bespoke architecture, colour and material. But one novel and potentially powerful application is the rise of digital pharmacies - 3DP of personalised medicine.[53] The ability to 3D print medicines into any dosage,[54] any shape,[55] tuned drug release kinetics,[56] and multiple active pharmaceuticals will be incredibly disruptive to the pharmaceutical market.[57] The market of wound dressing can also be tailor made but also deliver the required drugs from anti-bacterial to pain relief,[58] and also 3D printed models to test a wide application of pharmeuticals.[59]

Figure 1.7: 3D printed paracetamol with different geometries. Reproduced with permission from Elsevier.[60]

An example of the impact of 3D printed pharmaceuticals can be seen by the work of Gaisford *et al.* whereby they 3D printed paracetamol, Figure 1.7, with caffeine at different dosages but additional undertook work to optimise the shape and design of the 3D printed object.[56]

In addition to oral 3D printed drug delivery systems, transdermal and implantable drug delivery systems are used to treat clinical conditions. Conventional methods of fabrication may be complex, involving complex shapes, control of internal architecture and control of complex drug release profiles. Lin *et al* .developed subdermal implants for drug delivery. In a similar manner to implanted drug delivery, transdermal delivery offers ease of administration for much more common diseases such as diabetes. Gaisford *et al*. has 3D printed a customised wound dressing for the nose, based off a 3D scan, Figure 1.8. The dressing displays a sustained drug delivery

profile and offered a bespoke and adaptable coverage against flat dressings. Another transdermal 3D printed device are microneedles, printed by CLIP technique. Johnson *et al.* showed a customised size and shape micro needle, Figure 1.9.

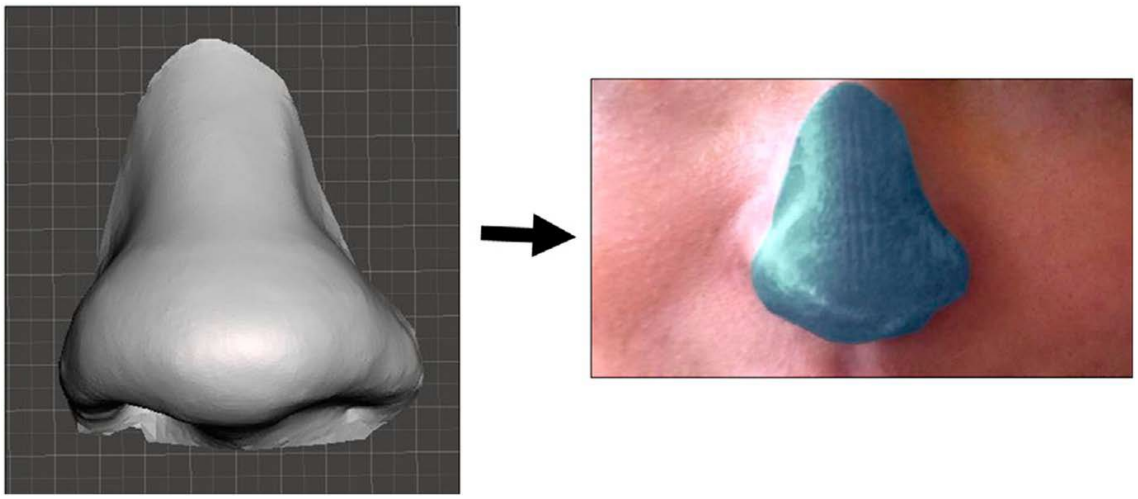

Figure 1.8: 3D scanned nose and 3D printed transdermal drug delivery, Reproduced with permission from Elsevier.[61]

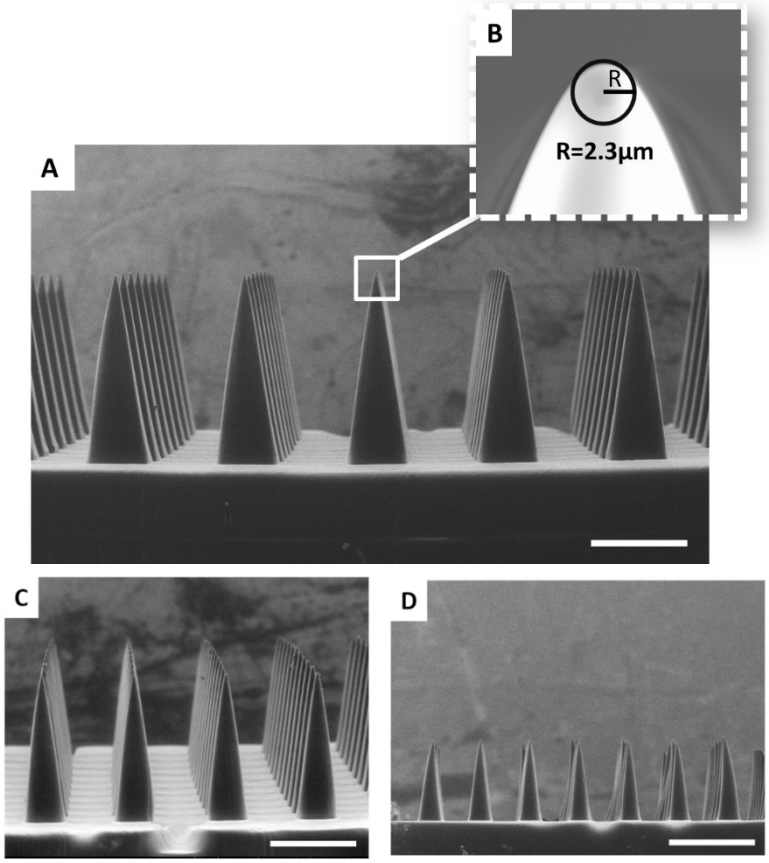

Figure 1.9: 3DP of microneedles using CLIP technology. Reproduced under the creative commons BY 4.0 from PLOS one.[62]

3DP offers a unique capability to fabricate different drug delivery systems but problems include low resolution, thermally unstable drugs, toxic 3D printable materials and limited biocompatible materials.

1.1.2.3. 3DP for education

The use of 3DP in chemistry teaching also helps many students and educators understand and visualise difficult concepts, such as 3D printed molecule to demonstrate stereochemistry,[63,64] or the atomic structure of elements, Figure 1.10. 3DP can also be used in the hospital environment by the 3DP of MRI brain scans to help demonstrate brain anomalies such as tumours; they may be also used by surgeons to visualise cancers in a physical 3D environment before costly surgery is undertaken.

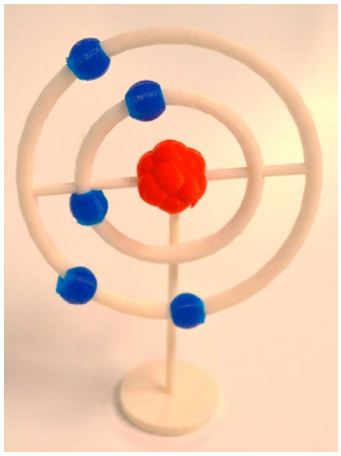

Figure 1.10: 3D printed Bohr model of Boron. Reproduced with permission from ref.[65] Copyright 2016 American Chemical Society

3DP can also be used to help visualise MOFs such as MIL-53, Figure 1.11, in a space filling model or the stick and ball model such as with SLA 3D printed NU-1000 in Figure 1.12. The model was produced by loading the CIF file c8ce00455b2 into Mercury v.3.10 and exporting as an STL to Preform v.3.01 software using 25 μm layer height.

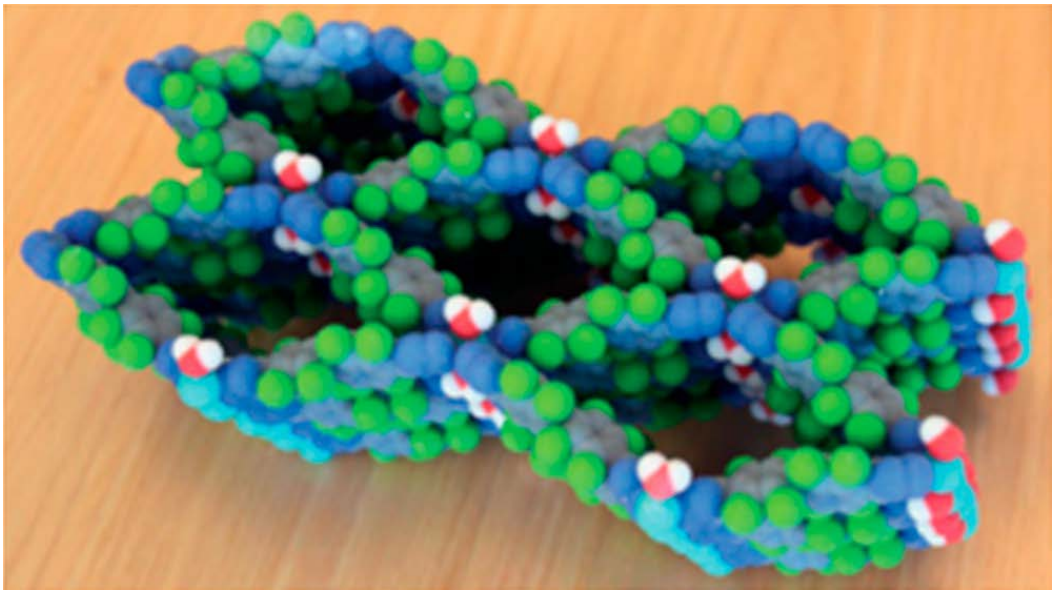

Figure 1.11: 3DP of MIL-53 MOF. Picture reproduced under creative commons BY-NC 3.0 from the Royal Society of Chemistry, 2014.[35]

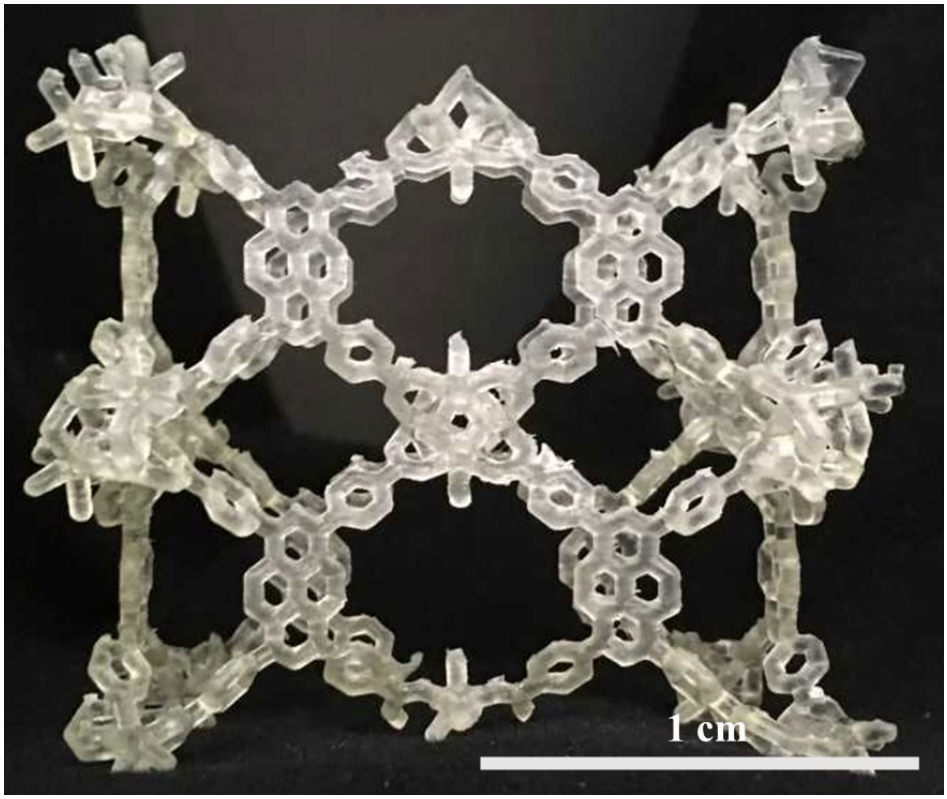

Figure 1.12: SLA 3DP of NU-1000 from CIF file c8ce00455b2.

1.1.2.4. 3D Printing for carbon capture

Carbon capture is an essential strategy for a carbon neutral or even carbon negative and a reduction of global climate change. Currently carbon capture has been used to capture CO_2 from

fossil fuelled power stations, cement factories or biomass power plants. The economies of scale make taking carbon from these heavy CO_2 producers commercially viable, using a series of scrubbers or even more novel technologies. Drax Power station have pioneered a new bioenergy carbon capture and storage system that includes turning CO_2 emission into fish food by means of fermentation with microbes.[66] Due to the price and infrastructure needed smaller manufacturing sites vent CO_2 to the atmosphere and add to the green-house effect. To combat this there a novel approach to carbon capture including: solvent impregnated polymers,[67] membranes,[68] and advanced CO_2 capture solvents.[69]

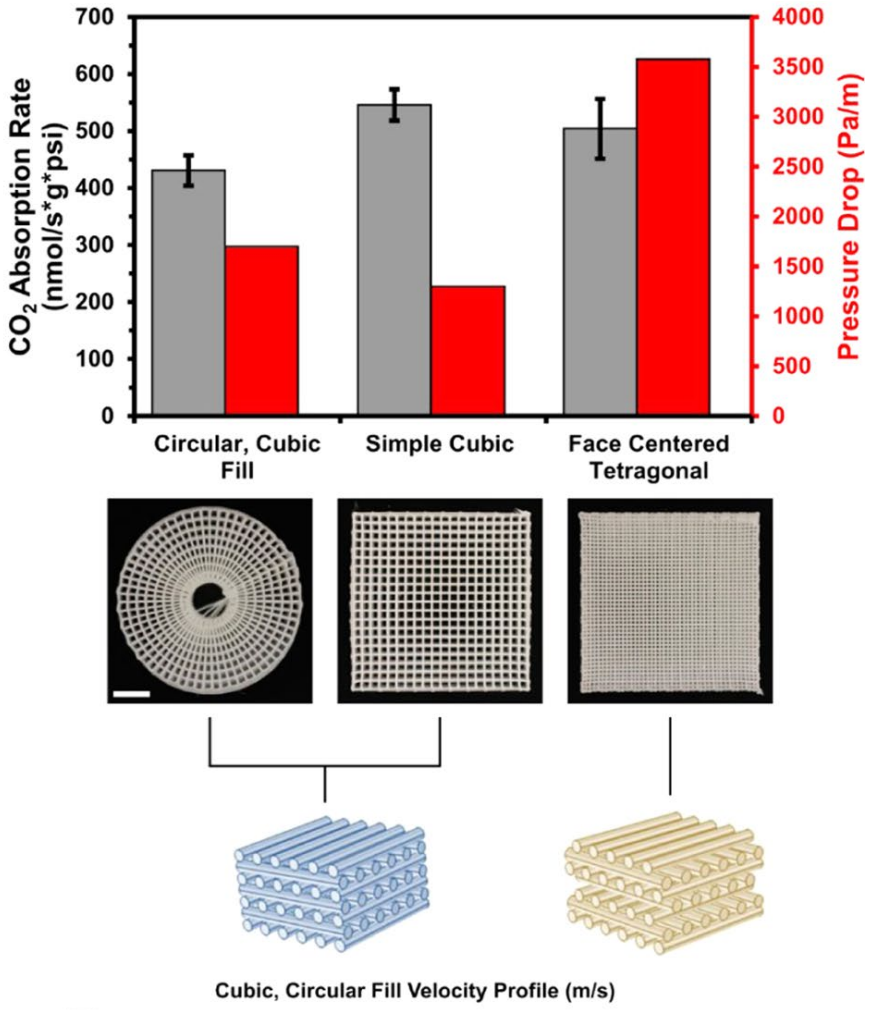

Figure 1.13: Impact of 3D printed geometry on CO_2 absorption. Reproduced with permission from ref. Copyright 2019 American Chemical Society.[71]

One more novel approach is to take an simple but effective approach to carbon capture using 3D printing and $NaCO_3$. The use of $NaCO_3$ ($Na_2CO_3 + CO_2 + H_2O \rightarrow 2NaHCO_3$) has been well documented and holds high efficiencies toward uptake of CO_2.[70] Stolaroff *et al.* combined $NaCO_2$ with a polymer ink to form a 3D printed polymer composite capable of CO_2 capture.[71] The group then went on to adjust the structure that was being 3D printed to allow maximum CO_2 uptake, Figure 1.13. In 2019 it was announced that the National Science Foundation have funded a project in the USA to 3D print concrete that incorporates CO_2 into the mixture.[72]

1.1.2.1. 3D Printing for pollutants.

The uptake of pollutants, much like carbon capture, relies on the absorption of the material to selectively absorb the polluting chemical. A known and well researched material for the removal of toxic metal pollutants in aqueous solutions are hydrogels. Hydrogels exist in a large variety of forms and recently, Smaldone *et al.* demonstrated the 3D printing of hydrogels that remove toxic metals from water and by using 3D printing they can create shapes that would be difficult to fabricate using traditional methods.[73] Another 3D printable material able to tackle pollutants TiO_2 nanoparticles in a 3DP thermoplastic to create a structure with active chemistry.[74] TiO_2 was incorporated at 1 – 10% concentrations and tested to be able to photo catalyse the degradation of a rhodamine solution. This area is greatly underappreciated and has potential to offer much more.

1.2. 4D Printing (4DP)

There have been many advances in additive manufacturing, one such advance is the 3D printing of smart materials that react to external stimuli. This has led to the development of an exciting new technology. 4DP technology is defined as 3DP a material that changes in the 4^{th} dimension – time. The 4D printed material changes shape, properties or composition respective to time by stimulation from an external source: light, magnetism, heat or chemical. 4DP puts the focus onto the material's physical properties rather than the engineering technology. The title of 4DP was

coined in 2013, but looking retrospectively, the work in many 3DP publications could be described as 4DP.

A few examples include work by Compton *et al.* on magnetic 3DP, whereby with the application of a magnetic field, the mechanical properties of the material are changed.[75] More common 4DP applications focus on a reactive shape change to an external source, with the potential for a 4D printed material to open when in contact with water, Figure 1.14.[76,77]

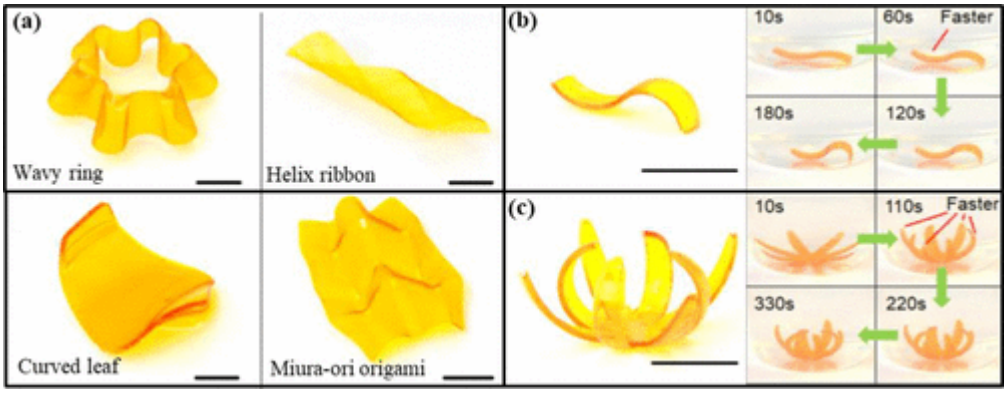

Figure 1.14: 4DP of shape changing when in contact with water. Reproduced with permission from ref. [77] *Copyright 2018 American Chemical Society.*

In microfluidics, the creation of values that are capable of controlling flow in response to changes in the flowing solution are of significance. A macroscopic valve that has been SLA 3D printed responds to fluctuation in temperature and pH, this has many applications including medical devises.[78] The future and finale of 4DP would be the printing of functional human organs, that respond to the body and that are made from the cells of the patient, alleviating the need for anti-rejection medication and alleviating the need for the oversubscribed donor transplant list. Also potentially classed as 4DP would be 3D printed catalyst that require activation by heat,[79] chemical activation, or light.

1.3. Survey of Metal-Organic Framework (MOF) Chemistry

MOFs (by their IUPAC definition) are coordination compounds continuously extending in 1D, 2D or 3D with an open framework containing potential voids.[80] Advances within the last 20 years has seen the term MOF used frequently, however the terminology and definition have been blurred with historic use of the terms coordination polymer and coordination networks. However,

coordination polymer and coordination network should not be used synonymously. Coordination networks are a subset of coordination polymers. Further still, MOFs are a subset of coordination networks.

A coordination polymer is defined as a coordination compound with repeating coordination entities extending in 1D, 2D or 3D.[81] A coordination network is a coordination compound extending through repeating coordination entities in 2D or 3D and in 1D can have cross-links between two or more chains, loops or spiro-links.[81] One thing is certain between all three nomenclatures is the linkage of metal nodes commonly from the d- or f-block and a ligand. Since around 1990 a large library of MOFs has been accessible to both researchers and industry, with 20,000 different structures of MOFs being reported and studied.[17]

1.3.1. History of MOFs

The field of MOFs has evolved rapidly over a period of 30 years to a stage where it is now one of the most widely investigated areas of materials chemistry. The family of extended coordination compounds can be traced back to uses in the eighteenth century when Prussian blue $Fe_4[Fe(CN)_6]_3$ (Figure 1.15), was used to dye uniform coats for the Prussian army.[82] The nineteenth century saw Prussian blue used to create blue prints but it was not until the twentieth century in 1916 where the compound was named - coordination polymer.[83] It is not until relatively recently that the term MOF has been used.

The attractiveness of MOFs is attributed to their high surface area generated by pores within the structure. The 3D arrangement of metal and ligands has led to many applications being discovered by chance but many MOFs having one or more application in gas storage,[84–86] catalysis,[87–89] energy storage,[90–92] drug delivery,[93–95] and sensing.[96–98] Depending on the final structure and properties of the MOF, they may be prepared using several distinct synthetic methods: solvothermal,[99,100] electrochemical,[101] mechanochemical,[102] microwave,[103] ultrasound,[104] and

slow diffusion.[105] The morphology of the MOF can also be tuned from rods, to cubes such as Prussian Blue seen in Figure 1.16.

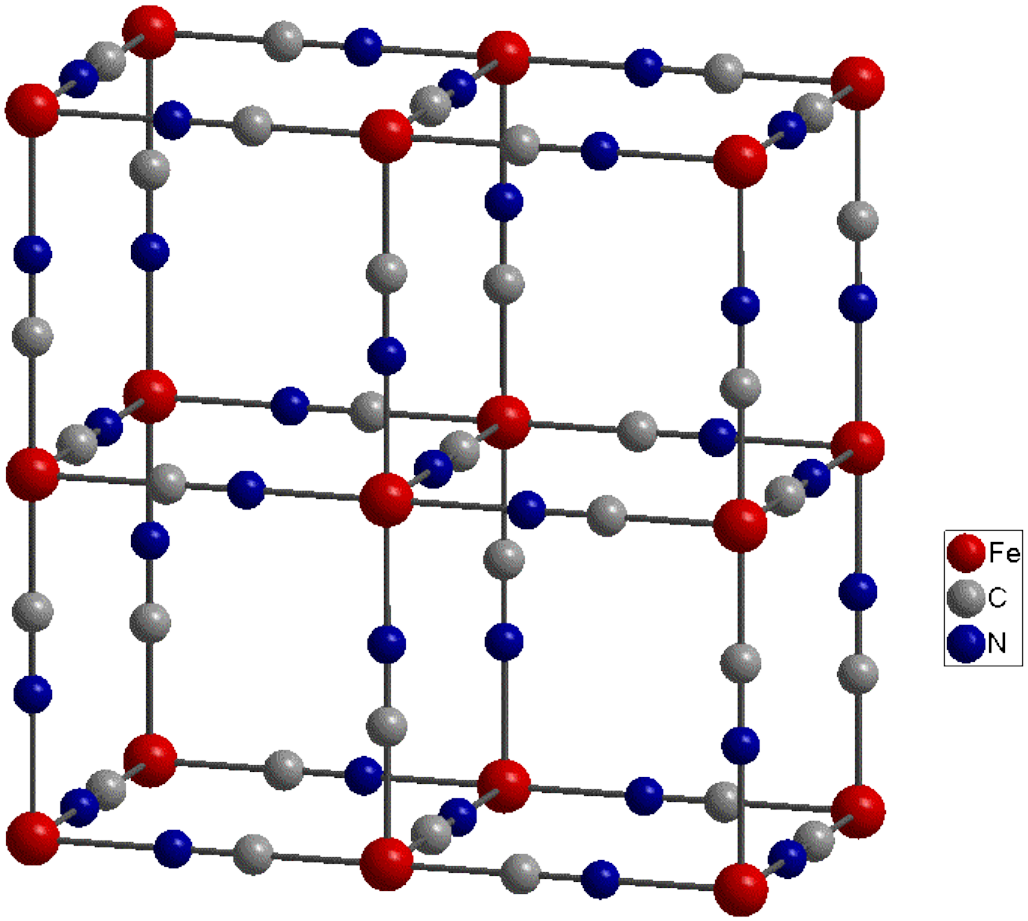

Figure 1.15: Prussian Blue.

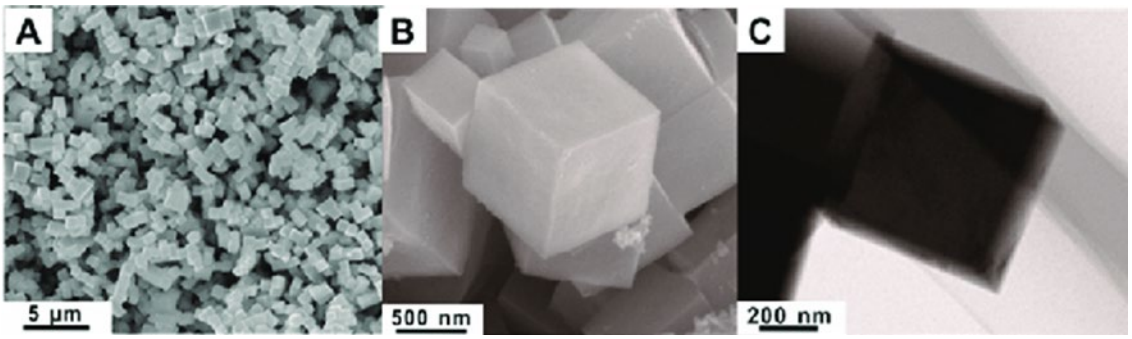

Figure 1.16: Prussian Blue MOF cubes viewed by an SEM (A and B) and by TEM (C). Reproduced with permission from ref.[106] Copyright 2017 American Chemical Society.

1.3.2. Nomenclature

MOFs have no systematic way of naming but have been named to show how the composition or structure has evolved. In such instances, MOFs are named as UiO, NU and the MIL series

representing research groups based at the Universität i Oslo, Northwestern University and Materials of Institut Lavoisier, respectively. Succeeding the acronym is a number series which is frequently trivial in origin but offers a chance for an institution to make a series or family of MOFs for example, UiO-66, UiO-67, UiO-68 or NU-109 and NU-110. The larger the number may offer some indication as to the porosity of the network but is not definitive and comparable across MOF families. Alternatively, they could be labelled simply MOF or zeolitic imidazole framework (ZIF), the latter being a topic in itself through their unique similarities to zeolite-topologies.[107,108]

1.3.3. Applications of MOFs

MOFs have many multifaceted applications but their affinity for gas sorption, separation and storage properties are most notable.[109] The properties of MOFs for these applications can be altered by functionalisation of the surface or internal pore structure. Surface modification of MOFs can enhance stability and selectivity and control hydrophobic/hydrophilic properties. Functionalisation of the internal pores can be achieved using functionalised linkers, such as amino-terephthalic acid or nitro-terephthalic acid. However, the modification may lead to reduced absorption, as the pore volume is reduced,[110] but it does allow for post-synthetic modification of the surface of the MOF,[111] allowing a larger range of functionalisation leading to a higher selective and higher capacity of the MOF.

1.3.3.1. Catalysis

MOFs are attracting considerable attention as heterogenous catalysts under moderate temperature. There is a wide selection of MOFs that are suitable for catalysis with incredibly diverse applications from hydrogen evolution,[112] esterifications,[113–115] to polymerisation.[116] This it to name but a few catalytic reactions performed by MOFs, due to diverse range of metal centres, high surface area and porosity they make incredibly efficient heterogenous catalysts. Structural stability is one of the major concerns for MOFs in liquid-based catalysis, as many reported MOFs

are unstable and lack structural and chemical robustness if they are agitated during catalysis. To that end the most commonly used MOF for catalysis is the zirconium-based UiO-66, hailed for its mechanical strength and chemical stability.[117–120] UiO-66, Figure 1.17, has been widely studied in recent years as a heterogenous Lewis acid catalyst. The presence of the Zr^{4+} metal sites, and their affinity for catalysis, has led to the study of a variety of catalytic reactions being undertaken including aldol condensation and cyclization of citronellal among others.[121] Strategies have also been developed to increase the catalytic ability of UiO-66 by defect engineering,[122,123] a process of dihydroxylation and thermal activation, creating more active sites and increasing rate of catalysis.

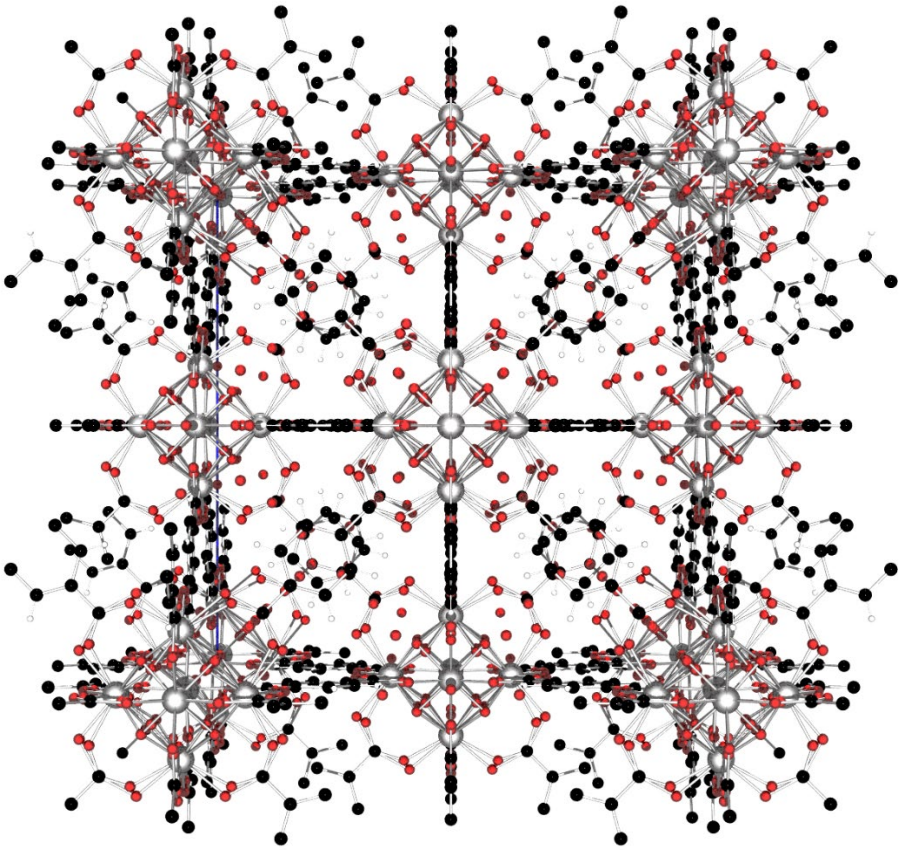

Figure 1.17: UiO-66 modelled from Cif 4152072 using Mercury v.3.10

Other such MOFs that have been demonstrated as catalysts include MIL-125, MIL-53 and UiO-66-NH_2. The introduction of the NH_2 group onto the ligand of the MOF can change the ability of the MOF, for instance in photocatalysis the addition of the NH_2 groups results in a MOF

producing a new band in the visible region resulting in application.[124] MOFs may also be used in electrochemical catalysis, with examples including MOF thin films being studied for the CO_2 reduction and water oxidation.[106] In summary, there may be existing MOFs with currently unknown potential for catalysis and still new MOFs to be discovered and new catalytic routes uncovered.

1.3.3.2. Adsorption, Separation and Storage

Many MOFs, particularly divalent Cu^{2+} based HKUST-1, show high performance in CH_4 and H_2 storage due to the exceptional porosity.[85] While other MOFs, such as zirconium-based MOF-801 and MOF-841, showed good performance in the adsorption and release of water, especially useful for applications such as thermal batteries, dehumidification and delivery of drinking water to dry areas.[121,125,126] Not every MOF is suitable, as some may susceptible to hydrolysis, or not possess the correct pore size and flexibility to contain gases. However, due to MOFs high tunability and versatility they could be utilised to remove toxic gases from the air.[127] Toxic gases can be captured in MOFs by controlling the pore and functionalisation of the pore environment, examples include H_2S adsorption using MIL-53,[128] and even the use of the MOFs functionalisation to degrade toxic gases into non-toxic substances.

1.3.3.3. Sensing

MOFs can be tuned to act as sensing devices either by fluorescence sensing or directly converting a stimuli into an electronic signal. MOFs are an attractive alternative in sensing applications as traditionally and most frequently used methods are based on gas-chromatography. Although it is a precise technique, it is less than practical a smaller MOF device. MOF-801, mentioned above, offers selective H_2S detection in low concentration of 100 ppb while its detection of CH_4, NO_2, H_2 and toluene were in the region of 10 ppm.[129]

1.3.3.4. Energy Storage

The world is turning to more renewable energy sources such as wind or solar, however they are intermittent. To deal with this issue research is being carried out into electrochemical and photoelectric energy storage. MOFs are being used in devices such as fuel cells, metal-ion batteries, Li-ion batteries and supercapacitors. MOFs are attractive to the field of energy storage for a variety of reasons:

a) MOFs can act as electron reservoirs and improve the capability of the batteries, Figure 1.18a.
b) Some batteries such as lithium-sulphur batteries require a store of lithium sulphide ions, which can be trapped in a MOF, Figure 1.18b.
c) MOFs are very efficient catalysts and could reduce or evolve O_2 from reactive species, Figure 1.18c.
d) MOFs can be used to store charged species, due to their ultrahigh surface area, Figure 1.18d.

The limitation of MOFs is that a composite slurry must be made, which limits their ability to function. To address this issue, MOF films can be employed using a polymer composite limits function by reducing charge conduction pathways. New forms of MOFs such as amorphous MOF gels, liquid and glasses show promise in the area of energy storage as transparent materials with high flexibility, high charge mobility and no grain boundary.

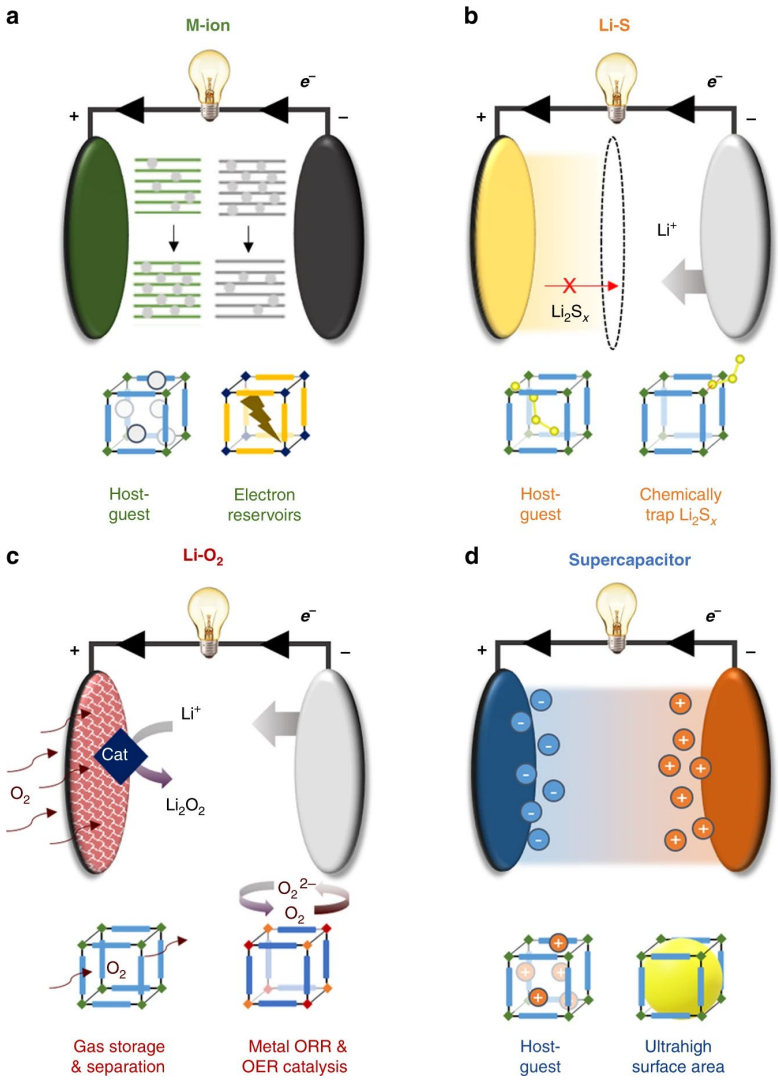

Figure 1.18:Schematic of how MOFs interact or can be used in metal-ion batteries (a), how MOFs can be used in lithium-sulphur (b) batteries, how MOFs can be used as catalyst is lithium-oxide batteries (c) and how MOFs can be used in supercapacitors(d). Reproduced under creative commons BY from Springer Nature, 2019.[106]

1.3.4. Glass and Liquid MOFs

Crystalline MOFs, as discussed and exampled above, have applications for a variety of situation that take advantage of their highly ordered and porous structure. Non-crystalline, or amorphous MOFs are relatively new and theoretically lack the porosity that is the attractiveness of MOFs, Figure 1.19. However, recent work has shown both glass and liquid MOFs to have porosity.

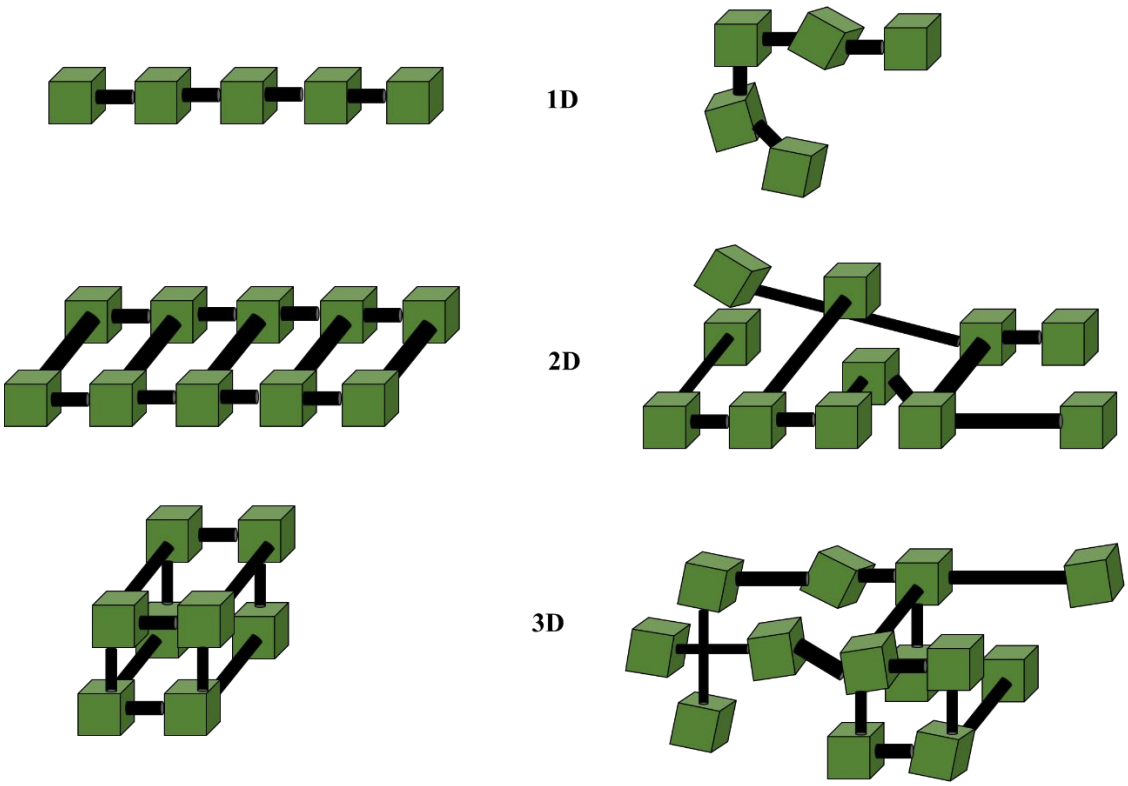

Figure 1.19: Demonstration of 1D, 2D, 3D crystalline and amorphous MOFs

Amorphous MOFs or glass MOFs can be formed by the avoidance of crystallisation, this can be achieved by rapid cooling of a liquid to form the glass state.[130] Recently the formation of the glass state was studied by the Hybrid Materials group led by Dr. Tom Bennett at the University of Cambridge, the group showed that a glass MOF is possible.[130] The formation of a glass MOF makes prime candidates for gas separation membranes.[131] The group then went on to demonstrate that liquid MOFs are possible and their ability to blend two MOFs.[132,133] The processing technique named 'flux melting' employs the use of one MOF, that has a high temperature liquid state' as a solvent for the secondary MOF. While the technique is not novel the ability to blend two MOFs in a composite that demonstrate isotropy with limited grain-boundary is novel and an up and coming research that may overcome MOFs lack of processability but is still in its infancy.

1.3.5. Reproducibility Crisis

It is due to a large expanse of synthetic methods that MOFs are undergoing somewhat of a reproducibility crisis. In 2017, Park *et al.* demonstrated that for CO_2 adsorption there are only 15

of thousands of known MOFs for which enough experiments have been reported to allow reliable conclusions to be drawn about the reproducibility of these measurements.[134] This is an important stage in the development of useable MOFs. Taking a view from other fields of research improving reproducibility has been developed, as there are many recent publications on reproducibility in research and science,[135–137] but they should not apply to all fields without some investigation. A formula has been hypothesised by Scholl *et al.* outlining a potential power law existing for the repeat synthesis of materials.[138] The equation is a power law. Power laws have been found to describe many phenomena including size of cities,[139] wealth distributions,[140] and number of citations in academic papers.[141] While Scholl *et al.* concluded that from the 130 MOF materials investigated 65% were modified synthesis that had been reported without information about a repeat synthesis of the original material.[138] Scholl *et al.* identified that a synthesis may have been performed but the results left unreported, this may be true in published work were words are limited and content scrutinised for relevance or scientific progress. A gap has been identified and the realisation that reproducibility of experiments is important, and it should direct future efforts of the MOF community to learn about the reproducibility of materials synthesis.

1.3.6. Scalability of MOF synthesis

MOFs have many promising properties and applications but to be of societal use, they need to be produced in large quantities. There are only a few companies commercially producing MOF products, outlined in Table 1.2. Some of the companies are established chemical suppliers such as Sigma-Aldrich, while others are new to the market such as Immaterial, who do not actively sell MOF product but instead sell their process to bespoke manufacture MOFs to the desired application. Taking Sigma-Aldrich as an example, MOF products, such as HKUST-1, are expensive at £7710.00 per 500 g.[142] For MOFs to be produced sustainably - in a green, cost-effective manor there are a few considerations:

- Use of cheap, renewable, recycled and recyclable starting reagents
- Use of solvent-less or green solvent systems.

- Use of cost-effective energy sources
- Optimisation of synthetic method

These are difficult considerations to achieve but active research is taking place. The employment of green chemicals based on renewable sources is showing promising results, by the replacement of *N,N*-dimethylformaide (DMF) which is toxic, flammable and teratogenic with water and less hazardous modulators such as fumaric acid. There are synthetic techniques which are solvent-less and rely on grinding two powders and placing into an autoclave, and heated they may still be energy intensive and so must use cost effective energy sources.[143] There are many synthetic methods used for MOF synthetic with some outlined in Table 1.2, others include ultrasound, water-reflux, steam assisted and the most commonly used is solvothermal and continuous flow.

Table 1.2: MOF manufacturers, process and available information on MOF products available on the market

Company	Process	Available MOF products
MOF Technologies Ltd, UK.[144]	Mechanochemical	MOF-74 (Mg) HKUST-1 ZIF-8 MIL-53 (Al) MOF-74 (Mg)
Promethean Particles, UK.[145]	Continuous flow	MIL-53 (Al) ZIF-8
Immaterial, UK.[146]	Continuous flow	ZIF-8 Bespoke manufacture
novoMOF, CH.[147]	Continuous flow	ZIF-8 Bespoke manufacture
Sigma-Aldrich, DE.[142]	Electrochemical	ZIF-8 MIL-53(Al) HKUST-1 Fe-BTC MOF-177
MOFapps, NO.[148]	Solvothermal, mechanochemical, microwave-assisted	UiO-66 series MIL-53 (Al) ZIF-8 ZIF-67 HKUST-1
NuMAT, USA.[149]	Solvothermal	Nu- series Bespoke manufacture
Strem Chemicals Inc, USA. [148]	Solvothermal	MIL-100 (Fe) PCN-250 (Fe) ZIF-8

Solvothermal is a batch process whereby the reagents are sealed into an autoclave with solvent and heated to elevated temperatures and then allowed to cool down. This is a common technique in academia but not too commercially viable unless using green solvents and recycling waste. Many companies are choosing continuous flow, outlined in Figure 1.20. The process works by dissolving vast quantities of metal salt, ligand and modulator in solvent and injecting into a micro-reactor where the reaction takes place and MOF formed.

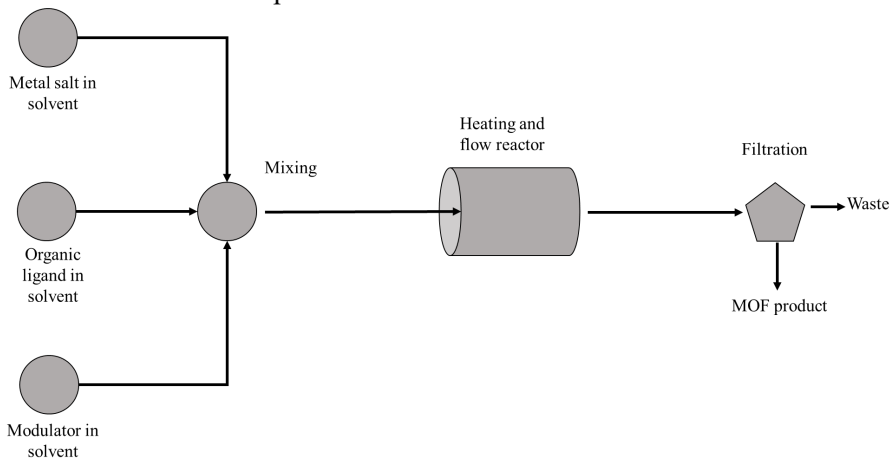

Figure 1.20: Schematic of continuous flow reactor.

1.3.7. MOF-gel

The MOF-gel is in the family of coordination polymers, an arrangement of atoms containing metal cations linked to ligands. When mixed in solution there are three main kinds of aggregates:

1. MOFs, aggregates with long- and short-range order.

2. Metal-organic gels, random aggregates with no order

3. Coordination polymer gel, aggregates with short-range order but no long-range order.

MOF-gels belong to the later subset of coordination polymer gels. The MOF-gel differs to metal-organic gel- which contain linked metal cations and ligands but are not crystalline. Figure 1.21 helps to distinguish the difference between MOF-gel, MOF precipitate or powder and amorphous metal-organic gels.[150]

The MOF-gel state is a colloidal network of aggregated crystalline MOF nanoparticles throughout a liquid phase.[151] A MOF-gel is the result of a concentrated solution of ligand and metal precursors being reacting to form discrete nanoparticles of crystalline MOF.[152–159] The formation of the MOF-gel is the consequence of rapid nucleation of nanocrystals in the high concentration of precursor. The nanocrystals then aggregate, held together by Van der Waals forces, to form a colloidal network. The growth of the nanocrystals into larger microcrystals is hindered as the reactants are consumed in the precursor solution. Bennett *et al.* highlighted several parameters necessary for the formation of UiO-66, MOF-801, MOF-808 and NU-1000.[160] The group showed that the choice of metal, ligand concentration and presence of water play pivotal roles. If nucleation is too fast the result is an amorphous metal organic gel, which displays shear-thinning properties but is an amorphous gel with no properties of a MOF. If nucleation is too slow the result is a precipitate of solid MOFs. A study undertaken by Bennett *et al.* demonstrated the synthetic conditions required to generate a MOF-gel and exhibited the MOF-gels porosity by creating a monolithic MOF xerogel.[151]

On formation of the MOF-gel it exhibits interesting rheological properties, the MOF-gel can transform from a non-flowing gel, to a flow gel by means of a shear force, such as shaking the sample vial. These interesting rheological properties are viscoelastic properties of the gel and typically tested by the inversion of the sample in a test tube, Figure 1.22, presently MOF-gels have not been widely understood for their rheological properties.

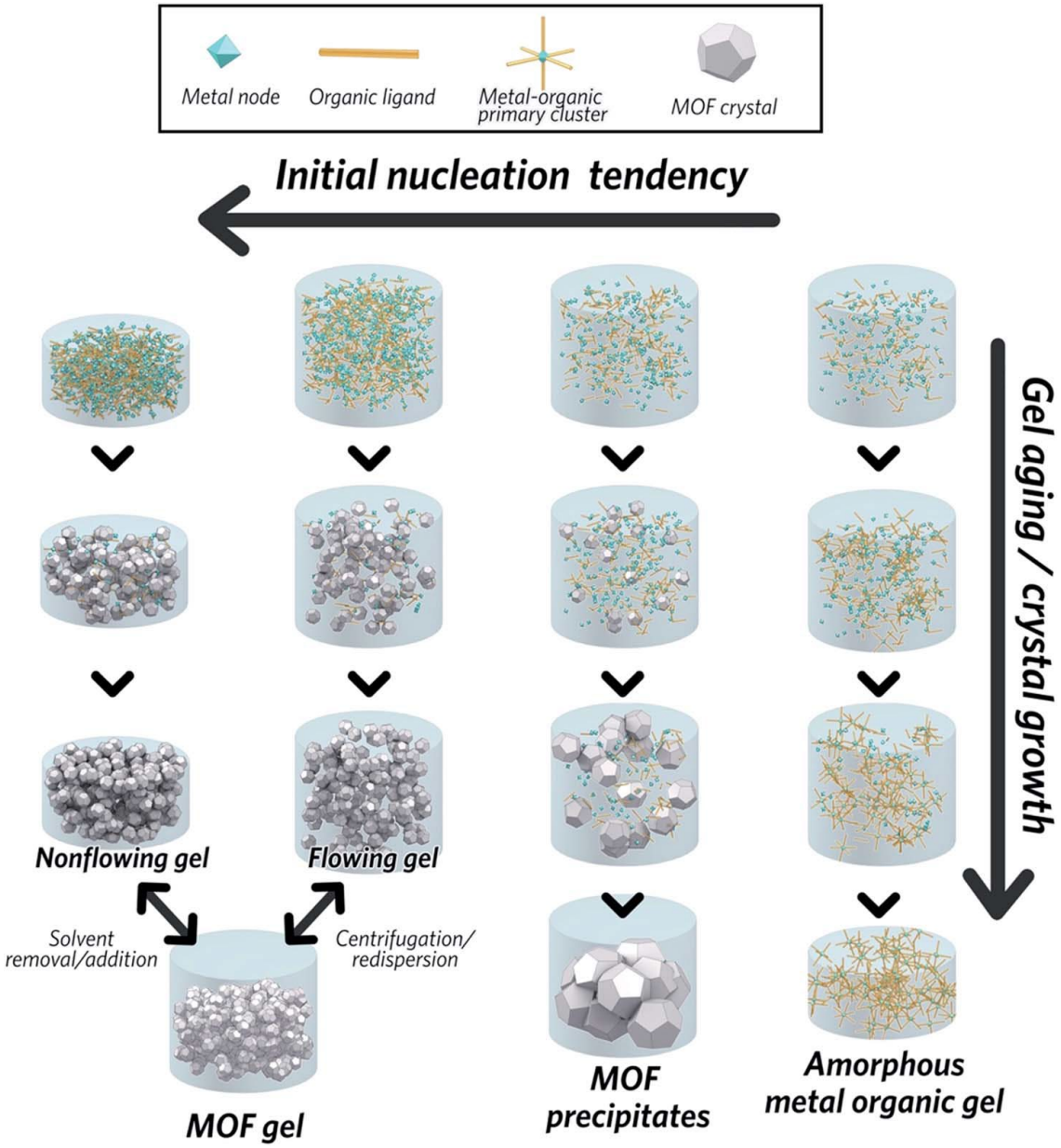

Figure 1.21: Diagram visualising the formation of MOF-gel, ‚MOF precipitate and metal-organic gels. Reproduced under the Creative Commons (BY 3.0) from Ref. [151] *with permission from the Royal Society of Chemistry.*

Figure 1.22: UiO-66 MOF-gel demonstrating the rheological properties by sample vial inversion. Reproduced under creative commons BY-NC 3.0 from Royal Society of Chemistry, 2017.[160]

MOF-gels have found applications in luminescent sensing,[161] adsorption,[162,163] separation,[151] and catalysis.[164]MOF-gels have been shown to be efficient catalysts, which is exacerbated by under-coordinated metal sites within the MOF-gel.[164] It has been suggested by Bennett *et al.* the use of MOF-gels in energy-related fields, but the field currently lacks a scalable fabrication method for MOF-gels.[151]

1.4. Composites

The natural world displays an abundance of composite materials with outstanding mechanical properties. Bone is an excellent example of such material, as it displays fracture toughness comparable to cold steel.[165] However, the constituent materials of bone, collagen and calcium phosphate, are weak on their own and as discrete materials are brittle or difficult to process. The outstanding fracture toughness of bone derives from its hierarchical structure; features at smaller length scale form the basis for features at larger ones. The scientific community has been working towards the imitation of these natural material leading to a new research field labelled bioinspired. These bioinspired materials can exhibit enhanced properties by local alignment of anisotropic fibrils, fibres, and particulates.[32,166] Many fabrication techniques such as lamination and casting

have been used to construct such materials, but an emerging technology such as 3DP shows great promise.

Two 3DP technologies of interest are extrusion-based and stereolithography (SLA). The 3DP of anisotropic fibres is well-established for extrusion-based techniques; anisotropic materials are deposited layer by layer in a bottom up assembly and can be aligned by shear alignment,[31,167] or by external forces such as magnetism.[168]

The alignment of anisotropic particulates for SLA 3DP has also been achieved and has been demonstrated by Martin *et al.* by the 3DP of aligned anisotropic fibres coated in a magnetic particulate, with fibre orientation controlled by electromagnets.[30] Both SLA and extrusion-based techniques ultimately led to a hierarchical composite material of long-range order with increased mechanical properties.

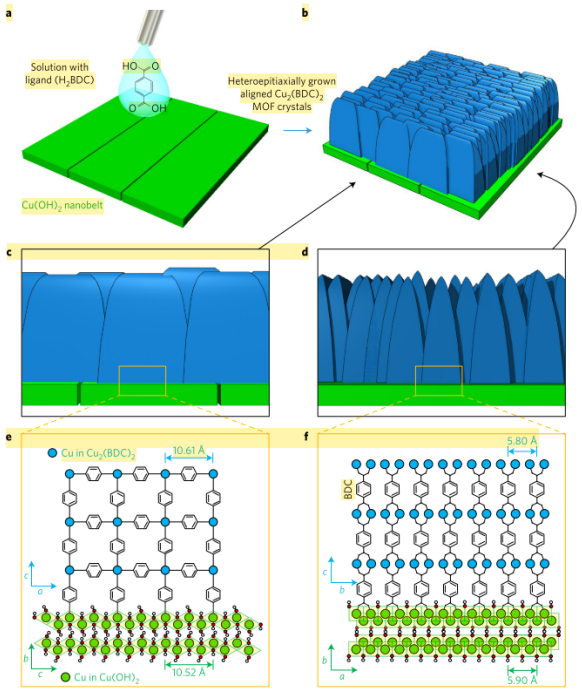

Figure 1.23: Schematic diagram showing heteroepitaxial growth of $Cu_2(BDC)_2$ membrane. Reproduced with permission from ref.[169] Springer Nature, 2017.

1.4.1. MOF polymer composites

MOFs have a great potential for a variety of applications, including but not limited to: gas diffusion,[170,171] useful optical activity,[172] and thermal conductivity.[173] To be the most efficient at these applications the MOFs are tuned to be anisotropic by addition of a coordination modulator to promote crystal growth. Anisotropy is key to these applications as a flow of material is required through the MOF. It is then important if these anisotropic MOFs are to be used that their crystal orientation is controlled, or else the flow of material will not be maximised. Previous innovations for the tuning of MOF orientation have relied on heteroepitaxial growth of growth of MOF crystallites onto a substrate, Figure 1.23, by pre-doping the metal ion onto a substrate before being exposed to a concentration organic linker solution.[174,175] A more recent example required the growth of highly aligned $Cu(OH)_2$ nanotubes on a substrate, before heteroepitaxial growth of MOF crystallites.[169,176] The resulting material being a thin film that is highly efficient for adsorbing florescent dyes and demonstrated an optical polarization of an incident light dependent on orientation.

1.4.2. Processability of MOFs

The ability of MOFs to be processed into different polymer media for applications in membranes, fibres and thin films has been limited by their highly ordered, rigid, crystalline nature. On exposure to external factors such as pressure, shear stress and high temperatures the brittle framework can collapse.[16,17] To surmount these drawbacks, MOFs can now be tuned and synthesised with improved mechanical and thermal properties. For example, Smit *et al.* have used and discussed the effects of modifying the primary or secondary network of ZIF networks on mechanical stability. This is achieved by addition of extra linkers (primary),[177] or the functionalisation of ligands (secondary) to create ZIF networks. This work concluded that mechanical stability can be increased and it functions much like retrofitting a building with supporting beams or the caryatids holding up the porch of the Erechtheion on the Acropolis.[178]

However, there has been limited success at MOF processing within a polymer media, as the polymer blocks the active pores of the MOFs. Advances in the processing methods have led to MOFs being deposited or grown on a porous substrate, showing good applicability towards gas separation on 2D surfaces such as thin films or membranes.[179] However, the need for more complex shapes arises and a better method of processing MOFs that can maintain high flow rates need for efficient practise, is required. To push the boundaries of MOFs new fabrication methods have been trialled such as 3D printing.[180–182] The combination of these two topics (3D printing and MOFs) in which composite materials are extruded layer by layer should enable unlimited amounts of 3D shapes with high surface areas.

1.5. 3D printing of MOFs

MOFs have the potential application to capture CO_2 to help tackle the world's increased CO_2 concentration brought on by the release from fossil fuels. However, their powdered unprocessable forms hinders their application, as they would need recovering from the process by filtration. To overcome this, the MOF can be fabricated with a polymer binder producing a 3D printable ink. Work by Thakkar *et al.* demonstrated two 3D printable inks for two types of MOFs MOF-74(Ni) and UTSA-16(Co) contained in a clay binder.[18] They went onto demonstrate that the 3D printed MOFs are free standing, stable and capable of gas adsorption at a similar rate to their equivalent MOF powders. Another example of a 3D printed MOF was with poly(lactic acid) (PLA) - a common thermoplastic commonly used in FDM 3D printing. Evans *et al.* demonstrated the fabrication of ZIF-8 with PLA to generate another stable, free standing structure with a similar high surface area to the powdered MOF.[181]

Recently, it has been demonstrated that a 3D printed material produced a chemically active architecture for organic reactions.[79] The 3D printed architecture was the site for the active catalysis and was designed for use *in situ* for UV-Vis spectrometry, which allowed the kinetics of the Mannich reaction to be tracked, which was previously impossible due to solids scattering

the signal. This is a clear demonstration of how 3D printing has outperformed traditional processing methods to arrive at an output only achievable by 3D printing.

1.6. Aims & Objectives

The aim of this body of work is to explore how MOFs can help tackle environmental problems including climate change and pollution, for example by reducing CO_2 levels, by employing additive manufacturing techniques. Chapter two outlines some commonly used experimental methods and techniques used through the body of work.

MOFs lack processability, when they are handled, they have the potential to lose functionality. The anisotropic nature of rod shaped MOFs such as MIL-53(Al), MIL-68(In), MIL-68(Ga) and NU-1000 require macro-scale alignment to be able to efficiently use their micro and nano pores, without alignment the MOFs will be inefficient in use. The objective of chapter three is to understand how such MOFs may be aligned and to investigate magnetic alignment of MOFs using iron salts and iron oxide nanoparticles. Proceeding is the fabrication of a novel MOF composite that displays real-world application and demonstrates the novel technique of 4DP for anisotropic MOFs composites which could be applied to future MOFs to tackle by storage of CO_2.

Another key aim is to tackle the problem of pollutants in the environment, relating to climate change. Pollutants such as persistent organic pollutants (POP) need cleaning up from the environment; they damage wildlife and can destroy habitats, ecosystems and because of their persistence impact on human health. Further to the effect on human health some POPs, especially organophosphate based have been weaponised and have been used as nerve agents. Some MOFs namely zirconium-based UiO-66 and NU-1000 have been shown to have great utility at the degradation of nerve agents. But the fabrication for real-world applications, such as nerve-agent degradation, requires the MOF to be submerged in the aqueous solution, this then will require a time intensive step to remove the MOF from the solution by filtration. For the process to be continuous the MOF requires careful fabrication into a composite, to allow the MOF/composite

to function. The objective of chapter four is to develop a novel 4DP technique for the fabrication of a UiO-66 composite that shows good efficiency to degrade nerve agent.

The final objective is to understand how MOF-gels may impact the fabrication of new MOF-based applications. MOF-gels are a lesser known subject when compared to MOFs, however, possess the same or greater catalytic or adsorptive ability. However, MOF-gels lack an efficient fabrication technique. Therefore, the work in chapter five is to achieve a greater understanding of MOF-gels and its viscoelastic properties and how the MOF-gels could be applied to 3DP.

1.7. References:

1 BBC News, UK Parliament declares climate change emergency, https://www.bbc.co.uk/news/uk-politics-48126677, (accessed 9 September 2019).

2 K. Galloway, *Eureka Str.*, 2018, **28**, 45.

3 D. J. Frame, L. J. Harrington, J. S. Fuglestvedt, R. J. Millar, M. M. Joshi and S. Caney, *Environ. Res. Lett.*, 2019, **14**, 84009.

4 C. Heaviside, *Atmosphere (Basel).*, 2019, **10**, 119.

5 M. Lebrato, D. Iglesias-Rodríguez, R. A. Feely, D. Greeley, D. O. B. Jones, N. Suarez-Bosche, R. S. Lampitt, J. E. Cartes, D. R. H. Green and B. Alker, *Ecol. Monogr.*, 2010, **80**, 441–467.

6 J. Blunden and D. . Arndt, *State of the Climate in 2018*, 2019.

7 D. Spratt and I. Dunlop, *The third degree : Evidence and implications for Austrialia of existential climate-related security risk*, Breakthrough - National Centre for Climate Restoration, Melbourne, Austrailia, 1st edn., 2019.

8 Earth's CO2 Home Page, https://www.co2.earth/, (accessed 19 March 2020).

9 M. R. Hartings and Z. Ahmed, *Nat. Rev. Chem.*, 2019, **3**, 305–314.

10 J. Kim, L. C. Lin, J. A. Swisher, M. Haranczyk and B. Smit, *J. Am. Chem. Soc.*, 2012, **136**, 18940–18943.

11 Y. Zheng, X. Li and P. K. Dutta, *Sensors*, 2012, **12**, 5170–5194.

12 S. M. Hyun, J. H. Lee, G. Y. Jung, Y. K. Kim, T. K. Kim, S. Jeoung, S. K. Kwak, D. Moon and H. R. Moon, *Inorg. Chem.*, 2016, **55**, 1920–1925.

13 O. Shekhah, J. Liu, R. A. Fischer and C. Woell, *Chem. Soc. Rev.*, 2011, **40**, 1081–1106.

14 Z. Wang, H. Ren, S. Zhang, F. Zhang and J. Jin, *J. Mater. Chem. A*, 2017, **5**, 10968–10977.

15 Z. Kang, L. Fan and D. Sun, *J. Mater. Chem. A*, 2017, **5**, 10073–10091.

16 N. C. Burtch, J. Heinen, T. D. Bennett, D. Dubbeldam and M. D. Allendorf, *Adv. Mater.*, 2017, **30**, 1–18.

17 H. Furukawa, K. E. Cordova, M. O'Keeffe and O. M. Yaghi, *Science*, 2013, **341**, 974–988.

18 H. Thakkar, S. Eastman, Q. Al-Naddaf, A. A. Rownaghi and F. Rezaei, *ACS Appl. Mater. Interfaces*, 2017, **9**, 35908–35916.

19 S. C. Ligon, R. Liska, J. Stampfl, M. Gurr and R. Mülhaupt, *Chem. Rev.*, 2017, **117**, 10212–10290.

20 C. Buchanan and L. Gardner, *Eng. Struct.*, 2019, **180**, 332–348.

21 U. G. K. Wegst, H. Bai, E. Saiz, A. P. Tomsia, R. O. Ritchie, C. Ortiz, M. Boyce, U. G. K. Wegst, H. Bai, E. Saiz, A. P. Tomsia and R. O. Ritchie, *Nat. Mater.*, 2014, **14**, 23–36.

22 S. C. Paul, G. P. A. . van Zijl, M. J. Tan and I. Gibson, *Rapid Prototyp. J.*, 2018, **24**, 784–798.

23 G. Ji, T. Ding, J. Xiao, S. Du, J. Li and Z. Duan, *Materials (Basel).*, 2019, **12**, 1–14.

24 N. Sigaux, L. Pourchet, P. Breton, S. Brosset, A. Louvrier and C. Marquette, *J. Stomatol. Oral Maxillofac. Surg.*, 2019, **120**, 128–132.

25 ISO/ASTM 52900:2015 - Additive manufacturing -- General principles -- Terminology, https://www.iso.org/standard/69669.html, (accessed 29 July 2019).

26 Charles W. Hull, Patent No. 4575330, 1984, 16.

27 Q. Fu, E. Saiz and A. P. Tomsia, *Acta Biomater.*, 2011, **7**, 3547–3554.

28 S. V Murphy and A. Atala, *Nat. Biotechnol.*, 2014, **32**, 773–785.

29 S. Rudykh, C. Ortiz and M. C. Boyce, *Soft Matter*, 2015, **11**, 2547–54.

30 J. J. Martin, B. E. Fiore and R. M. Erb, *Nat. Commun.*, 2015, **6**, 1–7.

31 B. G. Compton and J. A. Lewis, *Adv. Mater.*, 2014, **26**, 5930–5935.

32 X. Mu, T. Bertron, C. Dunn, H. Qiao, J. Wu, Z. Zhao, C. Saldana and H. J. Qi, *Mater. Horiz.*, 2017, **4**, 442–449.

33 D. Kokkinis, M. Schaffner and A. R. Studart, *Nat. Commun.*, 2015, **6**, 1–10.

34 R. Goodridge and S. Ziegelmeier, in *Laser Additive Manufacturing: Materials, Design, Technologies, and Applications*, Elsevier Inc., 1st edn., 2017, vol. 1, pp. 181–204.

35 V. Gupta, P. Nesterenko and B. Paull, in *3D Printing in Chemical Sciences*, Royal Society of Chemistry, 2019, pp. 1–21.

36 M. Zenou and L. Grainger, in *Additive Manufacturing*, Elsevier, 2018, pp. 53–103.

37 P. J. Kitson, R. J. Marshall, D. Long, R. S. Forgan and L. Cronin, *Angew. Chemie - Int. Ed.*, 2014, **53**, 12723–12728.

38 P. J. Kitson, S. Glatzel, W. Chen, C.-G. Lin, Y.-F. Song and L. Cronin, *Nat. Protoc.*, 2016, **11**, 920–936.

39 M. R. Penny, Z. X. Rao, B. F. Peniche and S. T. Hilton, *European J. Org. Chem.*, 2019, **2019**, 3783–3787.

40 G. Scotti, S. M. E. Nilsson, M. Haapala, P. Pöhö, G. Boije af Gennäs, J. Yli-Kauhaluoma and T. Kotiaho, *React. Chem. Eng.*, 2017, **2**, 299–303.

41 C. Yu, F. Tang, X. Qian, Y. Chen, Q. Yu, K. Ni and X. Wang, *Sci. Rep.*, 2017, **7**, 1–9.

42 A. Oedit, P. Vulto, R. Ramautar, P. W. Lindenburg and T. Hankemeier, *Curr. Opin. Biotechnol.*, 2015, **31**, 79–85.

43 A. Brimmo, P.-A. Goyette, R. Alnemari, T. Gervais and M. A. Qasaimeh, *Sci. Rep.*, 2018, **8**, 1–8.

44 W. Lee, D. Kwon, W. Choi, G. Y. Jung, A. K. Au, A. Folch and S. Jeon, *Sci. Rep.*, 2015, **5**, 7717.

45 S. Cinti, D. Moscone and F. Arduini, *Nat. Protoc.*, 2019, **14**, 2437–2451.

46 R. Hernández Vera, P. O'Callaghan, N. Fatsis-Kavalopoulos and J. Kreuger, *Sci. Rep.*, 2019, **9**, 1–10.

47 T. Monaghan, M. J. Harding, R. A. Harris, R. J. Friel and S. D. R. Christie, *Lab Chip*, 2016, **16**, 3362–3373.

48 M. D. Symes, P. J. Kitson, J. Yan, C. J. Richmond, G. J. T. Cooper, R. W. Bowman, T. Vilbrandt and L. Cronin, *Nat. Chem.*, 2012, **4**, 349–354.

49 P. J. Kitson, M. H. Rosnes, V. Sans, V. Dragone and L. Cronin, *Lab Chip*, 2012, **12**, 3267.

50 G. Scotti, S. M. E. Nilsson, M. Haapala, P. Pöhö, G. Boije af Gennäs, J. Yli-Kauhaluoma and T. Kotiaho, *React. Chem. Eng.*, 2017, **2**, 299–303.

51 Z. X. Rao, University College London School of Pharmacy, 2019.

52 M. R. Penny and S. T. Hilton, *React. Chem. Eng.*, , DOI:10.1039/c9re00492k.

53 A. J. Capel, R. P. Rimington, M. P. Lewis and S. D. R. Christie, *Nat. Rev. Chem.*, 2018, **2**, 422–436.

54 A. Goyanes, A. B. M. Buanz, A. W. Basit and S. Gaisford, *Int. J. Pharm.*, 2014, **476**, 88–92.

55 A. Goyanes, P. Robles Martinez, A. Buanz, A. W. Basit and S. Gaisford, *Int. J. Pharm.*, 2015, **494**, 657–663.

56 S. A. Khaled, M. R. Alexander, D. J. Irvine, R. D. Wildman, M. J. Wallace, S. Sharpe, J. Yoo and C. J. Roberts, *AAPS PharmSciTech*, 2018, **19**, 3403–3413.

57 A. Goyanes, P. Robles Martinez, A. Buanz, A. W. Basit and S. Gaisford, *Int. J. Pharm.*, 2015, **494**, 657–663.

58 J. Long, A. E. Etxeberria, A. V. Nand, C. R. Bunt, S. Ray and A. Seyfoddin, *Mater. Sci. Eng. C*, 2019, **104**, 109873.

59 B. C. Sil, A. Patel, J. M. Crowther, D. J. Moore, J. Hadgraft, S. T. Hilton and M. E. Lane, *Pharmaceutics*, 2019, **11**, 250.

60 A. Goyanes, M. Scarpa, M. Kamlow, S. Gaisford, A. W. Basit and M. Orlu, *Int. J. Pharm.*, 2017, **530**, 71–78.

61 Z. Muwaffak, A. Goyanes, V. Clark, A. W. Basit, S. T. Hilton and S. Gaisford, *Int. J. Pharm.*, 2017, **527**, 161–170.

62 A. R. Johnson, C. L. Caudill, J. R. Tumbleston, C. J. Bloomquist, K. A. Moga, A. Ermoshkin, D. Shirvanyants, S. J. Mecham, J. C. Luft and J. M. DeSimone, *PLoS One*,

2016, **11**, e0162518.

63 M. R. Penny, Z. J. Cao, B. Patel, B. Sil dos Santos, C. R. M. Asquith, B. R. Szulc, Z. X. Rao, Z. Muwaffak, J. P. Malkinson and S. T. Hilton, *J. Chem. Educ.*, 2017, **94**, 1265–1271.

64 P. A. Wood, A. A. Sarjeant, I. J. Bruno, C. F. Macrae, H. E. Maynard-Casely and M. Towler, *CrystEngComm*, 2017, **19**, 690–698.

65 K. Smiar and J. D. Mendez, *J. Chem. Educ.*, 2016, **93**, 1591–1594.

66 Could turning carbon dioxide into fish food feed the future?, https://www.drax.com/technology/turning-carbon-dioxide-fish-food-feed-future/, (accessed 28 April 2020).

67 T. Moore, M. Biviano, K. A. Mumford, R. R. Dagastine, G. W. Stevens and P. A. Webley, *Ind. Eng. Chem. Res.*, 2019, **58**, 6626–6634.

68 G. He, S. Huang, L. F. Villalobos, J. Zhao, M. Mensi, E. Oveisi, M. Rezaei and V. Agrawal, *Energy Environ. Sci*, 2019, **12**, 3305.

69 S. Fajardo, García-Galvan, F. R., V. Barranco, J. C. Galvan and S. F. Batlle, *Solvents for Carbon Dioxide Capture*, 2018, vol. 8.

70 T. Nelson, L. Coleman, D. Green and R. Gupta, *Energy Procedia*, 2009, **1**, 1305–1311.

71 D. Nguyen, M. Murialdo, K. Hornbostel, S. Pang, C. Ye, W. Smith, S. Baker, W. Bourcier, J. Knipe, R. Aines and J. Stolaroff, *Ind. Eng. Chem. Res.*, 2019, **58**, 22015–22020.

72 $1.5 million grant for environmentally friendly 3D printed concrete | 3D Printing Progress, https://www.3dprintingprogress.com/articles/17993/1-5-million-grant-for-environmentally-friendly-3d-printed-concrete, (accessed 28 April 2020).

73 G. A. Appuhamillage, D. R. Berry, C. E. Benjamin, M. A. Luzuriaga, J. C. Reagan, J. J. Gassensmith and R. A. Smaldone, *Polym. Int.*, 2019, **68**, 964–971.

74 M. R. Skorski, J. M. Esenther, Z. Ahmed, A. E. Miller and M. R. Hartings, *Sci. Technol. Adv. Mater.*, 2016, **17**, 89–97.

75 B. G. Compton and J. A. Lewis, *Adv. Mater. (Weinheim, Ger.)*, 2014, **26**, 6043.

76 J. Wu, M. Isakov, Y. Mao, H. J. Qi, C. Yuan, T. Wang, Z. Ding and M. L. Dunn, *Sci Rep*, 2016, **6**, 24224.

77 Z. Zhao, X. Kuang, C. Yuan, H. J. Qi and D. Fang, *ACS Appl. Mater. Interfaces*, 2018, **10**, 19932–19939.

78 S. Dutta and D. Cohn, *J. Mater. Chem. B*, 2017, **5**, 9514–9521.

79 J. Sebastián, S. Manzano, Z. B. Weinstein, A. D. Sadow and I. I. Slowing, *ACS Catal.*, 2017, **7**, 7567–7577.

80 S. R. Batten, N. R. Champness, X.-M. Chen, J. Garcia-Martinez, S. Kitagawa, L. Öhrström, M. O'keeffe, M. P. Suh and J. Reedijk, *Pure Appl. Chem*, 2013, **85**, 1715–1724.

81 S. R. Batten, N. R. Champness, X.-M. Chen, J. Garcia-Martinez, S. Kitagawa, L. Öhrström, M. O'keeffe, M. P. Suh and J. Reedijk, *Pure Appl. Chem*, 2013, **85**, 1715–1724.

82 Prussian blue - American Chemical Society, https://www.acs.org/content/acs/en/molecule-of-the-week/archive/p/prussian-blue.html,

(accessed 28 July 2019).

83 Y. Shibata, *J. Fac. Sci. Imp. Univ. Tokyo*, 1916, 1–17.

84 M. Alhamami, H. Doan and C. H. Cheng, *Materials (Basel).*, 2014, **7**, 3198–3250.

85 K. Konstas, T. Osl, Y. Yang, M. Batten, N. Burke, A. J. Hill and M. R. Hill, *J. Mater. Chem.*, 2012, **22**, 16698.

86 S. Yuan, L. Zou, J. S. Qin, J. Li, L. Huang, L. Feng, X. Wang, M. Bosch, A. Alsalme, T. Cagin and H. C. Zhou, *Nat. Commun.*, 2017, **8**, 1–10.

87 N. Van Velthoven, S. Waitschat, S. M. Chavan, P. Liu, S. Smolders, J. Vercammen, B. Bueken, S. Bals, K. P. Lillerud, N. Stock and D. E. De Vos, *Chem. Sci.*, 2019, **10**, 3616–3622.

88 D. Yang and B. C. Gates, *ACS Catal.*, 2019, **9**, 1779–1798.

89 Y. S. Kang, Y. Lu, K. Chen, Y. Zhao, P. Wang and W. Y. Sun, *Coord. Chem. Rev.*, 2019, **378**, 262–280.

90 A. E. Baumann, D. A. Burns, B. Liu and V. S. Thoi, *Commun. Chem.*, 2019, **2**, 1–14.

91 X. Zhang, A. Chen, M. Zhong, Z. Zhang, X. Zhang, Z. Zhou and X.-H. Bu, *Metal–Organic Frameworks (MOFs) and MOF-Derived Materials for Energy Storage and Conversion*, Springer Singapore, 2019, vol. 2.

92 H. Wang, Q. L. Zhu, R. Zou and Q. Xu, *Chem*, 2017, **2**, 52–80.

93 W. Cai, J. Wang, C. Chu, W. Chen, C. Wu and G. Liu, *Adv. Sci.*, 2019, **6**, 1801526–1801546.

94 A. Guo, M. Durymanov, A. Permyakova, S. Sene, C. Serre and J. Reineke, *Pharm. Res.*, 2019, **36**, 36–53.

95 I. Abánades Lázaro and R. S. Forgan, *Coord. Chem. Rev.*, 2019, **380**, 230–259.

96 Q. Qiu, H. Chen, Y. Wang and Y. Ying, *Coord. Chem. Rev.*, 2019, **387**, 60–78.

97 B. Yan, *J. Mater. Chem. C*, 2019, 8155–8175.

98 X. Fang, B. Zong and S. Mao, *Nano-Micro Lett.*, 2018, **10**, 1–19.

99 P. A. Julien, C. Mottillo and T. Friščić, *Green Chem.*, 2017, **19**, 2729–2747.

100 Q. Qiu, H. Chen, Y. Wang and Y. Ying, *Coord. Chem. Rev.*, 2019, **387**, 60–78.

101 J.-Z. Wei, F.-X. Gong, X.-J. Sun, Y. Li, T. Zhang, X.-J. Zhao and F.-M. Zhang, *Inorg. Chem.*, 2019, **58**, 6742–6747.

102 K. Užarević, T. C. Wang, S.-Y. Moon, A. M. Fidelli, J. T. Hupp, O. K. Farha and T. Friščić, *Chem. Commun.*, 2016, **52**, 2133–2136.

103 V. The Ky, V. N. Le, K. S. Yoo, M. Song, D. Kim and J. Kim, *Cryst. Growth Des.*, 2019, **19**, 4949–4956.

104 M. Homaee, H. Hamadi, V. Nobakht, M. Javaherian and B. Salahshournia, *Polyhedron*, 2019, **165**, 152–161.

105 Y. Zhao, Q. Zhang, Y. Li, R. Zhang and G. Lu, *ACS Appl. Mater. Interfaces*, 2017, **9**, 15079–15085.

106 M. A. Tekalgne, H. H. Do, A. Hasani, Q. Van Le, H. W. Jang, S. H. Ahn and S. Y. Kim, *Mater. Today Adv.*, 2020, **5**, 100038.

107 L. B. Mccusker and D. H. Olson, *Atlas of Zeolite framework types*, Elsevier Science Ltd., Amsterdam, 1st edn., 2007.

108 P. Guo, J. Shin, A. G. Greenaway, J. G. Min, J. Su, H. J. Choi, L. Liu, P. A. Cox, S. B. Hong, P. A. Wright and X. Zou, *Nature*, 2015, **524**, 74–78.

109 H. Li, K. Wang, Y. Sun, C. T. Lollar, J. Li and H.-C. Zhou, *Mater. Today*, 2018, **21**, 108–121.

110 J. M. Moreno, A. Velty, U. Díaz and A. Corma, *Chem. Sci.*, 2019, **10**, 2053–2066.

111 T. C. Wang, N. A. Vermeulen, I. S. Kim, A. B. F. Martinson, J. F. Stoddart, J. T. Hupp and O. K. Farha, *Nat. Protoc.*, 2015, **11**, 149–162.

112 B. Zhu, R. Zou and Q. Xu, *Adv. Energy Mater.*, 2018, **8**, 1801193.

113 C. Caratelli, J. Hajek, F. G. Cirujano, M. Waroquier, F. X. Llabrés i Xamena and V. Van Speybroeck, *J. Catal.*, 2017, **352**, 401–414.

114 C. Zhang, G. Zhang, S. Luo, C. Wang and H. Li, *Org. Biomol. Chem.*, 2018, **16**, 8467–8471.

115 K. Zhou and S. Chaemchuen, *Int. J. Environ. Sci. Dev.*, 2017, **8**, 251–254.

116 C. Zhang, G. Zhang, S. Luo, C. Wang and H. Li, *Org. Biomol. Chem.*, 2018, **16**, 8467–8471.

117 A. J. Howarth, Y. Liu, P. Li, Z. Li, T. C. Wang, J. T. Hupp and O. K. Farha, *Nat. Rev. Mater.*, 2016, **1**, 1–15.

118 H. Wu, T. Yildirim and W. Zhou, *J. Phys. Chem. Lett.*, 2013, **4**, 925–930.

119 B. Van de Voorde, I. Stassen, B. Bueken, F. Vermoortele, D. De Vos, R. Ameloot, J.-C. Tan and T. D. Bennett, *J. Mater. Chem. A*, 2015, **3**, 1737–1742.

120 P. G. Yot, K. Yang, F. Ragon, V. Dmitriev, T. Devic, P. Horcajada, C. Serre and G. Maurin, *Dalt. Trans.*, 2016, **45**, 4283–4288.

121 J. Lee, O. K. Farha, J. Roberts, K. A. Scheidt, S. T. Nguyen and J. T. Hupp, *Chem. Soc. Rev.*, 2009, **38**, 1450.

122 M. Vandichel, J. Hajek, F. Vermoortele, M. Waroquier, D. E. De Vos and V. Van Speybroeck, *CrystEngComm*, 2015, **17**, 395–406.

123 G. Gatto, A. Macchioni, R. Bondi, F. Marmottini and F. Costantino, *Inorganics*, 2019, **7**, 123.

124 R. Liang, L. Shen, F. Jing, W. Wu, N. Qin, R. Lin and L. Wu, *Appl. Catal. B Environ.*, 2015, **162**, 245–251.

125 Y. Chen, X. Mu, E. Lester and T. Wu, *Prog. Nat. Sci. Mater. Int.*, 2018, **28**, 584–589.

126 C. H. Hendon and A. Walsh, *Chem. Sci.*, 2015, **6**, 3674–3683.

127 T. Grant Glover, G. W. Peterson, B. J. Schindler, D. Britt and O. Yaghi, *Chem. Eng. Sci.*, 2011, **66**, 163–170.

128 E. Barea, C. Montoro and J. A. R. Navarro, *Chem. Soc. Rev.*, 2014, 43, 5419–5430.

129 O. Yassine, O. Shekhah, A. H. Assen, Y. Belmabkhout, K. N. Salama and M. Eddaoudi, *Angew. Chemie - Int. Ed.*, 2016, **55**, 15879–15883.

130 T. D. Bennett and S. Horike, *Nat. Rev. Mater.*, 2018, **3**, 431–440.

131 Y. Wang, H. Jin, Q. Ma, K. Mo, H. Mao, A. Feldhoff, X. Cao, Y. Li, F. Pan and Z. Jiang, *Angew. Chemie - Int. Ed.*, 2020, **132**, 4595–4399.

132 R. Gaillac, P. Pullumbi, K. A. Beyer, K. Chapman, D. A. Keen, T. D. Bennett and F. X. Coudert, *Nat. Mater.*, 2017, **16**, 1149–1155.

133 L. Longley, S. M. Collins, S. Li, G. J. Smales, I. Erucar, A. Qiao, J. Hou, C. M. Doherty, A. W. Thornton, A. J. Hill, X. Yu, N. J. Terrill, A. J. Smith, S. M. Cohen, P. A. Midgley, D. A. Keen, S. G. Telfer and T. D. Bennett, *Chem. Sci.*, 2019, **10**, 3592–3601.

134 J. Park, J. D. Howe and D. S. Sholl, *Chem. Mater.*, 2017, **29**, 10487–10495.

135 *Reproducibility and Replicability in Science*, National Academies Press, 2019.

136 F. Prinz, T. Schlange and K. Asadullah, *Nat. Rev. Drug Discov.*, 2011, **10**, 712–713.

137 P. B. Stark, *Nature*, 2018, **557**, 613.

138 M. Agrawal, R. Han, D. Herath and D. S. Sholl, *Proc. Natl. Acad. Sci. U. S. A.*, 2019, **117**, 887–882.

139 L. Benguigui and E. Blumenfeld-Lieberthal, *Comput. Environ. Urban Syst.*, 2007, **31**, 648–666.

140 M. Brzezinski, *Phys. A Stat. Mech. its Appl.*, 2014, **406**, 155–162.

141 M. Brzezinski, *Scientometrics*, 2015, **103**, 213–228.

142 Metal Organic Frameworks | Sigma-Aldrich, https://www.sigmaaldrich.com/technical-documents/articles/materials-science/metal-organic-frameworks.html, (accessed 17 March 2020).

143 M. Jin, X. Qian, J. Gao, J. Chen, D. K. Hensley, H. C. Ho, R. J. Percoco, C. M. Ritzi and Y. Yue, *Inorg. Chem.*, 2019, **58**, 8332–8338.

144 | MOF Technologies' new partnership for the development of novel MOF-based CO2 capture technology, https://www.moftechnologies.com/mof-technologies-new-partnership-for-the-development-of-novel-mof-based-co2-capture-technology/, (accessed 17 March 2020).

145 Promethean Particles Ltd | Formulating solutions with nanomaterials, https://www.prometheanparticles.co.uk/, (accessed 17 March 2020).

146 Immaterial - Home, http://www.immaterial.co/, (accessed 5 October 2019).

147 novoMOF | Metal-Organic Frameworks (MOFs) production, https://novomof.com/, (accessed 5 October 2019).

148 Chemical Manufacturers | Speciality Chemicals | High Purity, https://www.strem.com/, (accessed 17 March 2020).

149 NuMat Technologies, https://www.numat-tech.com/, (accessed 5 October 2019).

150 J. Zhang, Y. Hu and Y. Li, *Gel Chemistry: Metal–Organic Gels*, Springer Singapore, Singapore, 2018.

151 J. Hou, A. F. Sapnik and T. D. Bennett, *Chem. Sci.*, 2020, **11**, 310–323.

152 A. Mahmood, W. Xia, N. Mahmood, Q. Wang and R. Zou, *Sci. Rep.*, 2015, **5**, 10556.

153 P. Su, W. Li, C. Zhang, Q. Meng, C. Shen and G. Zhang, *J. Mater. Chem. A*, 2015, **3**, 20345–20351.

154 J. Zhang, X. Wang, L. He, L. Chen, C.-Y. Su and S. L. James, *New J. Chem.*, 2009, **33**, 1070.

155 Y. Hu, Y. Fan, Z. Huang, C. Song and G. Li, *Chem. Commun.*, 2012, **48**, 3966.

156 S. K. Nune, P. K. Thallapally and B. P. McGrail, *J. Mater. Chem.*, 2010, **20**, 7623.

157 L. Liu, J. Zhang, H. Fang, L. Chen and C. Y. Su, *Chem. - An Asian J.*, 2016, **11**, 2278–2283.

158 Q. Wei and S. L. James, *Chem. Commun.*, 2005, 1555–1556.

159 J. Zhang and C. Su, *Coord. Chem. Rev.*, 2013, **257**, 1373–1408.

160 B. Bueken, N. Van Velthoven, T. Willhammar, T. Stassin, I. Stassen, D. A. Keen, G. V. Baron, J. F. M. Denayer, R. Ameloot, S. Bals, D. E. De Vos and T. D. Bennett, *Chem. Sci.*, 2017, **8**, 3939–3948.

161 S. J. Qin, X. L. Qu and B. Yan, *Inorg. Chem. Front.*, 2018, **5**, 2971–2977.

162 A. Rezk, R. Al-Dadah, S. Mahmoud and A. Elsayed, *Int. J. Heat Mass Transf.*, 2012, **55**, 7366–7374.

163 L. Liu, J. Zhang, H. Fang, L. Chen and C.-Y. Su, *Chem. - An Asian J.*, 2016, **11**, 2278–2283.

164 F. Vermoortele, B. Bueken, G. Le Bars, B. Van De Voorde, M. Vandichel, K. Houthoofd, A. Vimont, M. Daturi, M. Waroquier, V. Van Speybroeck, C. Kirschhock and D. E. De Vos, *J. Am. Chem. Soc.*, 2013, **135**, 11465–11468.

165 R. O. Ritchie, M. J. Buehler and P. Hansma, *Phys. Today*, 2009, 41–47.

166 H. L. Tekinalp, V. Kunc, G. M. Velez-Garcia, C. E. Duty, L. J. Love, A. K. Naskar, C. A. Blue and S. Ozcan, *Compos. Sci. Technol.*, 2014, **105**, 144–150.

167 J. J. Martin, M. S. Riederer, M. D. Krebs and R. M. Erb, *Soft Matter*, 2014, **11**, 400–5.

168 D. Kokkinis, M. Schaffner and A. R. Studart, *Nat. Commun.*, 2015, **6**, 8643.

169 P. Falcaro, K. Okada, T. Hara, K. Ikigaki, Y. Tokudome, A. W. Thornton, A. J. Hill, T. Williams, C. Doonan and M. Takahashi, *Nat. Mater.*, 2017, **2**, 342–348.

170 J. Jiang, A. M. Plonka, A. I. Frenkel and D. Gersappe, *J. Phys. Chem. Lett.*, 2018, 1092–1096.

171 A. C. Forse, M. I. Gonzalez, R. L. Siegelman, V. J. Witherspoon, S. Jawahery, R. Mercado, P. J. Milner, J. D. Martell, B. Smit, B. Blümich, J. R. Long and J. A. Reimer, *J. Am. Chem. Soc.*, 2018, **140**, 1663–1673.

172 A. V. Vinogradov, V. A. Milichko, H. Zaake-Hertling, A. Aleksovska, S. Gruschinski, S.

Schmorl, B. Kersting, E. M. Zolnhofer, J. Sutter, K. Meyer, P. Lönnecke and E. Hey-Hawkins, *Dalt. Trans.*, 2016, **45**, 7244–7249.

173 Y. Ming, H. Chi, R. Blaser, C. Xu, J. Yang, M. Veenstra, M. Gaab, U. Müller, C. Uher and D. J. Siegel, *Int. J. Heat Mass Transf.*, 2015, **82**, 250–258.

174 D. Zacher, O. Shekhah, C. Wöll and R. A. Fischer, *Chem. Soc. Rev.*, 2009, **38**, 1418–1429.

175 S. Li, W. Shi, G. Lu, S. Li, S. C. J. Loo and F. Huo, *Adv. Mater.*, 2012, **24**, 5954–5958.

176 N. R. Champness, *Nat. Mater.*, 2017, **16**, 283–284.

177 E. A. Kapustin, S. Lee, A. S. Alshammari and O. M. Yaghi, *ACS Cent. Sci.*, 2017, **3**, 662–667.

178 S. M. Moosavi, P. G. Boyd, L. Sarkisov and B. Smit, *ACS Cent. Sci.*, 2018, **4**, 832–839.

179 Y. Zhang, X. Feng, S. Yuan, J. Zhou and B. Wang, *Inorg. Chem. Front.*, 2016, **3**, 896–909.

180 I. D. Williams, *Nat. Chem.*, 2014, **6**, 953–954.

181 K. Evans, Z. C. Kennedy, B. W. Arey, J. F. Christ, H. T. Schaef, S. K. Nune and R. L. Erikson, *ACS Appl. Mater. Interfaces*, 2018, **10**, 15112–15121.

182 M. R. Channell, M. N., Sefa, M., Fedchak, J. A., Scherschligt, J., Miller, A. E., Ahmed, Z., & Hartings, *Polym. Adv. Technol.*, 2018, **29**, 867–873.

2. Experimental

Experimental principles and techniques that are general to this thesis are reported here. This chapter outlines commonly used synthetic methods for MOF synthesis, a list of materials used, 3D printers and their modifications, and characterisation methods.

2.1. Materials

Provided here is a list of materials and suppliers for the chemicals used in this work.

2-aminoterephthalic acid (99%), terephthalic acid, aluminium nitrate nonahydrate, indium nitrate hexahydrate, gallium nitrate hexahydrate, iron nitrate nonahydrate, iron (III) chloride, poly(acrylic acid) sodium salt, glacial acetic acid and hydrochloric acid (HCl) were purchased from Sigma Aldrich. DMF (99.5%) was purchased from Merck. Isopropyl alcohol was purchased from VWR. Iron (II) chloride, zirconyl chloride octahydrate and polyvinylpyrrolidone (PVP) were purchased from Alfa Aesar. Ammonium hydroxide solution (35%) was purchased from Prime Chemicals. All chemicals and reagents were used as received, unless otherwise indicated. 1 litre Schott bottle and Teflon lined autoclaves were purchased from Fisher Scientific.

2.2. Synthetic methods

Outlined herein are synthetic methods that can be found in the literature and any modifications are noted.

2.2.1. Synthesis of MIL-68(In) microrods

The synthetic procedure was taken from the literature and used unmodified. [1] Summarised here is the synthetic method for the creation of MIL-68(In). Indium nitrate hexahydrate (0.24 g, 0.80 mmol) was dissolved in DMF (2.40 mL) and added to a solution of terephthalic acid (0.10 g, 0.6 mmol) in DMF (2.40 mL). The resulting solution was placed in a 25 mL round bottom flask with a magnetic stirrer bar and heated to 100 °C for 6 hours. The samples were allowed to cool radiatively. The samples were then centrifuged and washed with DMF (2 x 15 mL) and ethanol

(3 x 15 mL) before being dried in an oven at 50 °C overnight. The solid was composed of white needles.

2.2.2. Synthesis of MIL-68(Ga) microrods

The synthetic procedure was taken from the literature and used unmofidied.[1] Summarised here is the synthetic method for the creation of MIL-68(Ga). Galium nitrate hexahydrate (0.19 g, 0.75 mmol) was dissolved in DMF (2.40 mL) and added to a solution of terephthalic acid (0.10 g, 0.6 mmol) in DMF (2.40 mL), the resulting solution was placed in a 25 mL round bottom flask with a magnetic stirrer bar and heated to 100 °C for 6 hours. The samples were allowed to cool radiatively. The samples were then centrifuged and washed with DMF (2 x 15 mL) and ethanol (3 x 15 mL) before being dried in an oven at 50 °C overnight. The resulting solid was dry white needles.

2.2.3. Synthesis of NH_2-MIL-53(Al) microneedles

NH_2-MIL-53(Al) MOF microneedles for work presented in chapter 3. The MOFs were synthesised in accordance with a previously reported literature procedure,[2] with minor modifications. 2-aminoterephthalic acid (1.13 g, 6.24 mmol) and acetic acid (7.80 g, 0.13 mol) were added to DMF (30 mL). Aluminium nitrate nonahydrate (1.58 g, 4.20 mmol) in DMF (30 mL) was subsequently added to the vessel and sonicated for 4 minutes at 60 °C until a clear solution was obtained. The solutions were then placed in a 150 mL Teflon-lined vessel stainless steel autoclave, sealed and reacted for 72 hours at 120 °C in a preheated oven. The samples were allowed to cool radiatively. The MOF solids were collected by filtration and washed with acetone. The MOFs were then purified by heating in DMF (100 mL) at 120 °C for 6 hours. The MOFs were collected *via* filtration, washed with ethanol (10 mL) and dried at 85 °C overnight to yield a yellow powder.

2.2.4. Synthesis of NH_2-MIL-68(In) microrods

NH_2-MIL-68(In) MOF rods used in chapter 3 and were synthesised in accordance with the literature, with minor modifications. Indium nitrate hexahydrate (1.15 g, 3.84 mmol) dissolved in DMF (10 mL) and amino-terephthalic acid (0.23 g, 1.29 mmol) and polyvinylpyrrolidone (PVP) (0.1 g, 0.025 mmol) dissolved in DMF (5 mL) were sonicated until the solution was clear. The solutions were mixed and sealed in a 100 mL Teflon coated sealed stainless-steel autoclave at 150 °C for 12 hours. The product was filtered, washed with DMF (3 x 20 mL) then ethanol (3 x 20 mL) and dried at 100 °C for 12 hours. The resulting solid was a yellow powder.

2.2.5. Synthesis of iron oxide nanoparticles

The procedure was adapted from literature and used in chapter 3.[3] In brief, a solution of poly(acrylic acid) sodium salt (1.00 g, 0.19 mmol, average molecular wt. 5100) was dissolved in 2M hydrochloric acid (40 mL). Iron (III) chloride (2.84 g, 17.50 mmol) and iron (II) chloride (1.74 g, 8.75 mmol) were dissolved in 2M hydrochloric acid (40 mL) and added to the poly(acrylic acid) reaction mixture. The solution was refluxed at 60 °C for 30 minutes. 35% aqueous ammonia solution (20 mL) was quickly added to the reaction mixture and heated at 60 °C for 30 mins, and left to cool with stirring, under an inert atmosphere. The resulting iron oxide solution was placed in dialysis tubing (MW cutoff 12,000-14,000 g mol^{-1}, wall thickness 20 μm) and immersed in distilled water, where the water was changed once a day for seven days. After 7 days, the conductivity of the dialysis solution became stable to give a brown-black iron oxide nanoparticle solution with a concentration of 14.90 mg ml^{-1}.

2.2.6. Synthesis of UiO-66 nanoparticles

UiO-66 nanoparticles for work in chapter 4. The MOFs were synthesised following literature procedure, and scaled up as summarised below.[4] Zirconyl chloride octahydrate (5.725 g, 0.54 mmol), DMF (206 mL) and hydrochloric acid (45.8 mL, 37 %) were placed in a 1 litre Schott bottle and sonicated until fully dissolved. Terephthalic acid (5.663 g, 0.75 mmol) was solubilised

in DMF (481 mL) by sonication before being added to the zirconium chloride solution and vortexed for 5 minutes to allow homogenisation.

The bottle was sealed and placed in a preheated 80 °C oven for 16 hours. The solution was allowed to cool radiatively. The white solid was collected by filtration and washed with DMF (30 mL x 2) and subsequently ethanol (30 mL x 3). The solid was left to dry overnight in a 50 °C oven.

2.2.7. Synthesis of UiO-66 MOF-gel

UiO-66 MOF-gel used for work in chapter 5, was adapted from a literature procedure.[5]

Zirconyl chloride octahydrate (3.22 g, 10.00 mmol) was dissolved in DMF (30 mL) and added to a solution of terephthalic acid (2.41 g, 14.51 mmol) and DMF (30 mL). The solution was then placed into a 100 mL Teflon lined autoclave and placed in a preheated 80 °C oven for 2 hours and left to cool to room temperature. The resulting material was an opaque white gel.

2.2.8. Synthesis of UiO-66- NH_2 MOF-gel

UiO-66- NH_2 MOF-gel used for work in chapter 5, was adapted from a literature procedure.[5]

Zirconyl chloride octahydrate (3.22 g, 10.00 mmol) was dissolved in DMF (30 mL) and added to a solution of amino terephthalic acid (2.60 g, 14.51 mmol) and DMF (30 mL). The solution was then placed into a 100 mL Teflon lined autoclave and placed in a preheated 80 °C oven for 2 hours and left to cool to room temperature. The resulting material was yellow-brown gel.

2.3. Characterisation Methods

The main and most frequently used instrumental methods for characterisation within this body of work were SEM-EDX, PXRD, TGA, Rheology, FTIR-ATR and optical microscopy. The methods provide a mixture of qualitative and quantitative analysis to give the most relevant information required. Instruments that were infrequently used were BET and TEM. Other instrumental methods used are outlined in the experimental section of the respective chapter. A description of each technique is outlined below and the make, model and any sample preparation undertaken.

2.3.1. Scanning Electron Microscopy (SEM) & Energy-dispersive X-ray Spectroscopy (EDX)

Scanning electron microscopy allows the observation of fine structure (less than 1 μm), with a greater depth of focus than optical microscopy. These images can be achieved by scanning the surface of a sample with a finely converged electron beam in a vacuum. A detector senses the secondary electron signals produced near the sample surface and an image can be constructed from the data, revealing the fine topographical structure of the sample. Characteristic X-rays are released from sample and captured by an X-ray analyser attached to the electron microscope, allowing the mapping of elements, and quantification of abundances can be mapped. The X-rays are emitted when a sample is bombarded by the electron beam of the SEM. An electron is ejected from an atom. The resulting vacancy is then filled by an electron from a higher energy state and a characteristic X-ray is emitted to balance the energy between electron states. As the incident X-ray strikes the detector, it creates a charge pulse proportional to the energy of the X-ray. The charge pulse is converted to a voltage pulse and the energy of each X-ray is computed and the spectrum of X-ray energy can be displayed and matched against a known library of elements.

As shown in Figure 2.1, the SEM consists of a column and specimen chamber.

Throughout this body of work two models of SEM were utilised, where appropriate the make and model of SEM used to capture the image has been quoted. For clarity there are two models used:

Hitachi TM4000

Cambridge Stereoscan 360

Both models utilise tungsten wire filaments to generate the electron beam and are in principle the same. However, the Hitachi is a benchtop compact model of SEM with a maximum magnification of x 100, 000 and pre-programmed kV of 5, 10 and 15 kV. The Cambridge Stereoscan 360 is more powerful and adaptable table top SEM capable of a variable kV from 1 to 25 kV, but older

technology only capable of a magnification of x 50,000. It can also be fitted with a tilt stage to enable a sample to be investigated at different angles.

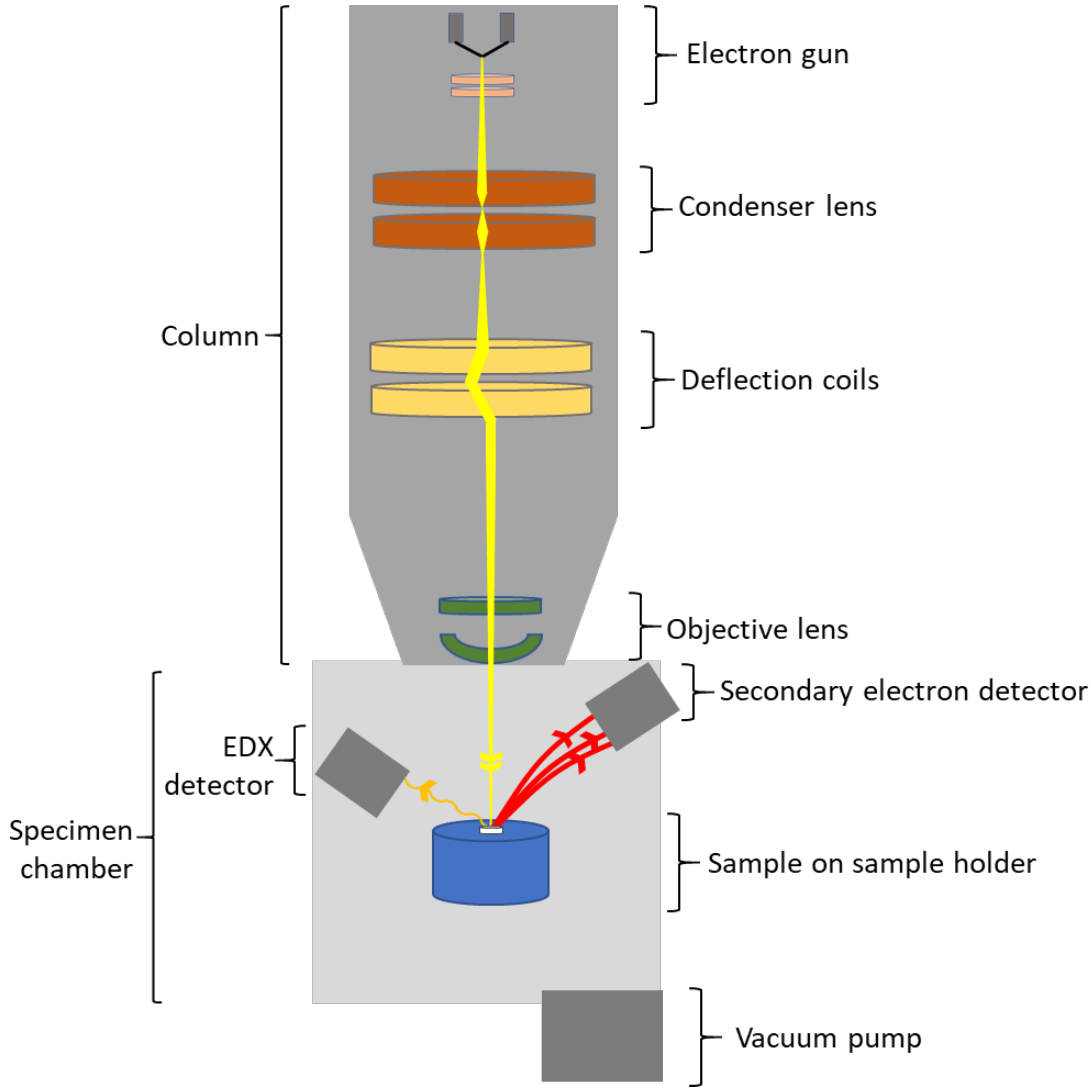

Figure 2.1: Schematic drawing of an SEM

2.3.2. Powder X-ray diffraction (PXRD)

X-ray diffraction (XRD) is a rapid analytical technique for phase identification of crystalline materials. It was first used for the analysis of very simple structures, such as rock salt by W.H. and W.L. Bragg.[6] Advances in XRD techniques have now allowed for smaller samples to be analysed by Powder X-ray diffraction (PXRD). This can allow extremely rapid identification of the crystalline phase(s) present within a powder sample.

Figure 2.2 outlines a simple schematic of PXRD. X-rays are generated from the source, in this case the anode within the X-ray source is Cu and produces X-rays over a broad wavelength range. The characteristic radiation for Cu is Kα and Kβ. The Kα radiation splits into $K\alpha_1$ and $K\alpha_2$ by spin-orbit coupling effects. The monochromator then selects a single narrow range of X-rays, in this instance $K\alpha_1$ to produce monochromatic radiation of $CuK\alpha_1$ $\lambda = 1.54056$ Å.

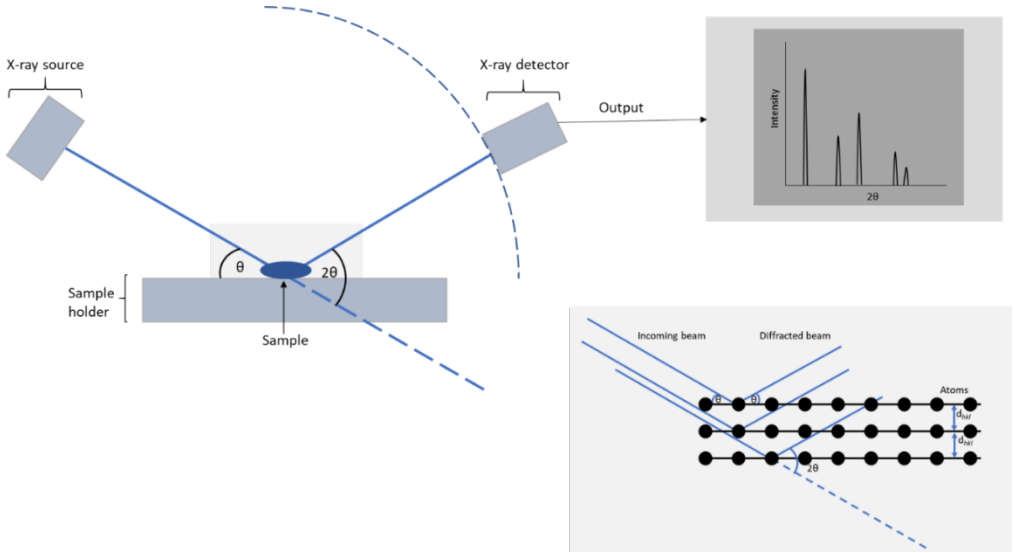

Figure 2.2: Schematic of PXRD and demonstration of d spacing

The interaction of the incident ray with the atoms in the sample produces constructive interference and a diffracted ray. However, this only happens when conditions satisfy Braggs Law $n\lambda = 2dsin\theta$. The law relates the wavelength of the X-ray to the diffraction angle and the lattice spacing of the crystalline sample. The diffracted rays are then detected, processed and counted and by moving the detector in a circle around the sample. The angle (2θ) of the detector relative to the primary beam is recorded and a graph can then be plotted of intensity against 2θ.

PXRD was vital for the data collected within this body of work, as the crystallites were micronized powders. The PXRD used was a PANAnalytical Empyrean Series 2 Diffractometer.

2.3.3. Thermogravimetric Analysis (TGA)

Thermogravimetric analysis (TGA) provides information regarding composition, thermal stability, kinetics of reaction and identification of compounds by their thermal decomposition, typically polymers and organics. The method as outlined in Figure 2.3 demonstrates the sample being heated in a furnace, at a controlled ramp rate. As the crucible and sample heat up constituents of the sample change the weight change recorded on the balance. The environment could be inert or reactive by use of nitrogen, air or other gases. The crucible is placed onto a pin, connected to a microbalance that measures any weight change during analysis. The resulting graph is a weight change (normally loss) curve over time.

Samples were analysed on a Perkin Elmer TGA 4000, from 30 – 800 °C with a heating rate of 10 °C min^{-1} under 30 mL min^{-1} gas flow with either compressed air or nitrogen dependent on samples.

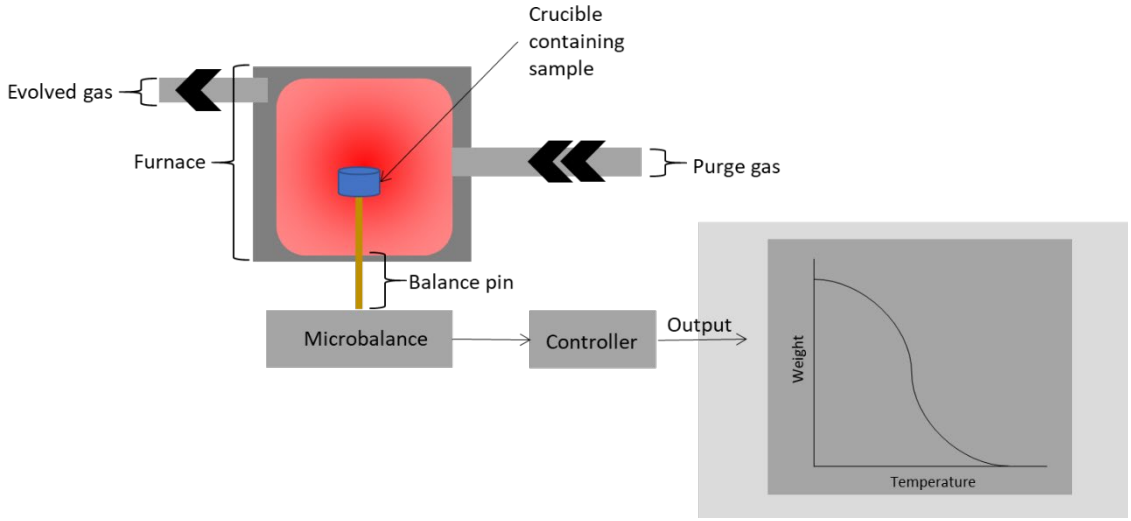

Figure 2.3: Schematic of TGA

2.3.4. Rheology

Rheology derives from the Greek words for study (logia) and flow (rheo) and is a powerful technique to understand the complex elastic or viscous behaviour of materials. The technique works by loading a sample between two plates, a fixed and a rotational plate, as shown in Figure 2.4. A torque is then applied to the top plate which exerts a rotational shear stress onto the material resulting in a measurable shear rate. The resistance of the material to the shear rate applied

indicates the viscosity of the material, as derived from Newtons law $\tau=\eta\cdot\dot{\gamma}$. Where τ is shear stress in Pa (Nm^{-2}), γ is the viscosity in Pa.s and η is the shear rate in s^{-1}. If the shear rate of a material does not change with shear stress then the fluid has a constant viscosity and is defined as Newtonian (indicated by the dashed line in Figure 2.4). However, non-Newtonian fluids react to the shear stress and can increase or decrease in viscosity presenting shear-thinning or shear-thickening properties.

Rheometers are versatile and can measure material properties at ambient or elevated temperatures, humidity and pressures too using a humidity cover and Peltier plate capable of temperatures from –40 to 70°C. The rheometer used for this body of work was a Bohlin rheometer with a PP40 or CP 40 plate at 20 °C fitted with a humidity cover.

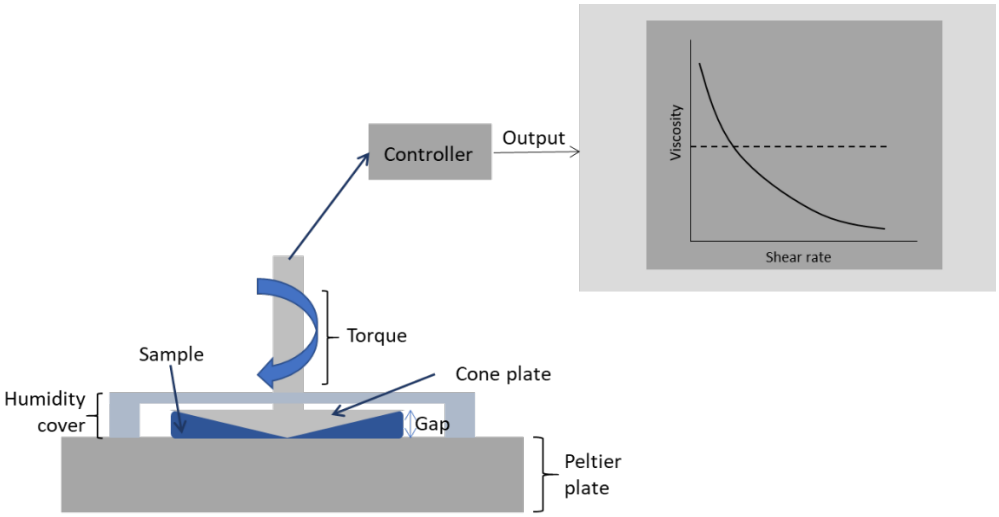

Figure 2.4: Schematic of a Rheometer

2.3.5. Fourier Transform Infrared-Attenuated Total Reflection (FTIR-ATR)

Fourier Transform Infrared (FTIR) is a key technique for the identification and characterisation of organic and polymeric materials. It is a powerful technique that can help identify unknown compounds and contaminants, but it can also be used to track changes to chemical properties, for instance the polymerisation of a monomer. The technique uses infrared radiation applied to the materials, and the absorption by the sample is measured. A characteristic graph is derived from

the data showing energies of stretches and bending of the molecules. The technique used throughout this body of work was a FTIR- Attenuated Total Reflection (ATR) shown in Figure 2.5. The model and make of the instrument is a Thermo Fisher Scientific, Nicolet iS5 FTIR with a PIKE Miracle ATR attachment. This technique was chosen for its ability to produce excellent signal to noise for solids such as powders, with no need to heat, press into pellets or grind. This technique works by IR radiation penetrating through a diamond (or germanium) crystal into the sample. When the IR beam is in contact with the sample an evanescent wave penetrates the sample and is attenuated, the beam then returns to the crystal and exits the reflected infrared beam is measured by the detector. The output is then displayed as a graph where it can be interpreted or compared to an existing database of known chemical compositions.

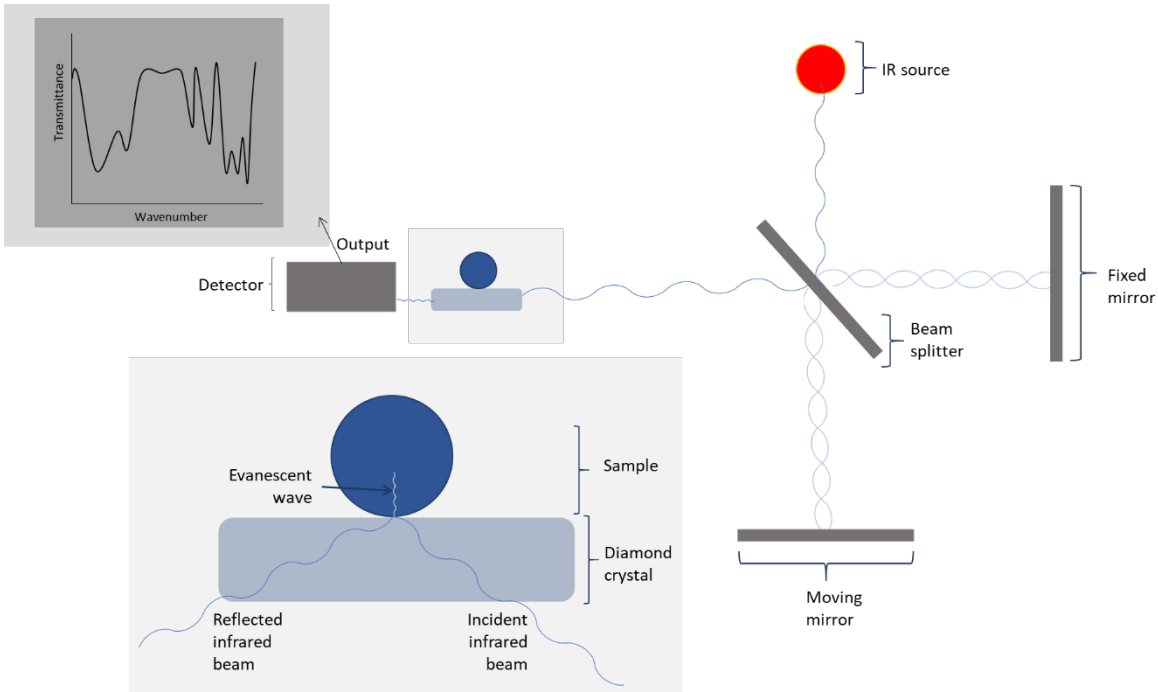

Figure 2.5: Schematic of FTIR-ATR

2.3.6. Optical Microscopy

Optical images were obtained using a Gatan Ultrascan 4000 digital camera or iPhone 5SE. However, the naked eye can only view details up to 0.1 mm and so to observe details beyond this range samples were magnified under a microscope. Typical microscopes can view up to 1 µm and

give good detail of orientation, position and size of microparticles in 2D. The technique works by the transmission of light through a sample, and multiple lenses to a digital output that can be viewed on a computer. The optical microscopes used within this body of work was an Olympus BX51 polarizing microscope.

2.3.7. Inductively Coupled Plasma - Optical Emission Spectroscopy (ICP-OES)

The Inductively Coupled Plasma (ICP) technique is coupled with Optical Emission Spectroscopy (OES) system. The plasma flame excites atoms in a sample, and they relax with characteristic emission spectra. The intensity of these lines is representative of how much of an element is present. ICP-OES analysis was performed on a Perkin Elmer Optima 5300DV ICP-OES spectrometer and was calibrated against 10 ppm standards and externally calibrated with a certified reference digest (CRM-ES).

2.3.8. Characterisation Limitations

In the research area of MOFs, the characterisation methods are not standardised across the board and are not routinely reproduced. Briefly mentioned previously in Section 1.3.5. is the work by Park *et al.,* looking into the reproducibility crisis of MOFs.[7] They report that only a small amount of known MOFs have been reproduced enough to allow reliable conclusions to be drawn about the reproducibility of the measurements. In addition to this argument it can be noted that on literature searches of MOFs there is no standard characterisation techniques used for MOFs or MOF-based materials. Within this body of work FTIR-ATR, PXRD, SEM, optical microscopy, TGA, ICP-OES where used. Below is an indication of how and why each technique was chosen.

For structural characterisation of MOF-based materials used in this body of work, FTIR-ATR provides information on the molecular vibrations which can be an aid to help elucidate the structure of a material. FTIR-ATR was also used to show the completion of a chemical reaction, in this case the curing of polymerised material by tracking the breaking and formation of bonds caused by free radical polymerisation. PXRD provided qualitative information regarding the

dimensions of the unit cell and for phase identification of crystalline material. PXRD is an essential technique for MOF manufacture and should be done for every batch of MOF produced, although the bulk structure of samples may be the same by PXRD, the pore opening may be different at the edges of the crystallite depending on how the samples are treated.

Two microscopy techniques were used to gain insight into the micro-structure of the materials. Optical microscopy allows investigation into the surface features of the material by use of visible light transmitting through the material, the technique can be used to distinguish MOF from the matrix with relative simplicity. Scanning electron microscopy (SEM) allows a closer look at the surface of a material at the micro or nano scale. SEM is frequently coupled with EDX, to allow the analysis, quantification and homogeneity of the elements through a sample. In the case of MOF-based materials it allows the user the ability to view the distribution of MOF within the sample, but also the aspect ratio of the MOF.

Another quantitative technique that was frequently used was TGA. This technique allows the quantification of MOF/matrix in a sample, but also the thermal stability of the composite up to 800 °c. In addition, it can also provide information on the amount of solvent intercalated into the MOF after the synthesis process or identify materials that have contaminated the MOF sample. ICP-OES is a quantitative technique used to identify the metals within the sample, a useful technique which can be compared to the results of the TGA to check accuracy of the sample against the desired composition.

The rheometer was used throughout and although should not be a standard characterisation technique for MOFs, it should be standard for any 3DP filament. To understand the material properties (thixotropy and the elastic or viscosity moduli) of the sample is key to its function and ease of use, it can be cut down on the time used for experimenting with different parameters on the 3DP itself.

One technique which was overlooked was BET and could have been more routinely used throughout to demonstrate the porosity and adsorption application of the MOF. By using this technique, results can be compared across the globe with other samples of the same constituents. Overall, five techniques should always be quoted for MOF characterisation: PXRD, SEM, TGA, FTIR and BET.

2.4. Equipment

2.4.1. Modified SLA 3D Printer

The 3D Printer used in Chapter 3 was a Form 1+, Figure 2.6. The printer required no modification to function, other than the placement of two magnets on the resin tray, which conveniently magnetised to the resin tray mounting – holding them in place.

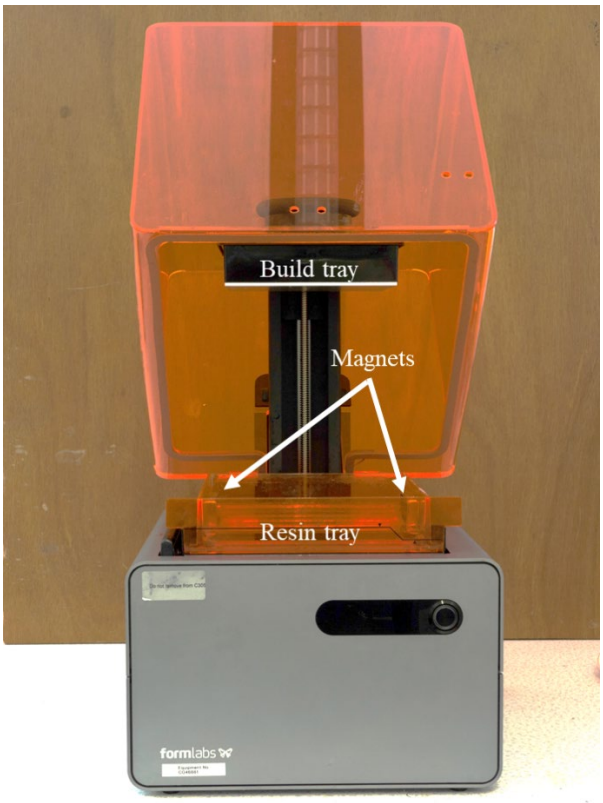

Figure 2.6: Modified Form 1+ 3D printer with magnets placed in the resin tray.

2.4.2. Modified Direct-write 3D Printer

The 3D printer used in Chapters 4 and 5 was a Velleman K8200 purchased from RS Components. The printer required assembly, soldering and wiring before the use of the 3D Printer. The syringe extruder was downloaded as an .STL file from the Velleman website,[8] and the bracket, slider and syringe holders required 3DP. A stepper motor and 1 driver board modification were included in the purchased kit, which was installed onto the 3DP as shown in Figure 2.7.

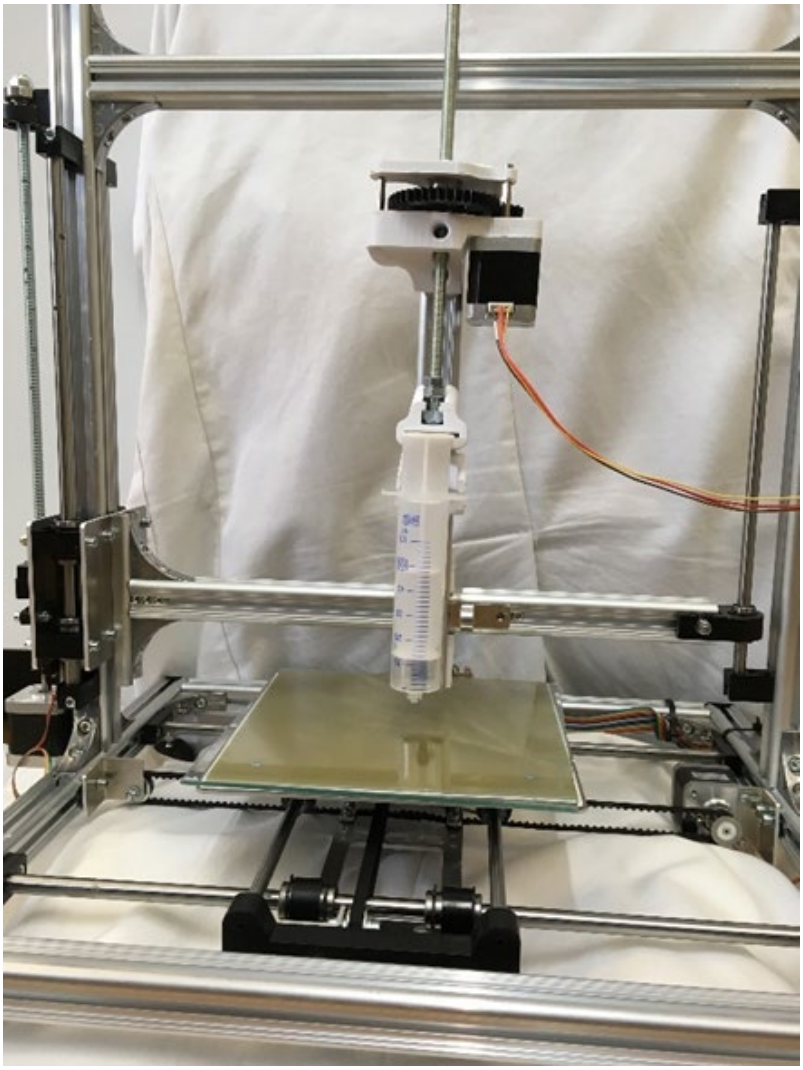

Figure 2.7: Images of the Vellemen K8200 used with the syringe pump attached.

Modifications to the G-code of the 3D printer was required to set the extrusion rate of the syringe. Figure 2.8 shows the final G-code used when using the syringe extruder, included was the exclusion of any heating of the bed or nozzle, a larger stepper motor rate and a pre-extrusion of 10 mm to allow the nozzle to be primed ready for printing.

```
;Sliced at: {day} {date} {time}
;Basic settings: Layer height: {layer_height} Walls: {wall_thickness} Fill: {fill_densit
;Print time: {print_time}
;Filament used: {filament_amount}m {filament_weight}g
;Filament cost: {filament_cost}
;M190 S{print_bed_temperature} ;Uncomment to add your own bed temperature line
;M109 S{print_temperature} ;Uncomment to add your own temperature line
G21        ;metric values
M82        ;set extruder to absolute mode
T1        ;set Paste extruder #2
M302       ; Allow Cold Extrusion
M92 E3000 ; Set Extruder EEPROM for Paste
G28
G1 F4000 X150 Y180
G92
G92 E0                  ;zero the extruded length
G1 F200 E10             ;extrude 10mm of feed stock
G92 E0                  ;zero the extruded length again
G1 F{travel_speed}
;Put printing message on LCD screen
M117 Printing...
```

Figure 2.8: Beginning G-code for using the Vellemen K8200 with the syringe pump

2.5. References

1 C. Volkringer, M. Meddouri, T. Loiseau, N. Guillou, M. Haouas, F. Taulelle, N. Audebrand, M. Latroche and D. V. Saint Quentin, *Inorg. Chem.*, 2008, **47**, 11892–11901.

2 J. M. Chin, E. Y. Chen, A. G. Menon, H. Y. Tan, A. T. S. Hor, M. K. Schreyer and J. Xu, *CrystEngComm*, 2013, **15**, 654–657.

3 C.-L. Lin, C.-F. Lee and W.-Y. Chiu, *J. Colloid Interface Sci.*, 2005, **291**, 411–420.

4 M. J. Katz, Z. J. Brown, Y. J. Colón, P. W. Siu, K. A. Scheidt, R. Q. Snurr, J. T. Hupp and O. K. Farha, *Chem. Commun.*, 2013, **49**, 9449–9451.

5 B. Bueken, N. Van Velthoven, T. Willhammar, T. Stassin, I. Stassen, D. A. Keen, G. V. Baron, J. F. M. Denayer, R. Ameloot, S. Bals, D. E. De Vos and T. D. Bennett, *Chem. Sci.*, 2017, **8**, 3939–3948.

6 W. H. Bragg and W. L. Bragg, *R. Soc. London.*, 1913, **88**, 428–438.

7 J. Park, J. D. Howe and D. S. Sholl, *Chem. Mater.*, 2017, **29**, 10487–10495.

8 Velleman, Velleman Syringe Pump, https://www.vellemanstore.com/en/velleman-k8205-paste-extruder-upgrade-for-k8200-3d-printer.

3. 4DP – Time dependent 3DP and magnetic alignment of MOF composites

3.1. Introduction

MOFs can be tuned to display a specific pore size, functionality and even aspect ratio. The pore volume of MOFs can range from 5.02 cm^3g^{-1} to 0.02 cm^3g^{-1},[1,2] with the record for the largest MOF pore volume currently held by DUT-60, Figure 3.1.

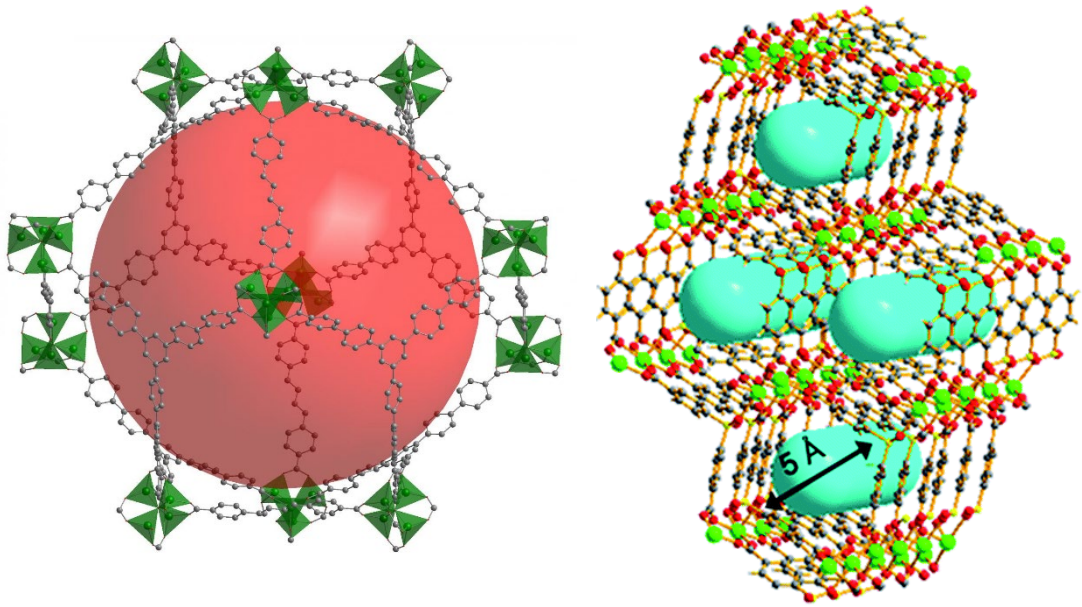

Figure 3.1: Pore volume of DUT-60 (5.02 cm^3g^{-1}) and CaSDB (0.02 cm^3g^{-1})

The tuneability of pore volume allows MOFs to be fabricated for specific applications such as separations. The specific ability of the MOF can be dependent on functional groups used in the MOF, for example the use of amines or long chain alkenes presenting the desired effects such as increased absorption or hydrophobicity.[3,4] While tuning the aspect ratio allows the formation of isotropic micro-MOFs such as in Figure 3.2, which displays square, hexagonal and pyramidal morphology of MOF-5.[5]

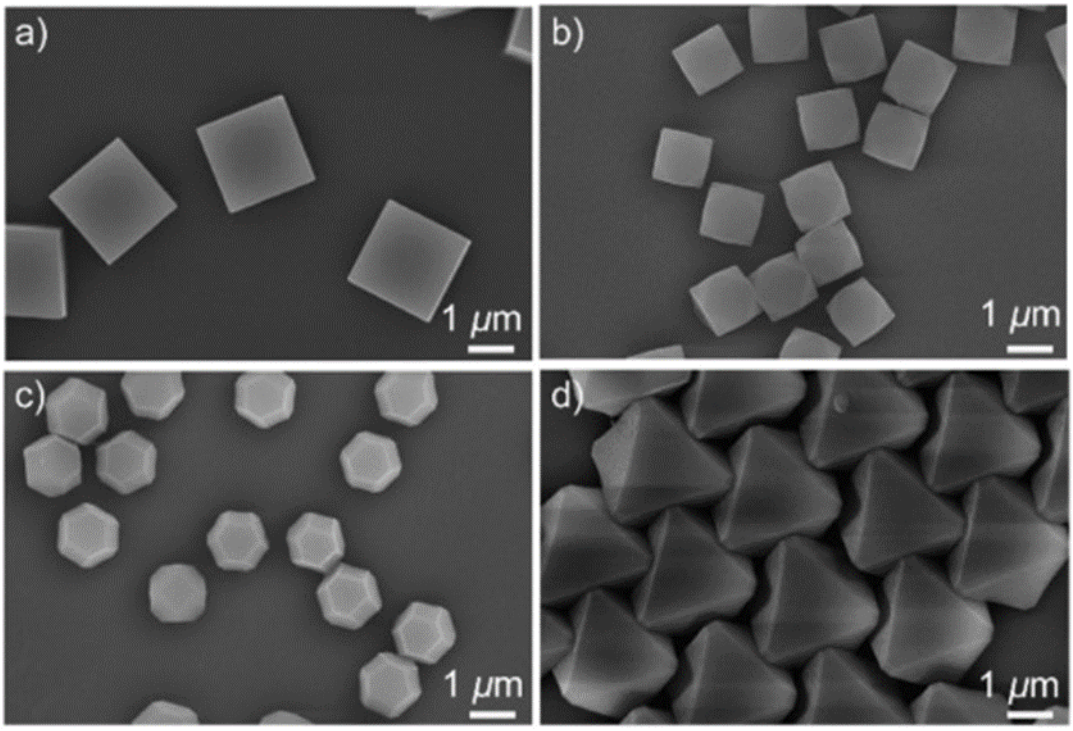

Figure 3.2: Tuning the crystal morphology of MOF-5 by addition of modulators.[5]

Not only can MOFs be isotropic, they may also be tuned to be anisotropic micro-scale rods or needles, [6]Figure 3.3, which display unique crystallites with an increased surface area. Anisotropic MOFs may have greater efficiencies per molecule.[7]

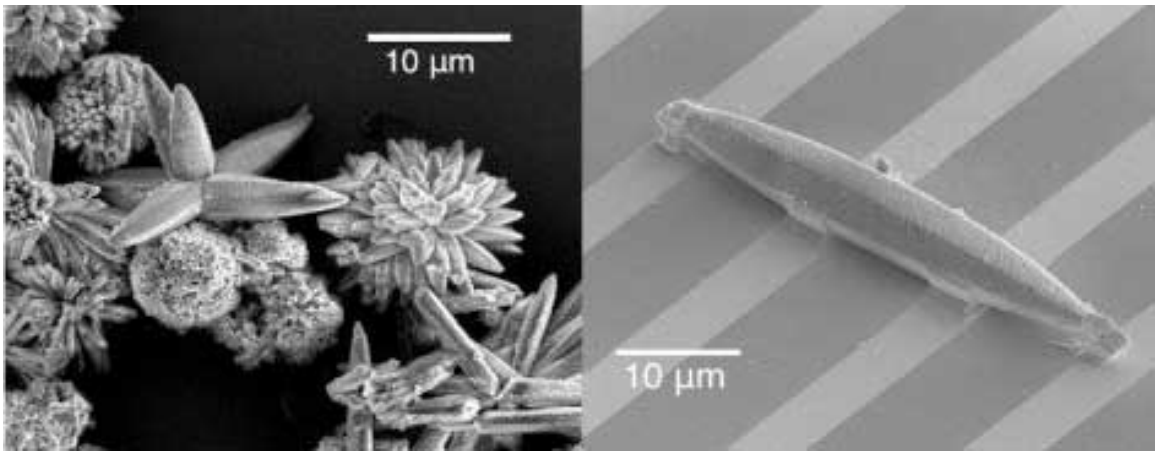

Figure 3.3: Iron BDP MOF modulated in size from small clusters measuring 10 μm to individual rods measuring 10 μm.[6]

However, the application of anisotropic MOFs relies on the favourable orientation of the MOFs crystal structure, which is controlled by the alignment of the macroscopic crystal. For example, a needle or rod-like MOF morphology is required to be aligned for an application such as the flow-through of gaseous or aqueous material into and out of the MOF. However once aligned the MOFs will be highly efficient in the catalysis of a reaction or capture chemical components.[8,9] Alignment

of bulk anisotropic MOFs can also cause useful optical activity, as the combined effect of alignment of many luminescent particles can cause a measurable optical response.[7,10] However, the processing of a bulk material to possess favourable alignment is limited to a number of effects.

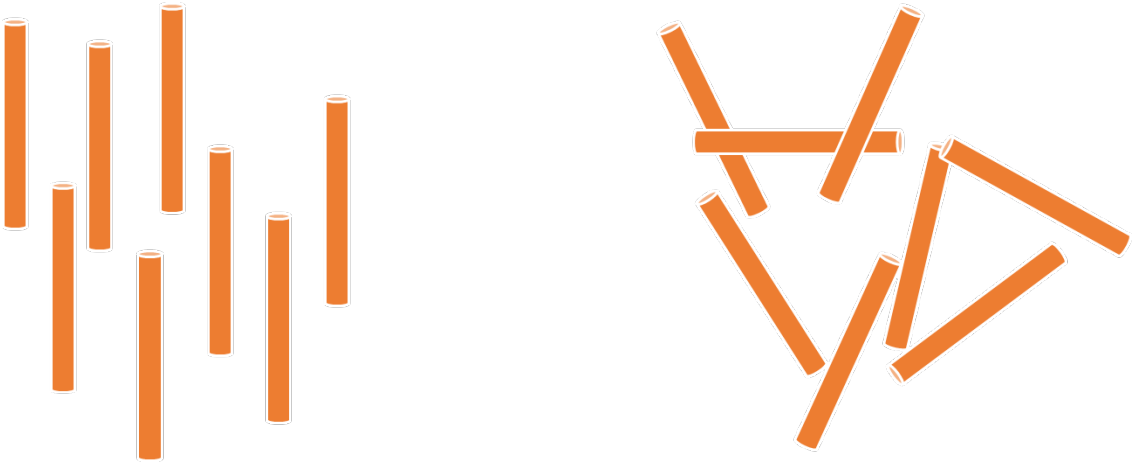

Figure 3.4: Picture of unaligned anisotropic MOFs against unaligned anisotropic MOFs.

One method of alignment control is by the epitaxial growth – crystal growth on a crystalline substrate that produces well-defined orientation, Figure 3.2.[11,12] But this method requires large amounts of time and creates a 2D thin-film of material that is difficult to utilise and process.

Other methods of MOF orientation have been investigated such as control by an external magnetic field; by the use of metal centres susceptible to a magnetic field,[13] or by the electrostatic adsorption of nanoparticles,[13,14] onto surface of the MOF.

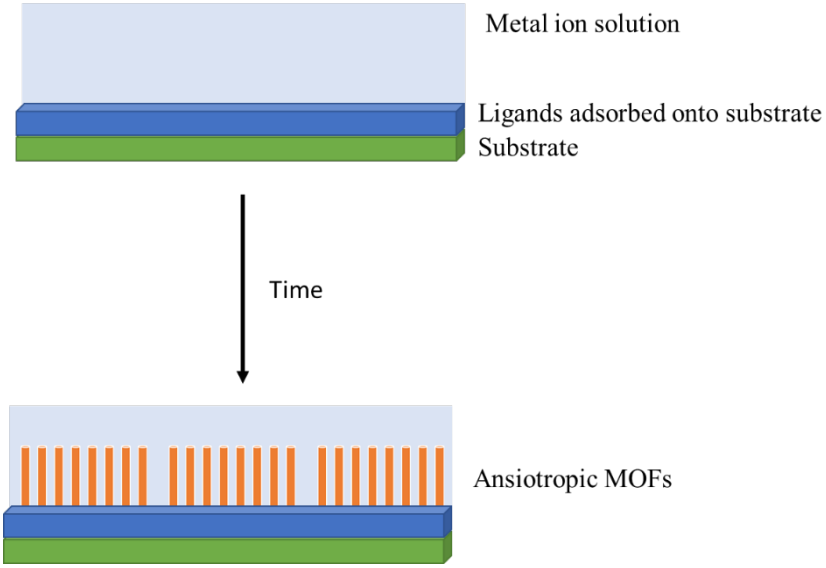

Figure 3.5: Picture of epitaxially grown MOFs, demonstrating how ligands may be adsorbed onto a substrate, metal ion solution added and MOFs grow on the surface, aligned and anisotropic.

The principle remains the same, whereby the magnetic material is exposed to a magnetic field and aligns to the field. One major drawback to these magnetic MOFs is the lack of a fabrication techniques which can utilise the dynamic magnetic alignment and fix into position. It is therefore necessary to fabricate a composite which allows the aligned particles to be set into position, to grant access to their unique properties.

Herein explored is the combination of MOF anisotropy with dynamic magnetic alignment to demonstrate an application and their 4D printability.

3.2. Chapter Overview

The objectives of the work in this chapter is to develop 4DP composites of magnetically aligned MOFs. The alignment will be achieved by the adaption of an SLA 3D printer with neodymium magnets.

The fabrication of magnetised MOF particles is then explored by two different approaches 1) by the synthesis of MIL-68(Ga) and MIL-68(In) doped with iron 2) by the fabrication of NH_2-MIL-53(Al), NH_2-MIL-68(In) and NU-1000 with adsorbed iron oxide nanoparticles. The first method will investigate the effect of adding iron salts to MIL-68(In) and MIL-68(Ga) and the potential for MOFs alignment in a magnetic field will be explored. The second method investigates the potential for alignment of anisotropic particles NH_2-MIL-68(In), NH_2-MIL-53(Al) and NU-1000 with adsorbed iron oxide nanoparticle. The potential for alignment of these anisotropic particles will be explored. Successful results will be used for further demonstrations of a 4DP material.

3.3. Results and Discussion

To achieve magnetic alignment of particulates, the magnets had to be attached or in the presence of the 3D printer. There were three approaches to achieve this, outlined in Figure 3.6.

a) Place magnets around the nozzle of a direct-write 3D printer to achieve alignment while printing.
b) Place the magnets onto the resin tray of an SLA 3D printer.
c) Place the magnets into the build tray of an SLA 3D printer

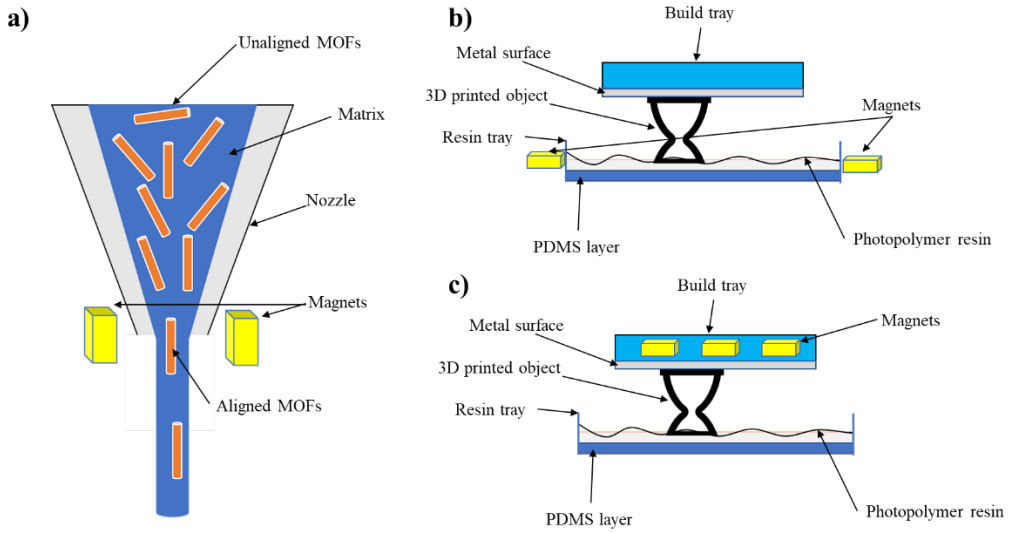

Figure 3.6: Schematic of the three approaches trialled to achieve magnetic alignment.

The first approach (Figure 3.6a) involved developing a holder for magnets to sit while material was extruded out of the nozzle of a direct-write printer. While this method may appear simple, the modification to design a holder that would not get in the way of the nozzle during printing was difficult, the holder appeared big and bulky and never developed past the drawing board.

The next approach (Figure 3.6b) was to place magnets either side of an SLA resin tray, to align the magnetic MOFs through the entire vat of photopolymeric resin. This was tested with 2700 G strength neodymium magnets, fortunately the magnets attached onto metal brackets that hold the resin tray in place, so they could remain in position without any modification. This was a successful technique (as evidenced later in this chapter), however the area aligned was only small. To achieve better results, it was thought an electromagnet may be worth trialling – however, the power of the electromagnet might have disrupted the electronics or metallic components of the SLA 3D printer and was not pursued.

The final technique (Figure 3.6c) was to place 2700 G neodymium magnets into the build tray and lower the build tray into the polymeric resin with the magnetic MOFs inside. However, this method simply pulled all the magnetic MOFs out of solution depositing them onto the metal of the build tray.

The successful technique (Figure 3.6c) was taken forward using a Form 1+ SLA 3D printer, Figure 3.7, mounted with neodymium magnets on the inside of the resin tray.

Once the 3D printer was successfully modified the next stage was to create magnetic MOFs by two methods; doping iron into MOFs or adding iron oxide nanoparticles onto MOFs. The two methods of magnetisation were used due to cost. The use of magnetic nanoparticles such as magnetic cobalt nanoparticles is more expensive and much more toxic than iron oxide nanoparticles. Iron salts are relatively cheap and readily available to purchase with a lot of literature on the success for the magnetisation of other anisotropic materials.[15]

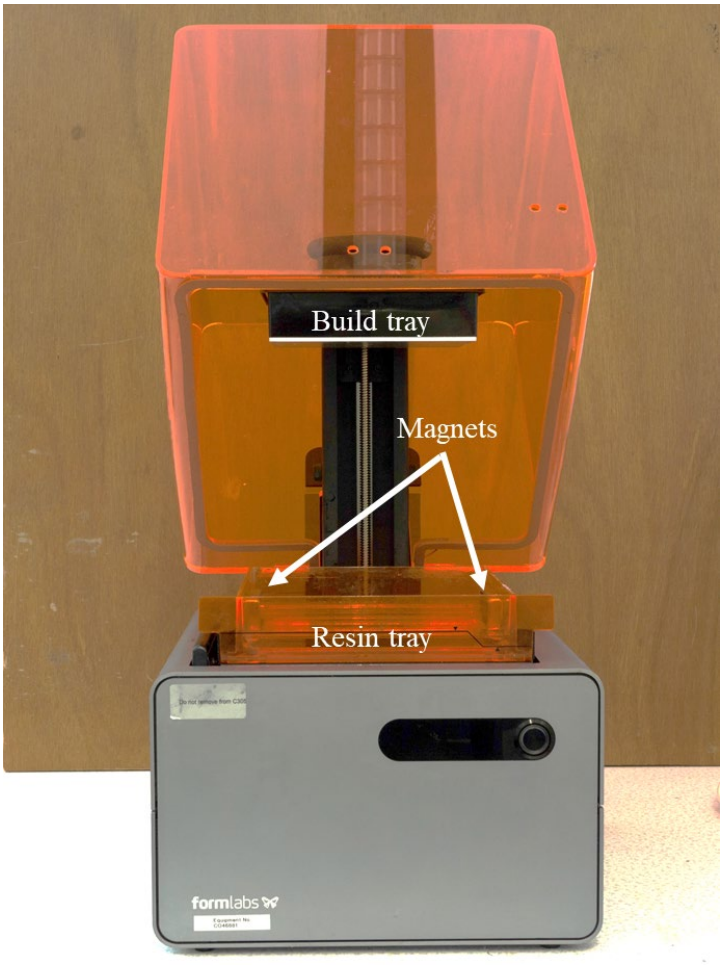

Figure 3.7: Formlabs 1+ 3D printer adapted with magnets inside the resin tray.

3.3.1. Doping iron into MIL-68(Ga)

Characterisation by ICP-OES was ran and analysed by technical staff - Mr Bob Knight within the Department of Chemistry.

The first set of experiments involved investigating if iron could be doped into a MOF and generate a magnetic response. The chosen MOF was MIL-68.MIL-68 was chosen here for its unique Kagomé architecture, the name inspired by Kagomé origami, with the repeating hexagonal and triangular pattern. MIL-68 is was also cheap to synthesise and easy to repeat.

MIL-68, shown below in Figure 3.8 and Figure 3.9, is made up of either gallium, indium or aluminium metal nodes co-ordinately bound to terephthalic ligands. In the basic synthetic pot for the synthesis of MIL-68 is a metal nitrate solution and ligand solution, both fully dissolved in a suitable solvent, usually DMF. The combined solution is then placed into a sealed autoclave, heated and cooled as outlined inSection 3.5.2.

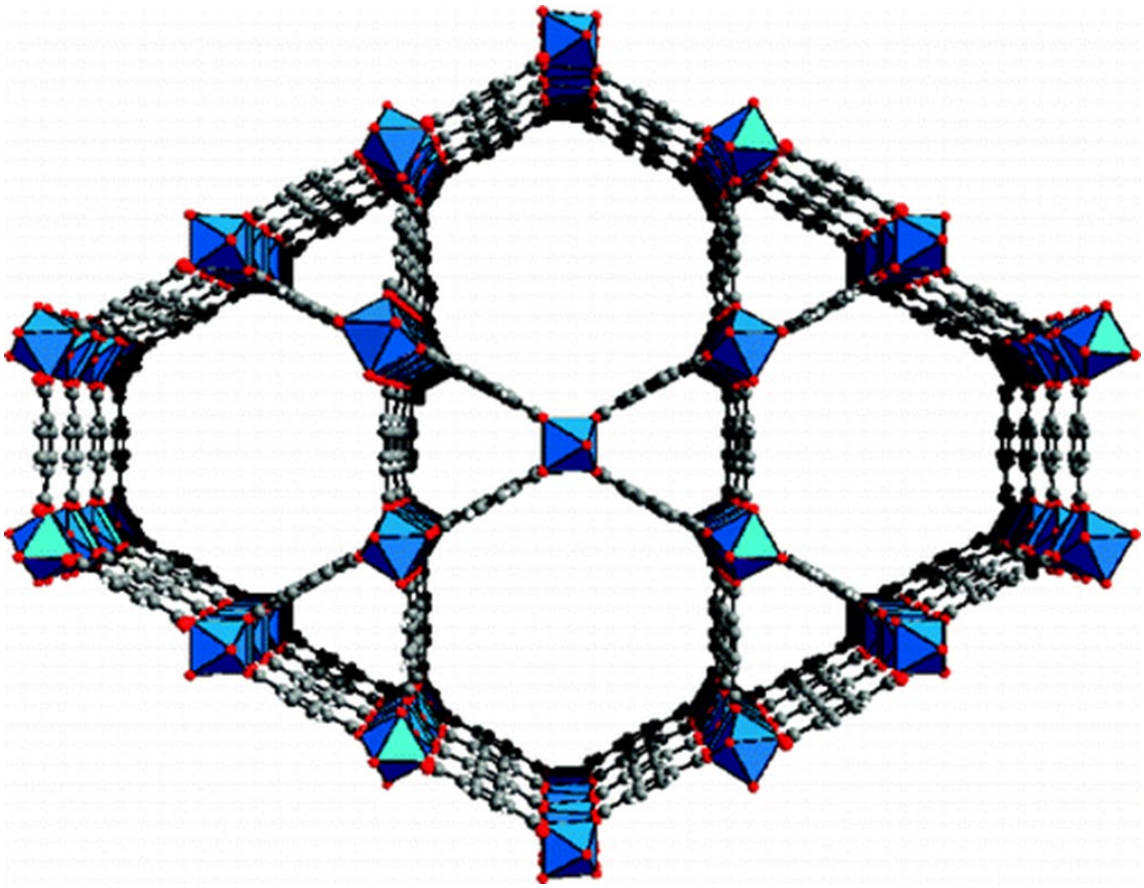

Figure 3.8: Crystallographic image of MIL-68. Reproduced with permission ref.[16]*copyright 2008 American Chemical Society*

Out of the wide selection of metal nitrates available for MIL-68 synthesis (gallium, indium, iron or aluminium), only two were chosen. The synthesis of MIL-68(Al) was avoided for its ability to form its polymorph MIL-53(Al) by very subtle differences in synthetic procedure. MIL-68(In)

and MIL-68(Ga) were chosen for their ease of synthesis, known and well characterised form and ability to generate anisotropic rods.

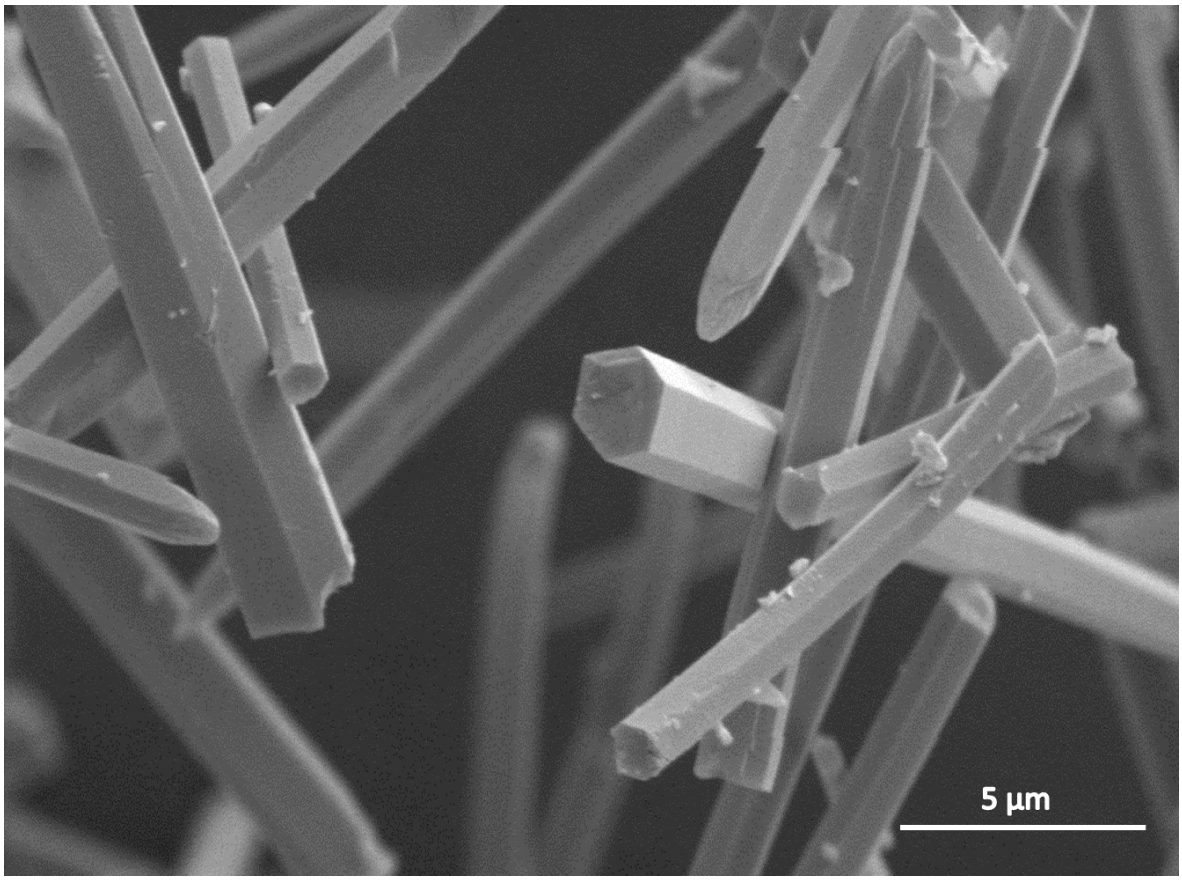

Figure 3.9: SEM (Cambridge Stereoscan 360) of MIL-68(In)

If iron could be successfully doped into the MOF architecture, it could then be controlled in a magnetic field and grant controllable and dynamic crystal orientation. This first section will explore the approach of doping MIL-68(Ga) with iron during synthesis with five different amounts of $Fe(NO_3)_2 \cdot 9H_2O$, labelled **1A-E**, as in Table 3.1.

Table 3.1: Percentages of iron and gallium content for the synthesis of MIL-68(Ga)

MIL-68(Ga)	**1A**	**1B**	**1C**	**1D**	**1E**
$Ga(NO_3)_3 \cdot 6H_2O$	100 %	95 %	90 %	85 %	80 %
$Fe(NO_3)_2 \cdot 9H_2O$	-	5 %	10 %	15 %	20 %

This will be followed by an in-depth characterisation of the synthesised material to explore the success of iron added into MIL-68(Ga) by quantitively and qualitatively demonstrating how much

iron is present. Fe-MIL-68(Ga) samples were produced by introducing iron nitrate into the reaction as described in Section 3.5.2.

Samples **1A-E** powders were sent for ICP-OES analysis as a preliminary test to determine the percentage of metals (Ga and Fe) in each sample and the success of the synthesis. Sample **1A** was MIL-68(Ga) with no addition of iron. The next four samples, **1B-E,** had increasing amounts of $Fe(NO_3)_2 \cdot 9H_2O$ added, expecting that iron will replace gallium in the MOF architecture, however this technique cannot confirm the location of iron, only its presence and quantity.

The results in Table 3.2 suggest four samples do contain iron. Sample **1B** has a slightly higher iron content than expected. For the three most iron-rich samples, **1C-E**, the amount of iron included in the product is less than expected. This suggest that the amount of iron which could be included in MIL-68(Ga) is limited. It is notable that these iron-rich samples are rather difficult to dissolve for chemical analysis. After attempting to dissolve the MOFs in aqua regia for ICP-OES analysis, the samples were filtered onto filter paper; remaining on the filter paper was a black solid, which may explain the lower amount of iron in samples **1C-E.** However, using a paired two tailed t-test all samples **1B** was within an error of 95% accuracy, while samples **1C-E** were within an error of 80 % accuracy. Overall, it can be concluded from the results that iron was present in the samples and iron content increased following the trend. The next step is to confirm whether the material is a crystalline MOF and displays MIL-68(Ga) architecture.

Table 3.2: ICP-OES values of MIL-68(Ga) with incremental addition of iron

Samples	Theoretical Gallium Content / %	Theoretical Iron Content / %	Experimental Gallium Content / % (ICP-OES)	Experimental Iron Content / % (ICP-OES)
1A	21.81	0	20.18	None
1B	20.45	1.11	18.10	1.46
1C	19.08	2.22	17.45	2.08

1D	17.72	3.33	15.06	2.86
1E	16.36	4.44	15.93	3.24

3.3.1.1. PXRD analysis for MIL-68(Ga)

PXRD was used to confirm if the synthesised powder was indeed crystalline and that MIL-68 was synthesised, because following the literature synthetic protocols outlined in Section 3.5.2, it is expected to yield MIL-68 morphology. This will be proven by examining the five observed PXRD patterns against simulated literature PXRD patterns from Volkringer *et al.*[16]

Figure 3.10 displays six PXRD patterns, the first observed pattern (**1A**) is unadulterated MIL-68(Ga) and matches with the literature pattern displaying distinctive peaks at 2θ = 8, 10, 15, 19° which agrees with the expected pattern.[16] This confirmed the synthesised samples were that of MIL-68(Ga). As iron is added (**1B-**E) the intensity of the peaks changes. Intensity depends on the atoms present and their positions while peak position depends on the unit cell parameters. As such intensity changes as the crystal structure changes with the addition of iron and peak position remains consistent.

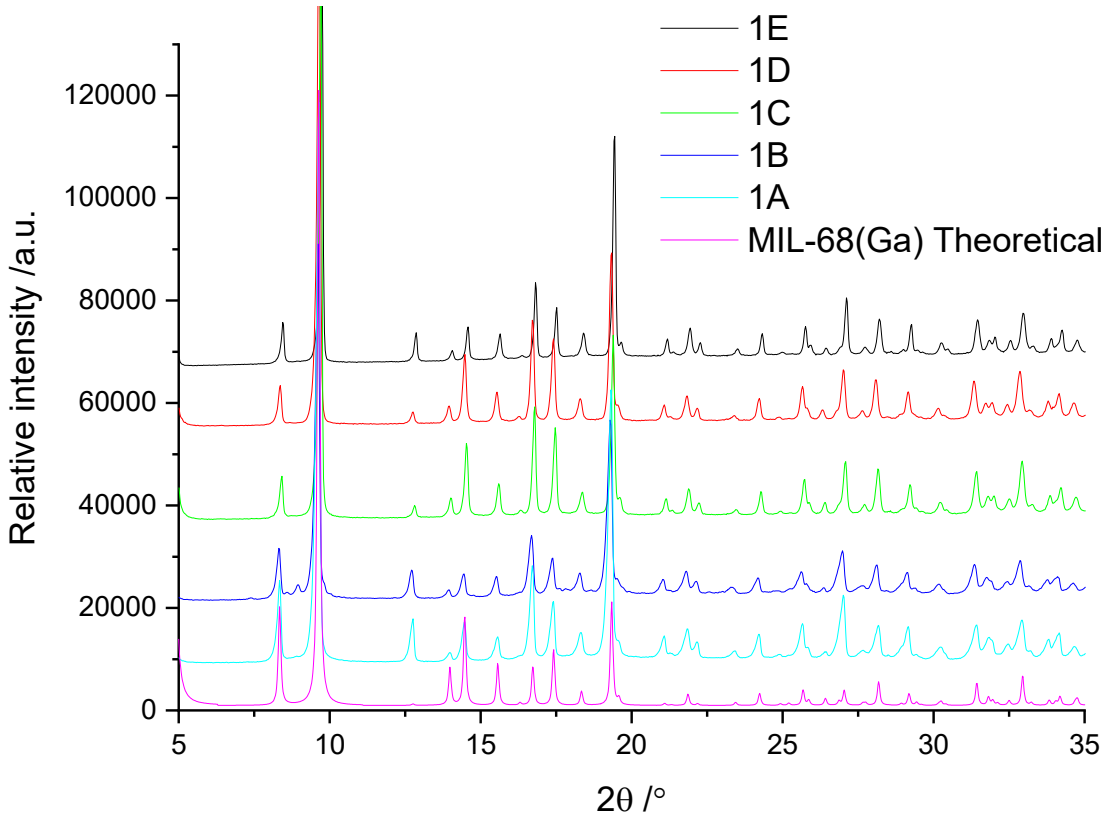

Figure 3.10: PXRD patterns of MIL-68(Ga) from the literature and synthesised samples with increasing amounts of iron moving up the graph.

The simulated pattern reported by Volkringer *et al.*[16] has weaker intensities at peaks 2θ = 13, 21 and 25 than samples **1A-E**. This due to the presence of a trapped species in the channel of the structure, the mostly likely cause is DMF - the solvent used in the synthesis. The phenomenon has been seen before by Volkringer *et al.*[16] whereby they proved, by NMR and IR, that DMF resided in the small triangular tunnels and the large hexagonal channels of MIL-68. DMF was held in the pores by strong hydrogen bonding interactions between the oxygen atom of the formamide of DMF and the hydroxyl group bridging the metal. Further testing would identify if DMF was indeed present in the synthesised samples. CHN elemental analysis was undertaken to identify the presence DMF, by nitrogen content, and is investigated next.

The PXRD patterns confirm that the synthesised samples **1A-E** have the MIL-68(Ga) structure, though there is no information as to the extent the addition of iron has on the unit cell: unit cell volume, unit cell parameters. This information can be gained by computational comparison of the theoretical PXRD pattern against the PXRD patterns of samples **1A-E**, this is investigated in a later section.

3.3.1.2. Elemental analysis of MIL-68(Ga)

CHN analysis carried out by Mrs Carol Kennedy.

In the previous paragraph it was outlined that DMF may be present, resulting in variation in intensities on the PXRD pattern. CHN elemental analysis could be used determine whether DMF was indeed present by the detection of nitrogen in the samples. DMF and its hydrolysis product dimethylamine (Figure 3.11) are possible sources of nitrogen in this reaction, along with any nitrate salts from the metal reagents.

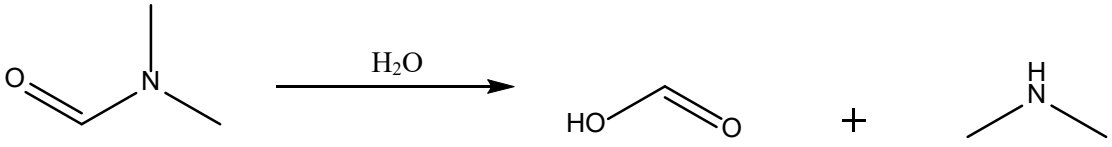

Figure 3.11: N,N–Dimethylformamide (DMF) acid hydrolysis reaction to formic acid and dimethylamine.

Table 3.3 displays the data received from CHN analysis, it displays percentages of carbon, hydrogen and nitrogen as received from the technique. As its been previously discussed, the presence of nitrogen is not surprising and confirms the presence of DMF in the samples. The variation in nitrogen (and also carbon and hydrogen) content is most likely due to more DMF being present.

Table 3.3: CHN analysis data for samples MIL-68(Ga) ***1A-1E***

Samples	**Carbon Content / %**	**Hydrogen Content / %**	**Nitrogen Content / %**
1A	39.63	4.45	5.18
1B	39.78	4.36	5.53
1C	38.23	3.59	2.85
1D	38.57	3.35	2.78
1E	39.76	4.56	5.28

The scope of this study is to investigate whether the addition of iron causes the MOF to display magnetic properties and how the iron interacts with the MOF. It is not within the scope of this study to identify how much of the nitrogen was DMF or dimethyl amine, as they can be concluded as contaminants, these are usually removable by further post-synthesis washing and so no further tasks are undertaken to identify the compound.

3.3.1.3. Effect of iron on the unit cell of MIL-68(Ga)

Semi-quantitative analysis (Section 3.5.4) of the powder diffraction patterns yields information about the crystal structure of the product. Data on the cell volume and unit cell are collected by overlaying the theoretical pattern, obtained by generating a PXRD pattern from CIF file 4306785 using Mercury, and the experimental pattern observed. The resulting information of peak height, intensity, d-spacing is used to calculate the unit cell length a, b and c and volume. The changes in volume and unit cell length were then tracked and plotted against the values of iron experimentally obtained from ICP-OES analysis.

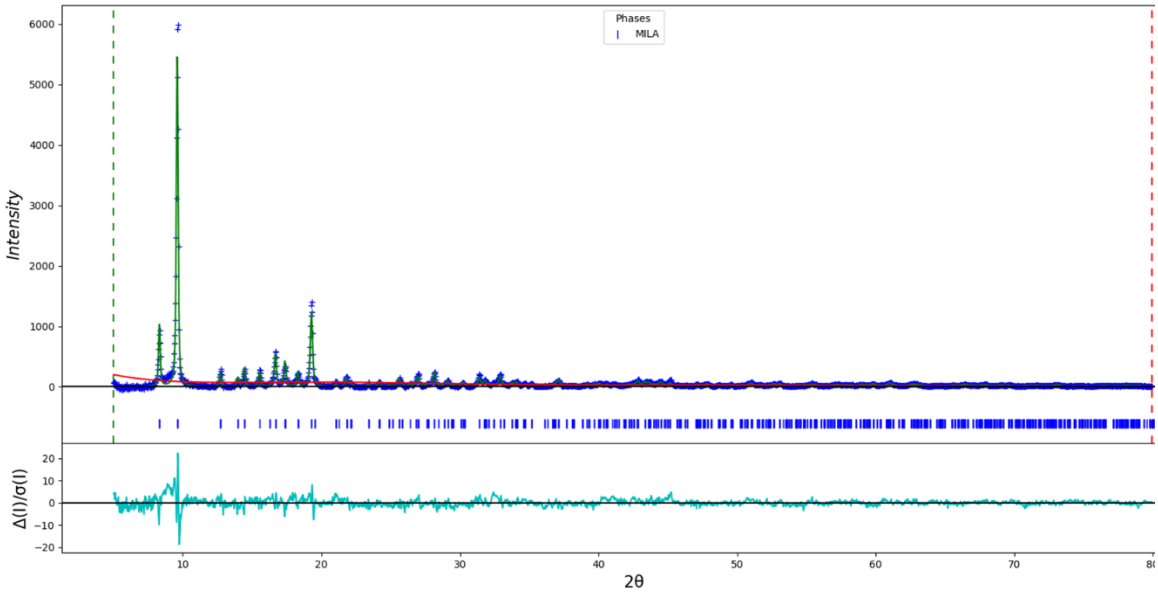

*Figure 3.12: Quantitative analysis of samples **1A,** against the literature in GSAS2.*

The technique allows the refinement of the model to fit experimental patterns, shown in Figure 3.13, observed for samples **1A-E**. By fitting the data, using the analysis detailed in experimental, three graphs were generated to display the trend observed from samples **1A-E**. The graphs display volume and unit cell length a, b or c against iron content as found by ICP-OES. Using the data, it can be seen which axis is greatly impacted by the doping of iron into the unit cell.

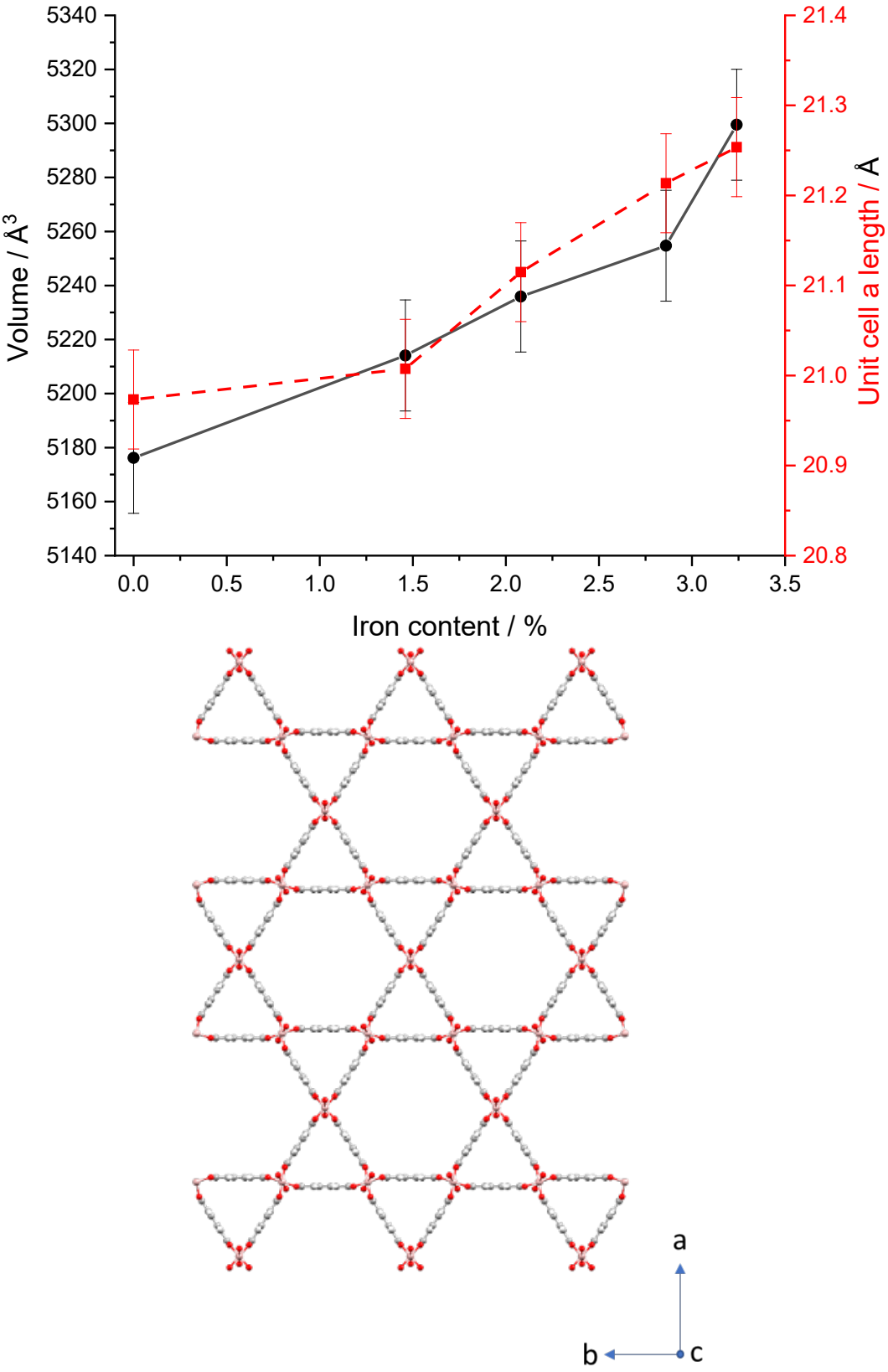

*Figure 3.13: Quantitative analysis of samples **1A-E**, displayed graphically with unit cell volume and unit cell parameter a against iron content. Displayed on the right is the view down the c axis of MIL-68(Ga) displaying the Kagomé architecture and how the cell may change on expansion.*

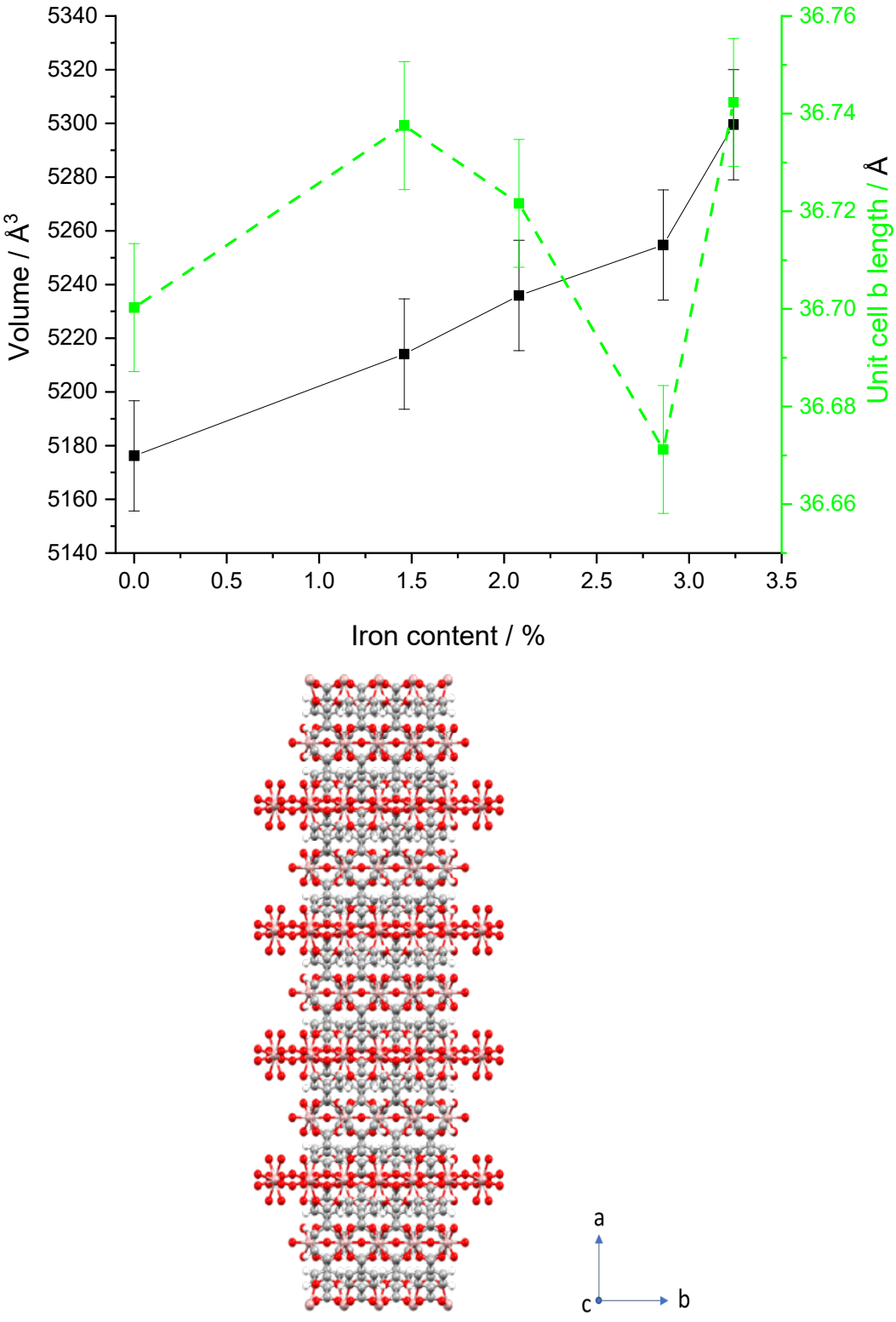

*Figure 3.14: Quantitative analysis of samples **1A-E**, displayed graphically with unit cell volume and unit cell parameter b against iron content. Displayed on the right is the view down the c axis, showing how b changes.*

Figure 3.13 shows the variation of unit cell parameter a and the unit cell volume with iron content. Both increase as iron content increases. This suggested that the iron replacing the gallium was indeed larger. This was of significance because of the variance in the atomic radii Ga^{3+} 62 pm, Fe^{2+} 70 pm and Fe^{3+} 60 pm.[18] Although not proven here, it gives some evidence that Fe^{2+} is doped into the structure, however this was not investigated further but played an important role when determining the magnetic properties of the MOF.

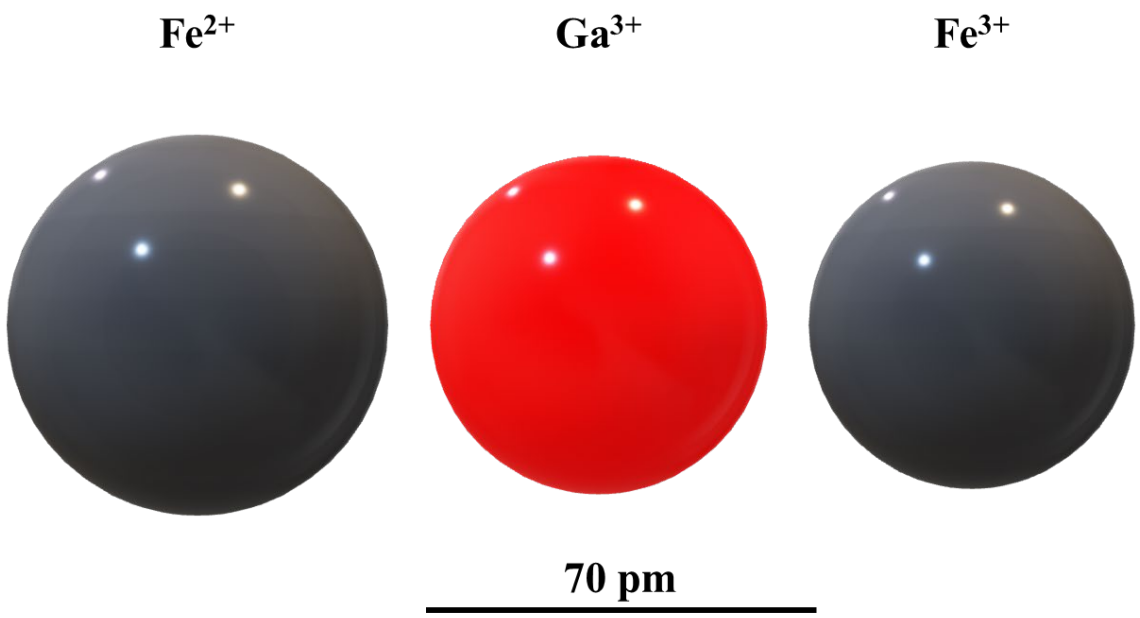

Figure 3.15: Representation of Fe^{2+}, Ga^{3+} and Fe^{3+}, to scale, showing the difference is size between the three atoms.

For now, as the iron content increases so does the unit cell parameter a and also the volume of the unit cell. MIL-68 is known for its tessellation of hexagonal and triangular shapes termed Kagomé. This style in the image in Figure 3.13, additionally MIL-68 is anisotropic along the c axis and so if the unit cell does expand here with increasing iron so does the pore size and cell volume. Figure 3.14 shows that unit cell parameter b remains unchanged, within the given error, upon introduction of iron. One outlier at iron content 2.86 % is shown to not fit the data set. By observing the model of MIL-68(Ga) crystallographic b axis, it can be noted the compactness of the network and lack of porosity, any change or increase to the metal centre size (gallium or iron) will have minimal effect on unit cell b.

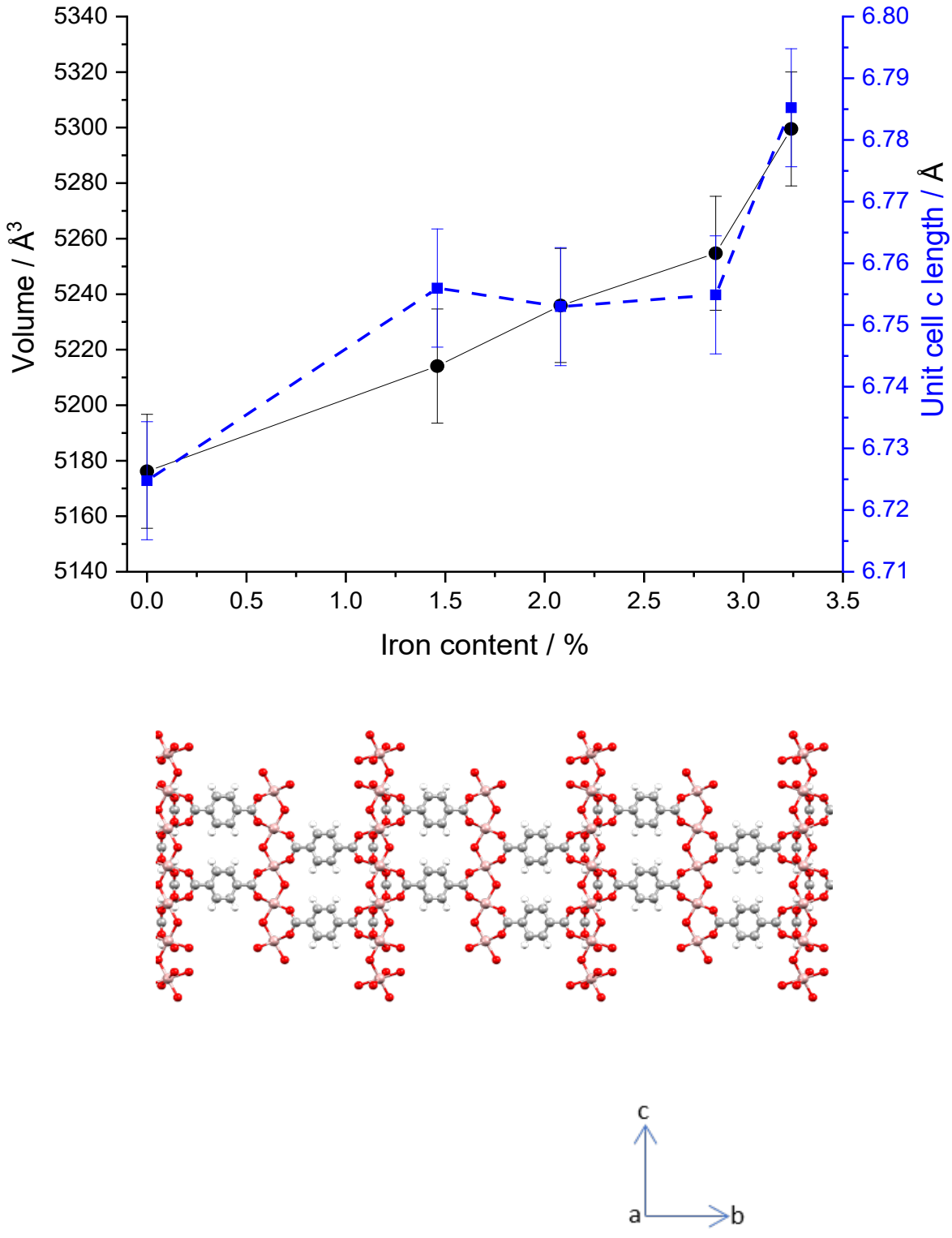

*Figure 3.16: Quantitative analysis of samples **1A-E**, displayed graphically with unit cell volume and unit cell parameter c against iron content. Displayed on the right is the view down the a axis, displaying how the cell could change.*

Figure 3.16 shows that unit cell c does not change with iron content within error. The view of the unit cell down the a axis demonstrates the shape and how there is now much room for expansion. The increase in volume as iron content increases is mostly seen in the expansion unit cell a creating larger pores and a greater surface area.

3.3.1.4. Observing MIL-68(Ga) using SEM

SEM was used to view the surfaces of the crystalline materials to gain an insight into the ranging sizes of the MOFs. Specimens were taken for each sample and viewed under SEM, after being gold-coated to increase conductivity and image quality. The images are used to show if the samples are monodisperse whereby the particles are of uniform size throughout the batch.

Figure 3.17 show samples **1A-E** under the electron beam with sample **1C** being a great example of the expected hexagonal morphology of MIL-68 with a particulate length of 2.01 ± 0.60 μm and width 0.27 ± 0.06 μm. Sample **1D** displays a greater monodispersity with lengths of 1.06 ± 0.12 μm and a width of 0.22 ± 0.03 μm. Sample **1E** however displays limited or no monodispersity (length: 2.11 ± 1.00 μm width: 0.53 ± 0.08 μm) and it appears from the image there are small crystals growing on the larger MOF crystals. The micro-crystal growth could either be small crystals of MIL-68(Ga) or potentially an iron-based MOF with different structure, however if it was in such large amounts the iron-based MOF would have been evidenced by PXRD, which cannot be seen. It is more likely they are small crystallites of MIL-68.

Interestingly, samples **1A-B** were unstable under the electron beam and were therefore difficult to measure as they can be seen to be bent and misshapen in the images. However, under the same electron beam parameters (reduced to 5 keV, normal operating voltages are 15 keV) samples **1C-E** were stable. It may be the case that introducing small amounts of iron renders this structure more stable to electron beam damage.

The samples **1A-E** have been successfully characterised by PXRD and SEM to be a MOF and accordingly MIL-68. The amount of iron has been verified by ICP-OES and it has been noted that

elemental nitrogen has been detected in the MOFs, which has been assumed to be either DMF or dimethylamine.

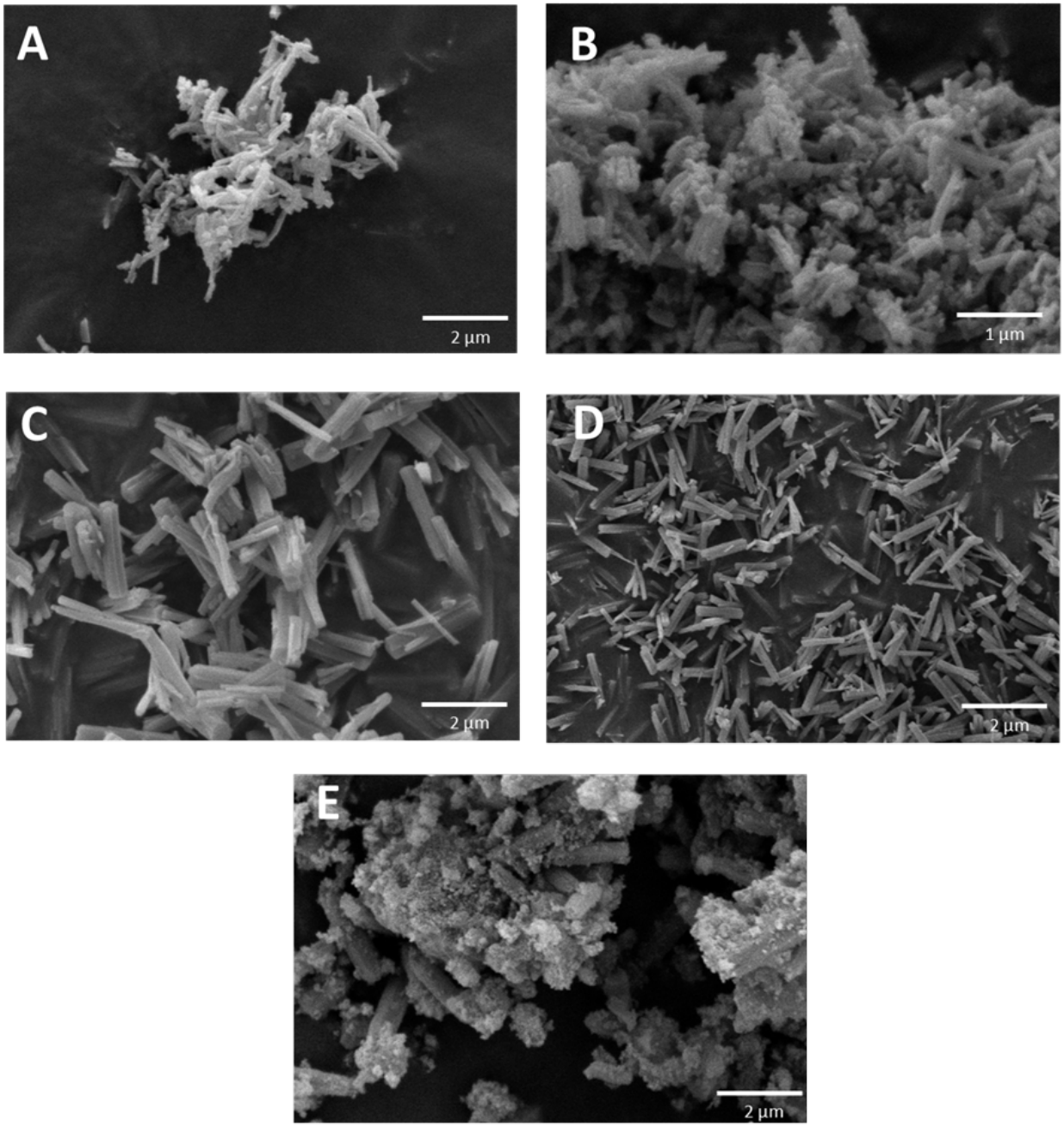

*Figure 3.17: SEM (Hitachi TM4000) of MIL-68(Ga) samples **1-5** labelled A-E.*

Analysis of the PXRD patterns of the samples shows that the MIL-68(Ga) architecture is retained as iron is introduced and increased. Additionally, as the iron content is increased the unit cell parameters and volume increased respectively. The next step is to determine whether the inclusion of iron into the MOF has altered the magnetic properties of the MOF, but first another further experimentation of the MIL-68 architecture will be tested with the use of MIL-68(In).

3.3.2. Doping iron into MIL-68(In)

In the previous section the introduction of small amounts of iron into MIL-68(Ga) were demonstrated. The technique was trialled with a second material of the same architecture but with a different metal centre, MIL-68(In). In^{3+} has a larger atomic radius and on addition of Fe^{3+} to this unit cell it is expected that the unit cell parameters and volume will shrink. Incremental amounts of iron were added to the MIL-68(In) synthesis, as outlined in Section 3.5.3. ICP-OES was used to show that iron was present in the MOF, PXRD was used to confirm the crystallinity of MIL-68(In) and CHN analysis to identify contaminants. Analysis of powder diffraction data showed changes in the unit cell volume and SEM was used to confirm the morphology. All these techniques were preceding magnetic susceptibility testing as without confirmation of the creation of MIL-68(In) with iron there was no requirement to go ahead with the testing.

If the addition of iron to MIL-68(In) is successful, the MOF could be controlled in a magnetic field and grant controllable and dynamic crystal orientation. To identify if the modified synthesis was a success ICP-OES was utilised to show percentages of indium and iron in samples **2A-E**. The resulting data was useful to determine if iron was indeed doped into the MOF structure. Results shown in Table 3.4, the iron-rich species contain less than expected. This suggests the amount of iron which is included into MIL-68(In) is limited (and greater than MIL-68(Ga)). It is notable that these samples were difficult to dissolve for testing with ICP-OES, as sample was left on the filter paper.

Table 3.4: ICP-OES values of MIL-68(In) with incremental additions of iron

Samples	**Theoretical Indium Content / %**	**Theoretical Iron Content / %**	**Experimental Indium Content / % (ICP-OES)**	**Experimental Iron Content / % (ICP-OES)**
2A	38.46	0	37.97	None
2B	36.05	1.10	36.02	1.06
2C	33.65	2.21	28.77	1.17

2D	31.25	3.32	27.85	2.49
2E	26.44	4.43	22.13	3.71

3.3.2.1. PXRD pattern analysis of MIL-68(In)

PXRD was used to confirm if the synthesised powder was indeed crystalline and that MIL-68(In) was synthesised, because following the literature synthetic protocols outlined in Section 3.5.3, it is expected to yield MIL-68(In) morphology. This will be proven by examined the five observed PXRD patterns against simulated literature PXRD patterns from Volkringer *et al.*[16]

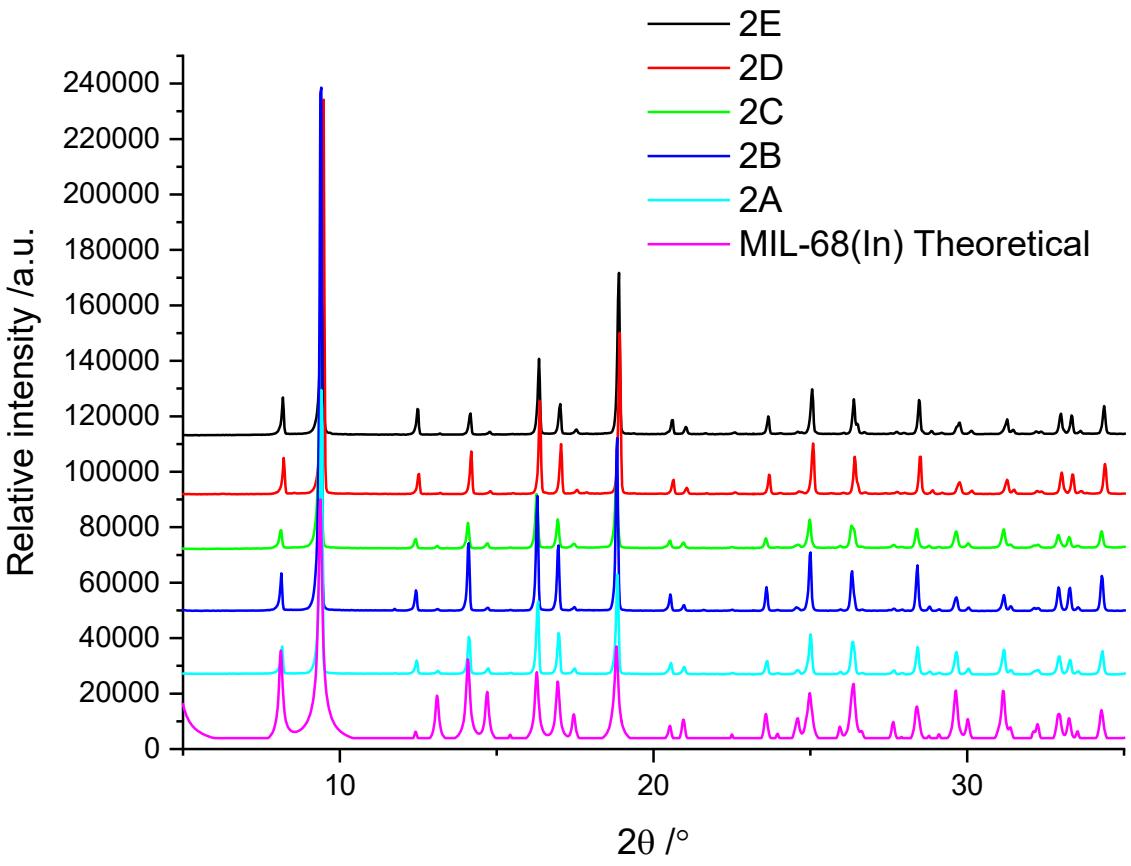

Figure 3.18: PXRD patterns of MIL-68(In) from the literature and synthesised samples with increasing amounts of iron moving up the graph.

Figure 3.18, displays six patterns of MIL-68(In), comparing the literature synthesised pattern against synthesised patterns of MIL-68(In) **2A-E**. The synthesised patterns (**2A-E**) are MIL-68(In) and all match the expected pattern in the literature with varying intensities.[16] The theoretical PXRD pattern used for MIL-68(In) in Figure 3.18 takes into account the DMF resident

in the pores and so is a better match than the previous MIL-68(Ga). However, intensities vary and this is not uncommon when comparing MOFs with varying properties and it may be due to the anisotropy of the MOF and its preferred orientation. As it has been stated previous there is very likely DMF present in the pores, to check this phenomenon CHN analysis grants information regarding the amount of nitrogen present in the samples.

3.3.2.2. Elemental analysis of MIL-68(In)

CHN analysis carried out by Mrs Carol Kennedy.

As with MIL-68(Ga) samples **1A-E**, CHN analysis was used to verify that a nitrogen containing compound was indeed present in samples **2A-E**.

*Table 3.5: CHN analysis results for samples **2A-E***

Samples	Carbon Content / %	Hydrogen Content / %	Nitrogen Content / %
2A	34.48	2.65	1.88
2B	31.67	2.56	1.99
2C	34.93	3.45	3.96
2D	34.35	3.36	3.01
2E	36.32	3.94	5.56

Nitrogen will be present due to the aforementioned presence of DMF in the pores of the MOF. Analysis revealed in Table 3.8, nitrogen was present in all the samples in varying amounts ranging from 1.88 – 5.56 %. The nitrogen content increases as the iron content increases. This may be due to DMF, and the oxygen lone pair formed from its resonance structure shown in Figure 3.19, binding more strongly to iron than indium. This is evidenced by the bond dissociation energy of Fe-O (409 kJ mol^{-1-}) compared to In-O (360 kJ mol^{-1}).[19] This was not looked into further, but a more rigorous washing process could have been undertaken after synthesis to remove excess DMF. However, the problem of DMF remaining in the pores is well documented,[20] and steps have been taken to replace DMF as the solvent, to avoid any contamination of DMF.[21]

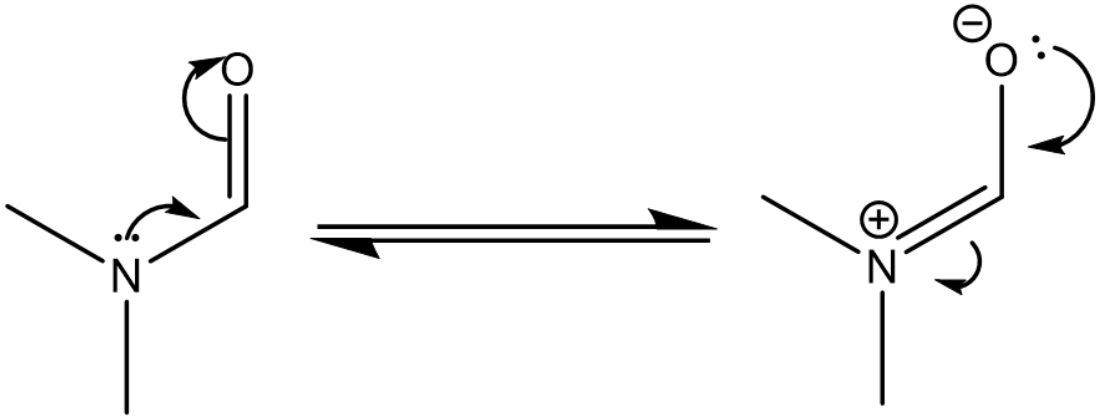

Figure 3.19: Resonance structure of DMF.

3.3.2.3. Effect of iron on the unit cell of MIL-68(In)

Semi-quantitative analysis (Section 3.5.4) of the powder diffraction pattern yields information about the crystal structure of the product. The effect of replacing indium with iron has an impact on the unit cell parameter and volume, the model requires refinement of the model to fit the experimental pattern observed. By fitting the data, three graphs were generated displaying unit cell a, b and c respectively against volume and iron content, found by ICP-OES. Figure 3.20, displays unit cell a against volume and iron content. The model shown, displays unit cell a by looking down c axis. The clear Kagomé structure can be seen and as iron is added the general trend is a decrease in unit cell a.

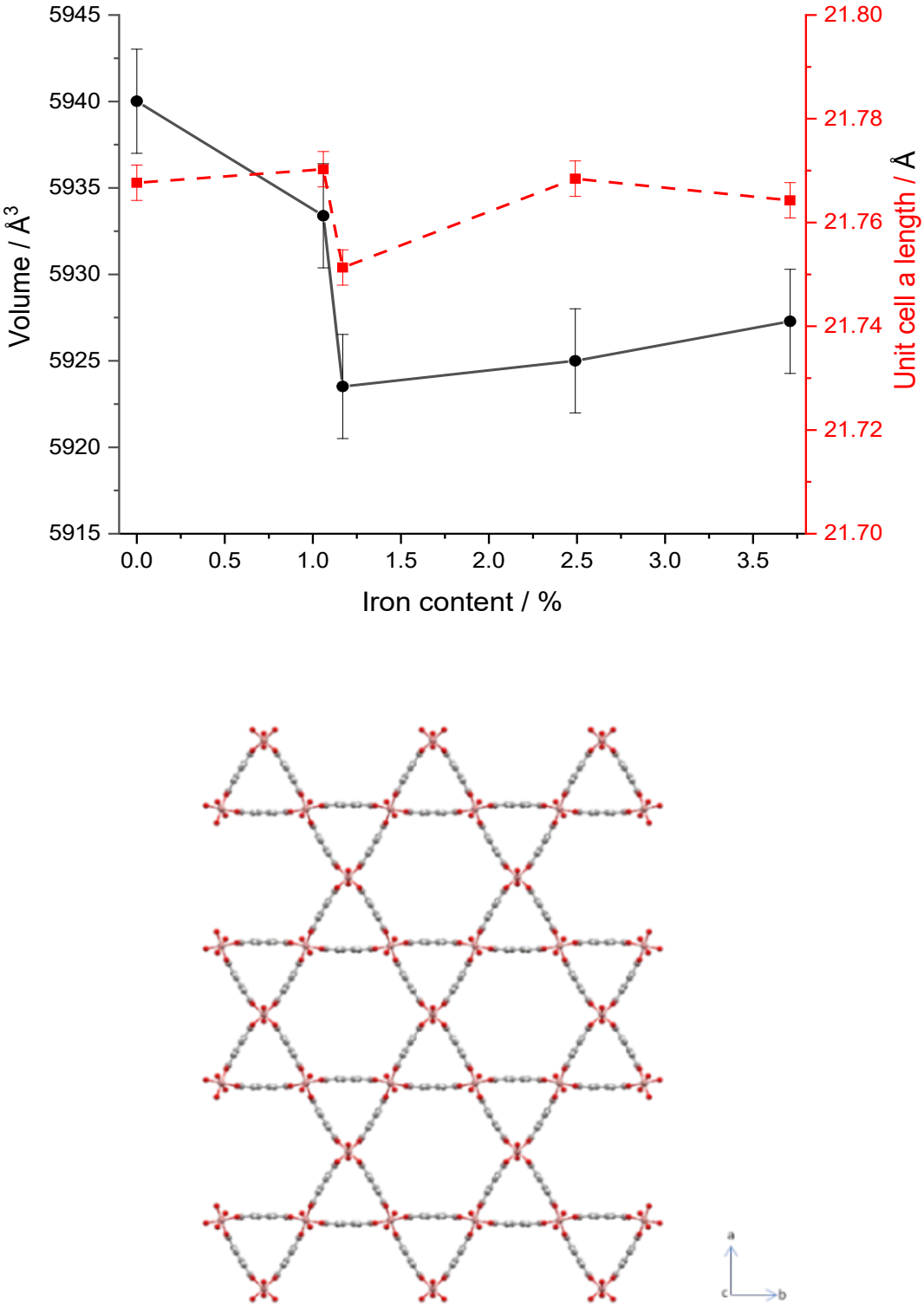

*Figure 3.20: Quantitative analysis of samples **2A-E**, displayed graphically with unit cell volume and unit cell parameter a against iron content. Displayed on the right is the view down the c axis of MIL-68(In) displaying the Kagomé architecture and how the cell may change on expansion.*

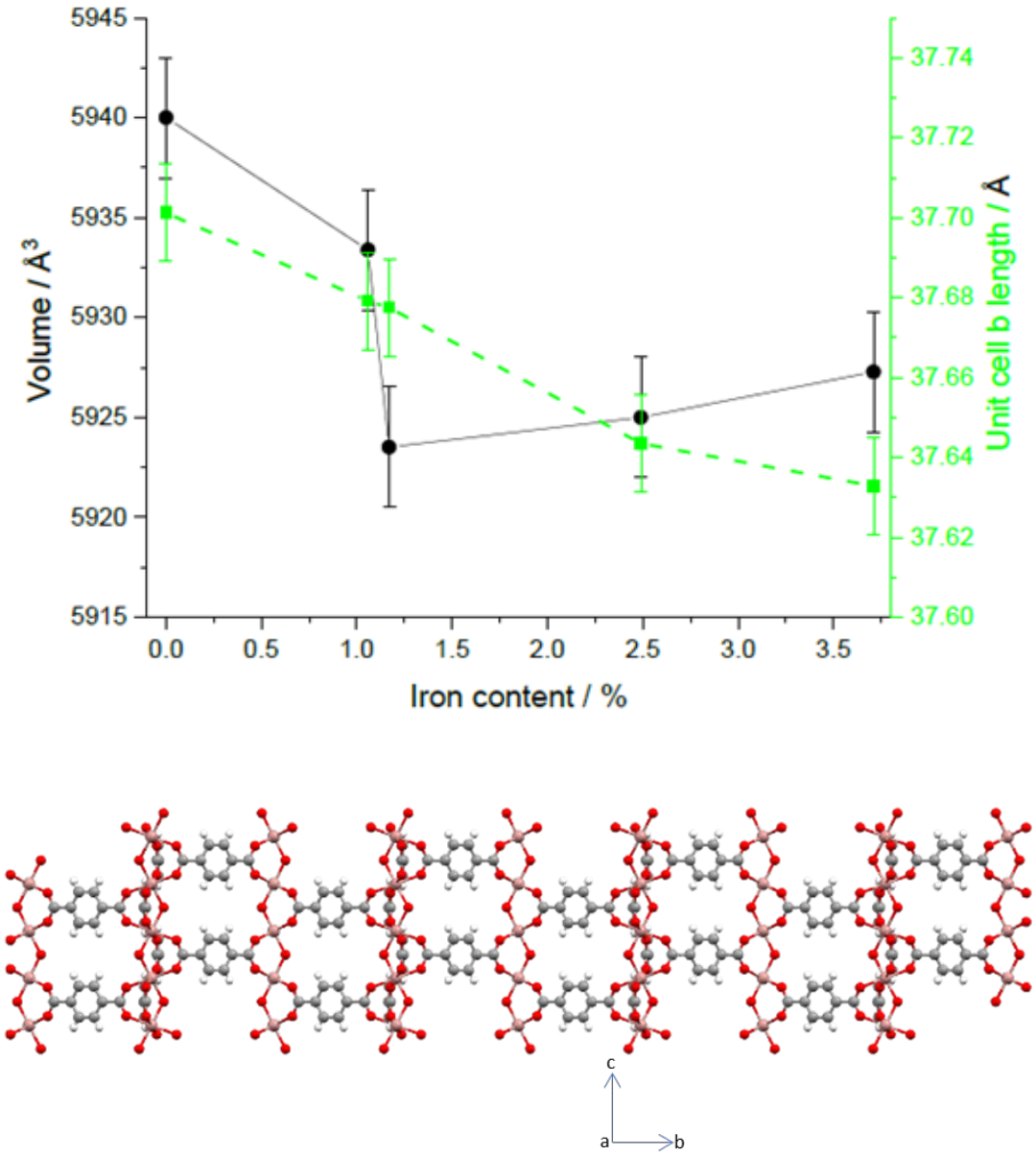

*Figure 3.21: Quantitative analysis of samples **2A-E**, displayed graphically with unit cell volume and unit cell parameter b against iron content. Displayed on the right is the view down the a axis of MIL-68(In).*

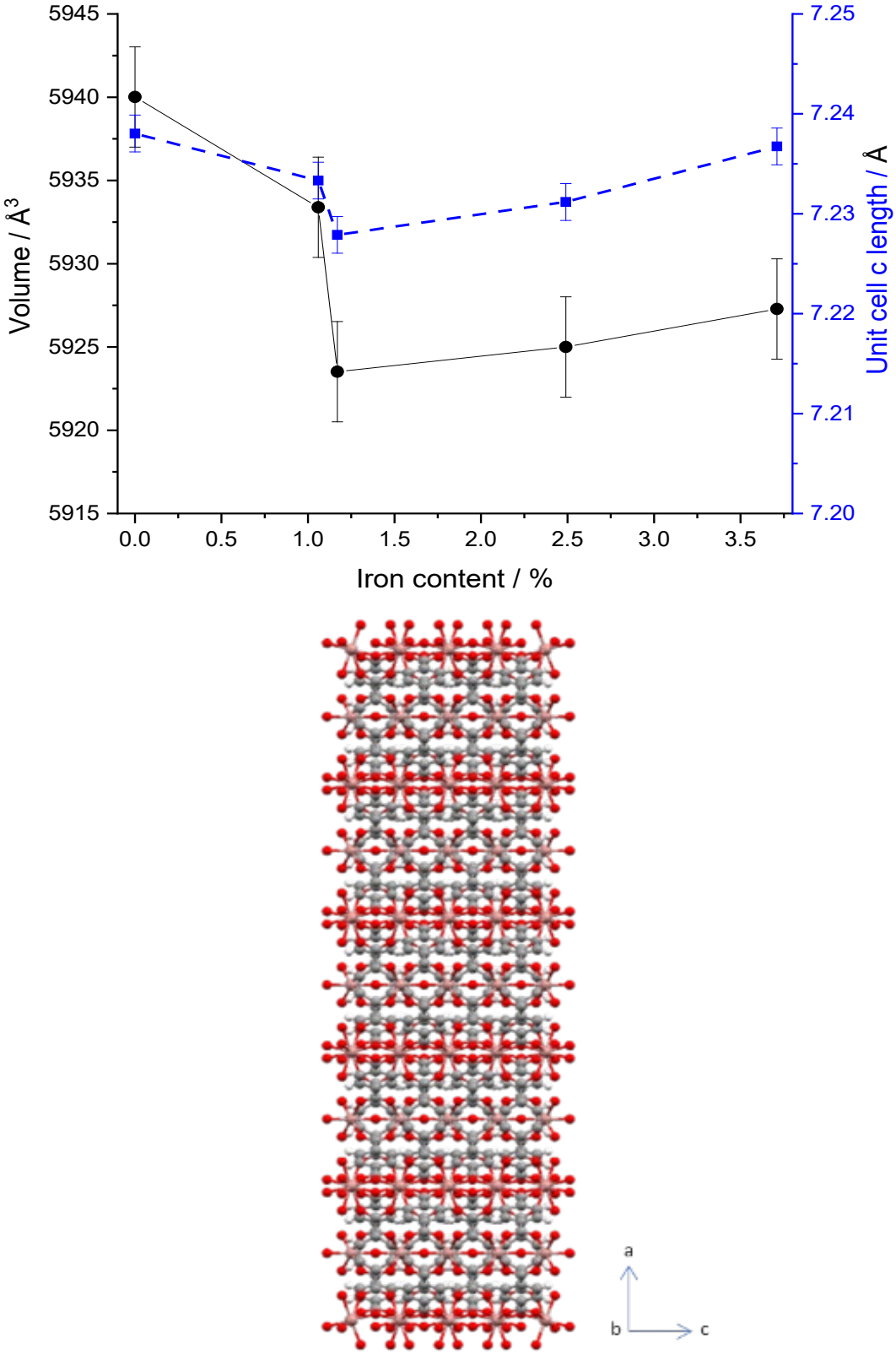

*Figure 3.22: Quantitative analysis of samples **2A-E**, displayed graphically with unit cell volume and unit cell parameter c against iron content. Displayed on the right is the view down the a axis of MIL-68(In).*

There is only a minor trend in unit cell b observed, and as can be predicted by the difference in molecular size between iron and indium, the unit cell is decreasing in size as can be seen in Figure 3.21. By observing the model of MIL-68(In) crystallographic b axis, it can be noted the compactness of the network and lack of porosity, any change or decrease to the metal centre size (indium or iron) will have minimal effect on unit cell b. Figure 3.22 shows that unit cell c does not change with iron content. The view of the unit cell down the a axis demonstrates how the cell could change and is not the cause of the increase in volume of the unit cell.

As previously mentioned with MIL-68(Ga), the decrease in volume for samples **2A-E** has a relationship with the increase in iron content. The replacement of indium with iron is seen as a decrease, mostly seen in the contraction of unit cell a creating reduced pore size and having a smaller surface area.

3.3.2.4. Observing MIL-68(In) under SEM-EDX

SEM was used to view the crystalline morphology of the crystalline materials, to gain an insight into the ranging sizes of the MOFs. Specimens were taken for each sample and viewed under SEM, after being gold-coated to increase conductivity and image quality. The images are used to show if the samples are monodisperse whereby the particles of uniform size throughout the batch.

Figure 3.23 displays SEM images of samples **2A-E** ran at 15 keV. The voltage was important as the previous samples MIL-68(Ga) **1A-B** were unstable under the electron beam and shrunk. The evidence suggests the lack of stability of MIL-68(Ga) but the comparable stability of MIL-68(In) is linked to the dissociation energy of the In-O and Ga-O bond.

Table 3.6: Dissociation energies of In-O, Ga-O and Fe-O.[19]

Bond	Dissociation energy /kJ mol^{-1}
In-O	360
Ga-O	285
Fe-O	409

Table 3.6 shows the dissociation energy of In-O is greater than that of Ga-O. It can be suggested that the electron beam of the SEM was strong enough to dissociate Ga-O bond and so the destroy MOF architecture. With the addition of iron to the MIL-68(Ga) the MOF became more stable and could be successfully viewed.

From the SEM images in Figure 3.23 it can also be seen that across the range of sample size is similar. Sample **2A** shows needles of length 10.98 ± 3.69 μm and width 1.63 ± 0.54 μm. Sample **2B** displays needles, rods and debris of broken MOF with lengths of 23.17 ± 12.50 μm and widths of 2.22 ± 1.51 μm. Sample **2C** displays large rod shapes and lots of broken MOF, lengths of the sample are 26.39 ± 16.12 μm and widths of 3.88 ± 2.51 μm. Sample **2D** length of 31.20 ± 9.57 μm and width 4.85 ± 2.16 μm. Sample **2E** 30.18 ± 18.62 μm and width 2.77 ± 1.03 μm. From the samples **2A-E** the size of the MOF particles does increase in both length and width, but so does the error in sample size, this could be due to the increased amount smaller MOFs as well as MOF debris caused by post-synthetic processing. But it does suggest that the addition of iron to the MOF synthesis has two effects; large aggregations of physically fragile MOF-rods and very fine MOF-needles. Through the imaging there is no display of monodispersity unlike previous MIL-68(Ga), it could suggest that the synthetic conditions for this reaction were not tuned to allow monodispersity and in many MOFs the use of a capping agent (such as polyvinylpyrrolidone) could be used to control particle size.[22] However, for the application desired here, monodispersity is not key but anisotropy and the ability to be controlled under a magnetic field is paramount. The next section explores the potential of each sample to be affected by an applied magnetic field.

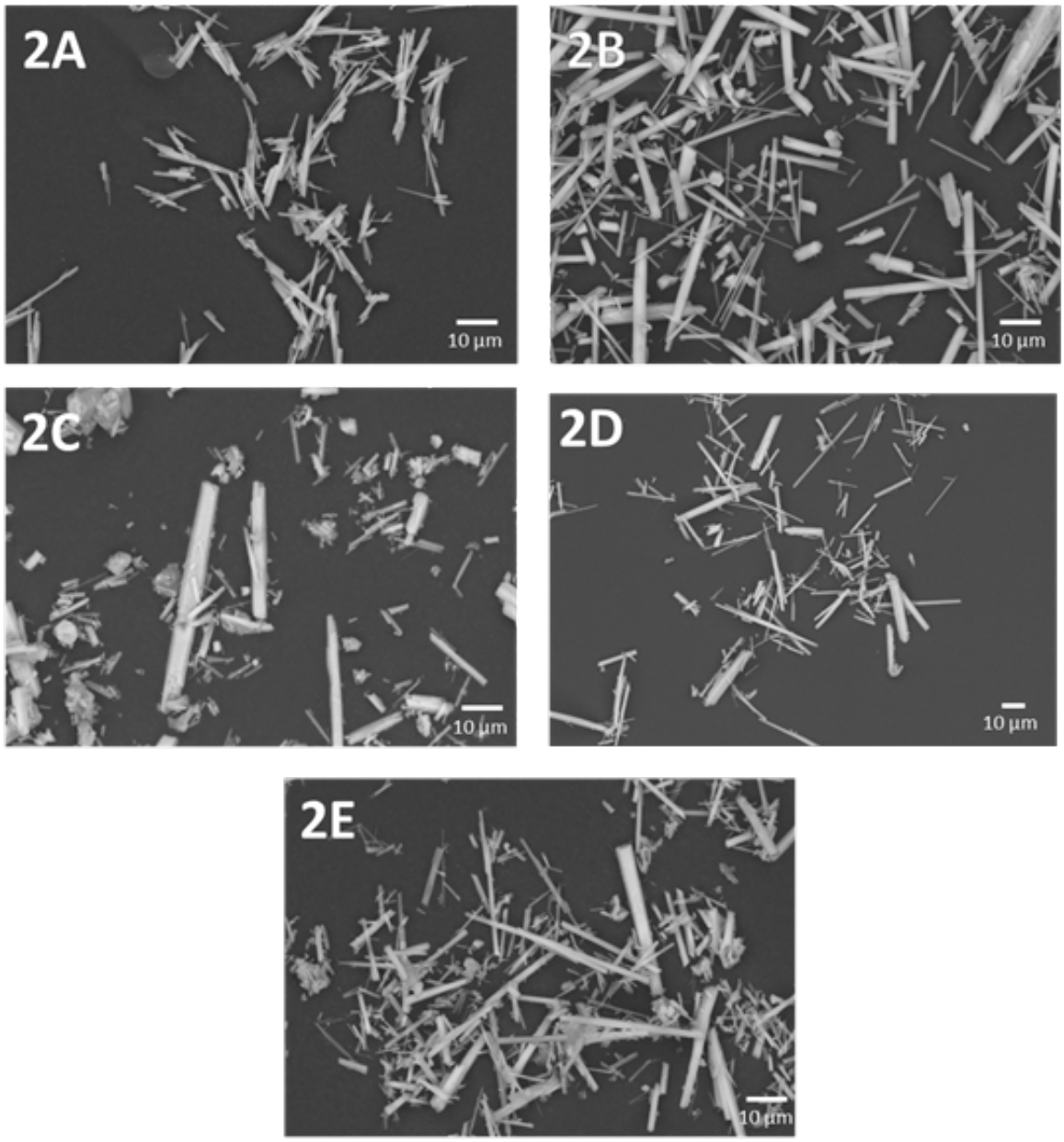

*Figure 3.23: SEM (Hitachi TM4000) images of samples **2A-E**.*

3.3.3. Comparison of the magnetic character of MIL-68(In) and MIL-68(Ga)

VSM data collected by Mr. Alex Gee.

The amount of iron present in the MOF samples was confirmed and the effect of iron on the crystal lattice has been affirmed by computational PXRD analysis, as such it was theorised that the iron doped MOFs will display small-amounts of magnetic character due to the presence of iron. To investigate the extent of magnetism the MOFs possess, magnetic mass susceptibility testing was undertaken. The test indicates the strength of magnetisation per unit mass in an applied

field. Equation 3.1 displays the magnetic mass susceptibility (χ_{mass}) equation (as measured on an Evans balance) which takes into account the length of the sample in the specimen tube (l), mass of the sample (m), calibration constant of the balance (C), balance reading of the empty tube (R_0) and balance reading for the sample in the tube (R).

$$\chi_{mass} = \frac{Cl(R - R_0)}{10^9 m}$$

Equation 3.1: Mass susceptibility

If χ_{mass} is positive the material could be paramagnetic whereby the magnetic field of the material is strengthened by the induced magnetisation. If χ_{mass} is negative, the material is diamagnetic, and the magnetic field is weakened by the materials presence. This experiment is not able to determine whether a material is ferromagnetic or antiferromagnetic, but if a sample did display these characteristics a large χ_{mass} would be expected. The results in Table 3.7 show that samples with low amounts of iron display a negative magnetic susceptibility and consequently are diamagnetic, as the magnetic field is weakened by the presence of these samples. Samples with >2% iron did display positive χ_{mass}, indicating the samples are paramagnetic and the magnetic field is strengthened by the samples presence.

Table 3.7: Magnetic mass susceptibility results against iron content as received from ICP-OES.

Samples	Iron Content (ICP-OES) / %	Magnetic Mass Susceptibility / m^3kg^{-1}
1A MIL-68(Ga)	None	-1.82871E-08
1B	1.46	-1.04684E-08
1C	2.08	9.28287E-09
1D	2.86	2.25781E-08
1E	3.24	2.19198E-08
2A MIL-68(In)	None	-1.79991E-08
2B	1.06	-1.04351E-08

2C	1.17	4.32811E-09
2D	2.49	2.33124E-10
2E	3.98	4.67005E-10

These results however, are limited, due to the fact that as previously stated they do not allow the characterisation of ferromagnetism or antiferromagnetic. To test the magnetic properties of the sample a vibrating sample magnetometer (VSM) was utilised. The device, as shown in Figure 3.24, works by applying a uniform magnetic field while the sample is mechanically vibrated along the z axis, the sample is analysed for changes in magnetisation in relation to the sample movement. If a material is ferromagnetic, a sigmoid loop will be observed in the data as the material displays residual magnetism. If a material is diamagnetic no hysteresis will be observed but has very weak repulsion by the field.

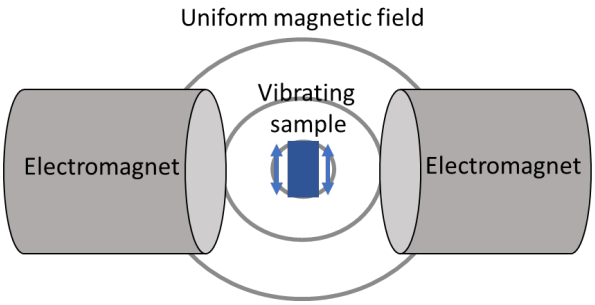

Figure 3.24: Schematic of vibrating sample magnetometer (VSM) with electromagnets generating a uniform magnetic field while the sample is vibrating along the z-axis.

The technique (Section 3.5.5) takes time and is costly to prepare and so only two samples with the strongest χ_{mass} were chosen, specifically samples **1D** and **2C**. As can be seen in Figure 3.25, there is no hysteresis loop which suggests the material is not ferromagnetic, additionally an extremely low magnetisation result was recorded, for reference the literature reports the magnetisation of iron oxide nanoparticles, well characterised for their strong magnetism, reaching 70 EMU g^{-1}.[23]

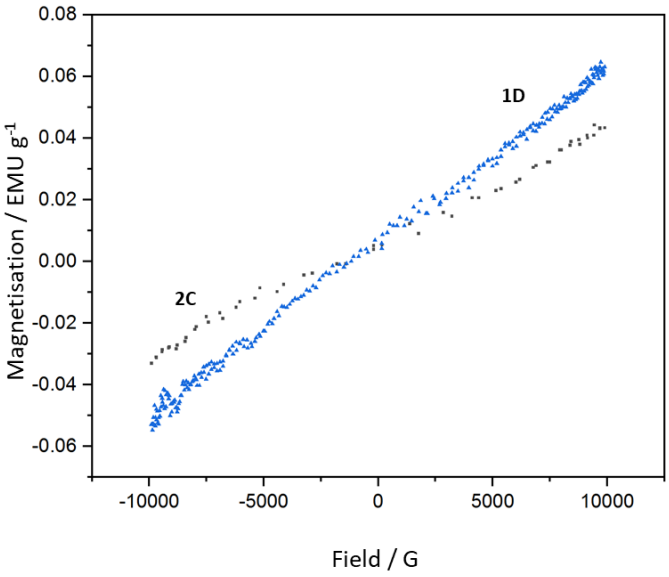

*Figure 3.25: VSM data for samples **1D** and **2C**, displaying very weak magnetisation when the magnetic field is induced.*

A simple experiment was trialled by placement of a 40 x 10 x 20 mm neodymium bar magnet of 5100 G, within 1 cm of a sample of **1D** dispersed in silicone oil. The result was observed by optical microscopy and is shown in Figure 3.26, display. The first image demonstrates the MOF dispersed in silicone oil with no applied magnetic field. A graph was plotted of particle percentage against the orientation of the particulates, where 0° is horizontal and parallel to the plane. When no magnetic field is applied there is no clear major orientation of the particles. When a magnetic field is applied there is a significant amount of particle alignment, Figure 3.27. To quantify how closely the data fits in relation to the angle of the applied field, the R value was calculated, shown in Section 3.5.16. A value close to R = 1 suggests unaligned particles and R ≈ 0 suggests good alignment. For the aligned particles a value of R=0.602 was returned and unaligned R=0.833.

A greater level of magnetic field would be required to better align the particles, however, there was no access to electromagnets capable of producing a 10000 G magnetic field that can be fitted to the 3D printer or optical microscope without great cost or the potential of destroying the internal electronics.

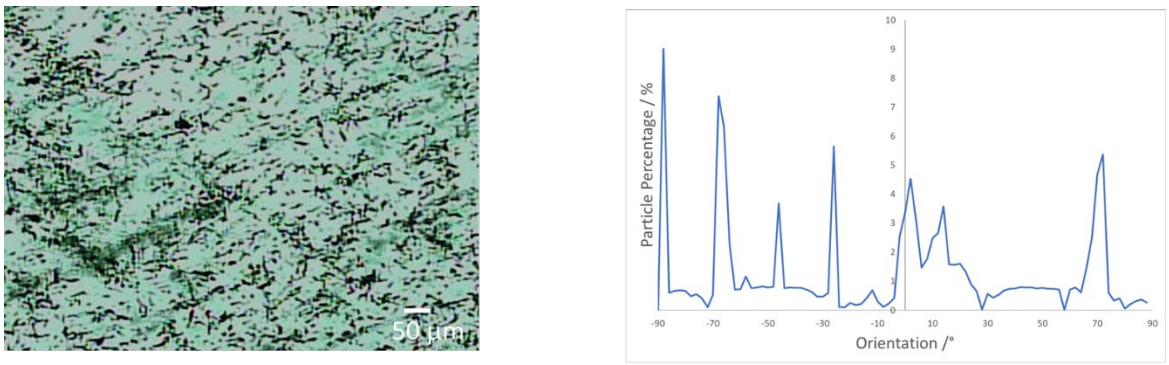

*Figure 3.26: Unaligned particles of iron rich **1D** and respective graph, R=0.833*

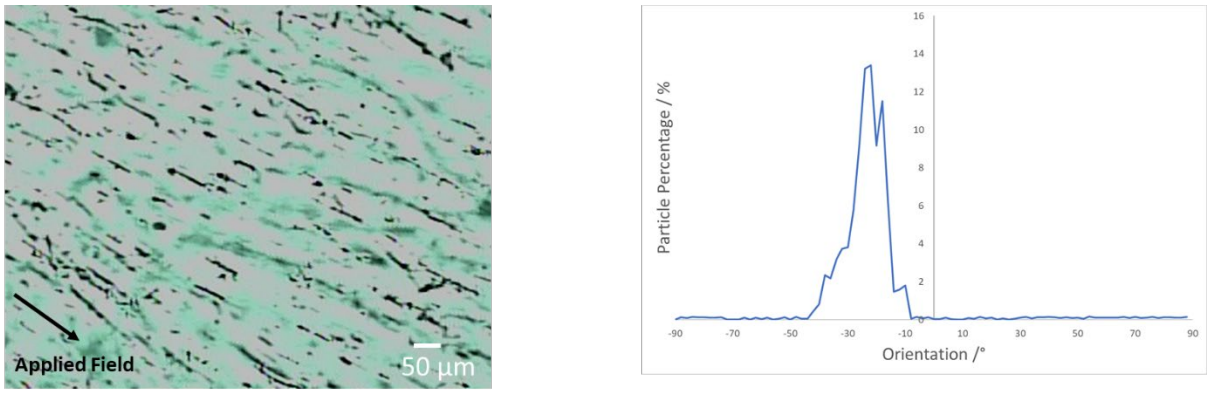

Figure 3.27: Aligned particles of iron rich 1D and respective graph, R=0.603

3.3.4. Addition of iron oxide nanoparticles to MOFs

The intended application for the metal-doped MOFs was an SLA 3D printer. The MOF must align in a polymer matrix over a distance of 7.5 cm. To do so the material must be highly susceptible to a magnetic field. The results previously discussed MIL-68(In) or MIL-68(Ga) doped with iron reported a maximum of 2.19198 E-08 m^3kg^{-1} and 0.06 EMU g^{-1}. The strength of magnet could be increased to overcome this weak magnetic susceptibility but then electromagnets must be created and fitted, at extra expense, time and engineering. Therefore, a material with greater magnetic susceptibility had to be sought; in this instance, iron oxide nanoparticles were chosen for their comparably larger magnetic susceptibly measurement of 0.024 – 1.302 m^3kg^{-1}.[24]

Iron oxide nanoparticles consist of two forms of iron oxide; the first is magnetite which exists as $Fe^{2+}Fe_2^{3+}O_4$ with both Fe^{2+} and Fe^{3+} centres, the second is maghemite- $Fe_2^{3+}O_3$ with Fe^{3+}. The two materials are ferromagnetic. Other ferromagnetic materials such as Co and Ni-based particulates were also considered, but have a higher toxicity, are more expensive and were not readily

available in the laboratory. The choice of MOF is paramount and, as with the previous experiment, the particles must be anisotropic to be able to observe alignment. To aid in the adsorption of iron oxide nanoparticles onto the surface, amine groups were added to the MOF network to increase hydrogen bonding, as it plays an important role in a MOFs adsorption ability.[25] MOFs: NH_2-MIL-68(In), NH_2-MIL-53(Al) and NU-1000 were chosen to attach iron oxide nanoparticle too, to experiment with different morphologies, surface area, architecture and metal centres.

3.3.4.1. Adsorption of iron oxide nanoparticle onto NH_2-MIL-68(In)

Here it is investigated if processing NH_2-MIL-68(In) with iron oxide nanoparticles retains structural characteristics. NH_2-MIL-68(In) was chosen as a comparable MOF to the previous iron-doped MIL-68(In) MOF.

Initially, NH_2-MIL-68(In) was prepared solvothermally with a modulator (Section 2.2.4), synthesised iron oxide nanoparticles (Section 2.2.5) were added in excess to NH_2-MIL-68(In), surplus nanoparticles were then washed off and the samples dried (Section 3.5.7). To observe if the adsorption of nanoparticles was successful, NH_2-MIL-68(In) was viewed by SEM and TEM. Viewed under SEM NH_2-MIL-68(In) presents as anisotropic hexagonal rods of length 10 ± 2 μm and an aspect ratio of 5.0 ± 1.3 displayed in Figure 3.28. After the addition of iron oxide nanoparticles, the MOF was viewed again by SEM. There are no visible signs of iron oxide nanoparticles on the surface. It is also notable that the MOFs appear thinner and misshapen. Experimentally, on the addition of iron oxide nanoparticles with NH_2-MIL-68(In) it was noted that the two components created effervescence in the sample vial. This could not be explained without further investigation by PXRD and FTIR-ATR to confirm what may be happening to either the iron oxide nanoparticle or the MOF.

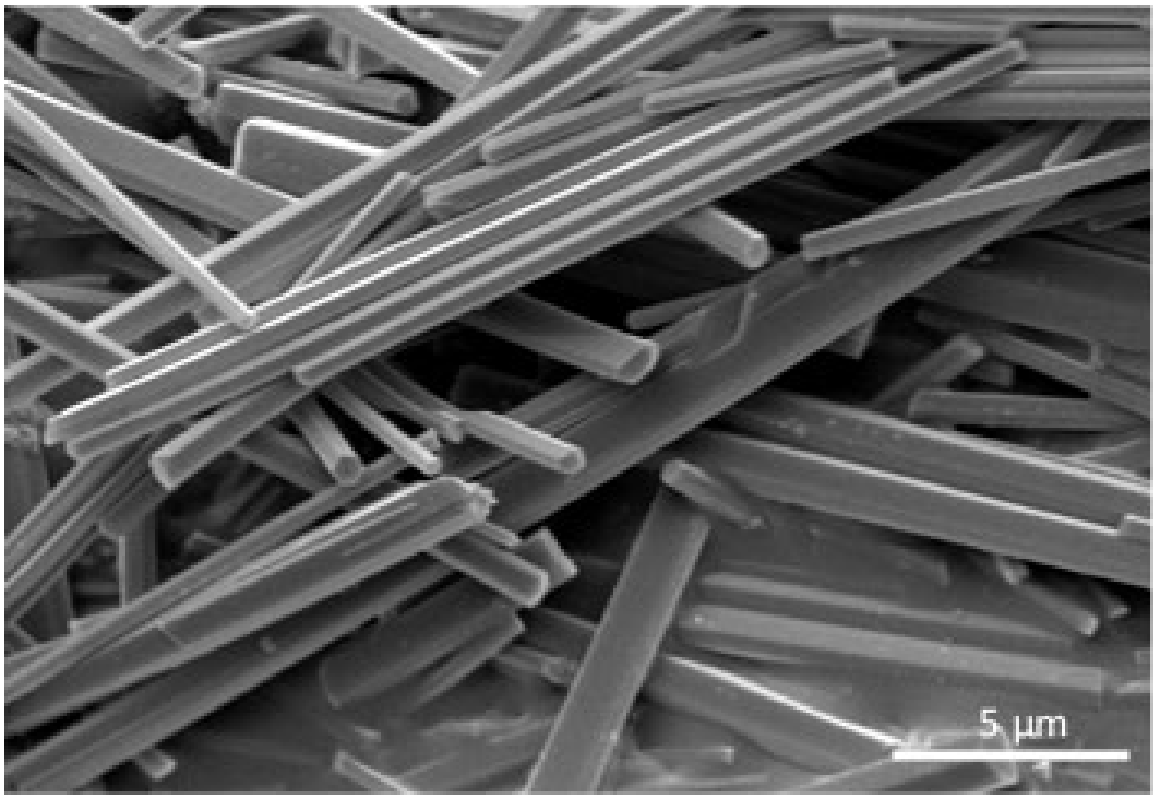

Figure 3.28: SEM (Cambridge Stereoscan 360) images of NH_2-MIL-68(In) and NH_2-MIL-68(In) with iron oxide nanoparticles at pH 5.9.

3.3.4.2. Structural analysis of NH_2-MIL-68(In)

The PXRD pattern of NH_2-MIL-68(In) displays peaks at 2θ = 7, 9, 14, 16, 17, 19 and 25° and does match with literature and theoretical patterns of the same MOF.[26] On addition of iron oxide nanoparticles there is a significant change in the PXRD pattern with decreased intensity and extra peaks appearing at 2θ = 9 and 23°. As discussed previously, there was effervescence noted when the aqueous iron oxide nanoparticle solution was added. The cause of effervescence is the rapid formation of gases, causing fizzing and bubbling, this points towards a reaction occurring between MOF and aqueous iron oxide nanoparticle solution. The potential gases produced could be CO_2 or H_2 however the nature of gas is unconfirmed and was not investigated. A possible explanation for the changing PXRD pattern could be the addition of acidic iron oxide nanoparticles (synthesised to be pH 5.9) onto NH_2-MIL-68(In). This has been investigated previously by Yang *et al.* whereby they established that NH_2-MIL-68(In) is acid-sensitive and susceptible to hydrolysis in water.[27] The extra peaks could then be due to degraded MOF creating unknown phases and decreasing crystallinity.

FTIR-ATR is a useful technique to determine chemical composition by identifying characteristic bond stretches and vibrations of functional groups, if there are any changes to the chemical composition after the addition of the nanoparticles, they would be shown on the FTIR spectra.

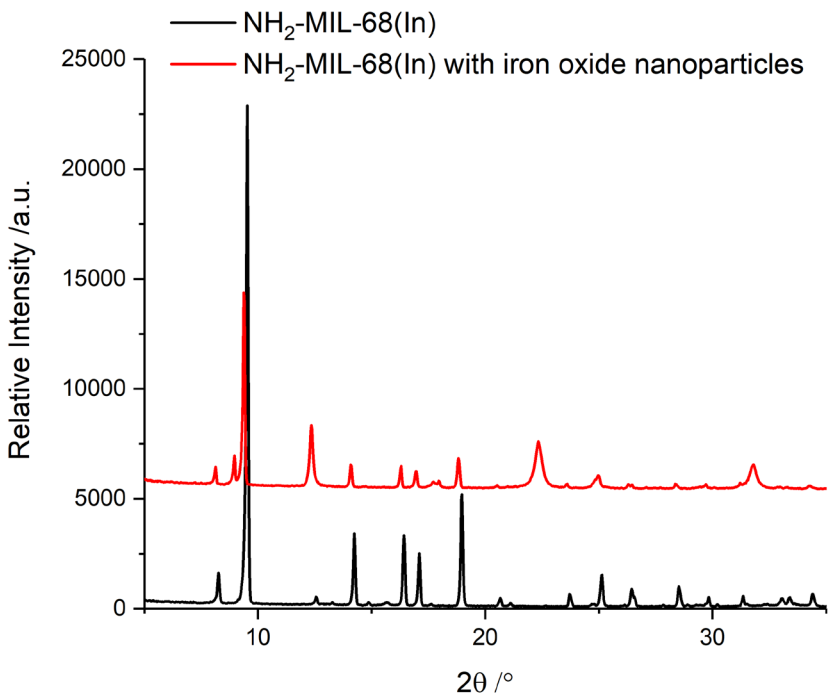

Figure 3.29: X-ray powder diffraction patterns of NH2-MIL-68(In) (black) and with iron oxide nanoparticles at pH 5.9 (red).

The spectrum of NH_2-MIL-68(In) is shown in Figure 3.30 with a broad peak at 3250 cm^{-1} indicating O-H carboxylate groups with sharp peaks in the 500 – 2000 cm^{-1} region representative of various bond stretches and vibrations characteristic of this MOF. There is no significant change to the FTIR-ATR spectrum when iron oxide nanoparticles are added, and it is expected that no peaks are to be observed as the adsorbed iron oxide nanoparticle signal would be too weak. The typical IR spectrum for iron oxide nanoparticles shows peaks at 3431, 1631, 991, 631 and 577 cm^{-1} taken from the literature and characteristic Fe-O vibrations would be from 500-991 cm^{-1} cannot be distinguished in Figure 3.30.

Peaks at 1631 and 3431 cm^{-1} are also too weak to be distinguished from the peaks of the MOF. This is contrary to SEM and PXRD results and it is likely the iron oxide nanoparticles did not adsorb onto the NH_2-MIL-68(In) and there is no iron present. It is also evident that there is no significant change to the chemical composition from the FTIR results, this indicates that the chemical composition is the same before and after addition of the nanoparticles.

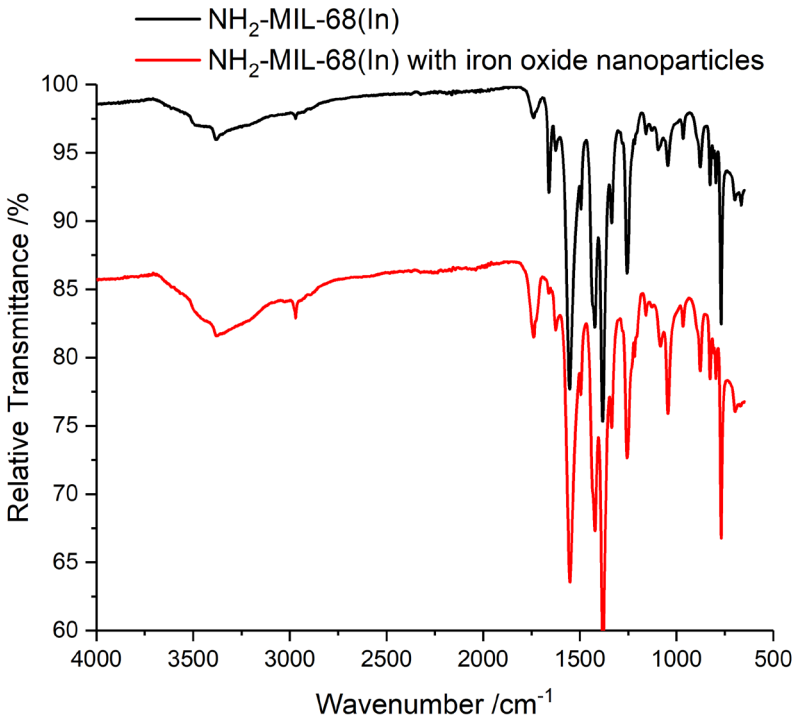

Figure 3.30: IR spectra of NH_2-MIL-68(In) (black) and with iron oxide nanoparticles measured at pH 5.9 (red).

These results contrast with the PXRD and SEM results that display a change in the morphology. However, FTIR only considers chemical bonds present and as the MOF is still intact and in a large abundance these vibrations and stretches will be larger than any hydrolysed bonds that might still be present. Given that the NH_2-MIL-68(In) hydrolysed when iron oxide nanoparticles were added, it would be very unlikely to display any usable magnetic properties, and so was not tested any further.

3.3.4.3. Adsorption of iron oxide nanoparticles onto NU-1000.

NU-1000, shown in Figure 3.31, is a Zr-based MOF with pyrene-based linkers - 1,3,6,8-tetrakis-(p-benzoate)pyrene ($TBAPy^{4-}$), possesses mesoporous 31 Å hexagonal channels and microporous 12 Å triangular channels with orthogonal 8 Å windows connecting the channels.

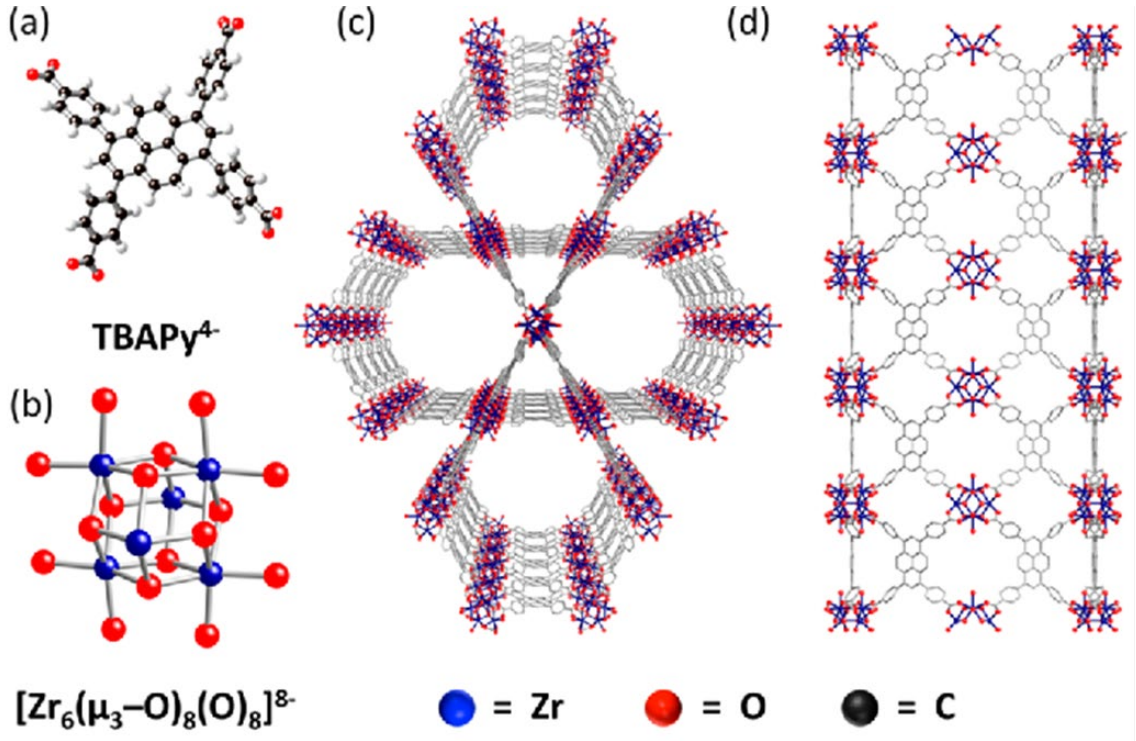

Figure 3.31: NU-1000 and the building blocks of $TBAPY^{4-}$ (a) and zirconium clusters (b) to create the NU-1000 with mesopores (c) and micropores (d). Reproduced with permission ref.[29] copyright 2014 American Chemical Society

Due to its high surface area, it is an attractive material to demonstrate in filtration, gas capture and catalysis.[30–32] As such it is used here for its ability to adsorb particulates onto the surface. Here, the effect of iron oxide nanoparticles have on the architecture of NU-1000 will be investigated. To start with, synthesised iron oxide nanoparticles (Section 2.2.5) were added in excess to NU-1000, surplus nanoparticles were then washed off and the samples dried (Section 3.5.7). To observe if the adsorption of nanoparticles was successful, NU-1000 was viewed by SEM and TEM.

Analysis by SEM (Figure 3.32, left) showed 'bowtie' shaped microrods (of length 3.7 ± 0.2 μm) bearing shape anisotropy. On addition of iron oxide nanoparticle (Figure 3.32**.**, right) the microrods appear smaller and are 3.7 ± 0.8 μm in length, and there are visible aggregations on the surface of the MOF. The aggregations could be large collections of nanoparticles adsorbed onto the surface but are more likely fragmented MOF artefacts created during the processing.

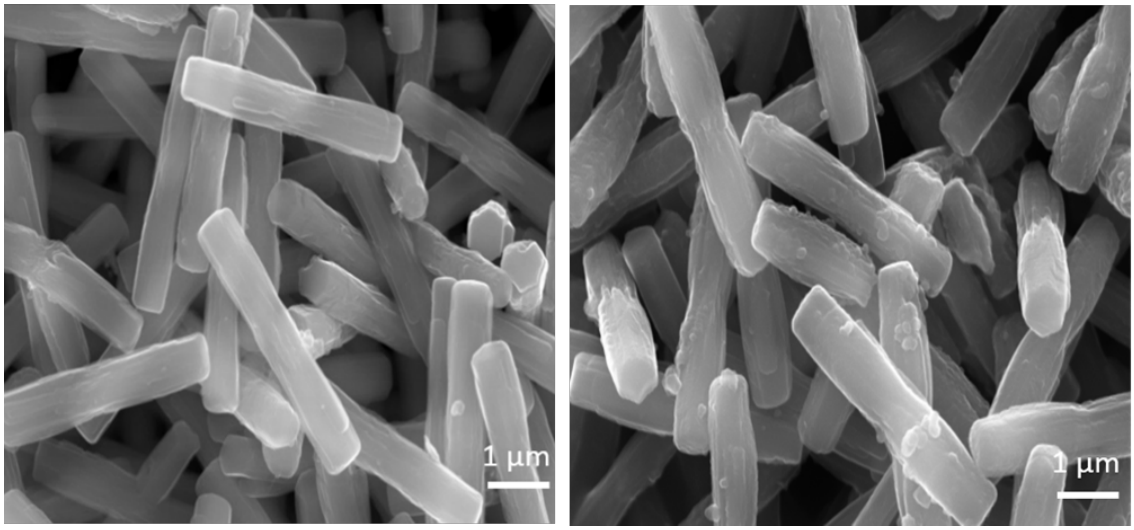

Figure 3.32: SEM (Cambridge Stereoscan 360) images of NU-1000 without (left), with iron oxide nanoparticles at pH 3.5 (right).

By viewing the MOFs under TEM (Figure 3.33) the nanoparticle attachment is seen more clearly by the dotting-effect of aggregated nanoparticles and the darker sample resulting from electron beam requiring more energy to pass through the MOF. The size of particle displayed in the TEM images are 4533 nm and 2812 nm in length (without and with nanoparticles respectively). This suggests that the particles may shrink on addition of the nanoparticles, however the TEM data is only taken from one MOF sample and particle size does vary, as shown in the SEM images.

Interestingly, the 'bowtie' shape of the samples suggests that the sample is not phase pure NU-1000, as MOFs would typically display no variation in shape. Extensive work has been carried out, by the Farha group, and the 'bow-tie' phenomenon is caused by structural motifs of NU-901- a polymorph of NU-1000. The NU-901 structure crystallises first and then NU-1000 encases the structure.[31] It can be seen from the images that nanoparticle adsorption was successful and visually the MOF remains intact, further investigation is required by PXRD and FTIR to confirm this suggestion.

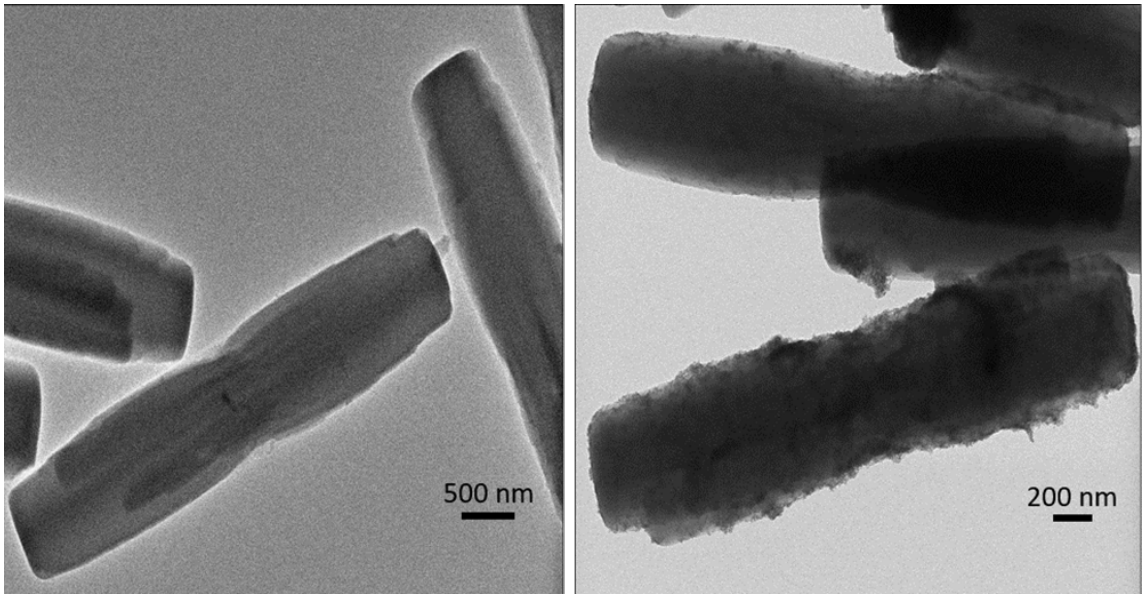

Figure 3.33: TEM images NU-1000 without iron oxide nanoparticles (left) and with iron oxide nanoparticles at pH 3.5 (right).

3.3.4.4. Structural analysis of NU-1000

Information regarding any structural changes because of the addition of iron oxide nanoparticles must be identified. To do so, two techniques have been utilised: PXRD and FTIR-ATR. The PXRD patterns for NU-1000 with and without iron oxide nanoparticles are shown in Figure 3.34. The pattern shows that the strong peaks representative of NU-1000 2θ = 3.4, 5.3 and 8.7 ° are retained after processing.[33] A discrete pattern for iron oxide nanoparticles could not be discerned from the pattern as the MOF masks the signal of the nanoparticles.

The second structural technique is FTIR-ATR, used to determine characteristic bond stretches and vibrations of functional groups. NU-1000 is expected to retain peaks that may pertain to Zr-O, carbonyl and hydroxyl groups. Figure 3.35 displays the spectrum for NU-1000 which shows strong absorbance at 600, 1450, 1650 cm^{-1}. Additional peaks between 500-900 cm^{-1} indicate iron oxide nanoparticles and are representative of Fe-O vibrations.[34] There is no evidence that the addition of the nanoparticles has effected the MOF and by combining all this data we can be assured that iron oxide nanoparticles adsorb onto NU-1000 with no changes to morphology and architecture of the MOF.

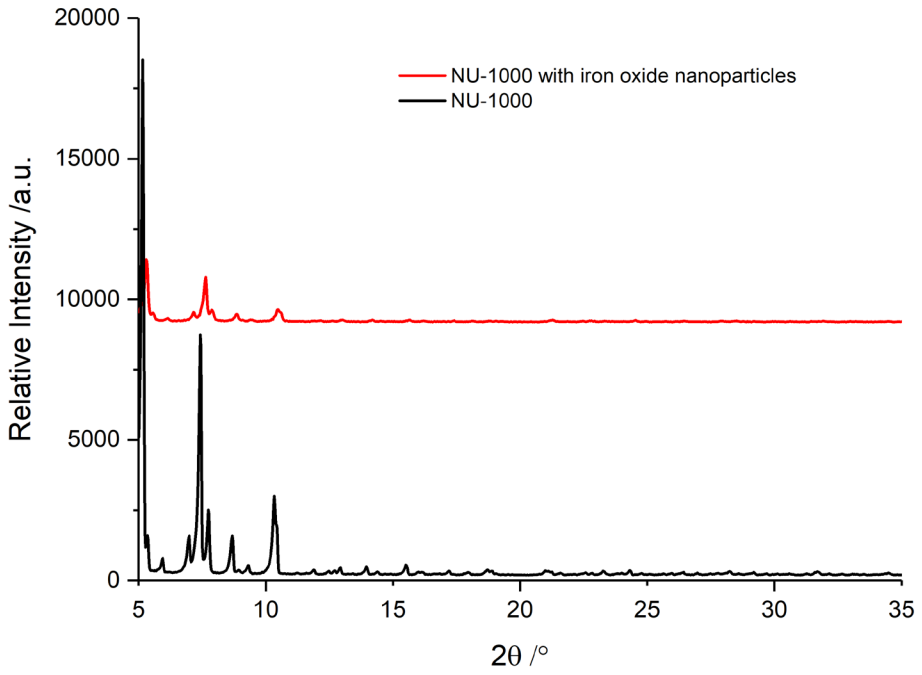

Figure 3.34: PXRD pattern of NU-1000 (black) and with iron oxide nanoparticles (red).

3.3.4.5. Adsorption of iron oxide nanoparticles onto NH_2-MIL-53(Al)

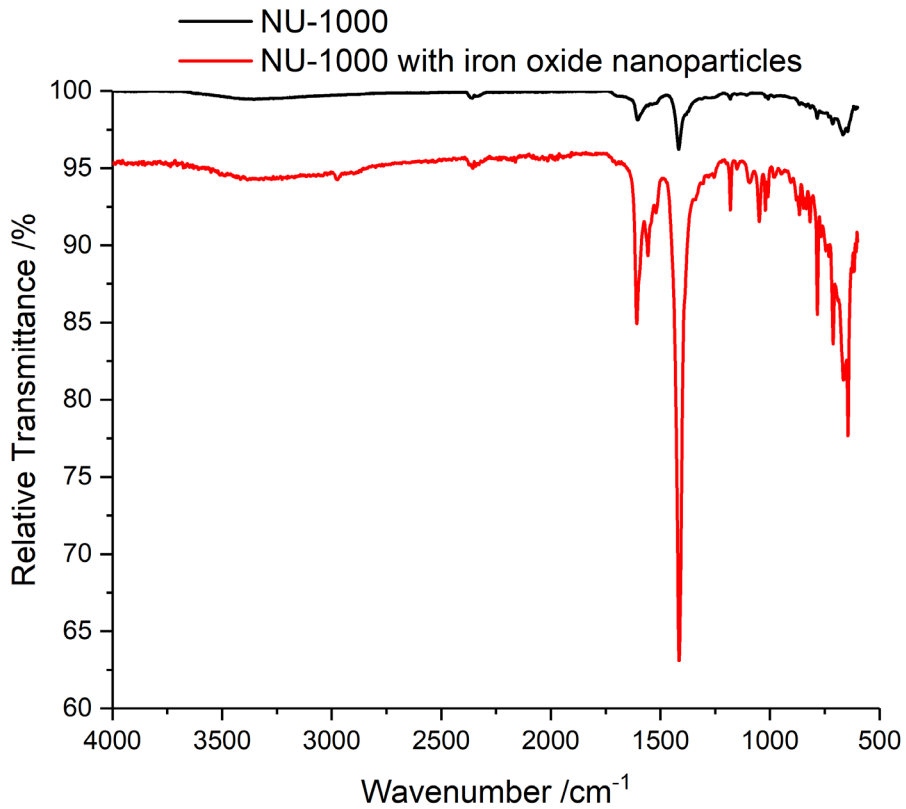

Figure 3.35: IR spectra of NU-1000 (black) and displaying additional peaks 500-900 cm^{-1} indicating the addition of iron oxide nanoparticles (red).

Here, it is studied if iron oxide nanoparticles can adsorb onto a MOF of different morphology and character than previously investigated whist still retaining structure and architecture. In this case, H_2-MIL-53(Al) was chosen for its needle-like shape, tuneable aspect ratio and aluminium-based metal centre.

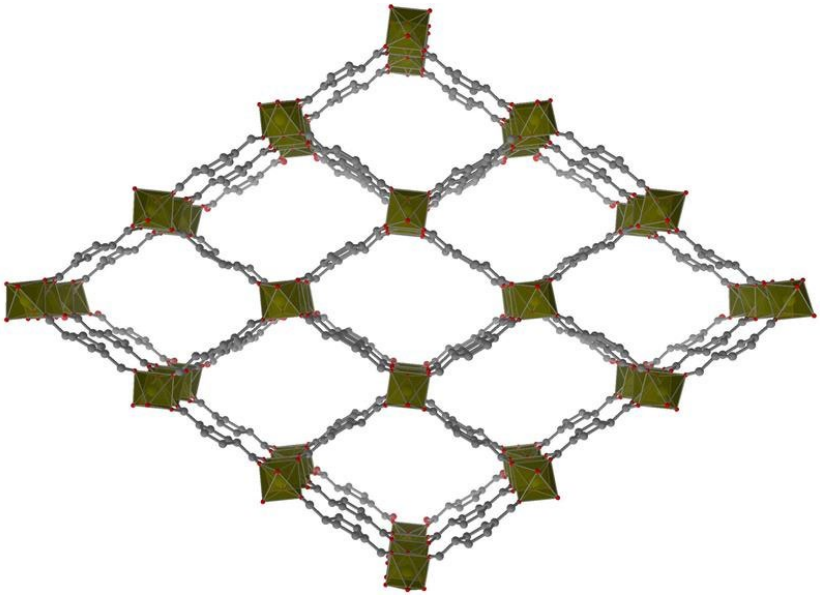

Figure 3.36: Crystallographic image of MIL-53(Al).Reproduced with permission from ref.[35] copyright 2004 John Wiley and Sons

The MOF was synthesised and tuned into an anisotropic microneedle shape using a modulator,[36] (Section 2.2.3) the shape was confirmed by SEM images shown in Figure 3.36. It was identified that the sample had microneedles of 8 ± 2 μm in length with an aspect ratio of 21 ± 7.

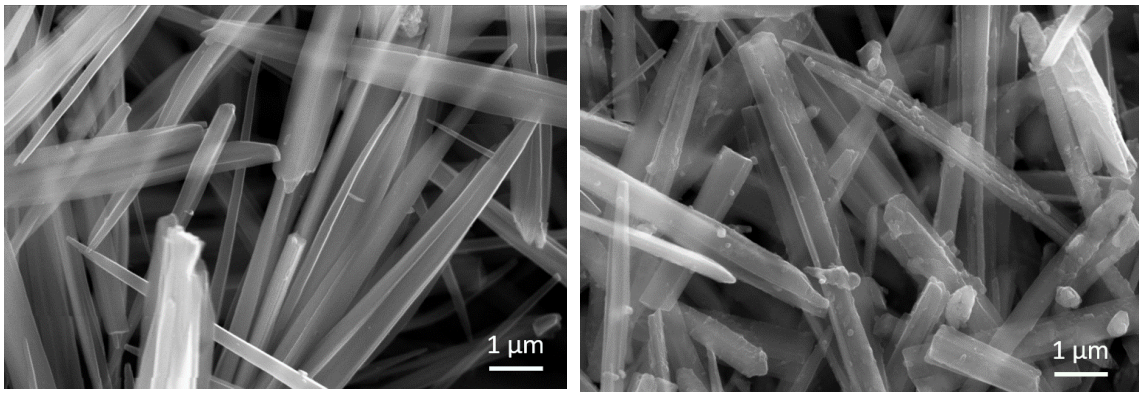

Figure 3.37: SEM (Cambridge Stereoscan 360) images of NH_2-MIL-53(Al) microneedles (left) and NH_2-MIL-53(Al) microneedles with the addition of iron oxide nanoparticles at pH 3.5 (right).

The iron oxide nanoparticle suspension was added and the sample subsequently dried as outlined in Section 3.5.7. Analysis under SEM showed small aggregates on the surface of the MOF. As with the previous sample of NU-1000 the aggregates could be artefacts from the washing process. TEM was not available for this sample and so the sample was analysed by SEM-EDX. Figure 3.38, shows the spectral analysis from SEM-EDX of the MOF with iron oxide nanoparticle. Although it cannot be confirmed whether the aggregates are MOF or aggregated iron oxide nanoparticles, the analysis shows the presence of iron.

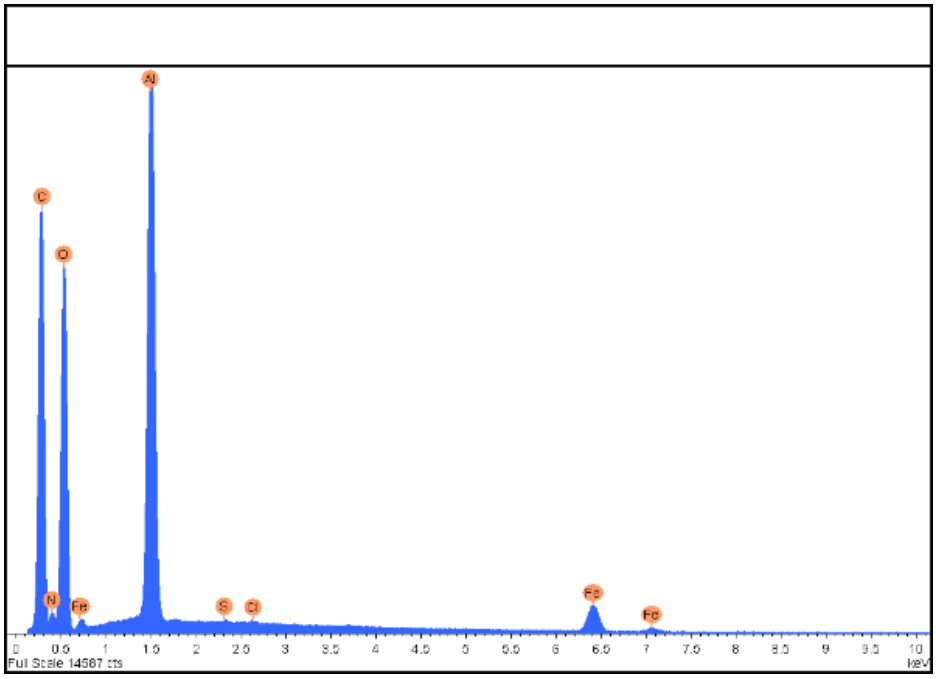

Figure 3.38: EDX spectrum of NH_2-MIL-53(Al) with iron oxide nanoparticles.

Analysis confirmed the presence of iron as expected, and aluminium, nitrogen, carbon, oxygen, silicon and chlorine. It would be expected that a large amount of aluminium would be present from the metal centres within the MOFs. The ligand – amino-terephthalic acid ($H_2NC_6H_3$-1,4-$(CO_2)_2$) accounts for the nitrogen, carbon and oxygen, unfortunately quantitative analysis by SEM-EDX was unavailable at the time. A small number of chlorine atoms are also present and are expected to be left over salts (chlorides) from the synthesis of iron oxide nanoparticles which may have been insufficiently washed. Silicon is also detected but this was a trace amount and very likely to come from the adhesive used on the carbon tab. SEM and further EDX confirm the creation of microneedles however they do not provide confirmation that the correct MOF structure

has been obtained. To confirm the structure including morphology and functional groups analysis of the PXRD pattern and FTIR-ATR spectra must be undertaken.

3.3.4.1. Structural analysis of NH_2-MIL-53(Al)

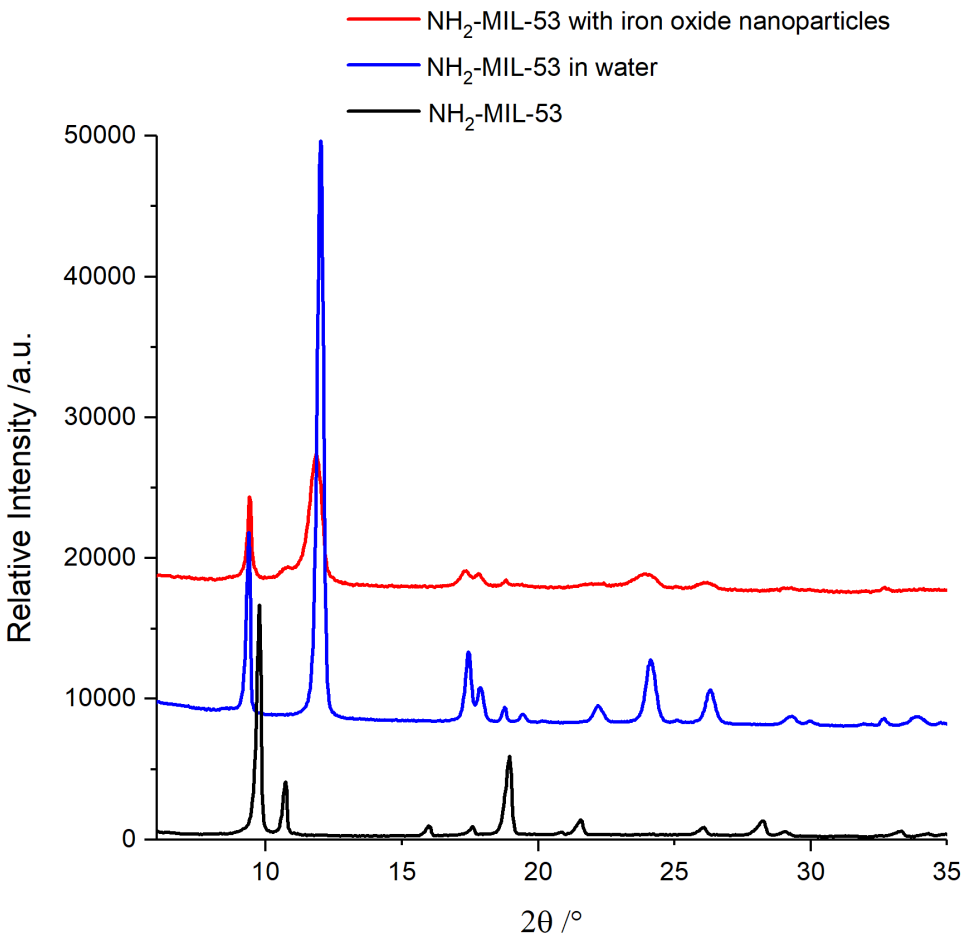

Figure 3.39: PXRD patterns of NH_2-MIL-53(Al) (black), in water (blue) and with the addition of iron oxide nanoparticles at pH 3.5 (red).

PXRD was used to confirm the synthesised MOF was indeed NH_2-MIL-53 structure. The PXRD pattern of the synthesised NH_2-MIL-53(Al) did match the literature values of 2θ = 9, 11 and 18 °.[37] However, it was noted that the sample of NH_2-MIL-53(Al) displayed a different PXRD pattern when aqueous iron oxide nanoparticles were added than washed with the standard work-up procedure of DMF. Demonstrated in Figure 3.39, additional peaks for the NH_2-MIL-53(Al) appeared at 2θ = 8, 13, 17 and 24° and peaks at 2θ = 10, 11 and 18° were lost. This phenomenon has been previously reported by Loiseau *et al*., and is associated with MIL-53's ability to expand and contract the framework dependent on guest molecule and is consequently called 'breathing'.[35] DMF molecules are bulky and fill the MOFs pores, subsequently expanding the crystal structure

of the MOF, resulting in a large pore variation and PXRD pattern observed in Figure 3.39.

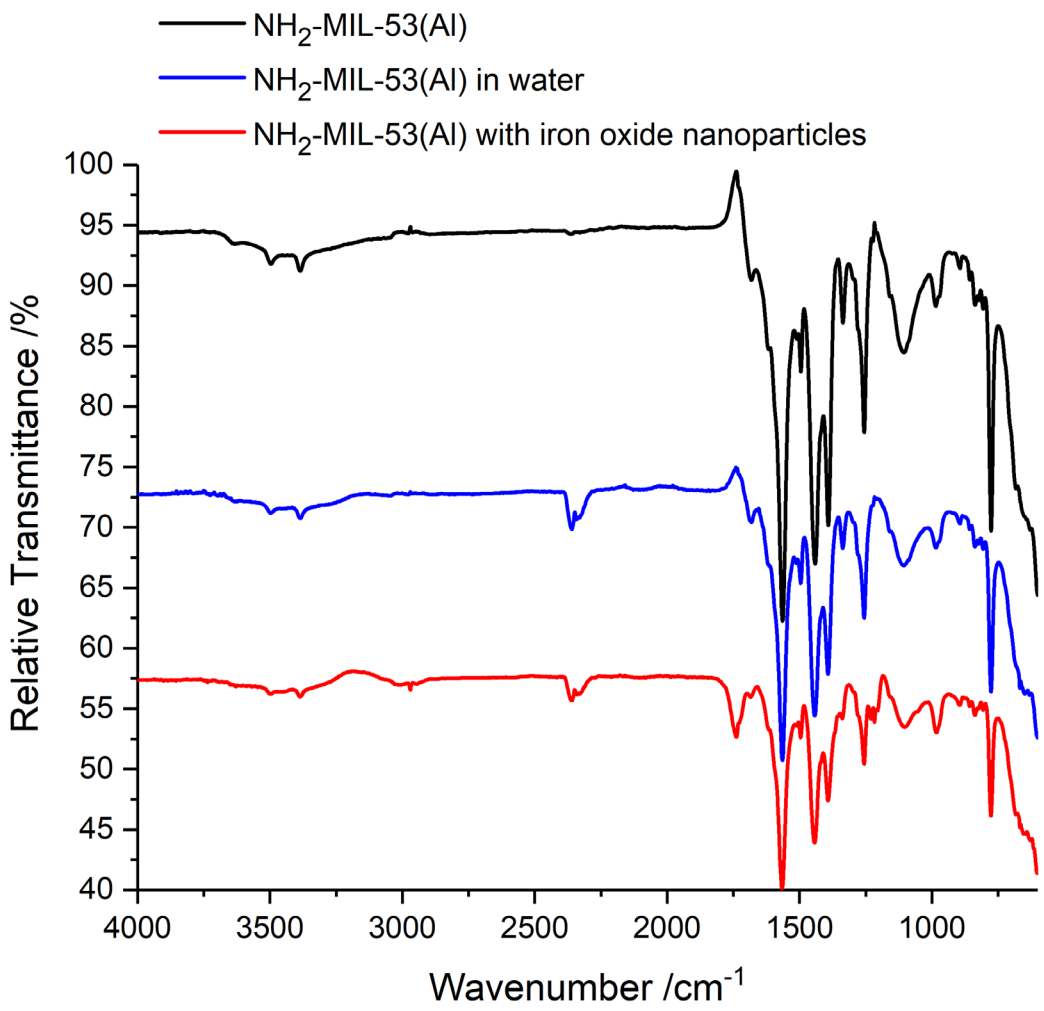

Figure 3.40: IR spectra of NH_2-MIL-53(Al) (black), in water (blue) and with the addition of adsorbed iron oxide nanoparticles at pH 3.5 (red)

On washing in an aqueous system, of which the iron oxide nanoparticles are suspended in water, water molecules replace DMF resulting in a smaller pore configuration, shrinking the crystal structure of the MOF and altering the PXRD pattern.

The FTIR spectra for NH_2-MIL-53(Al) with water or iron oxide nanoparticles is presented in Figure 3.40. The breathing effect, previously mentioned, cannot be demonstrated by FTIR-ATR as there no fewer or greater amount of chemical bonds, just an expansion of the crystal structure. However, the data shows the addition of one sharp peak at ~2300 cm^{-1} present after the addition of the aqueous medium. It would be misleading to suggest the sharp peak is water, as there is no significant peak at 3000 – 3700 cm^{-1} suggesting O-H vibrations and the sample was dried prior to

analysis. It is likely the peak is due to CO_2 being adsorbed into the MOF upon analysis and could be avoided by careful sample preparation or placing the sample in a vacuum. The iron present in the sample should also display Fe-O peaks at 500-900 cm^{-1} but they could be very minor in intensity and could be masked by vibrations and stretches from the more abundant chemical bonds.

No further significant peaks were observed between the different samples and it can be determined that the structure and functional groups remained unchanged throughout processing. It can be confirmed that iron oxide nanoparticles adsorb onto NH_2-MIL-53(Al) with no change in morphology and structure.

3.3.5. Tuning nanoparticle adsorption

It has been shown that MOFs NU-1000 and NH_2-MIL-53(Al) do adsorb iron oxide nanoparticles onto their surface. Here it will be investigated to what extent adsorption occurs and if the amount of iron oxide nanoparticle can be tuned to allow maximum adsorption. The interaction between MOF and nanoparticle is electrostatic and must be attractive forces or else the repulsive forces would greatly hinder the adsorption. This is a fundamental interaction and is dependent on the surface charge of the two particulates.

Surface charge is measured by the zeta potential of the particles when they are suspended in an aqueous medium, termed a colloidal suspension. The zeta potential can be positive, negative or zero and can be controlled by the concentration of H^+ ions, Equation 3.2.

$$pH = -\log[H^+]$$

Equation 3.2: pH related to the negative log function of H^+ ion concentration

The zeta potential of the synthesised iron oxide nanoparticles can be investigated as a function of pH. Also, MOFs NU-1000 and NH_2-MIL-53(Al) will be explored to understand their surface charge, experimentally the pH of the nanoparticles will then be adjusted to compliment the MOFs and allow favourable electrostatic interactions. Confirmation by ICP-OES and magnetic

susceptibility testing will demonstrate the effectiveness of the electrostatic interaction with the adjusted pH nanoparticles.

3.3.3.1. Effect of variable pH on iron oxide nanoparticles

Variation in pH of the iron oxide nanoparticles results in a zeta potential ranging from + 16 to – 43 mV and an isoelectric point of pH 2.8. The zeta potential of the synthesised iron oxide nanoparticles was plotted were pH was varied and the point at which the zeta potential crosses the x-axis is the isoelectric point, Figure 3.41.

The zeta potential of the iron oxide nanoparticles was investigated over a pH range of 1.2 – 10.5, by use of a zetasizer. From pH 1.2 the zeta potential is positive; a small increase is seen at pH 1.8 before it dramatically falls to below pH 2.8. At pH >2.8 the zeta potential is negative and becomes gradually more so as pH increases, from pH 7 onwards there is no further decrease in zeta potential.

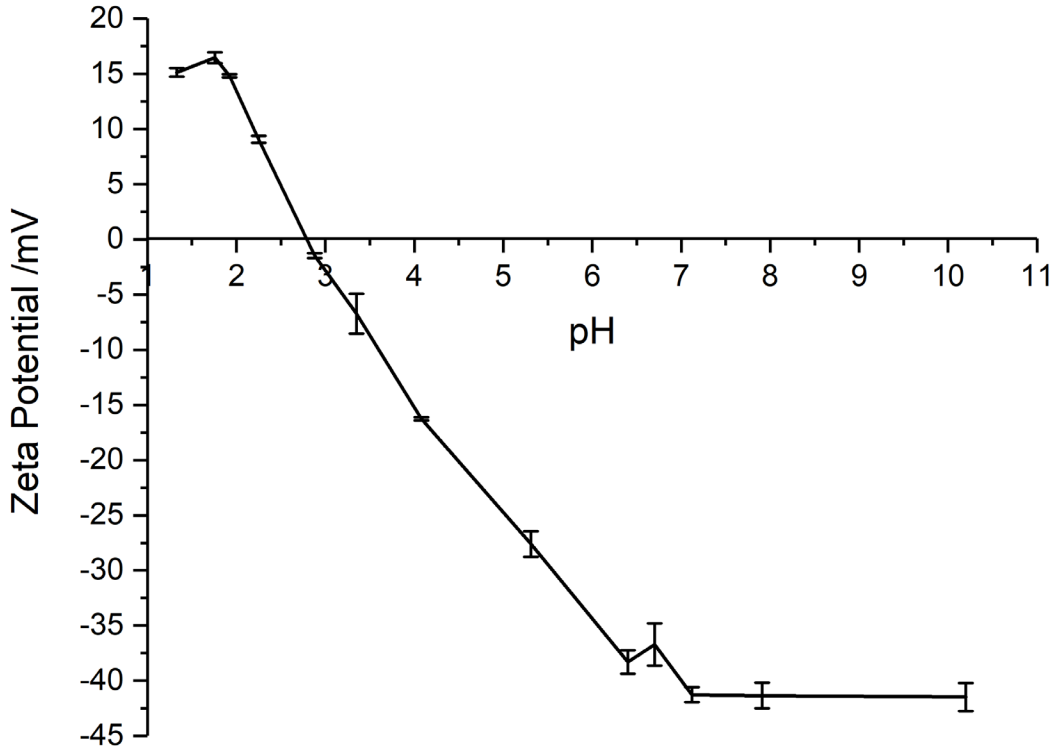

Figure 3.41: Isoelectric point of 1 wt.% iron oxide nanoparticles (14.9 mg/mL) in purified water, showing an isoelectric point of pH 2.8.

When the zeta potential was positive, the nanoparticles would flocculate and as pH increased the solution became increasingly more stable. The iron oxide nanoparticle solution after synthesis

was pH 8.0 and measured a zeta potential of 40 mV, at which point the surface charge of the particles would be negative. The pH of the iron oxide nanoparticles was adjusted by the addition of acid to pH 5.9 and pH 3.5. Shown at the intercept of the x-axis is the isoelectric point, which signals that above pH 2.8 the nanoparticles bear a negative electrostatic charge. NH_2-MIL-53(Al) has been investigated by Li *et al.* to be positively charged below pH 10.5.[4]. This is proposed to be due to the protonation of the amine groups on the linker molecules.[38] NU-1000 has been demonstrated to display an isoelectric point at pH 4.3.[38] Below this value NU-1000 particles are positively charged. Without the tuning of pH of the iron oxide nanoparticle solution, they would not adsorb onto the surface as there would be unfavourable electrostatic repulsion. To overcome this, the pH must be tuned to allow an attractive electrostatic force between the MOF and nanoparticle.

3.3.6. Magnetic character of MOFs with iron oxide nanoparticles

VSM data collected by Mr Alex Glee.

The effect of pH on nanoparticle adsorption was demonstrated in the previous section, here the amount of iron adsorbed to the MOF related to pH is presented by displaying and discussing the ICP-OES data. Also presented is the associated magnetic character the MOF displayed after the addition of iron oxide nanoparticles as evidenced by magnetic susceptibility testing.

Table 3.8: NH_2-MIL-53(Al) and NU-1000 with iron oxide nanoparticles placed in differing pH with measured magnetic mass susceptibility (χ_{mass}) and ICP-OES results.

	Buffer Solution, pH	**Magnetic Mass Susceptibility, χ_{mass} / m^3 kg^{-1}**	**ICP-OES result Fe / wt.%**
NH_2-MIL-53(Al) with iron oxide nanoparticles	3.5	9.09 x 10^{-6}	5.29
	5.9	8.30 x 10^{-6}	4.77
NU-1000 with	3.5	5.79 x 10^{-6}	3.93

iron oxide nanoparticles	5.9	0.62 x 10^{-6}	0.22

The two MOFs, NU-1000 and NH_2-MIL-53(Al) were placed with iron oxide nanoparticles, at pH 3.5 and 5.9, washed and dried (Section 3.5.6). The degree by which the MOFs are affected by the magnetic field is quantifiable by establishing their magnetic mass susceptibility (χ_{mass}).

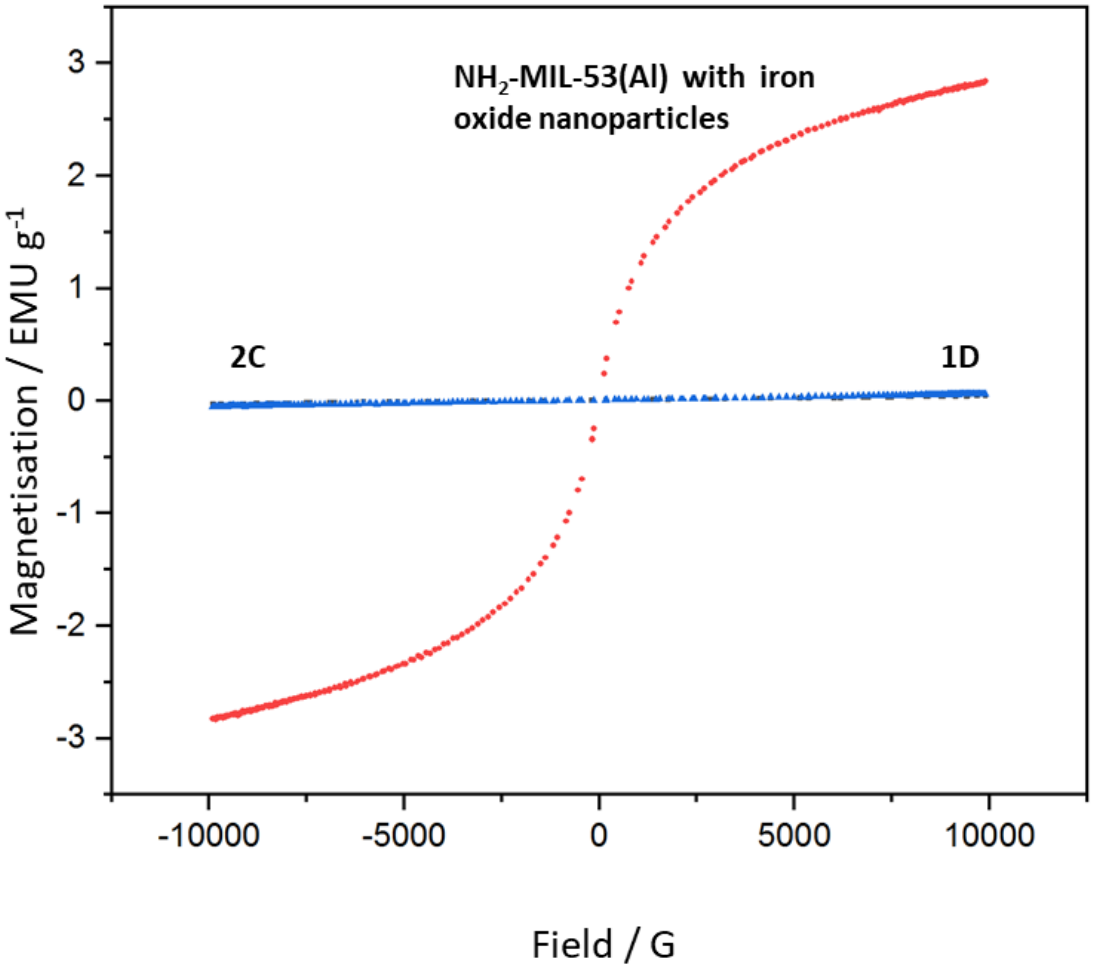

*Figure 3.42: VSM data for NH_2-MIL-53(Al) with iron oxide nanoparticles at pH 3.5, also displayed are the previous VSM results for samples **1D** and **2C** for comparison.*

Results presented in Table 3.8 show that after treatment of the MOF with iron oxide nanoparticles at pH 3.5 the MOFs display a response to the magnetic field, and so successful electrostatic adsorption of iron oxide nanoparticles. Results for NU-1000 and NH_2-MIL-53(Al) after treatment with iron oxide nanoparticle at pH 5.9 were 0.62 x 10^{-6} and 8.30 x 10^{-6} m^3 kg^{-1}, respectively. NU-1000 has an isoelectric point of pH 4.3. Therefore, above pH 4.3 NU-1000 displays a negative electrostatic charge, as do the iron oxide nanoparticles. Hence as pH changes the amount of Fe present on the NU-1000 changes.

Results are consistent with inductively coupled plasma – optical emission spectroscopy (ICP-OES) results, which was a technique chosen to investigate the wt.% of Fe present from iron oxide nanoparticles. To explore the characteristic magnetism the material possesses, the MOF with the highest magnetic susceptibility was sent for further testing. The highest magnetic susceptibility and also iron wt.% was NH_2-MIL-53(Al) with iron oxide nanoparticles at pH 3.5. The sample was ran under the same conditions as the previous test on MIL-68(In/Fe) and MIL-68(Ga/Fe) samples. The results, Figure 3.42, indicate that NH_2-MIL-53(Al) with iron oxide nanoparticles does possess ferromagnetic properties, characterised by the sigmoid curve. In order to discount the effect of loose iron oxide nanoparticles, the samples were washed with copious excess of ethanol. Unfortunately, not enough sample of NU-1000 was available for the testing to take place.

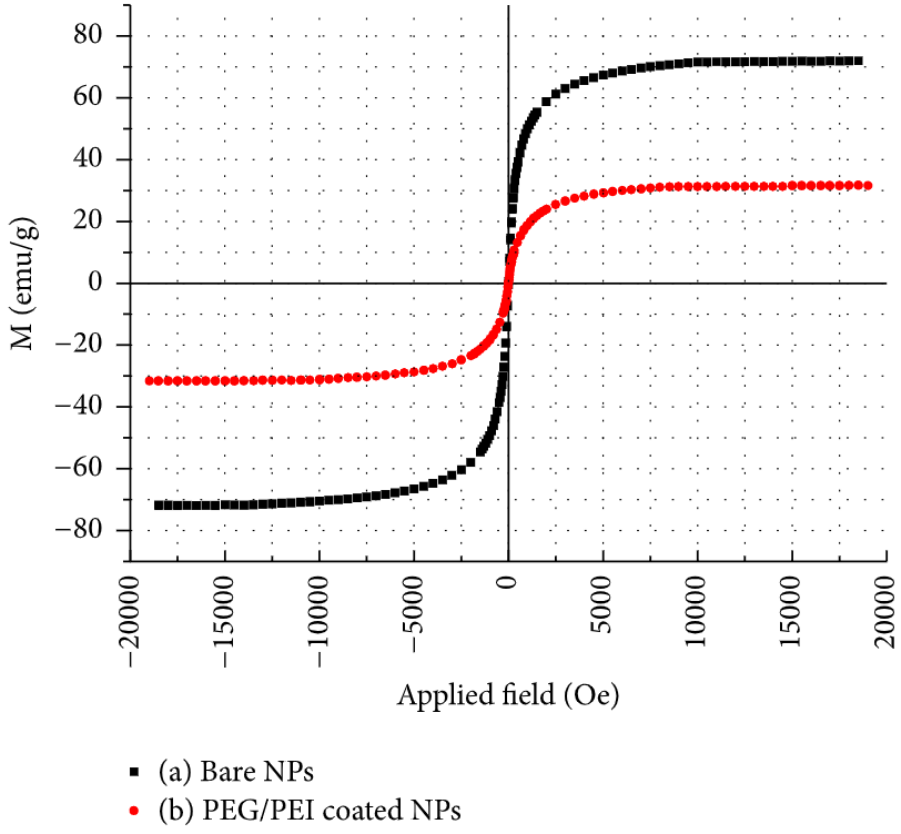

Figure 3.43: Graph of iron oxide nanoparticles, with and without a coating. Reproduced from ref. [39] *under creative commons BY 4.0.*

Also shown in Figure 3.42 are the previously investigated samples of **1D** and **2C** from the earlier investigation. While the iron oxide containing sample is greater than previous experimental (**2D and 1C**) of iron doped in MIL, the typical result of iron oxide nanoparticles for this technique are

approximately are a magnitude higher than results here, approximately -70 to 70 EMU g^{-1} shown in Figure 3.43.[39] It is clear that this method produces particles of defined shape that have significant magnetic susceptibility.

3.3.7. Demonstration of dynamic magnetic alignment

The MOFs with iron oxide nanoparticles have been tuned to display a strong response to a magnetic field by exploring the effect of pH on the electrostatic interaction between MOF and nanoparticles. The most successful magnetic samples, with the highest magnetic susceptibility, will be magnetically aligned in a polymer matrix.

The magnetised MOFs were dispersed in methacrylate-based photocurable polymer resin conventionally used in SLA 3D printers, named Formlabs 1+ Clear Resin (Section 3.5.10). They were then degassed under vacuum (Section 3.5.11) and cured with UV radiation while under the effect of a magnetic field. The resulting MOF composites displayed in Figure 3.44 show the polymer with no particulates and the polymer with magnetically aligned MOF particles, with the yellow colour caused by the presence of iron in the sample.

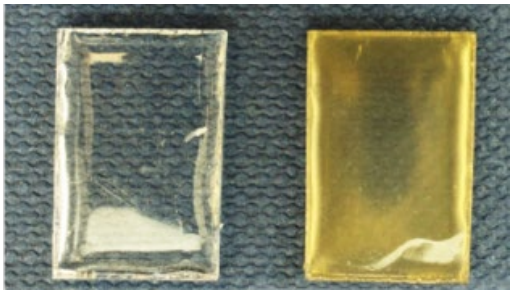

Figure 3.44: Two samples taken out of silicone moulds (1 cm x 2 cm). Left with Formlabs 1+ clear resin and the right with aligned NH_2-MIL-53(Al), pH 3.5.

The samples were then viewed under the optical microscope to verify successful alignment. To demonstrate the effect the magnetic field has on the samples two experiments were conducted 1) no magnetic field and 2) applied magnetic field.

3.3.7.1. Magnetic alignment of NU-1000

Optical microscopy was used to view NU-1000 with iron oxide nanoparticles at pH 3.5 dispersed in the polymer resin. Figure 3.45 displays optical microscopy images and results of NU-1000 micro-rods when exposed to a magnetic field.

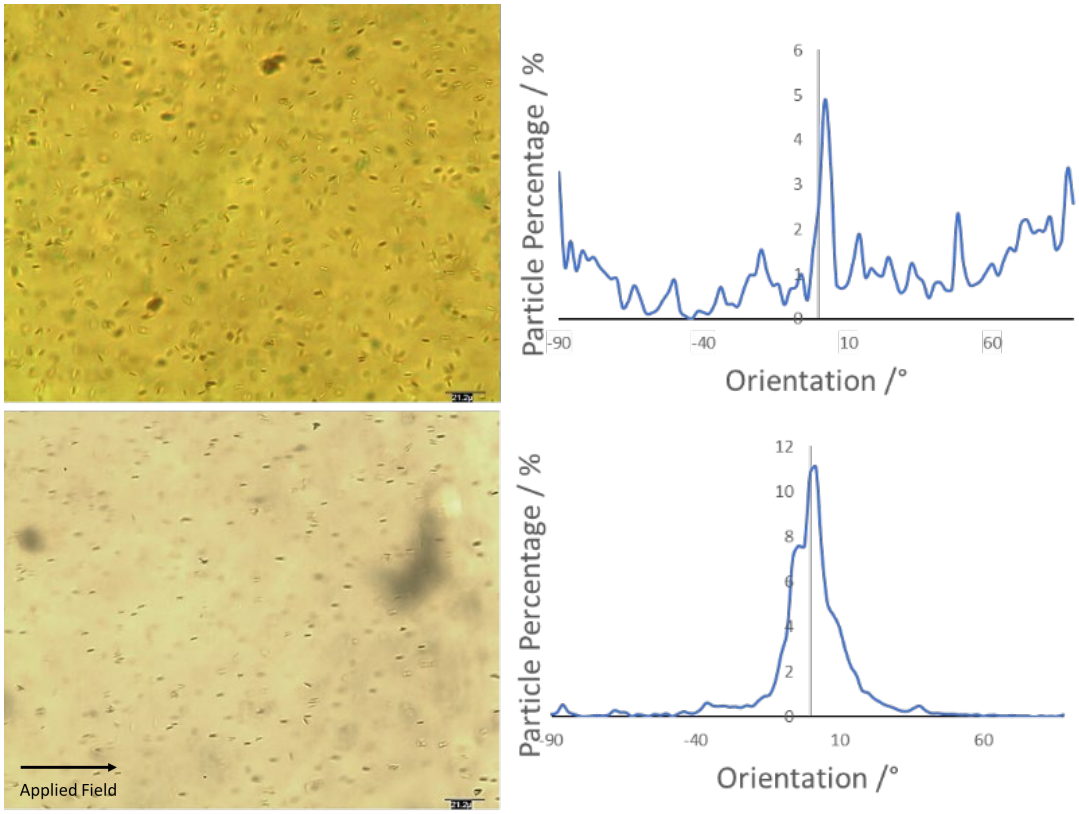

Figure 3.45: Optical microscopy images and corresponding orientation distribution of NU-1000 unaligned (top) and aligned (bottom).

The first image demonstrates the MOF dispersed in polymer resin with no applied magnetic field. A graph was plotted of particle percentage against the orientation of the particulates, where 0° is horizontal and parallel to the plane. When no magnetic field is applied there is only a minor spike at 2 °, demonstrating a small amount of particle alignment. When a magnetic field is applied there is a significant amount of particle alignment. To quantify how closely the data fits in relation to the angle of the applied field, the R value was calculated, shown in Section 3.5.16. A value close to R = 1 suggests unaligned particles and R ≈ 0 suggests good alignment.

There is significant evidence to suggest that NU-1000 with iron oxide nanoparticles does align in a magnetic field as an R value of 0.029 was returned. The unmagnetised sample returned a value

of R = 0.815, suggesting limited alignment and any significant alignment may have been dictated to the shape of the mould and flow dynamics as the material was added.

3.3.7.2. Magnetic alignment of NH_2-MIL-53(Al)

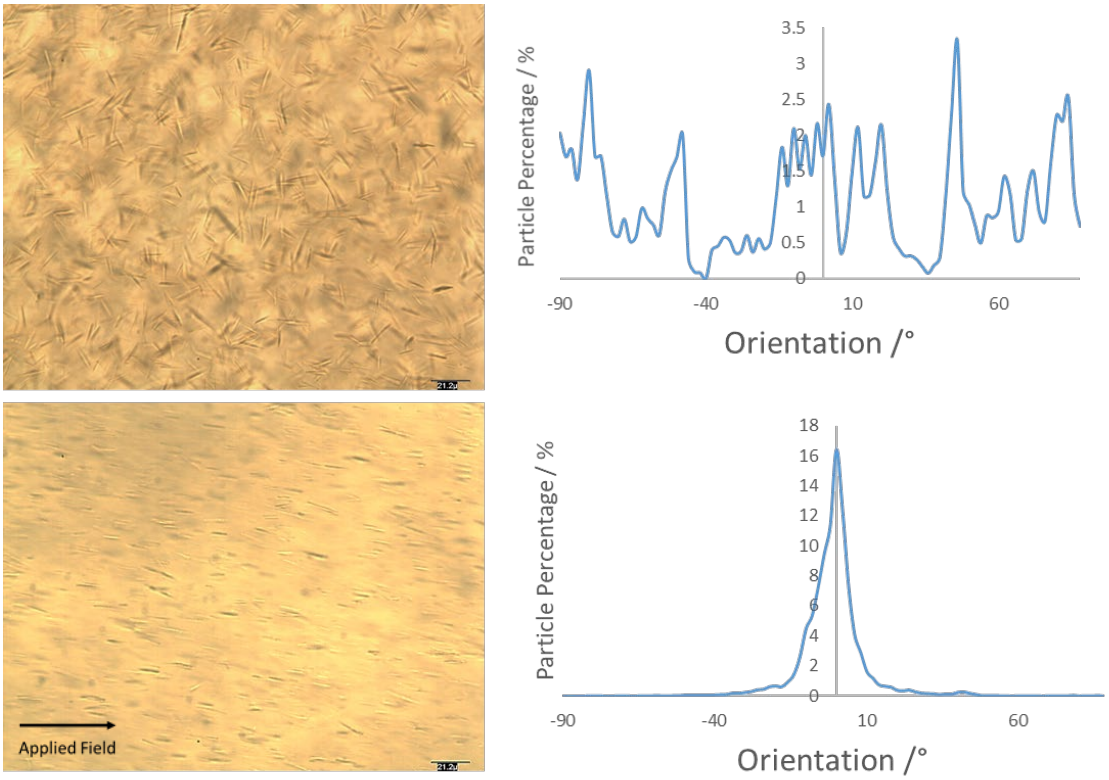

Figure 3.46: Optical microscopy images and corresponding orientation distribution of NH_2-MIL-53(Al), pH 3.5 unaligned (top) and aligned (bottom).

As with the previous experiment NH_2-MIL-53(Al) with iron oxide nanoparticles at pH 3.5 were dispersed in the polymer resin. Figure 3.46, displays micro needles 8 ± 2 µm in length, exhibiting a random orientation R=0.937 was returned and is also evidenced in the corresponding graph. Upon alignment there is a significant amount of particle alignment shown observed by optical microscopy, R=0.450 and the data in the graph suggests the same with a significant majority of particles aligned within the range of 0 ± 10°.

Overall, both NU-1000 and NH_2-MIL-53(Al) demonstrate that they can be aligned and cured in a polymer by applying a magnetic field, during the curing process. The next step is to demonstrate how the magnetic alignment can be applied to produce MOFs with a significant application.

3.3.8. Aligned NU-1000 for optical applications

Samples prepared by Mr. Adam Young and experiment ran by Mr. Peter Robinson

The reason to align MOFs is that they may be used to generate responses or effects along their anisotropic axis, without alignment the response would be weak and thus inefficient. Demonstrated here is the optical response of magnetically aligned NU-1000.

Preliminary experiments were trialled of NU-1000 in polymer resin (Formlabs 1+ resin), however, due to the fluorescence of the polymer resin, the signal of the NU-1000 wasn't able to be picked out above the polymer resin signal. This was demonstrated by NU-1000 in Formlabs 1+ resin and 3D printing the NU-1000 structure, Figure 3.47, the structure then had UV light applied and from the images it can be seen that the whole structure is UV active. The model was produced by loading the CIF file c8ce00455b2 into Mercury v.3.10 and exporting as an STL to Preform v.3.01 software using 25 µm layer height.

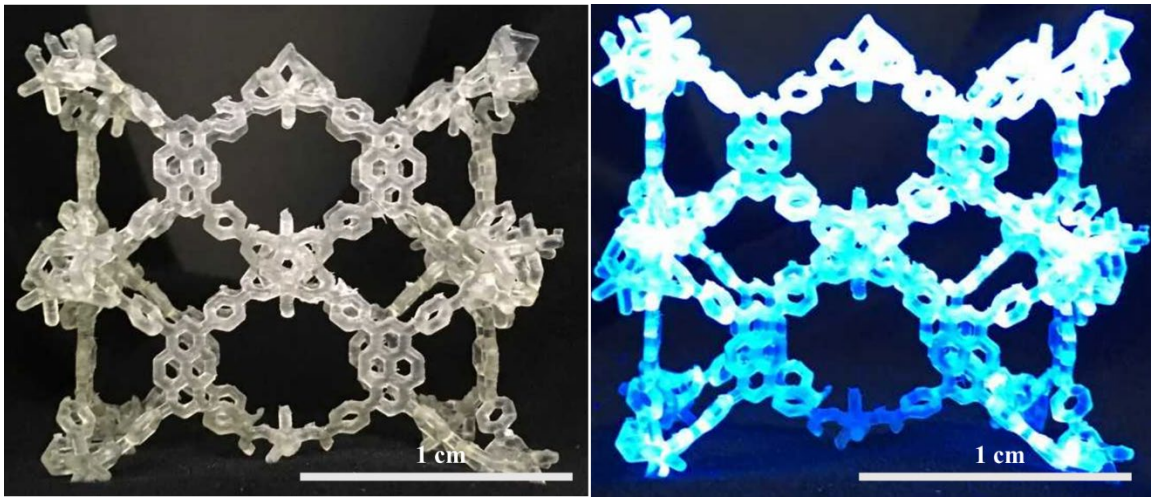

Figure 3.47: SLA 3D printed NU-1000 structure using NU-1000/Formlabs 1+ resin. The left image is with normal lighting and the right is UV (405 nm) light.

A method was devised by which NU-1000 was placed in polydimethylsiloxane (PDMS, trade name Sylgard® 184) which displays no background optical fluorescence (Sections 3.5.12 and 3.5.13). The aligned and unaligned samples were irradiated with a UV laser diode at normal incidence to the sample plane (Section 3.5.14).

The azimuthal plot (Figure 3.48) illustrates the impact of aligned and unaligned anisotropic NU-1000 crystals. By aligning NU-1000 micro-rods in a Sylgard® 184 composite, there is an anisotropic optical response to the linearly polarized UV excitation light. The optical response is a result of the alignment along the major axis of NU-1000 specifically the pyrene rings of the linker. The pyrene is planar conjugated ring system with a large amount of delocalisation and by alignment in the same plane an optical response is noted. The unaligned sample showed little response to the UV light while the aligned NU-1000 samples show a significant anisotropic response occurring at 90°. These results demonstrate that the intensity of the optical response is dependent on the angle between the linearly polarised excitation radiation and crystal lattice planes. Thus, by rotating the sample the signal can be switched on or off.

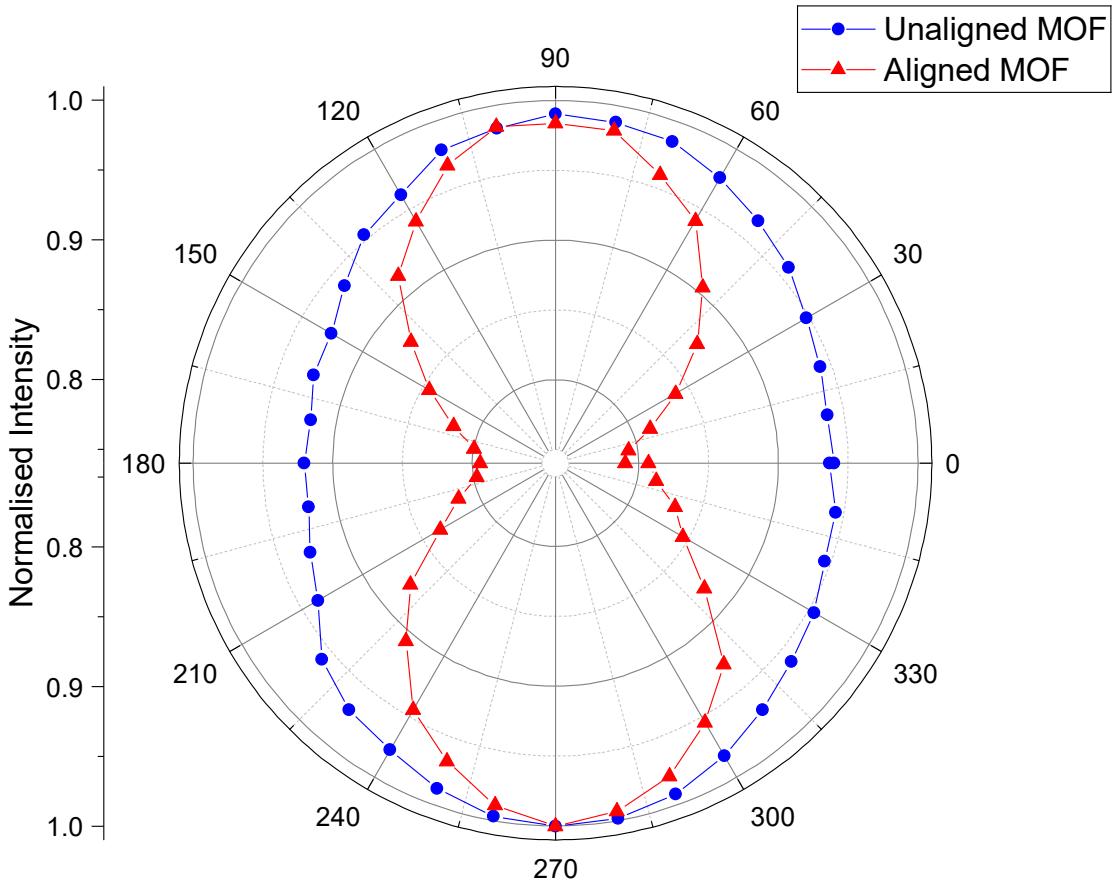

Figure 3.48: Azimuthal plot of 405 nm linearly polarized excitation light on NU-1000 unaligned (blue) and aligned (red).

3.3.9. 4DP – Time dependent 3DP of hierarchical MOF composite

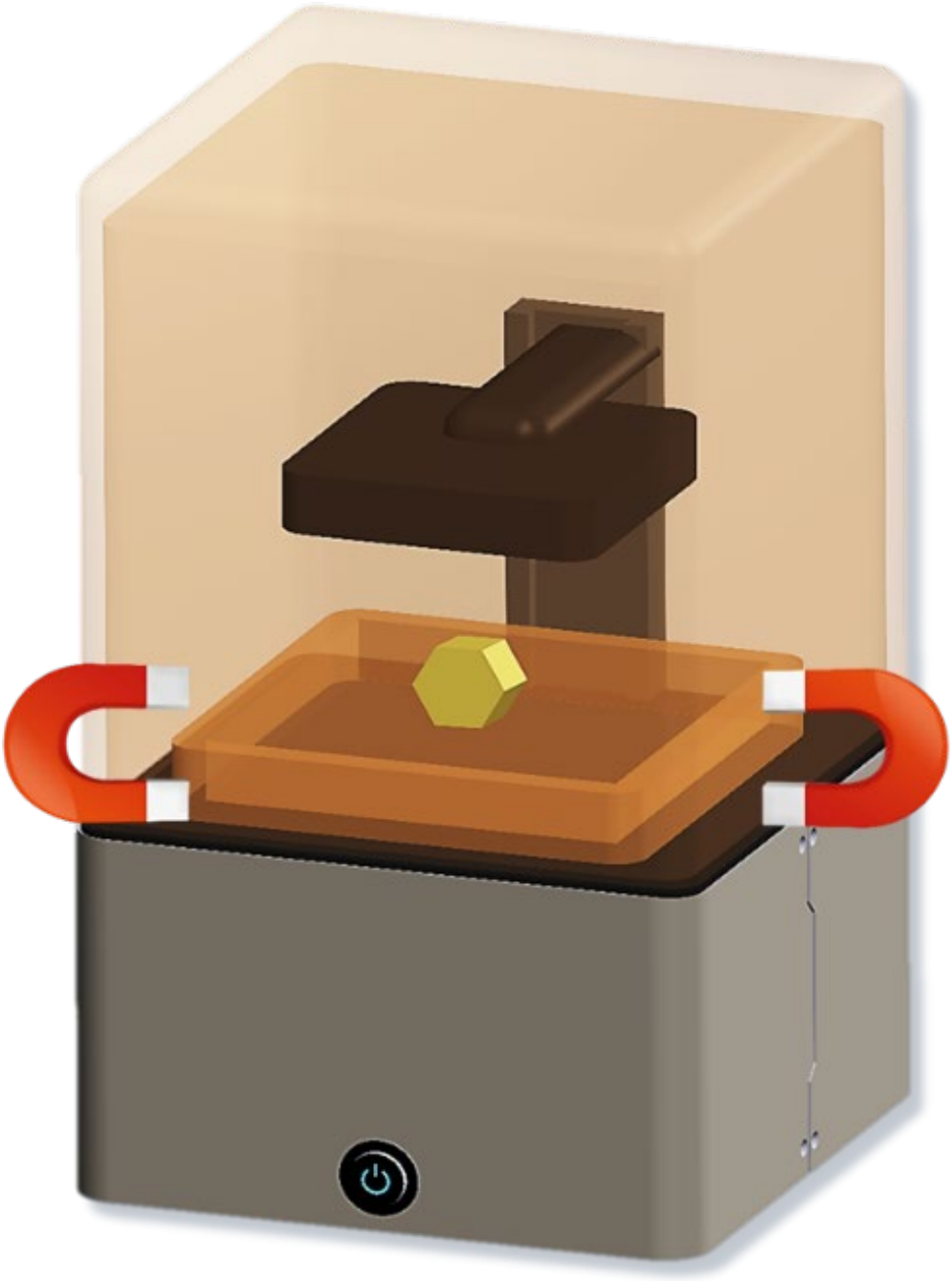

Figure 3.49: Rendered CAD image of Formlabs 1+ SLA 3D Printer showing the principal behind the magnetic alignment setup with magnets represented by horseshoe magnets.

The principle behind the magnetic alignment of MOFs has been demonstrated and applied by casting into moulds. But here the technique is applied to a fabrication process which allows the creation of intricate 3D hierarchical composites.

The benefit of this process allows the design of intricate architecture, fast manufacture and control of particle alignment during the printing process. These results are achieved using a Form 1+ SLA

3D printer with attached 2700 G neodymium magnets (Section 3.5.15) that imposed a static magnetic field and placed horizontally onto the resin tray. Figure 3.49 is a CAD drawn model of the Form 1+ SLA 3D printer, which functions by placing the mixture of the polymer resin and NU-1000 or MIL-53 magnetic MOFs into a resin tray. The resulting formulated was mixed and degassed before use (section 3.3.7).

As eluded to at the start of this chapter, different method of magnet placement was trailed including – in the build tray which was unsuccessful as it pulled all magnetic particles out of solution.

The black build tray is then lowered into the resin, approximately 2 mm from the bottom and patterned by a UV laser. The build tray rises each layer to allow more material to flood into the area. To allow the material time to align the build plate was paused for 1 minute between layers. Without the pause the process may have been to quick and alignment not possible.

Prior to printing, a model was designed in the 3D printing software and uploaded to the printer, in this instance 'HULL' was designed (Section 3.5.15). The model was designed on tinkerCAD, with a layer setting of 0.2 mm and included a 1 second pause on each layer to allow particles to align. The physical models, photographed by a digital camera in Figure 3.50, show significantly different colours. The sample containing NU-1000 has an intense yellow colour because of the powdered NU-1000, which itself is yellow.

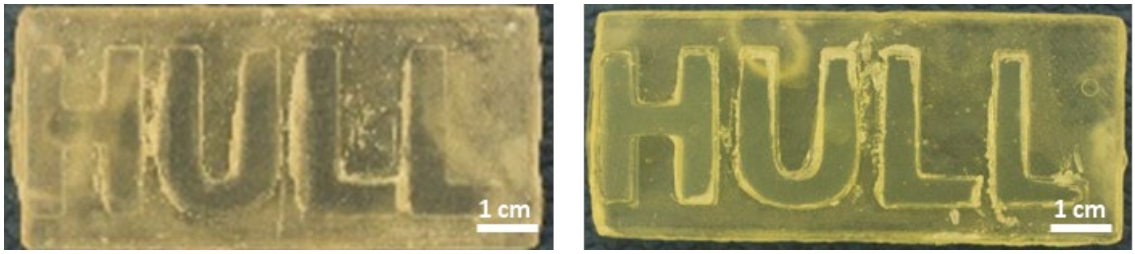

Figure 3.50: 4D printed 'Hull' with aligned MOFs; NH_2-MIL-53(Al) (left) and NU-1000 (right).

The two samples look different in quality but contained the same 1 wt. % MOF to resin. The samples show a difference in quality; this was discovered to be due to the ambient temperature in the laboratory. The ambient temperature of the laboratory varied ±20 °C, dependent on the season and effected the viscosity of the resin, impacting the ability for resin to flow back into position.

This was attempted to be overcome by localising the heat with a fan heater towards the 3D printer. This was not ideal and did not guarantee a good print; the next generation of Formlabs 3D printer – Form 2, has a heated resin bed to overcome this issue.

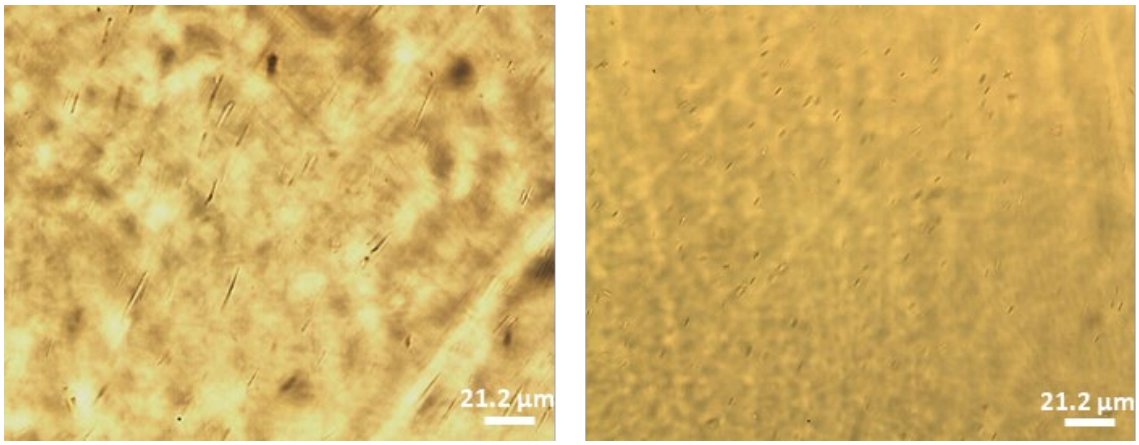

Figure 3.51: Optical microscopy images of aligned NH_2-MIL-53(Al) microneedles (left) and NU-1000 microrods (right) within the 3D printed composite.

Figure 3.51, shows optical microscopy images of the magnetically aligned and 3D printed MOFs in resin, exhibiting both the longer micro-needles of NH_2-MIL-53(Al) and micro rods of NU-1000. Both images were taken from the bar of the capital 'H'. Other areas of the sample were trailed and exhibited the similar orientation. By graphical representation of the orientation (Figure 3.52) there is significant alignment R = 0.367 and R = 0.503 for NH_2-MIL-53(Al) and NU-1000 respectively. The significant difference in partial alignment between the two MOFs is due to the amount of iron adsorbed onto the surface which was previously experimentally found to be 5.29 % and 3.93 % respectively.

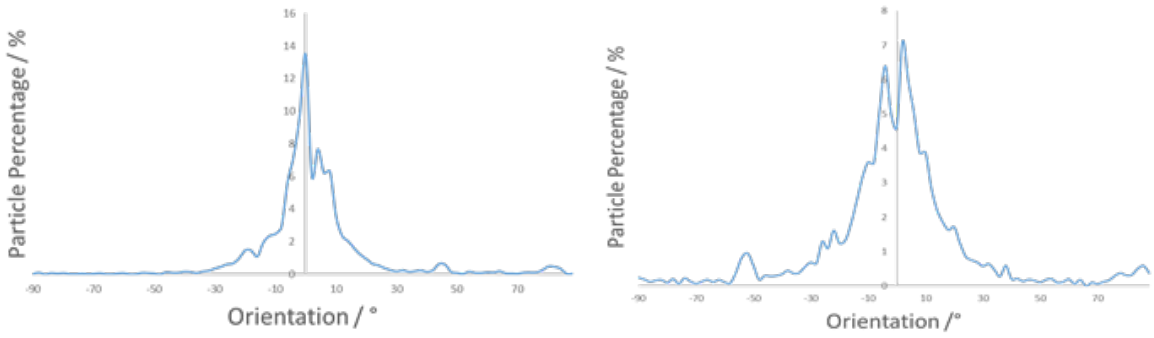

Figure 3.52: Optical microscopy images of aligned NH_2-MIL-53(Al) microneedles (left) and NU-1000 microrods (right) within the 4D printed composite.

3.4. Conclusion

The MOF magnetic alignment strategy represents an important addition to a scientists' toolbox. By demonstrating the technique of controlling crystal orientation, the technique can be utilised for many other anisotropic particulates. Although this study relies upon attractive electrostatic interactions between NU-1000 or NH_2-MIL-53(Al) and iron oxide nanoparticles, the exploitation of such interactions can be easily extended to other MOF/magnetic nanoparticle pairings, by adjusting the pH or other particle environmental factors. Crucially, this approach also eliminates the requirements for lattice matching of MOF to the substrate and the need for careful control of oriented MOF crystal growth. Additionally, the use of a magnetically aligned MOF (NU-1000), dispersed into a polymer matrix was explored. The MOF/polymer generated an optical anisotropic response by UV excitation, demonstrating that alignment of anisotropic particles could have uses in the optical applications. Also established is a fabrication technique to process magnetically aligned MOFs into 3D shapes. This method allows the production of MOF composites, and magnetic control of the orientation that display a hierarchical architecture.

3.5. Experimental

Herein are the experimental methods, materials and instruments specific to Chapter 3.

3.5.1. Materials, equipment and reagents

Sylgard® 184 silicone elastomer solution was purchased from Dow Corning. Dialysis cellulose tubing (MW cutoff 12,000-14,000 g mol^{-1}, wall thickness 20 μm) was purchased from Fisher Scientific. NU-1000 was obtained from Farha group and prepared in accordance to literature where reagents were obtained as indicated in the published procedure.[33] Neodymium magnets, measuring a size of 50 x 25 x 10 mm with a pull capability of 32.5 kg (2700 G) were purchased from First4magnets (www.first4magnets.com). 5 metre UV lights strip (12 V 395-405 nm) were purchased from AMARS. Formlabs 1+ Clear resin GPCL02 was purchased from Formlabs (www.formlabs.com) similarly Formlabs 1+ SLA 3D printer can be purchased from Formlabs directly.

3.5.2. Synthesis of MIL-68(Ga/Fe)

The synthetic procedure was taken from the literature with moderate modifications as displayed in Table 3.9.[40] $Ga(NO_3)_3 \cdot 6H_2O$ (0.75 mmol) and $Fe(NO_3)_2 \cdot 9H_2O$ w(0.05 mmol) were added to a solution of terephthalic acid (0.6 mmol) in DMF (70 mmol) and placed in a round bottom flask with a magnetic stirrer bar and heated to 100 °C for 6 hours. The samples were then centrifuged and washed with DMF (2 x 15 mL) and ethanol (3 x 15 mL) before being dried in an oven at 50 °C overnight.

Table 3.9: Modifications of iron and indium content for the synthesis of MIL-68(Ga)

MIL-68(Ga)	**1A**	**1B**	**1C**	**1D**	**1E**
$Ga(NO_3)_3 \cdot 6H_2O$	0.80 mmol	0.75 mmol	0.70 mmol	0.65 mmol	0.60 mmol
$Fe(NO_3)_2 \cdot 9H_2O$	-	0.05 mmol	0.10 mmol	0.15 mmol	0.20 mmol
Terephthalic acid	0.6 mmol	0.6 mmol	0.6 mmol	0.6 mmol	0.6 mmol
***N,N*-DMF**	70 mmol	70 mmol	70 mmol	70 mmol	70 mmol

3.5.3. Synthesis of MIL-68(In/Fe)

The synthetic procedure was taken from the literature with moderate modifications as displayed in Table 3.10.[40] $In(NO_3)_2 \cdot 6H_2O$ (0.75 mmol) and $Fe(NO_3)_2 \cdot 9H_2O$ w(0.05 mmol) were added to a solution of terephthalic acid (0.6 mmol) in DMF (70 mmol) and placed in a round bottom flask with a magnetic stirrer bar and heated to 100 °C for 6 hours. The samples were then centrifuged and washed with DMF (2 x 15 mL) and ethanol (3 x 15 mL) before being dried in an oven at 50 °C overnight.

Table 3.10: Modifications of iron and indium content for the synthesis of MIL-68(In)

MIL-68(In)	**2A**	**2B**	**2C**	**2D**	**2E**
$In(NO_3)_2 \cdot 6H_2O$	0.80 mmol	0.75 mmol	0.70 mmol	0.65 mmol	0.60 mmol
$Fe(NO_3)_2 \cdot 9H_2O$	-	0.05 mmol	0.10 mmol	0.15 mmol	0.20 mmol
BDC	0.6 mmol	0.6 mmol	0.6 mmol	0.6 mmol	0.6 mmol
***N,N*-DMF**	70 mmol	70 mmol	70 mmol	70 mmol	70 mmol

3.5.4. Crystallographic data collection

Indexing and refinements were performed using GSAS II software, the data was subject to Le Bail extraction and retained information about the unit cell volume and unit cell parameters.

3.5.5. Vibrating sample magnetometer (VSM)

A Lakeshore 7300 VSM with a Newport Instruments magnet was utilised. A custom LabView program controlled the applied field from +/- 10kG. A 10s integration time was used for each data point. The samples were placed in a Kel-F sample holder and it's contribution was subtracted from the sample signal by running the holder separately. Calibration of the VSM was made against a Ni reference sample provided by Lakeshore.

3.5.6. Preparation of buffer standard, pH 3.5 and pH 5.9

Anhydrous sodium acetate (0.22 g) dissolved in glacial acetic acid (2.70 mL) and made up to a 500 mL solution with distilled water was produced and was adjusted to yield a pH 3.5 buffer solution. Anhydrous sodium acetate (0.39 g) was dissolved in glacial acetic acid (0.15 mL) and made up to a 500 mL solution with distilled water and adjusted to yield a pH 5.9 buffer solution.

3.5.7. Preparation of MOF with iron oxide nanoparticles

MOF microcrystals (50 mg) were suspended in prepared buffer solution (pH 3.5 or 5.9, 20 mL) and sonicated for 25 minutes. Iron oxide nanoparticles (5 mg) were diluted in buffer solution (20 mL) and slowly added to the MOF solution. The reaction was stirred at room temperature for 3 hours, the solid was then washed with water (3 x 50 mL) and ethanol (3 x 50 mL). The resulting solid was dried in vacuo at 40 °C.

3.5.8. Dynamic Light Scatter (DLS)

Dynamic Light Scattering (DLS) is a technique used to measure the zeta potential, particulate size and particle concentration. The principle of DLS requires the sample (suspension) to be illuminated by a laser beam and the fluctuations of the scattered light are detected by a photon detector. DLS experiments were all captured using a Malvern Zetasizer Nanoseries NanoZS and was used to measure the zeta potential of MOFs with iron oxide nanoparticles.

3.5.9. Transmission Electron Microscopy (TEM)

The Transmission Electron Microscope (TEM) technique is similar, in principle, to an optical microscope but instead of light it uses electrons. The electron beam is passed through a thin sample and allows for fine detailed images of the structure, even down to individual atoms. TEM was performed on a Jeol 2010 TEM instrument running at 200 kV and was used for images of iron oxide nanoparticles adsorbed to NU-1000.

3.5.10. Mixing of magnetic MOF and Formlabs 1+ resin

Iron oxide nanoparticle-functionalized MOF crystals (0.3 wt.%) were mixed with Formlabs 1+ resin (7.5 mL) by homogenization at 3000 rpm for 3 minutes with an Ultra-Turrax homogenizer and then degassed under reduced pressure overnight.

3.5.11. Alignment of MOF in Formlabs 1+ resin

The MOF/resin mixture was poured into pre-cast moulds and degassed under reduced pressure. To align the sample in a horizontal orientation two 2700 G neodymium magnets were placed 5 cm apart either side of the sample (inside a UV box) under inert conditions for 10 minutes, Figure 3.53 Prior to exposure with UV light, the sample was pre-aligned for 2 minutes.

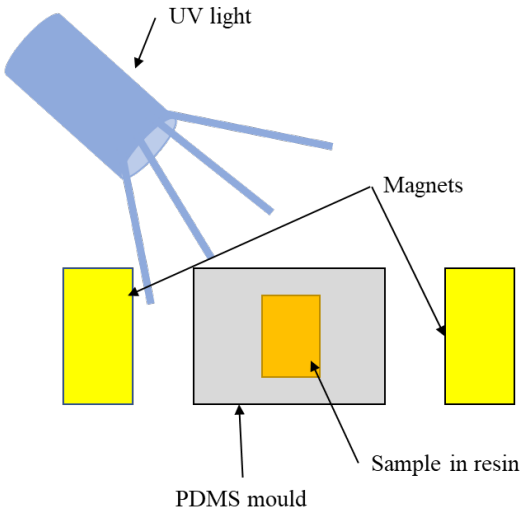

Figure 3.53: Experimental setup for samples used in polarisation measurements.

3.5.12. Mixing of magnetic MOF and Sylgard® 184

Iron oxide nanoparticle-functionalized MOF crystals (1.0 wt.%) were added to Sylgard® 184 Silicone elastomer (2.0 g) and mixed for 3 minutes by stirring, then degassed by centrifugation at 1250 rpm for 5 minutes.

3.5.13. Alignment of MOF in Sylgard® 184

MOF/Sylgard® 184 mixture was poured into pre-cast moulds created by 3DP and degassed under reduced pressure. To align the NU-1000 micro rods in a horizontal orientation, two 2700 G neodymium magnets (preheated to 50 °C) were placed 5 cm apart either side of the sample for 1 hour prior to curing. The sample was then left to cure for 12 hours at 50 °C. Generation of an unaligned sample was completed using the same procedure without the use of magnets.

3.5.14. Polarisation measurements

Fluorescence measurements (polarisation measurements) were collected by a ProEM CCD Camera, Princeton Instruments. A Becker and Hickl diode laser was used as an excitation source at 405 nm, 144 μW constant wave with linear polarisation. Fluorescence spectra were obtained using a PerkinElmer LS55 Fluorescence spectrometer, in conjunction with FL Winlab software.

A 144 μW constant wave 405 nm diode laser (linearly polarized) was used to illuminate the sample at normal incidence. The beam polarisation was cleaned using a linear polariser and subsequently adjusted using a half-wave plate. The resulting MOF fluorescence signal was collected in transmission by a 0.9 NA 100x objective lens and passed through a long pass filter to remove the laser excitation before being spectrally analysed by a Horiba μHR monochromator coupled to a Princeton Instruments ProEM CCD camera. The polarisation of incident light was rotated in 10° increment for each measurement, and the fluorescence spectra were taken with a 1-second integration time at a constant power and position on the sample. Each spectrum was background corrected and normalised to 1 before being integrated between wavelengths of 477 – 742 nm.

3.5.15. Alignment of MOF in Formlabs 1+ 3D SLA Printer

The MOF/resin mixture was poured into the resin tray of the 3D printer and degassed under reduced pressure. To align the MOFs two 2700 G neodymium magnets were placed on either side of the tray, Figure 3.54, and left for 1 hour prior to printing. One starting of the print, each layer received a one-minute delay to allow the particles time to realign after the 'peel' action of the printer. The pause was achieved by lifting the lid of the printer, which triggered a safety mechanism which stops the print instantly. On completion of the print, the structure was placed in an IPA bath overnight to remove excess polymer resin.

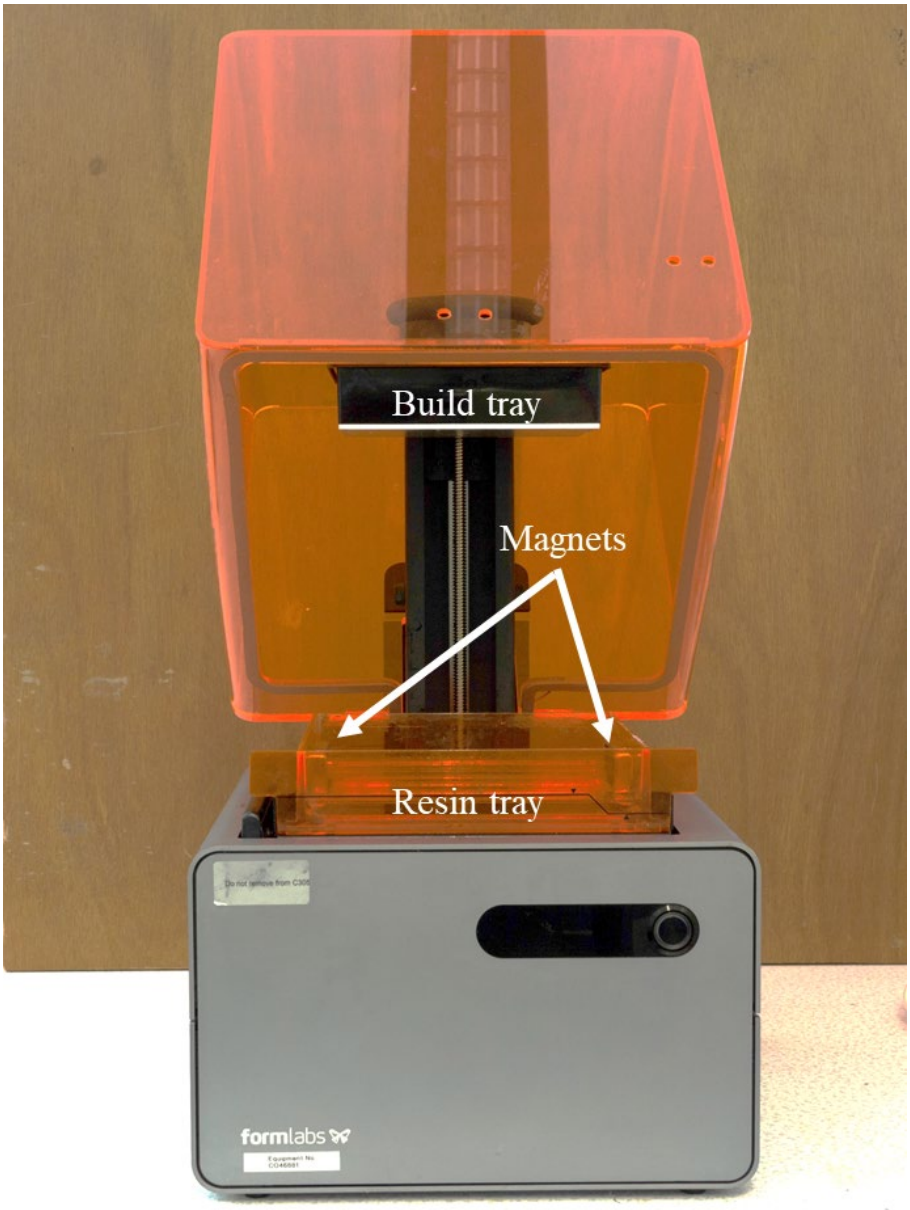

Figure 3.54: Formlabs 1+ 3D Printer with magnets inside the resin tray.

3.5.16. Calculation of R value

The value of *R* is 1 for randomly distributed data. For data perfectly aligned with the field *R* is zero. In the case where the particles are aligned opposing the field, the *R* is two. The data was fitted prior to analysis. Where n_i is the proportion of particles at each angle θ_i. The data extend out to $\theta_{\max}$ and there are N of them. The inclusion of the (1+1/N) term on the bottom returns the correct value when there is a bin centred on zero degrees.

$$R = \frac{\sum_i n_i \theta_i}{\frac{\theta_{\max}}{2}\left(1 + \frac{1}{N}\right)\sum_i n_i}$$

Equation 3.3: Equation for the calculation of R value

3.6. References

1 G. Yu, Y. Liu, X. Zou, N. Zhao, H. Rong and G. Zhu, *J. Mater. Chem. A*, 2018, **6**, 11797–11803.

2 I. M. Hönicke, I. Senkovska, V. Bon, I. A. Baburin, N. Bönisch, S. Raschke, J. D. Evans and S. Kaskel, *Angew. Chemie - Int. Ed.*, 2018, **57**, 13780–13783.

3 Y. Li, Z. Yang, Y. Wang, Z. Bai, T. Zheng, X. Dai, S. Liu, D. Gui, W. Liu, M. Chen, L. Chen, J. Diwu, L. Zhu, R. Zhou, Z. Chai, T. E. Albrecht-Schmitt and S. Wang, *Nat. Commun.*, 2017, **8**, 1–10.

4 C. Li, Z. Xiong, J. Zhang and C. Wu, *J. Chem. Eng. Data*, 2015, **60**, 3414–3422.

5 S. Wang, Y. Lv, Y. Yao, H. Yu and G. Lu, *Inorg. Chem. Commun.*, 2018, **93**, 56–60.

6 M. L. Aubrey, B. M. Wiers, S. C. Andrews, T. Sakurai, S. E. Reyes-Lillo, S. M. Hamed, C. J. Yu, L. E. Darago, J. A. Mason, J. O. Baeg, F. Grandjean, G. J. Long, S. Seki, J. B. Neaton, P. Yang and J. R. Long, *Nat. Mater.*, 2018, **17**, 625–632.

7 K. Mandel, T. Granath, T. Wehner, M. Rey, W. Stracke, N. Vogel, G. Sextl and K. Müller-Buschbaum, *ACS Nano*, 2017, **11**, 779–787.

8 J. Jiang, A. M. Plonka, A. I. Frenkel and D. Gersappe, *J. Phys. Chem. Lett.*, 2018, 1092–1096.

9 A. C. Forse, M. I. Gonzalez, R. L. Siegelman, V. J. Witherspoon, S. Jawahery, R. Mercado, P. J. Milner, J. D. Martell, B. Smit, B. Blümich, J. R. Long and J. A. Reimer, *J. Am. Chem. Soc.*, 2018, **140**, 1663–1673.

10 A. V. Vinogradov, V. A. Milichko, H. Zaake-Hertling, A. Aleksovska, S. Gruschinski, S. Schmorl, B. Kersting, E. M. Zolnhofer, J. Sutter, K. Meyer, P. Lönnecke and E. Hey-Hawkins, *Dalt. Trans.*, 2016, **45**, 7244–7249.

11 Y. Zhang, X. Feng, S. Yuan, J. Zhou and B. Wang, *Inorg. Chem. Front.*, 2016, **3**, 896–909.

12 S. Shahid, K. Nijmeijer, S. Nehache, I. Vankelecom, A. Deratani and D. Quemener, *J. Memb. Sci.*, 2015, **492**, 21–31.

13 P. Falcaro, F. Normandin, M. Takahashi, P. Scopece, H. Amenitsch, S. Costacurta, C. M. Doherty, J. S. Laird, M. D. H. Lay, F. Lisi, A. J. Hill and D. Buso, *Adv. Mater.*, 2011, **23**, 3901–3906.

14 X. Zhao, S. Liu, Z. Tang, H. Niu, Y. Cai, W. Meng, F. Wu and J. P. Giesy, *Sci. Rep.*, 2015, **5**, 1–10.

15 J. J. Martin, B. E. Fiore and R. M. Erb, *Nat. Commun.*, 2015, **6**, 8641.

16 C. Volkringer, M. Meddouri, T. Loiseau, N. Guillou, J. Marrot, G. Férey, M. Haouas, F. Taulelle, N. Audebrand and M. Latroche, *Inorg. Chem.*, 2008, **47**, 11892–11901.

17 A. Perea-Cachero, J. Sánchez-Laínez, B. Zornoza, E. Romero-Pascual, C. Téllez and J. Coronas, *Dalt. Trans.*, 2019, **48**, 3392–3403.

18 R. D. Shannon, C. T. Prewitt and IUCr, *Acta Crystallogr. Sect. B Struct. Crystallogr. Cryst. Chem.*, 1969, **25**, 925–946.

19 B. deB. Darwent, *Bond dissociation energies in simple molecules*, National Standard Reference Data Series, NationalBureau of Standards, Washington, 1st edn., 1970.

20 T. Kundu, M. Wahiduzzaman, B. B. Shah, G. Maurin and D. Zhao, *Angew. Chemie - Int. Ed.*, 2019, **58**, 8073–8077.

21 K. Y. Andrew Lin, H. A. Chang and C. J. Hsu, *RSC Adv.*, 2015, **5**, 32520–32530.

22 C. V Mcguire and R. S. Forgan, *Chem. Commun*, 2015, **51**, 5199–5217.

23 A. A. Alqadami, M. Naushad, Z. A. Alothman and A. A. Ghfar, *ACS Appl. Mater. Interfaces*, 2017, **9**, 36026–36037.

24 C. L. Lin, C. F. Lee and W. Y. Chiu, *J. Colloid Interface Sci.*, 2005, **291**, 411–420.

25 M. Alhamami, H. Doan and C. H. Cheng, *Materials (Basel).*, 2014, **7**, 3198–3250.

26 R. Liang, L. Shen, F. Jing, W. Wu, N. Qin, R. Lin and L. Wu, *Appl. Catal. B Environ.*, 2015, **162**, 245–251.

27 C. Yang, J. Cheng, Y. Chen and Y. Hu, *RSC Adv.*, 2016, **6**, 61703–61706.

28 S. W. Hwang, A. Umar, G. N. Dar, S. H. Kim and R. I. Badran, *Sens. Lett.*, 2014, **12**, 97–101.

29 N. Planas, J. E. Mondloch, S. Tussupbayev, J. Borycz, L. Gagliardi, J. T. Hupp, O. K. Farha and C. J. Cramer, *J. Phys. Chem. Lett.*, 2014, **5**, 3716–3723.

30 H. Furukawa, K. E. Cordova, M. O'Keeffe and O. M. Yaghi, *Science*, 2013, **341**, 974–988.

31 T. Islamoglu, K.-I. Otake, P. Li, C. T. Buru, A. W. Peters, I. Akpinar, S. J. Garibay and O. K. Farha, *CrystEngComm*, 2018, **20**, 5913–5918.

32 P. Deria, W. Bury, J. T. Hupp and O. K. Farha, *Chem. Commun. (Camb).*, 2014, **50**, 1965–1968.

33 T. C. Wang, N. A. Vermeulen, I. S. Kim, A. B. F. Martinson, J. F. Stoddart, J. T. Hupp and O. K. Farha, *Nat. Protoc.*, 2015, **11**, 149–162.

34 F. Montagne, O. Mondain-Monval, C. Pichot, H. Mozzanega and A. Elaïssari, *J. Magn. Magn. Mater.*, 2002, **250**, 302–312.

35 T. Loiseau, C. Serre, C. Huguenard, G. Fink, F. Taulelle, M. Henry, T. Bataille and G. Férey, *Chem. – A Eur. J.*, 2004, **10**, 1373–1382.

36 J. M. Chin, E. Y. Chen, A. G. Menon, H. Y. Tan, A. T. S. Hor, M. K. Schreyer and J. Xu, *CrystEngComm*, 2013, **15**, 654–657.

37 S. Couck, J. F. M. Denayer, G. V. Baron, T. Rémy, J. Gascon and F. Kapteijn, *J. Am. Chem. Soc.*, 2009, **131**, 6326–6327.

38 S. M. J. Rogge, A. Bavykina, J. Hajek, H. Garcia, A. I. Olivos-Suarez, A. Sepúlveda-Escribano, A. Vimont, G. Clet, P. Bazin, F. Kapteijn, M. Daturi, E. V. Ramos-Fernandez, F. X. Llabrés i Xamena, V. Van Speybroeck and J. Gascon, *Chem. Soc. Rev.*, 2017, **46**, 3134–3184.

39 I. Karimzadeh, M. Aghazadeh, T. Doroudi, M. R. Ganjali and P. H. Kolivand, *Hindawi, Adv. Phys. Chem.*, 2017, **2017**, 1–7.

40 C. Volkringer, M. Meddouri, T. Loiseau, N. Guillou, M. Haouas, F. Taulelle, N. Audebrand, M. Latroche and D. V. Saint Quentin, *Inorg. Chem.*, 2008, **47**, 11892–11901.

4. 4D direct-ink writing of catalytically active MOF composite

4.1. Introduction

MOFs are record breakers for their ultra-high surface area - enabled by their ability to form a repeating porous architecture. MOFs in their synthesised powdered state record surface areas up to 7000 m^2g^{-1}.[1] However, for many applications a powder of loose polycrystalline powder is unsuitable. For instance, using MOFs as a catalyst in a solution, the MOFs would need to be filtered through a fine filter to extract them from solution, adding potentially time-wasting steps to a simple catalysis reaction. Methods of mounting MOFs on a substrate have been achieved such as the creation of membranes, but this lessens the surface area available. The fabrication of a 3D monoliths embedded with MOFs results in macroscopically porous monoliths, Figure 4.1. However, for the MOF UiO-66, the surface area was less (982 m^2g^{-1}) than its powdered form (1178 m^2g^{-1}).[2]

Figure 4.1: Honeycomb, cylindrical monolith, flat membrane and loose particles.

The surface area could be increased by the deposition of the MOF into a high surface area shape, such as a honeycomb, Figure 4.1, which allows a greater amount of MOF to be available. However, MOF powder cannot be simply placed into shape and remain, it requires the use of a binder to 'fix' the MOF in place. There is, however, a problem with using a binder with a MOF, it would fill the pores of the MOF and slow or even stop any activity by blocking all available surface area. A new fabrication method would need to be devised to overcome MOFs lack of processability. The objectives would be to:

a) To deposit a material in the desired location, providing a honeycomb-like shape that may be useful for applications such as catalysis, by omitting the need for filtration.
b) To attain a high-level surface area which is comparable to loose MOF powdered sample.
c) To demonstrate the first two functions in a real-world application of a MOF composite.

The first function (a) is to deposit material into a desired shape, which can be achieved by 3D printing and more specifically, direct-ink write. This format of 3D printing has been extensively used and has been well documented by Lewis *et al.* who were the first to characterise the desired properties of a direct-ink, Figure 4.2.[3]

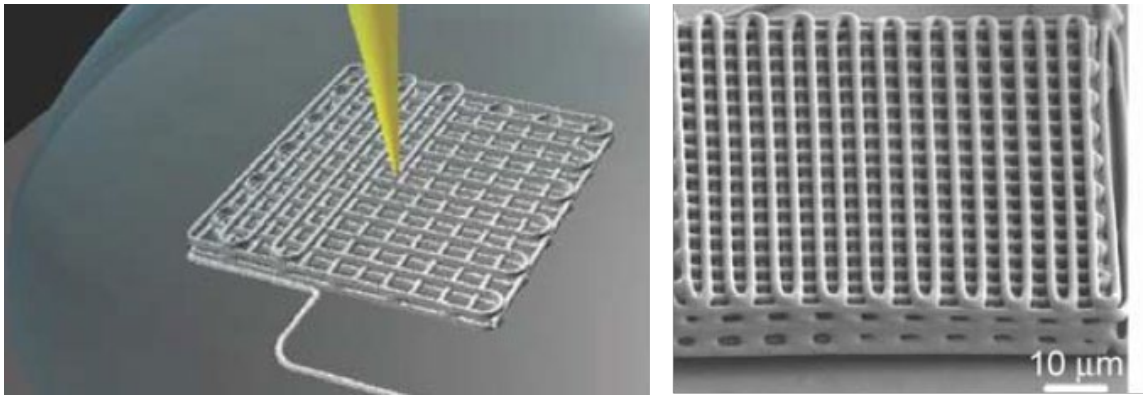

Figure 4.2: Demonstration of direct-ink write 3D printing of a woodpile structure using a shear-thinning material. Reproduced with permission from Ref.[3] Copyright Elsevier 2004

They determined that a direct-ink write must possess a shear-thinning property to be able to print successfully and generate intricate structures. Shear-thinning, as demonstrated in Figure 4.3, is defined as the property of a material to become less viscous when subjected to an applied shear stress. The most common example used to demonstrate shear-thinning is ketchup in a glass bottle. A force needs to be applied on the base of the bottle to allow the mixture to flow, after flowing the material returns to a very viscous material. The opposite of shear-thinning is shear-thickening and is well demonstrated by creating a cornflour solution and applying a force, and the solution becoming more viscous as a result. Figure 4.4 demonstrates viscosity over shear rate and the difference between shear-thickening and shear-thinning compared to a Newtonian liquid such as

water. However, shear-thinning is not dependent on time and is instantaneous, required for 3D printing is property that delivers a slower recovery rate, this property is thixotropy.

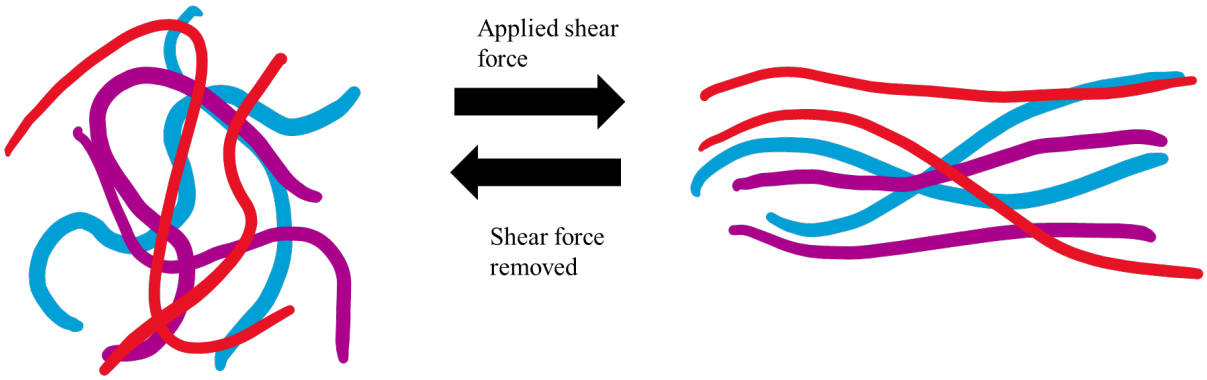

Figure 4.3: Example of a shear-thinning material undergoing an applied shear force and flowing. After the shear force is removed the material returns to its previous state.

Thixotropy is defined as time-dependent shear-thinning, and simply demonstrates that after a shear force has been applied, the material is able to increase viscosity over time to its original form. Lewis *et al.* demonstrated that by placing a thixotropic ink into a syringe and extruding shapes such as the wood pile in Figure 4.2 this was achievable.

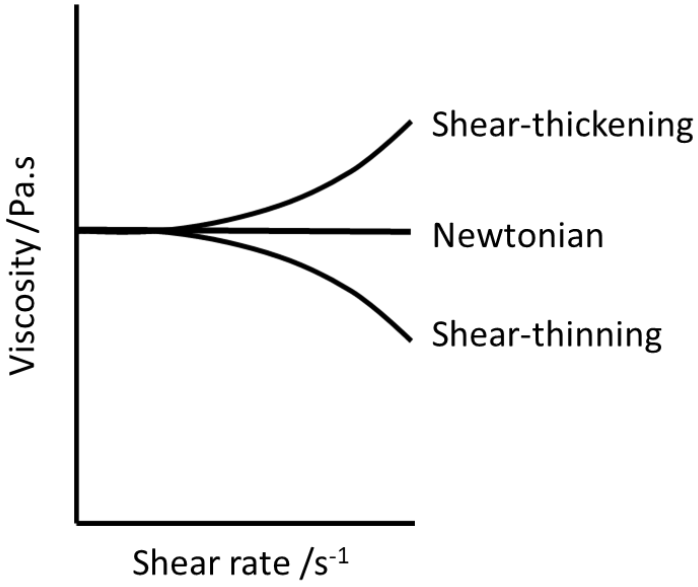

Figure 4.4: Viscosity over shear rate to demonstrate shear-thinning, shear thickening and a Newtonian fluid.

The second function (b) of the new fabrication method must allow the surface area of the MOF to be accessible. Thakkar *et al.* placed MOFs into a shear-thinning clay-based binder and subsequently was the first to publish work on 3D printing a MOF composite. However, the active surface area of the MOF - MOF-74(Ni) was 37 % less (737 m^2g^{-1}) than the loose MOF powder (1180 m^2g^{-1}).[4]

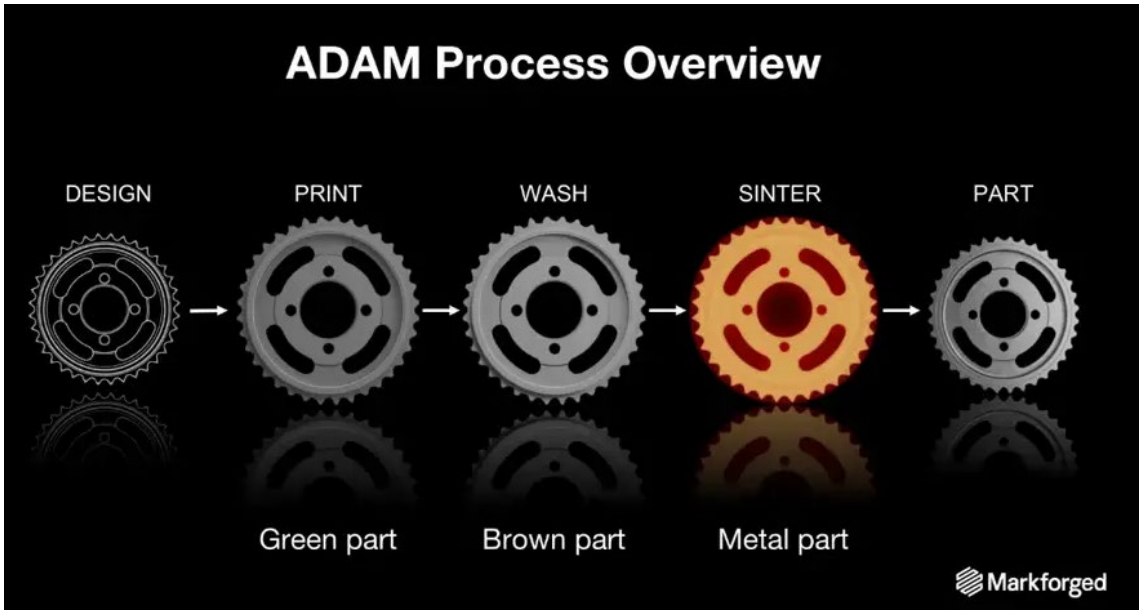

Figure 4.5: ADAM process of design, print, wash and sinter from Markforged.[5]

A process similar to a current 3D printing technique used by 3D printing company Markforged, atomic diffusion additive manufacturing (ADAM, Figure 4.5) allows a metallic powder in a binder to be 3D printed, washed and then sintered in a furnace to burn off excess material. This chapter details the development of a fabrication method based on the ADAM process, whereby a MOF composite ink is 3D printed, sintered and washed. In developing the process consideration of the application of the MOF was essential. Although MOFs are not known to be mechanically, thermally or chemically stable, one MOF does outperform all the others – UiO-66.[6–9] UiO-66 has been tested and displays a surface area of 1180 m^2g^{-1} but it has also been extensively fabricated into pellets, foams, membranes and polymer composites.[10–12] Analysis of UiO-66 has been shown that the exceptional mechanical stability of UiO-66 is derived from the restricted bond angles of the Zr-O bond and high Zr-O coordination, creating a rigid and stronger MOF than previous MOFs.[13]

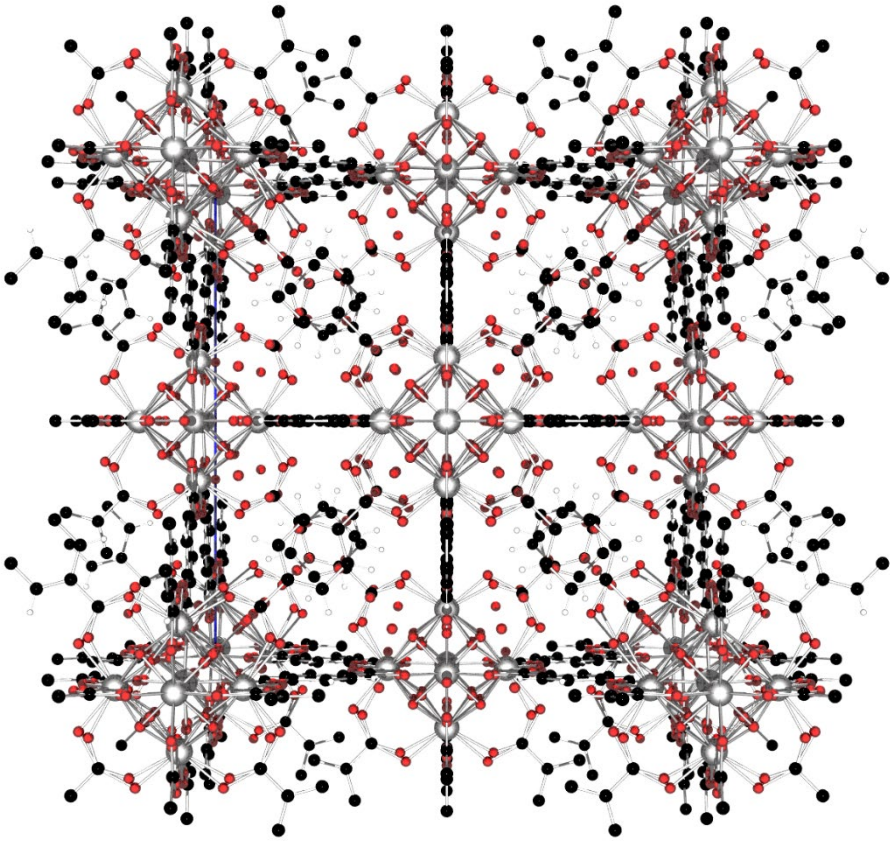

Figure 4.6: UiO-66 crystallographic representation from CIF file 4512072.

The third function (4c) of the new fabrication technique is to demonstrate the real-world application. The chosen MOF, UiO-66 is a zirconium-based MOF, it is well characterised and has a known ability to degrade nerve agents.[14] Nerve agents (Figure 4.7) have a devastating effect on the body and will kill on exposure. During the modern era, deadly nerve agents such as Sarin and Venomous Agent X have been developed since their use in the first world war,[15] and in recent years the infamous 'Novichok' family of nerve agents, notably compound A-230, seized world-wide attention since its use in Salisbury, U.K. The deadly feature of all nerve agents is the phosphonate ester linkage, which interrupts the function of an enzyme in the human nervous system. Typically, the degradation of nerve agents has been by enzyme-based systems. A recent study demonstrated that Zr-based MOFs such as UiO-66 have an affinity for the degradation of live nerve agents, but also the nerve agent simulant - methyl paraoxon (dimethyl 4-nitrophenyl phosphate, DMNP).[14,16–18]

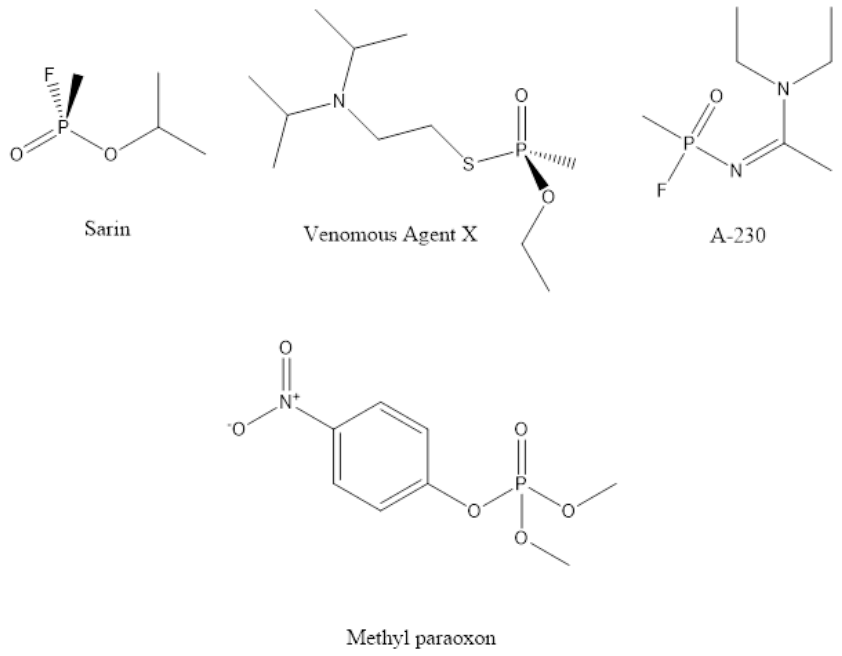

Figure 4.7: Nerve agents: Sarin, Venomous Agent X, A-230 and methyl paraoxon.

Use of a live nerve agent is heavily restricted and so a model compound with a similar structure and therefore methyl paraoxon was selected and the degradation of the chemical outlined in Figure 4.8

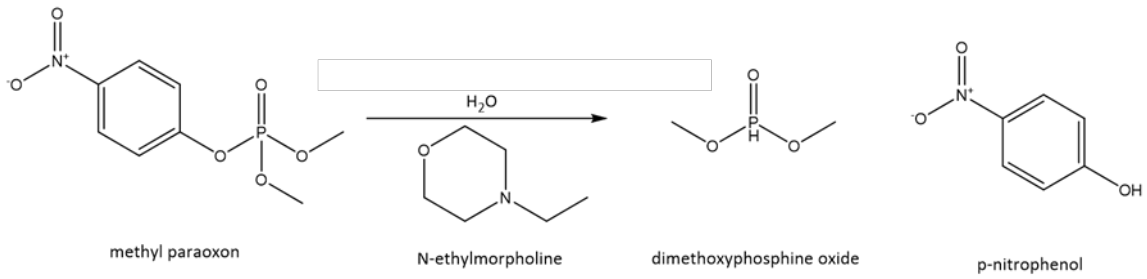

Figure 4.8: Reaction scheme of methyl paraoxon with N-ethylmorpholine to produce dimethoxyphosphine oxide and p-nitrophenol.

By employing 3D printing, it should be possible to fabricate a MOF polymer composite with the desired cross section, wall thickness and complexity to suit the application. However, as the composite here-in also employs a catalyst it goes beyond the classical 3 dimensions (X, Y, Z) and could be considered to use a 4th dimension – time. Catalysis is time dependent, whereby at time = 0 seconds there is no conversion and time =100 seconds a catalysed reaction could be complete. The MOF composite could either be titled a 'time-dependent 3D printed MOF polymer

composite' or '4D printed MOF polymer composite'. The latter is preferred for brevity, but they are synonymous.

This chapter aimed to use 4D direct-ink write printing of a UiO-66 polymer composite, to provide a catalyst material that could be handled with ease and to demonstrate its ability to degrade the nerve agent simulant methyl paraoxon.

4.2. Chapter Overview

Fabrication of a 4D direct-write ink using a UiO-66 polymer composite has not previously been demonstrated, furthermore the catalytic ability of a 4D printed composite for nerve agent degradation remained unexplored. The aim of the work in this chapter is to fabricate a UiO-66-based 4D direct-write ink and characterise the shear-thinning and thixotropic qualities appropriate for 4D printing. Also, this chapter will demonstrate the ability of UiO-66 to withstand harsh processing techniques including mixing with polymers and calcination to achieve a novel 4D printed UiO-66 polymer composite, *via* a novel technique. The final key demonstration is that of a satisfactory surface area and activity in the catalytic breakdown of a nerve agent simulant methyl paraoxon.

4.2.1. Definition of terms.

UiO-66 MOF: The synthesised UiO-66 MOF

UiO-66 EtOH: UiO-66 MOF (5 g) mixed with 7.5 mL ethanol, used for rheological measurements.

Polymer blend: A blend of TMPPA, EBECRYL® 8413 and photoinitiator blend as outlined in section 4.5.3.

Direct-write ink: Addition of UiO-66 to the polymer blend as described in 4.5.3.

4D printed UiO-66 polymer composite: As above formulation, after extrusion and exposure to UV light (365 nm).

4D printed UiO-66 polymer composite (calcined): 3D printed UiO-66 polymer composite after firing at 280 °C for 30 minutes and subsequently washed as outlined in 4.5.6.

4.3. Results and Discussion

The previous chapter utilised SLA 3DP to create a MOF composite material, this material and technique was tentatively investigated for this work. In order to achieve a surface area over and above previous 3DP MOF compsoites,[19] a percentage of over 50% MOF would be required. A mixture of 50% UiO-66 nanoparticles and Formlabs 1+ clear resin was mixed by homogenisation and degassed over night under vacuum to produce a MOF/photopolymer ink. On placing the MOF/photopolymer ink into the resin tray of an SLA 3D printer, not only did the nanoparticles fall out of suspension but attempts to cure the resin with the UV point-laser resulted in light scattering and an unpredictable curing of the photopolymer. A new method and technique had to be devised to 3D print MOFs in a direct-write application.

Some previous methods of 3DP MOFs use direct-write 3DP, by placing the material into a syringe and extruding. The material is a clay-based ink and to cures by the rapid loss of water. This method is good, but extra time must be granted to allow each layer to fully cure before the next layer can be deposited on top. A novel method was trialled here-in using the expertise gained from the work with photopolymeric materials when experimenting with SLA 3DP in chapter 3. The use of a photopolymeric material as the binder would allow rapid curing from the 3D printer. With this in mind a Vellemen K8200 3D printer was built, from a kit, and retrofitted with a 3D printed syringe holder to hold 50 mL syringes, with a luer-lock nozzle – as shown in Figure 4.9. A UV light was positioned 30 cm away from the printer and the whole setup covered in a sealed black plastic enclosure. During printing the syringe would be covered with aluminium foil to prevent curing.

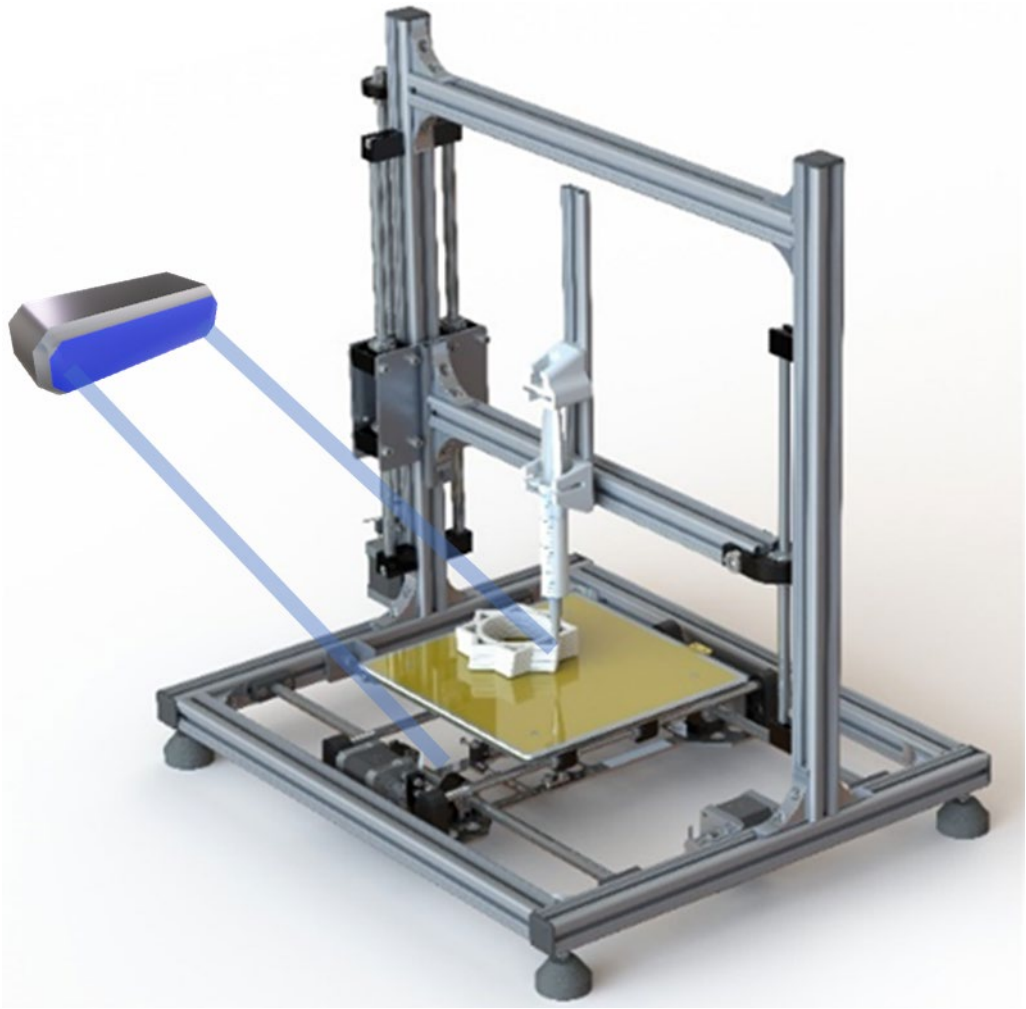

Figure 4.9: Setup of UV light with Vellemen K8200 produced using SolidWorks.

From experience and previous work with photopolymeric materials, it was understood and appreciated that oxygen is an inhibitor to photopolymerisation. To mitigate any effect of oxygen inhibition, the environment of the 3D printer was flooded with gaseous nitrogen and continuously supplied with nitrogen during printing, this was contained within the black plastic enclosure. The 4DP direct-write ink would then be formulated to cure under the UV light of 365 nm. This can be achieved by tuning amount of MOF/photopolymer the ink to cure while still maintaining structure and high loading of MOF.

4.3.1. Formulation of the direct-write ink

The 4D direct-write ink used henceforth was a tuned mixture of acrylates, photoinitator and UiO-66 in ethanol. The formulation was based around the high-loading of nanoparticulate UiO-66. The UiO-66 was synthesised following the procedure outlined in Section 2.2.6, with zirconium salts, terepthalic acid and DMF. When viewed under the SEM the nanoparticles displayed a size range 135 ± 35 nm, as measured by Image J software.

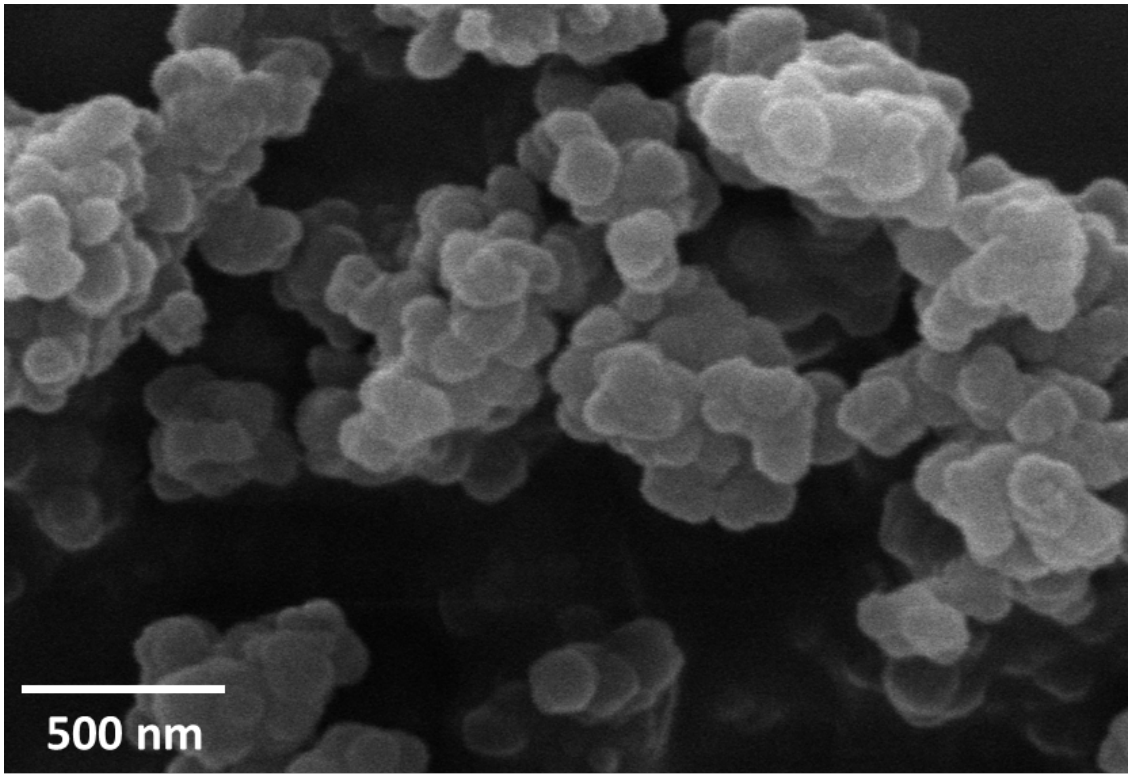

Figure 4.10: Cambridge Stereoscan 360 - SEM image of UiO-66 MOF with a particle size of approximately 135 ± 35 nm.

The image displayed in Figure 4.10 was taken by a SEM and confirms that the synthesised material possessed a size and shape similar to previously reported UiO-66.[20] It was discovered that on mixing powdered UiO-66 (5.0 g)with a minimal amount of ethanol (EtOH, 7.5 mL) as described in Section 4.5.3, a paste was formed that displayed shear-thinning properties. The image in Figure 4.11 shows the sample upended and it appears unchanged from a righted sample. The sample does not flow unless a shear force is applied. This was a primitive test and the rheology will be further investigated in the following section.

The addition of acrylates and photoinitators to UiO-66 in EtOH (Section 4.5.3) created a photo-active ink which was irradiated by UV light on extrusion and cured, this allowed the creation of a layer-by-layer model to be 4D printed. The photoinitators of choice were phenylbis (2,4,6-trimethylbenzoyl) phosphine oxide and 2-hydroxy-2-methylpropiophenone (Figure 4.12), they were chosen for their UV-activity at 365 nm and on their success in other UV-related applications.[21–24]

Figure 4.11: A rudimentary test of a sample vial upended containing UiO-66 in ethanol, demonstrating that the sample does not flow unless a shear force is applied.

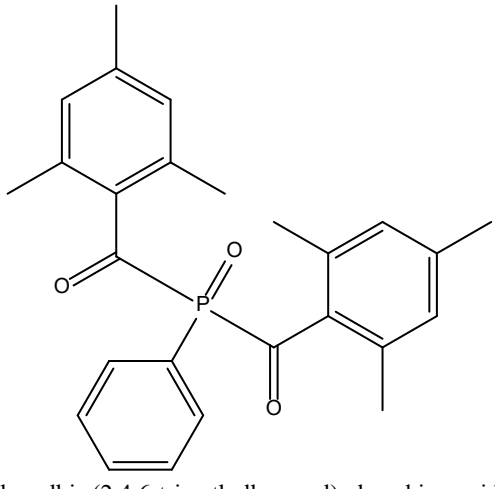

phenylbis (2,4,6-trimethylbenzoyl) phosphine oxide

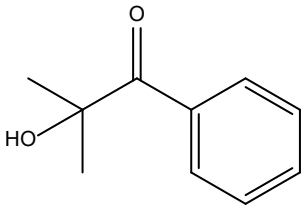

2-hydroxy-2-methylpropiophenone

Figure 4.12: Photoinitiators used in the direct-write ink: phenylbis (2,4,6-trimethylbenzoyl) phosphine oxide and 2-hydroxy-2-methylpropiophenone

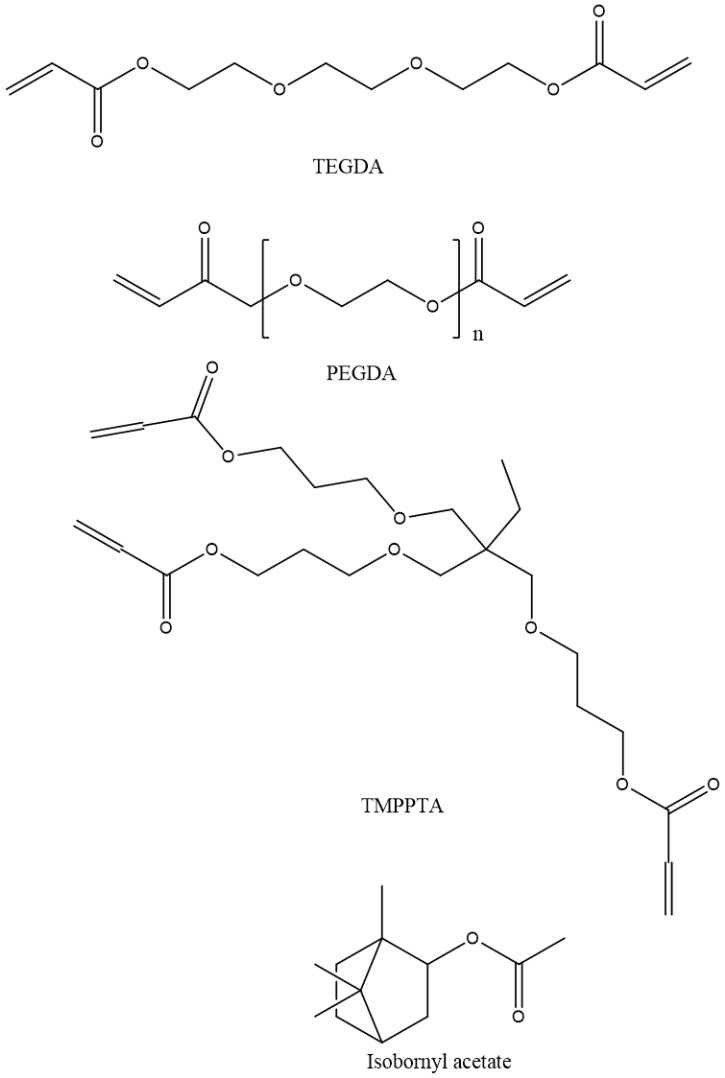

Figure 4.13: Acrylates TEGDA, PEGDA, TMPPTA, TMPTA which were tested along with isobornyl acetate found in Ebecryl 8413®.

The acrylates (Figure 4.13) of choice were TMPPTA and Ebecryl 8413®. TMPPTA is triacrylate system and would cure faster than diacrylate systems such as PEGDA and TEGDA. Ebecryl 8413® has had previously been used in the creation of UV curable elastomers.[25] Unfortunately, the exact formulation of Ebecryl 8413® is not known as it is a registered trademark product. However, it is known to be extremely viscous, fast curing and contains 33wt.% isobornyl acetate as a thinning agent. It is possible that the product contains a triacrylate system like TMPPTA. Mixtures of Ebecryl 8413® and TMPPTA were first trialled to generate a mixture that flowed, as the Ebecryl 8413® was extremely viscous and the TMPPTA had a very low viscosity, the success criteria was a mixture that flowed so a mix of 80:20 was successful. The photoinitiator and UiO-

66 in ethanol were then added until the success criteria; a photopolymer that displayed shear-thinning, thixotropic direct-write ink, was formulated, Section 4.5.3.

4.3.2. Key viscoelastic properties of the direct-write ink

The rheology of the direct-write ink provides information regarding material deformation and material flow. The direct-write ink must possess three key properties: 1. Shear-thinning 2. Thixotropy 3. An elastic modulus greater than viscosity modulus.[3]

4.3.2.1. Shear-thinning of the direct-write ink

To demonstrate that the direct-write ink possesses a shear-thinning property, a shear rheometer was used to collect information on the viscosity of the material as a shear rate is applied. In order to determine whether the shear-thinning property was caused by the polymer blend or the UiO-66 in ethanol, they were also tested.

Figure 4.14 shows the variation of shear rate as a function of viscosity for the direct-write ink and its constituent parts: polymer blend and UiO-66 EtOH. All samples display a fall in viscosity as shear rate increases, with the UiO-66 in ethanol possess the largest viscosity change. The polymer blend is displaying relatively minimal change as shear rate is increased, this could be because the sample is much more viscous, and a higher shear rate may be required. However, the shear rate was not tested above 100 s^{-1} as it caused samples to be expelled from the sample holder.

Demonstrated in Figure 4.15, is the expected results if the direct-write ink was a Newtonian fluid or a shear-thickening material. The Newtonian fluid, such as water, would show no increase or decrease in viscosity as shear rate increased, conversely a shear-thickening material, such as a colloidal mixture of cornflour, would increase in viscosity on increase of shear rate. Therefore, all 3 materials are showing shear-thinning character.

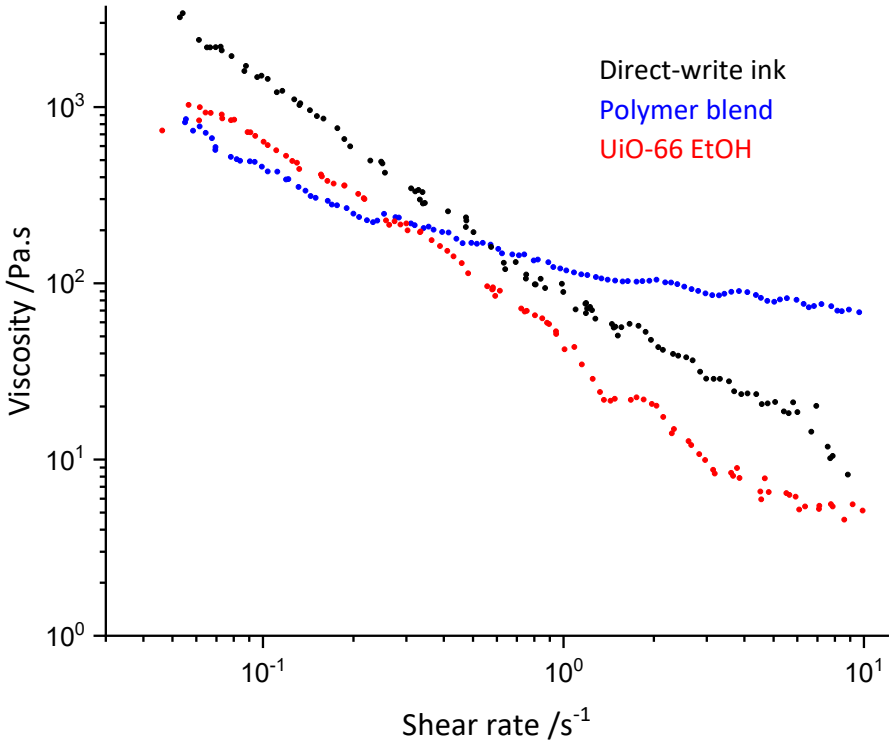

Figure 4.14: Log-log graph of viscosity over shear rate of UiO-66 polymer composite ink against shear rate.

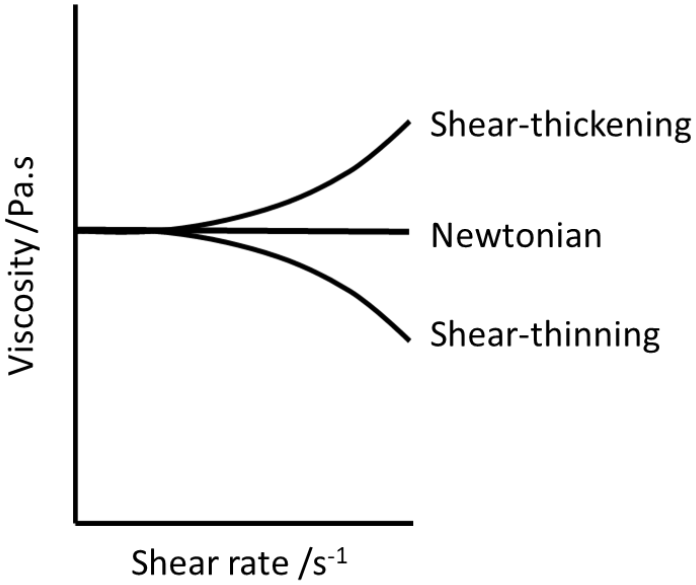

Figure 4.15: Demonstration of viscosities against shear rate if materials were shear-thickening, shear-thinning or Newtonian.

4.3.2.2. Thixotropy of direct-write ink

The previous section demonstrated that for the direct-write ink, on application of a shear rate, the viscosity decreases. However, 3DP requires a material to rapidly regain viscosity after extrusion to prevent the material wetting and spreading across the printed surface and retain the filamentary shape. This phenomenon is titled thixotropy and is defined as time-dependent shear-thinning. To investigate, viscosity was investigated as a function of time. Figure 4.16 shows the effects of a large shear rate applied rapidly to the direct-write ink. The viscosity dramatically drops and when shear is reduced the ink recovers its viscosity within seconds. This was repeated three times to demonstrate the efficient recovery of the ink over short bursts of time with no significant degradation of viscosity over the three events.

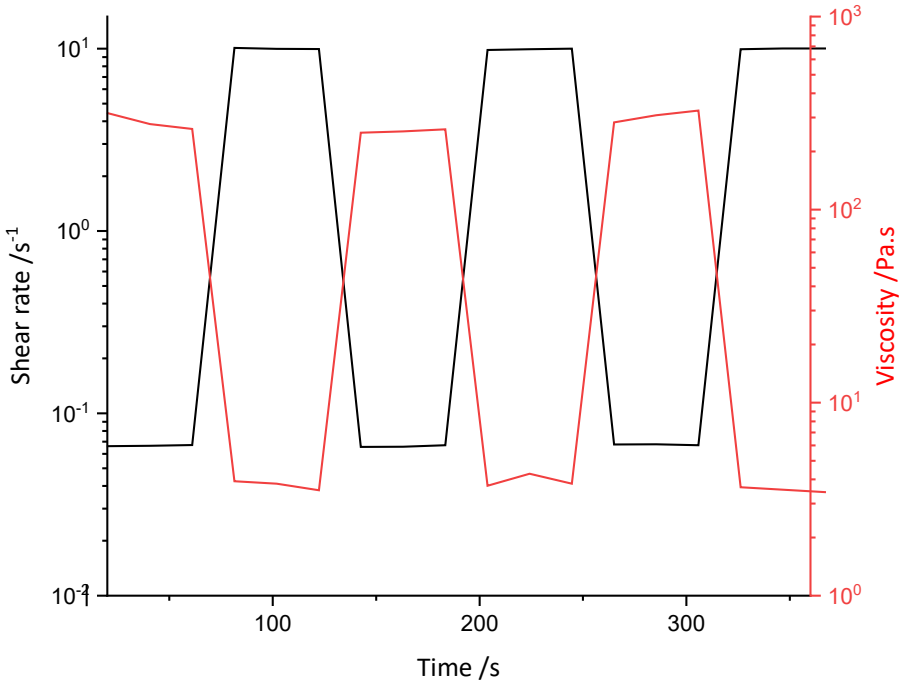

Figure 4.16: Graph of log shear rate and log viscosity over time, demonstrating thixotropy.

4.3.2.3. Elastic and viscosity modulus of the direct-write ink

Rheology can also be used to demonstrate the ability of a material to hold its shape after a deformation event, using the elastic (G′) and viscosity (G″) modulus parameters. Extruded material must possess a sufficiently high G′ to maintain the filamentary structure. Thus, when G′ is greater than G″, shape is maintained after extrusion. Conversely, when a shear stress is applied and G″ is greater, all retention of shape is lost, and the material spreads and wets the plate.

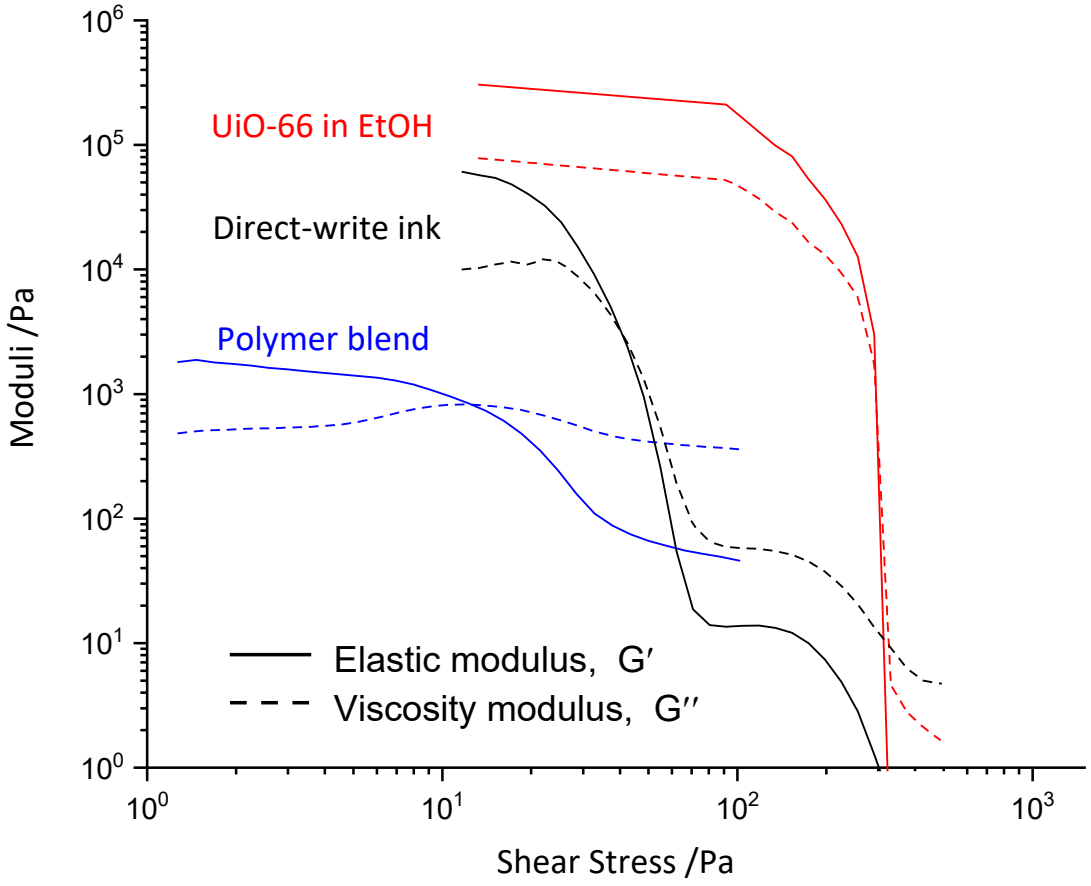

Figure 4.17: Log-log graph of moduli over shear elastic and viscosity moduli as a function of shear stress for varying components.

Figure 4.17 shows the application of relatively weak shear stress resulted in G′ being maintained for all three materials. Results preceding 10 Pa were not collected for UiO-66 polymer composite ink and UiO-66 EtOH due to the plate slipping on the sample causing erratic results. The polymer blend (Section 4.5.1) displayed a loss of the elastic modulus when there was a shear greater than 10 Pa was applied, whereby G″ was greater and all shape retention was lost.

UiO-66 EtOH (Section 4.5.1) displayed a more dramatic loss of G′ at a higher shear stress, indicating its ability to hold shape at greater shear stress. Unsurprisingly, the direct-write ink displayed two shear stress events, indicative of the two components – polymer blend and UiO-66 in EtOH. Incidentally, this confirmed that the viscoelastic properties of the direct-write ink were slightly controlled by the polymer blend. The MOF (UiO-66) was however acting as the foremost rheology modifier by displaying the largest drop in moduli as shear stress was applied.

4.3.3. 4D printing and physical properties

Once the direct-write ink had been formulated and mixed it was placed into a syringe and sealed, to stop excess evaporation of solvent. As discussed in the setup of the 3D printer, the syringe was covered in aluminium foil to stop curing in the syringe, there was no heated bed and the setup was enclosed in a black plastic which has a continuous flow of nitrogen. Prior to printing the software was loaded with a prepared G-code (Shown in the experimental chapter). Earlier experiments, up until the successful shapes shown in Figure 4.19 and Figure 4.20, faced a multitude of problems to overcome:

- Over/under extrusion
- Unsuccessful overhang
- Increase in material being extruded when material was running low
- Limited amount of material loaded into the syringe

On the Vellemen K8200 3D printer a stepper motor operates the rate at which the syringe extrudes, which was ultimately controlled by the G-code. The value on the G-code was adjusted to allow a smooth flow of material. However, it was noted that if you programmed the motor to stop extrusion and then restart, it would result in a build-up of material being released. This was caused by the material in the syringe regaining its high-viscous nature after the initial shear event and requiring a larger force to make the material flow. The top and start of material extrusion is a very common event seen in 3D printing, however for this material it required a continuous

extrusion with no stopping. Inspiration was taken from continuous line drawings, whereby an image is drawn without the pen lifting from the paper. These images are 2D and so a special shape had the be designed to allow continuous extrusion. A structure that could be printing continuously was a woodpile (Figure 4.19).

Another problem that had to be resolved was determining the maximum gap between extruded filament to allow overhang. Overhang, in 3D printing, is any part of a print that extends outwards beyond the previous layer, with no support. It is a useful phenomenon that can bridge two sections, which in the case of the 4D printed UiO-66 polymer composite is useful as it allows for a maximum surface area to be reached. There is a maximum gap to overhang, which is different dependent on material and printing conditions. Figure 4.18 demonstrates three two-layer prints, the first two images represent what happens if the gap between filaments is good. The final image shows what happens if the gap is too large and the filament appears to sag. The maximum gap achievable for a print with this material was 2.14 mm.

Figure 4.18: Demonstrating overhang

As the syringe filled with material was nearing empty the flow of material would increase. This was due to the same force being applied onto the syringe with less material to resist. This phenomenon coupled with the limited capacity of the syringe meant printing was limited to around 40 mL of material. The final shape was a continuously printed woodpile, as demonstrated in Figure 4.19. The woodpile shape was 15 × 5 × 4 cm (L × W × H) comprising 8 layers of self-supporting filament.

After extrusion and UV irradiation of the direct-write ink, the 3D shape was formed and named herein ‘4D printed UiO-66 polymer composite’.

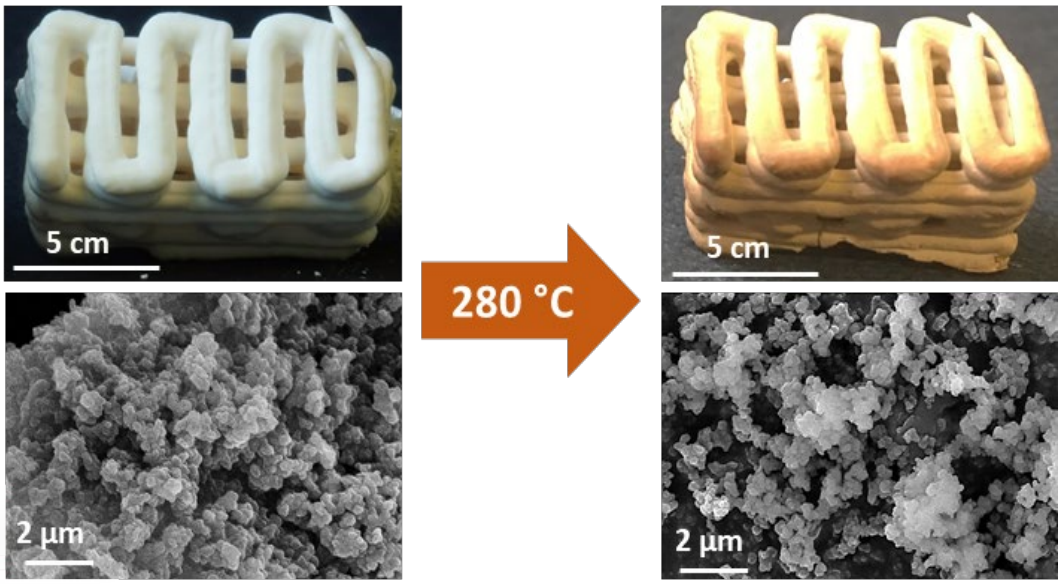

Figure 4.19: 4D printed UiO-66 polymer composite in a wood pile shape and respective SEM image (left). 4D printed UiO-66 polymer composite (calincated) and respective SEM image (right).

The 3D printer, as illustrated in Figure 4.20, can also recreate other designs such as a twisted star shape shown in the left image. This also demonstrates the inks ability to generate overhang as the shape is rotated slightly.

To activate the MOF-based structure it was calcined in an open-air furnace for 30 minutes at 280 °C. By placing in the furnace, any polymer blocking the pores was destroyed to leave a porous structure whilst retaining key physical properties. This was hereafter called '4D printed UiO-66 polymer composite (calcined)'.

Figure 4.19 displays optical and SEM images of the UiO-66 polymer composite before and after processing. Upon calcination the 4D printed structure retained its shape, structural integrity and demonstrated an increase in porosity post calcination, with some charring of the shape observed. In compressive testing the Young's modulus was found to be 24 ± 2 MPa and 31 ± 5 MPa before and after processing respectively. Statistically, there was no difference between the two results, but it could be theorised that there was a small difference in mechanical properties due to the structure still containing a small amount of polymer material gluing the UiO-66 MOF together. So the compressive strength measured may be due to the high compressive strength of the UiO-66 MOF over the polymer.[13]

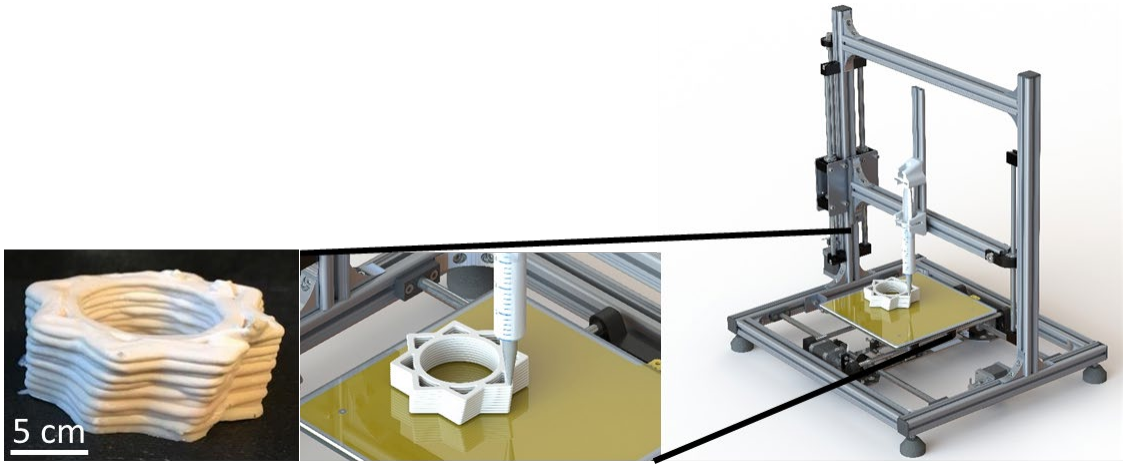

Figure 4.20: Autocad rendered image of Vellemen K8200 3D printer with syringe, extruding paste into the desired shape.

4.3.4. Specific surface area of the 4D printed polymer composite (calcined)

The 4D printed polymer composite (calcined) should have an increased porosity. To quantitively measure the porosity the surface area and pore volume the material was investigated by BET. BET works by measuring the adsorption and desorption of a N_2 at a standard temperature over a variable pressure (Section 4.5.7). To establish the success of the 4D printed calcined product it was compared to UiO-66 MOF powder. The N_2 adsorption-desorption isotherms shown in Figure 4.21 follow the same characteristic shape for both materials. The characteristic shape displayed indicates the microporous and mesoporous nature of UiO-66. Indicative of a micropore (less than 2 nm) character (type I isotherm) is a sharp rise at low partial pressure. The flat area corresponds

to a monolayer formation of gas molecules. At a higher partial pressure, a strong step rise was seen - a characteristic of capillary condensation where the pore fills with liquid instead of gas - indicating a mesoporous structure (type IV isotherm). Capillary condensation occurs when multilayer adsorption proceeds to a point where opposing walls meet and form a concave meniscus which enhanced adsorption and rapidly filled the mesopore.

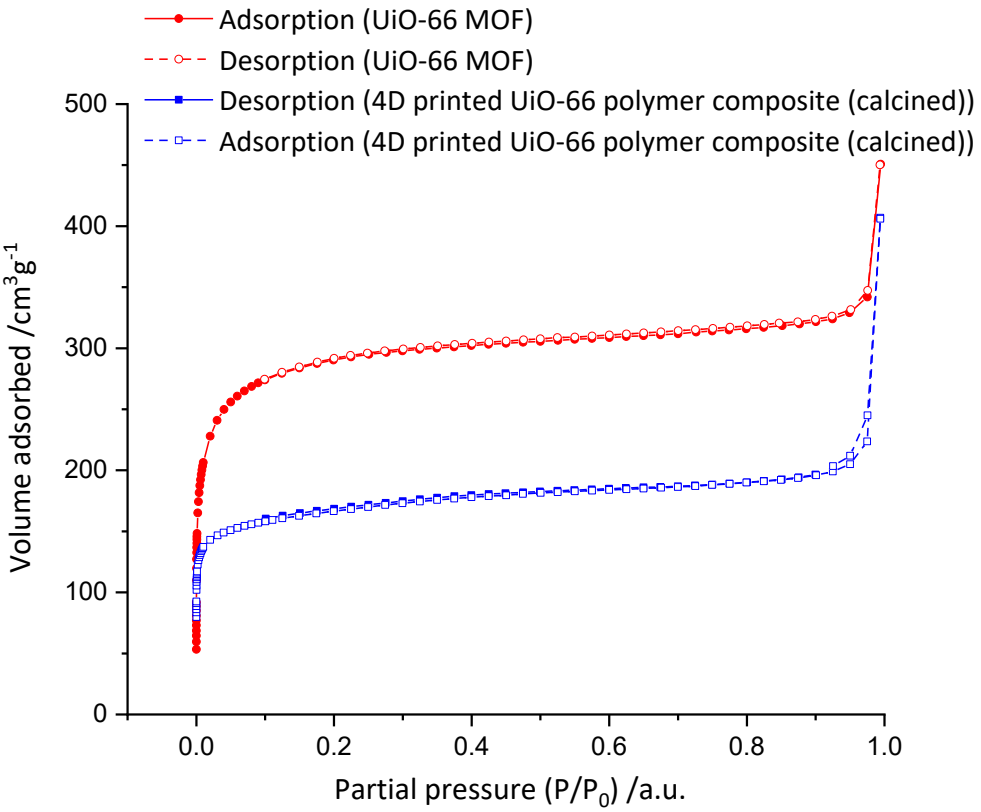

Figure 4.21: BET isotherm results for the UiO-66 MOF (red) and 4D printed UiO-66 polymer composite (calcined) (blue).

Table 4.1, displays the specific surface area and total pore volume of the UiO-66 powder< MOF and 4D printed UiO-66 polymer composite (calcined). Typically, UiO-66 MOFs are reported to have a specific surface area in the range of 1000 to 1300 m^2/g,[26] and the as-synthesised MOF displayed a specific surface area within this desired range, as shown in Table 4.1. The processed composite has a lower specific surface area compared to the UiO-66 MOF which is expected as the polymer could block some porosity within the MOF. However, the specific surface area reported here is higher than other UiO-66-polymer composites currently reported at 430 ± 1 m^2g^-

[1] and 511 ± 10 m^2g^{-1}.[11,27] This high specific surface area lends itself to catalytic applications, to be demonstrated later in Section 4.3.11.

Table 4.1: BET analysis of UiO-66 and 4D printed UiO-66 polymer composite (calcined)

BET Analysis	Specific surface area, m^2 g^{-1}	Total pore volume, cm^3 g^{-1}
UiO-66 MOF	1106	0.51
4D printed UiO-66 polymer composite (calcined)	633	0.32

4.3.5. Impact of processing on the crystallinity of UiO-66

4D printed UiO-66 polymer composite (calcined) shows approximately half the specific surface area of UiO-66 MOF. The cause of this decrease has not yet been investigated but a potential cause could be partial degradation of the MOF during calcination, particularly around the pore openings. Although the UiO-66 present in the composite is known to have a high shear modulus of 13.7 GPa,[13] it is not known if the MOF is still intact after the process of mixing, UV irradiation and calcination. To examine the crystallinity, the prepared UiO-66-based materials were examined by powder X-ray diffraction (PXRD). Figure 4.22 (black & red) represents the typical XRD diffraction pattern of simulated and as-synthesised UiO-66. The characteristic diffraction peaks of UiO-66 are observed at 2θ = 7.38, 8.52, 12.06, 17.04, 25.34, 28.14, 29.78 and 39.74 °, which are consistent with the reported literature and also the simulated pattern from CCDC deposition number 733458.[28]

Figure 4.22 (blue), displays peaks matching to the experimental and simulated UiO-66 MOF. This suggests that UiO-66 retains crystalline structure after the process of mixing, UV irradiation and calcination. However, the peaks displayed on Figure 4.22 (green), are two broad peaks observed at 2θ≈ 8 and 26 °, although they are broad, they are consistent with peaks of UiO-66. These broad

peaks are due to a poorly crystalline product of the 3D printed UiO-66 polymer composite and the polymer scattering incident x-ray making it difficult to detect the MOF.

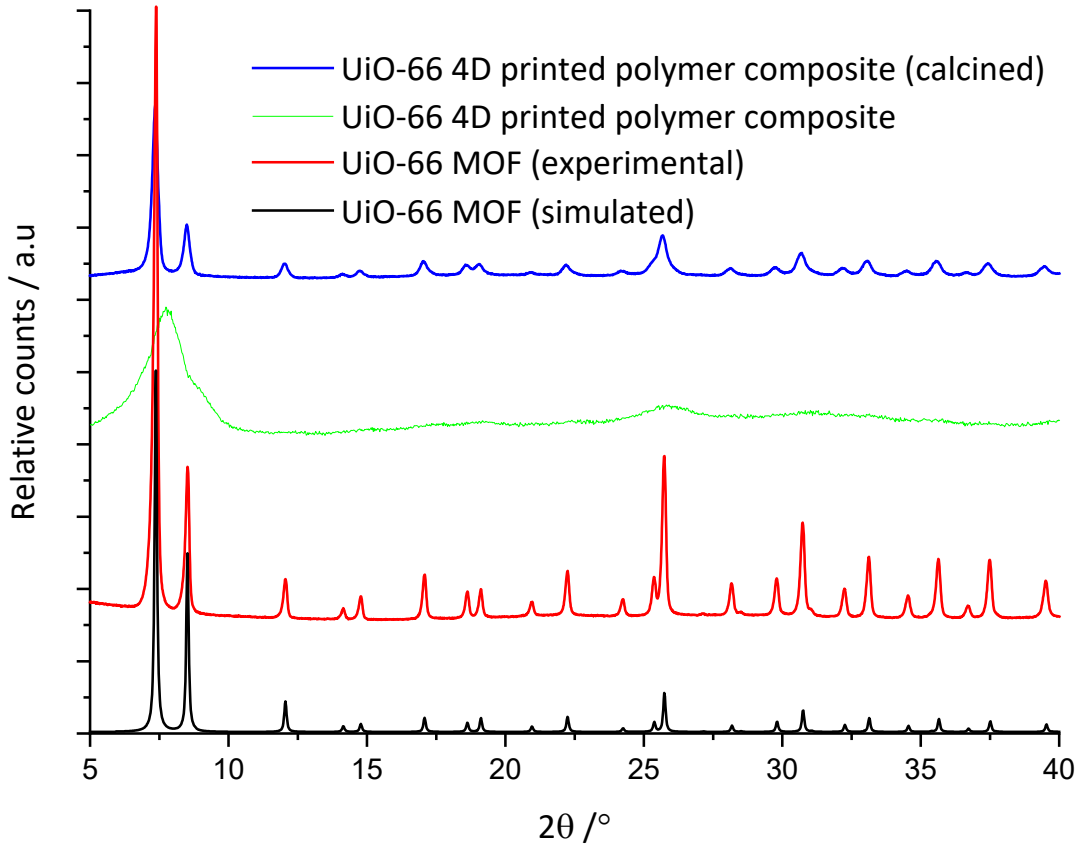

Figure 4.22: PXRD patterns of the UiO-66 MOF (red), UiO-66 4D printed composite (green) and UiO-66 4D printed composite post furnace treatment (blue); all samples show that the structure of UiO-66 is retained.

4.3.6. Detecting the effect of free radical polymerisation.

FTIR-ATR is a good technique for viewing characteristic bond stretches and was used to chart the polymerisation of the acrylate by observation of the effects of free radical polymerisation. Displayed in Figure 4.23 is the free radical polymerisation of one photoinitiator used in the direct-write ink with TMPPTA. The figure displays the breaking of the bond by UV irradiation creating two free radical compounds which propagate the polymer further until termination, whereby two radicals form a new bond and stopping further polymerisation. As can be noted there is a distinct lack of vinyl groups in the terminated polymer and as such would not be expected to be viewed by FTIR-ATR.

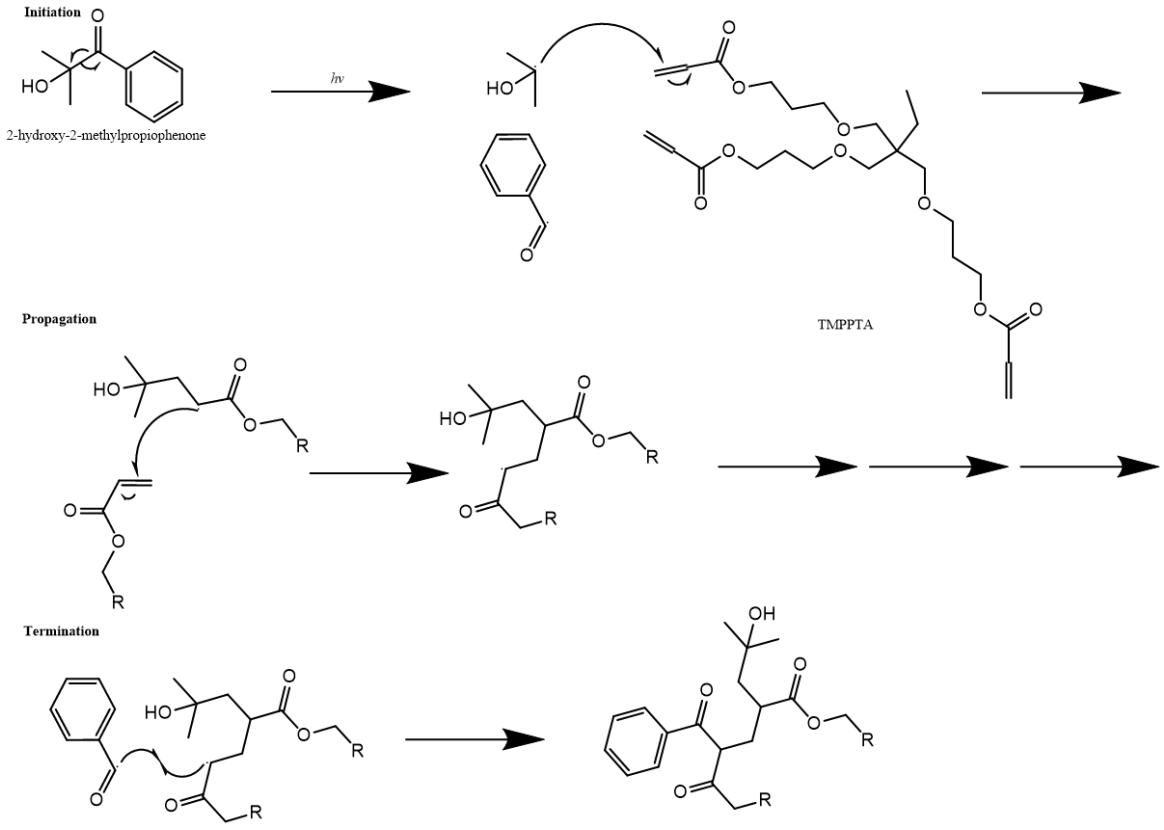

Figure 4.23: Free radical polymerisation of 2-hydroxy-2-methylpropiophenone and TMPPTA to chart the loss of the vinyl group.

The spectrum for direct-write ink (Figure 4.24, purple), represents the UiO-66 MOF mixed with two acrylates and photoinitator blend (Section 4.5.3). After exposure to UV radiation, (Figure 4.24, green) the vinyl groups presented at 900 and 2975 cm^{-1} are lost due to crosslinking and the broad peak at 3250 cm^{-1} fades as the photoinitiator is used up in free radical polymerisation. Additionally, two sharp peaks at 1100 and 1200 cm^{-1} due to the photoinitiator are lost as polymerisation occurs indicating this is used up in the process.

The as-synthesised UiO-66 MOF (Figure 4.24, red), displays peaks at 1100, 1200, 1350, 1550 and 1600 cm^{-1} throughout the full range of processing however a peak at 1650 cm^{-1} cannot be observed after calcination as the MOF becomes dehydroxylated.[29]

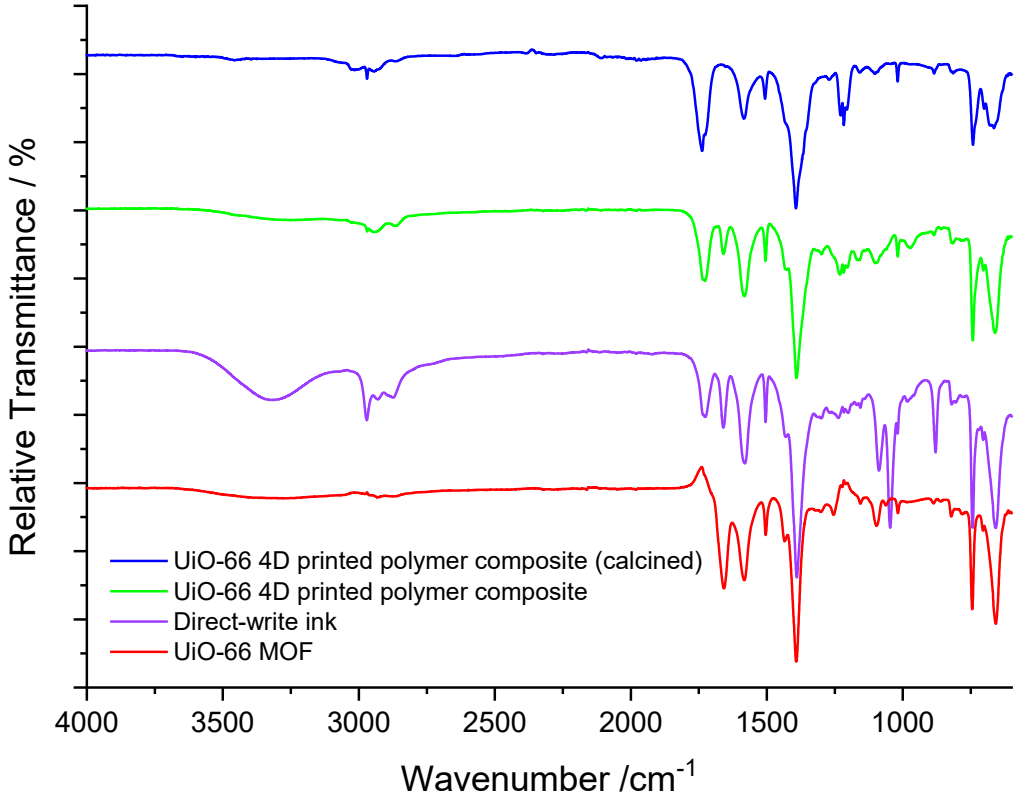

Figure 4.24: FT-IR spectra of the UiO-66 MOF (red), direct-write ink (purple), 4D printed UiO-66 polymer composite (green) and 4D printed UiO-66 polymer composite (calcined) (blue); all samples show that the structure of UiO-66 is retained.

4.3.7. Thermal stability of 4D printed UiO-66 polymer composite

Thermogravimetric analysis (TGA) was performed to determine any breakdown of UiO-66 MOF or 4D printed UiO-66 polymer composite when calcined by recreating the effects by isothermal analysis at 280 °C. When the 3D printed UiO-66 polymer composite is placed in the furnace, it is only exposed to elevated temperatures for 30 minutes. To see the full effects in the TGA the time was extended to 200 minutes.

As shown in Figure 4.25, the UiO-66 MOF displayed a weight loss of approximately 20% within the first 60 minutes. This could be attributed to many factors including: the loss of physiosorbed water, dehydroxylation of the $ZrO_4(OH)_2$ clusters,[30] decomposition of excess ligands in pores, and partial decomposition of linkers within the MOF structure.[31] The 3D printed UiO-66 polymer composite (Figure 4.25, blue), displayed two steps of dramatic weight loss in the first 60 minutes. The first weight loss could be attributed volatile components used in the processing such as

trapped solvent, photoinitiator and isobornyl acetate but also the partial destruction of the polymer network. The second step runs in parallel to the UiO-66 degradation and so could be due to similar effects as above. No further significant weight loss occurred during the 200-minute run at 280 °C.

4.3.8. Composition of 4D printed UiO-66 polymer composite

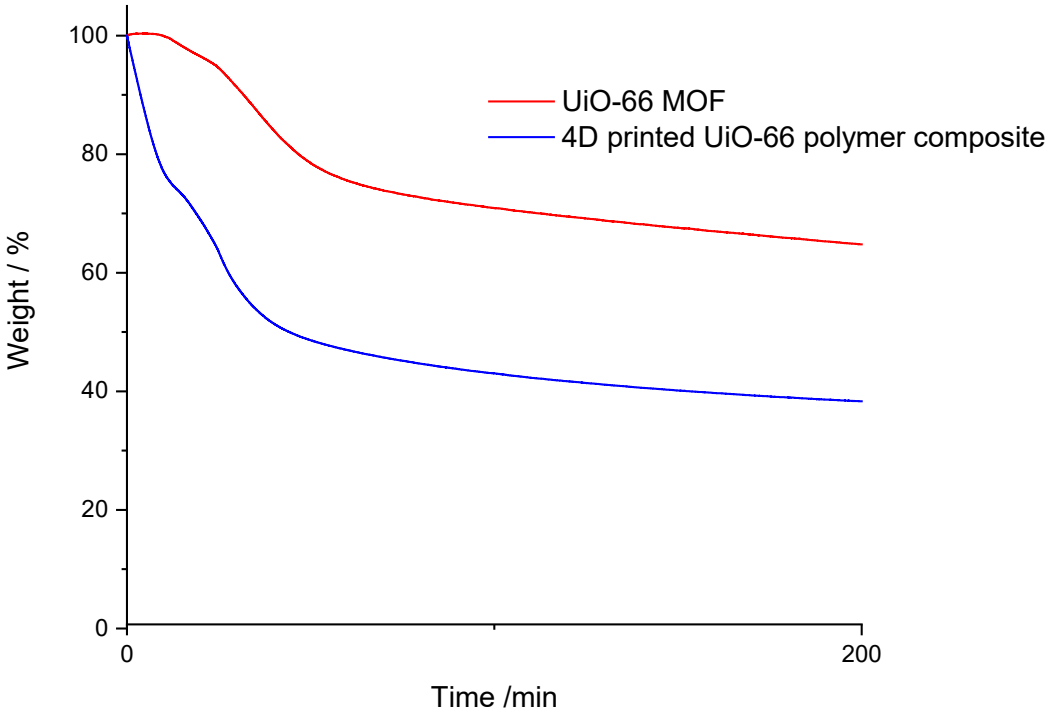

Figure 4.25: TGA isotherm at 280 °C for 200 minutes under an airflow (30 mL min^{-1}) of the UiO-66 MOF (red) and the 4D printed UiO-66 polymer composite (blue)

The exact composition of the 4D printed UiO-66 polymer composite (calcined) is unknown. Further TGA can be carried out to confirm the amount of MOF and polymer present. As the composite is a complex mixture of components, four experiments were completed involving the UiO-66 MOF, cured polymer blend, 3D printed UiO-66 polymer composite and the 4D printed UiO-66 polymer composite (calcined).

As shown in Figure 4.26 (red), there was a total weight loss of 63.8% from 30 – 700 °C for the UiO-66 MOF. The weight loss step can be attributed to the release of physiosorbed water, dehydroxylation, excess ligand and partial decomposition of linkers up to 300 °C. From 500 °C onwards the UiO-66 organic framework fully decomposes leaving stable and inert ZrO_2.

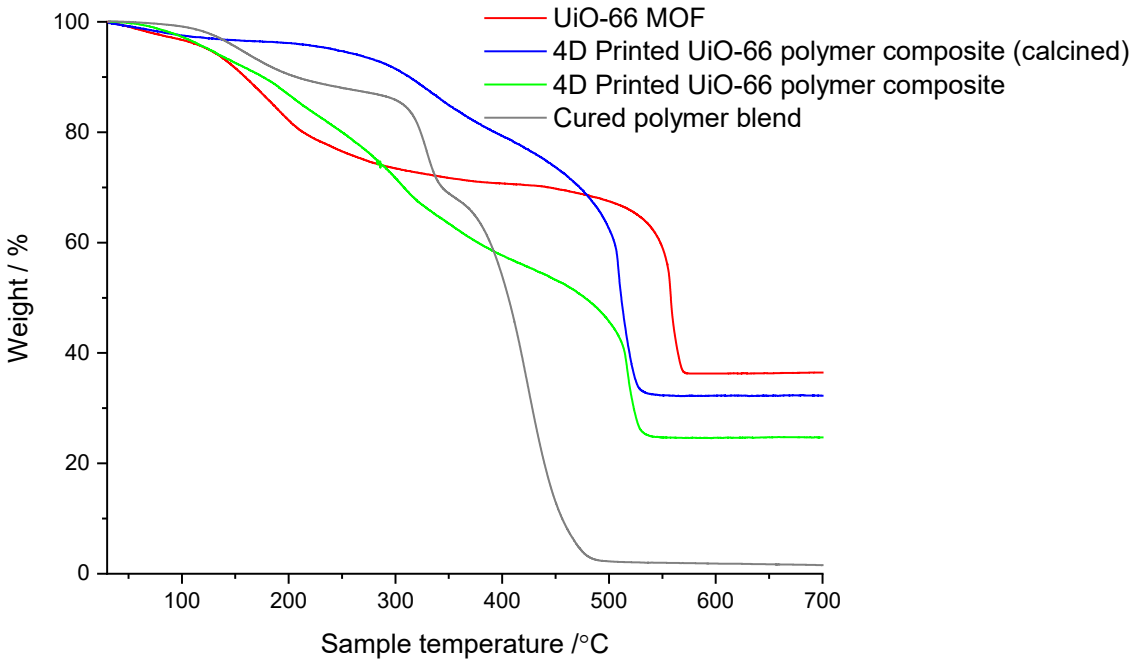

Figure 4.26: TGA isotherm at 30-700 °C under an airflow (30 mL min-1) of the UiO-66 MOF (red), 4D printed UiO-66 polymer composite (calcined) (blue), 4D printed UiO-66 polymer composite (green) alongside the cured binder mixture (black) of TMPPTA, Ebecyrl 8413® with PI mixture

The cured polymer blend contains Ebecryl 8413®, TMPPTA and the photoinitiator blend (Section 4.5.2). Figure 4.26 (black) shows three significant weight steps for the polymer blend. The first weight loss from 30 – 250 °C could be attributed to the release of water, photoinitiators and isobornyl acetate. The second weight loss from 250 – 350 °C could be due to less thermally stable photopolymer TMPPTA degrading. The third weight loss from 350 °C could be due to the degradation of Ebecryl 8413®. The TGA was performed under air and it can be expected the remainder is carbonised material.

The 3D printed UiO-66 polymer composite (Figure 4.26, green) exhibited a weight loss up to 400 °C accumulating the loss from the MOF and polymer blend. A final sharp weight loss was observed after 500 °C, because of the organic framework decomposing, leaving inert ZrO_2 and a remainder of carbonised material in the crucible.

The 4D printed UiO-66 polymer composite (calcined) (Figure 4.26, blue) displayed a slight weight loss up to 400 °C which could be attributed to the unbound water taken into the UiO-66

MOF after calcination. The weight loss step at 400 – 500 °C was the thermal degradation of the polymers, leaving inert ZrO_2 and carbonised material in the crucible.

It is difficult to confirm the composition of the 3D printed UiO-66 polymer composite as the weight losses of the cured polymer blend and UiO-66 MOF overlap below 300 °C. By calculation the amount of ZrO_2 left in the crucible may give insight to the amount of MOF which may have been present.

4.3.9. Amount of MOF present in the MOF polymer composites

Importantly for catalysis the amount of MOF present in the composite will need to be identified, to be able to offer a direct comparison between UiO-66 MOF and composite. Theoretically, by utilising the masses used for the direct-write ink composition (Section 4.5.3) there should be 52% MOF and 44% polymer. The 4% leftover have been expected to be the photoinitiator and solvent.

TGA and ICP-OES were studied to determine the amount of MOF present in the composite before and after calcination. The data collected from TGA gives the percentage of ZrO_2 left over in the crucible, an assumption was made that only ZrO_2 remained and no carbonised material because of this the results will be higher than expected. The TGA data is also corrected to display the amount of Zr, by calculation from ZrO_2. ICP-OES was also used and is much more powerful technique and can detect the percentage of chemical elements to a ppm level.

Table 4.2 displays the amount of elemental zirconium present in UiO-66 MOF and percentage of MOF present in the processed composites as measured by TGA and ICP-OES.

Table 4.2: TGA and ICP-MS results for 4D printed UiO-66 polymer composite and 4D printed UiO-66 polymer composite (calcined), displaying results for ZrO_2 and elemental Zr.

	Thermogravimetric Analysis (TGA).		**Inductively Coupled Plasma – Optical Emission Spectroscopy (ICP-OES).**	
	Elemental Zr. Wt.%	% of MOF present	Elemental Zr. Wt.%	% of MOF present
UiO-66 MOF	25.9	-	27.982	-
4D Printed UiO-66 polymer composite	17.8	68.7	17.107	61.1
4D Printed UiO-66 polymer composite (calcined)	23.7	91.5	22.446	80.2

The percentage of MOF present for the 3D printed UiO-66 polymer composite was found to be 61.1% and 68.7% respectively for ICP-OES and TGA. Following the experimental protocol (Section 4.5.3) it would be expected to be 52% MOF present in the 3D Printed UiO-66 polymer composite, but this fails to consider particle aggregation and loss of polymer during processing. No strong conclusion can be drawn about the amount of MOF present as it could range from 52% - 68.7%.

After calcination the 4D printed UiO-66 polymer composite (calcined) expectedly shows a higher zirconium and MOF content by ICP-OES and TGA. As with the previous sample, the techniques fail to consider any particle aggregation, loss of polymer or variation in samples. But drawing on the ICP-OES data we can expect at least 80.2% MOF to be present.

4.3.10. Chemical stability of 4D printed UiO-66 polymer composite (calcined)

Catalysis testing may take place in a wide range of solvents from chlorinated, to polar or non-polar solvents. Prior to catalysis testing, the samples were tested to establish their viability and chemical stability in a range of solvent. This was achieved by the placement of a small amount of

sample in various solvents. A small amount of 4D printed UiO-66 polymer composite (calcined) was placed in a sample vial and left for two days in the solvent. The samples were not heated but were agitated in the vial. All samples, as shown in Table 4.3, remained stable, they showed no sign of dissolution or miscibility, and could be picked back out of the solution with a pair of tweezers. The notable high stability of the composite could be due to the combined effect of the high chemical stability of UiO-66,[32] and stability of cured polymer material. Nonetheless this highly stable composite shows good viability to be used in catalysis in various solvent systems. The limitation of this testing method is the brevity and lack of measurement, should this be repeated callipers would be used to measure swelling and weights would be recorded.

Table 4.3: Stability of 4D printed UiO-66 polymer composite (calcined).

Solvent	**Stability of 4D printed UiO-66 polymer composite (calcined)**
Ethanol	Stable
Methanol	Stable
Isopropyl alcohol	Stable
DCM	Stable
DMF	Stable
Acetone	Stable
Deionised water (pH 5.8)	Stable

4.3.11. Catalysis of methyl paraoxon

UiO-66 is known for its catalytic ability in the degradation of nerve agents and their simulants, however in its powdered form it requires filtering to collect the sample after catalysis. The application of the 4D printed UiO-66 polymer composite (calcined) overcomes this problem as it can be collected by tweezers after a reaction.

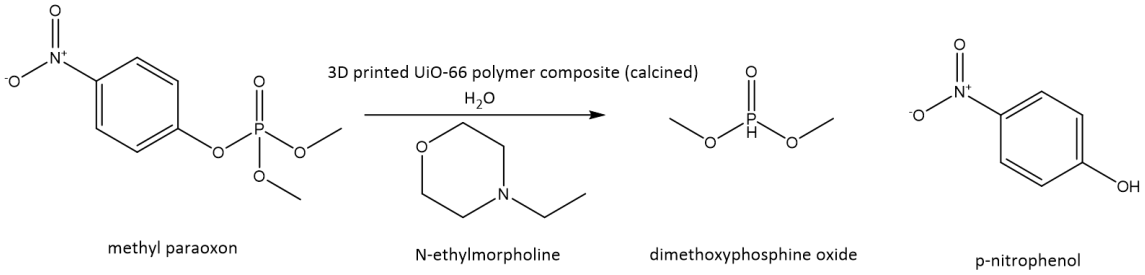

Figure 4.27: Scheme illustrating hydrolysis of methyl-paraoxon into dimethoxyphosphine oxide and p-nitrophenol, catalysed by 4D printed UiO-66 polymer composite (calcined).

Previous publications have utilised the reaction demonstrated in Figure 4.27,[33,34] whereby methyl paraoxon reacts with *N*-ethylmorpholine to produce dimethoxyphosphine oxide and *p*-nitrophenol. The reaction can be catalysed using UiO-66 MOF. Here 4D printed UiO-66 polymer composite (calcined) was added to the solution and the reaction was tracked by $^{31}P\{^{1}H\}$-NMR (Appendix). The results plotted in Figure 4.28 show that three tests were completed in total, the first was a blank with only methyl paraoxon and *N*-ethylmorpholine. The second used as-synthesised UiO-66 powder with *N*-ethylmorpholine. The third was the 4D printed UiO-66 polymer composite (calcined) with *N*-ethylmorpholine.

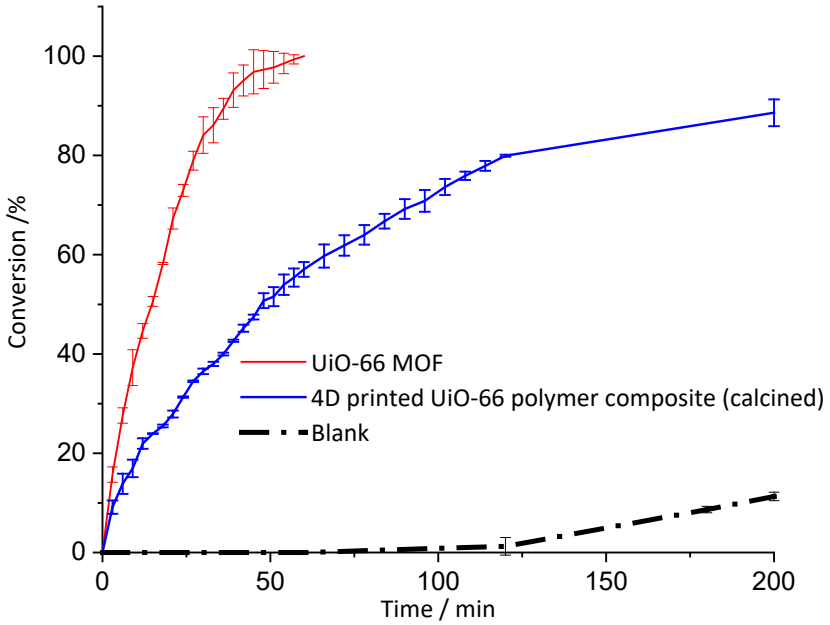

Figure 4.28: Hydrolysis of methyl-paraoxon in N-ethylmorpholine (black) using UiO-66 (red) and 4D printed UiO-66 polymer composite (calcined) (blue).

The graph displays concentration against time. The blank run demonstrates the slow reaction of methyl paraoxon with *N*-ethylmorpholine over time and reaches only 10% conversion after 200 minutes. The reaction for UiO-66 MOF powder had the fastest conversion rate and had a half-life ($t_{1/2}$) of 12 minutes. This improved on the literature values for UiO-66 (synthesised in DMF), of $t_{1/2}$ = 23-36 minutes.[35] The results for the same MOF when processed, printed and calcined to generate the 4D printed UiO-66 polymer composite (calcined) to have up to 80.2% MOF as demonstrated in Figure 4.29, in which the formation of yellow *p*-nitrophenol is observed. Overall, the calcinated composite has a $t_{1/2}$ four times less than the UiO-66 MOF. But is still able to act as heterogenous catalyst for the degradation of nerve agent simulant methyl-paraoxon with a conversion reaching 80% after 100 minutes.

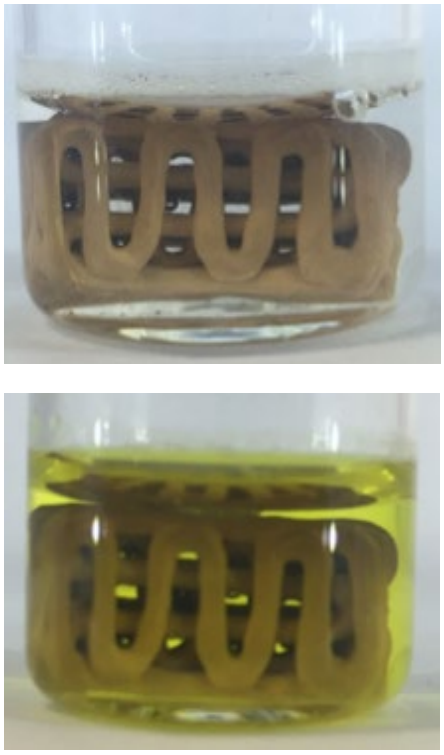

Figure 4.29: UiO-66 4D printed polymer composite (calcinated) in the water at t=0, and after catalysis at t=60 minutes, showing the generating of a yellow colour from the creation of p-nitrophenol.

4.4. Conclusion

In summary, UiO-66 was synthesised for use in a novel UiO-66-polymer composite that displayed promising rheological properties to function as a thixotropic direct-write ink practical for 3D

printing. The synthesised UiO-66 exhibited excellent crystallinity, thermal and textural properties that were retained throughout the harsh-processing. SEM and optical images revealed that the UiO-66 retained morphology and the 4D printed UiO-66 polymer composite (calcined) was stable with promising mechanical results. The 4D printed UiO-66 polymer composite (calcined) exhibited a micro and mesoporous structure with a high specific surface area of 633 m^2g^{-1} which was greater than current UiO-66 polymer composites. Furthermore, the UiO-66-polymer composite was employed as a catalyst for the degradation of nerve agent simulant – methyl paraoxon with a half-life of 48 minutes reaching 80% conversion at 100 minutes.

This fabrication technique demonstrates that by careful choice of 4D printable ink, it is possible to print catalytically active solids. The example here was for degradation of nerve agent simulant methyl paraoxon but this method could be used for other suitable MOFs unlocking a range of diverse applications.

4.5. Experimental

4.5.1. Definition of terms.

UiO-66 MOF: The synthesised UiO-66 MOF

UiO-66 EtOH: UiO-66 MOF (5 g) mixed with 7.5 mL ethanol, used for rheological measurements.

Polymer blend: A blend of TMPPA, EBECRYL® 8413 and photoinitiator blend as outlined in section 4.5.3.

Direct-write ink: Addition of UiO-66 to the polymer blend as described in 4.5.3.

4D printed UiO-66 polymer composite: As above formulation, after extrusion and exposure to UV light (365 nm).

4D printed UiO-66 polymer composite (calcined): 3D printed UiO-66 polymer composite after firing at 280 °C for 30 minutes and subsequently washed as outlined in 4.5.6.

4.5.2. Preparation of photoinitiator (PI) blend

The photoinitiator (PI) blend was produced by dissolving (*via* ultrasound bath) phenylbis (2,4,6-trimethylbenzoyl) phosphine oxide (0.5 g, 1.19 mmol) in 2-hydroxy-2-methylpropiophenone (2.0 g, 12.18 mmol).

4.5.3. Preparation of UiO-66 polymer composite ink

UiO-66 particles (5.0 g) were dispersed in a minimum amount of ethanol (7.5 mL), by means of sonication for 30 minutes. Afterwards the suspension was filled into a 25 mL Luer lock plastic syringe and the PI blend (0.38 g) was added and homogenised. To this mixture, EBECRYL® 8413 (3.27 g) and trimethylolpropane propoxylate triacrylate (TMPPTA) (0.962 g) were added and homogenised using an Ultra Turrax T18 mixer at 10,000 rpm for 3 minutes. The final ink was sealed and protected from light and stored at room temperature until used.

4.5.4. 4D printing of UiO-66 polymer composite

The UiO-66 ink was loaded into a 25 mL Luer lock plastic syringe fitted with a 16-gauge PTFE Luer lock needle. The syringe was positioned into the Velleman K8200 3D printer modified with a paste extruder. The 3D printer was placed in a black plastic casing through which a gentle stream of N_2 was flowed to decrease oxygen inhibition of polymer curing. G-code was created for the desired shapes and loaded onto K8200 Repetier-Host software, connected to the 3D printer. The sample was irradiated with 365 nm UV light during printing, which was kept 30 cm from the sample. The printed samples were then kept under UV irradiation for 3 minutes for post-curing.

4.5.5. 3D Printer

The Vellemen 8200 3D printer was purchased online and then modified with a paste extruder available from the same supplier. No further alternations were made.

4.5.6. Calcination of 4D printed UiO-66 polymer composite

3D printed UiO-66 polymer composite samples (or UiO-66 MOFs) were placed in a high purity alumina crucible and placed into a preheated furnace at 280 °C for 30 minutes. The heated samples

were then taken out and allowed to cool to room temperature before being washed with dichloromethane (DCM) and placed in a vacuum oven at 50 °C overnight.

4.5.7. BET

N_2 adsorption/desorption isotherm measurements at -196 °C were performed using an AutosorbiQ2-MP sorption instrument (Quantachrome Instruments, Boynton Beach, FL, USA). Prior to the measurements, samples were outgassed under vacuum at 150 °C for 12 h, unless otherwise indicated. The UiO-66comp sample was also outgassed under vacuum at 100 °C for 12 h. Apparent BET specific surface area, SBET, was determined via the BET equation using the Rouquerol et al. procedure for microporous adsorbents, and total pore volume was obtained at P/P_0 = 0.95 using the Gurvitch rule. Relevant pore size distribution was obtained from the adsorption branch of the isotherms by applying the kernel of (metastable) NLDFT adsorption isotherms, considering a polar surface and a cylindrical pore model. NLDFT micropore volume was determined using the same kernel. For comparison purpose, the micropore volumes were additionally determined using the tplot method in the range $0.15 \leq P/P_0 \leq 0.4$. The calculations were carried out using the ASiQWin software 5.0 provided by Quantachrome Instruments.

4.5.8. Catalysis of methyl-paraoxon using 4D printed UiO-66 polymer composite (calcined)

Hydrolysis experiments were carried out at room temperature. A solid sample of UiO-66 (2.5 mg, 6 mol.%) or post furnace 4D printed UiO-66 polymer composite (calcined) (2.7 mg, 92 wt.% of MOF) was added to an aqueous solution of *N*-ethylmorpholine buffer (0.45 M in 10% D_2O/H_2O, 1 mL) and shaken for 5 minutes. Added to the MOF suspension was dimethyl paraoxon solution (4 μL). The mixture was vigorously shaken for 10 seconds. The sample was transferred to an NMR tube whereby the catalysis was monitored *in-situ* by $^{31}P\{^1H\}$-NMR. The progress of the reaction was monitored with 3 minutes increments for the first 60 minutes, then 6-minute increments for the following 60 minutes and a final increment at 200 minutes. Control

experiments were conducted in an identical manner but in the absence of MOF material (background hydrolysis of agent). The half-lives were obtained by averaging duplicate experiments and plotting ln(concentration) versus time, as the reaction follows first order kinetics.

4.5.9. Nuclear Magnetic Resonance (NMR)

Nuclear Magnetic Resonance (NMR) is a spectroscopy technique commonly used to see the structure of organic molecules by observing local magnetic fields around atomic nuceli. It can be used to identify chemical environments and neighbouring molecules but also reaction dynamics. All NMR was run on JEOL ECZ 400S spectrometer, 31P{1H}-NMR spectra were recorded at 162.0 MHz and referenced externally to H_3PO_4 P = 0 ppm.

4.6. References

1 O. K. Farha, I. Eryazici, N. C. Jeong, B. G. Hauser, C. E. Wilmer, A. A. Sarjeant, R. Q. Snurr, S. T. Nguyen, A. Ö. Yazaydın and J. T. Hupp, *J. Am. Chem. Soc.*, 2012, **134**, 15016–15021.

2 B. M. Connolly, M. Aragones-Anglada, J. Gandara-Loe, N. A. Danaf, D. C. Lamb, J. P. Mehta, D. Vulpe, S. Wuttke, J. Silvestre-Albero, P. Z. Moghadam, A. E. H. Wheatley and D. Fairen-Jimenez, *Nat. Commun.*, 2019, **10**, 1–11.

3 J. A. Lewis and G. M. Gratson, *Mater. Today*, 2004, **7**, 32–39.

4 H. Thakkar, S. Eastman, Q. Al-Naddaf, A. A. Rownaghi and F. Rezaei, *ACS Appl. Mater. Interfaces*, 2017, **9**, 35908–35916.

5 No Title, www.markforgecd.com, (accessed 25 March 2020).

6 B. Van de Voorde, I. Stassen, B. Bueken, F. Vermoortele, D. De Vos, R. Ameloot, J.-C. Tan and T. D. Bennett, *J. Mater. Chem. A*, 2015, **3**, 1737–1742.

7 P. G. Yot, K. Yang, F. Ragon, V. Dmitriev, T. Devic, P. Horcajada, C. Serre and G. Maurin, *Dalt. Trans.*, 2016, **5**, 4283–4288.

8 H. Wu, T. Yildirim and W. Zhou, *J. Phys. Chem. Lett.*, 2013, **4**, 925–930.

9 J. H. Cavka, S. Jakobsen, U. Olsbye, N. Guillou, C. Lamberti, S. Bordiga and K. P. Lillerud, *J. Am. Chem. Soc.*, 2008, **130**, 13850–13851.

10 G. W. Peterson, A. X. Lu and T. H. Epps, *ACS Appl. Mater. Interfaces*, 2017, **9**, 32248–32254.

11 M. R. Armstrong, K. Y. Y. Arredondo, C.-Y. Liu, J. E. Stevens, A. Mayhob, B. Shan, S. Senthilnathan, C. J. Balzer and B. Mu, *Ind. Eng. Chem. Res.*, 2015, **54**, 12386–12392.

12 M. L. Pinto, S. Dias and J. Pires, *ACS Appl. Mater. Interfaces*, 2013, **5**, 2360–2363.

13 H. Wu, T. Yildirim and W. Zhou, *J. Phys. Chem. Lett*, 2013, **4**, 925–930.

14 J. E. Mondloch, M. J. Katz, W. C. Isley III, P. Ghosh, P. Liao, W. Bury, G. W. Wagner, M. G. Hall, J. B. Decoste, G. W. Peterson, R. Q. Snurr, C. J. Cramer, J. T. Hupp and O. K. Farha, *Nat. Mater.*, 2015, **14**, 512–516.

15 Y. C. Yang, *Acc. Chem. Res.*, 1999.

16 M. A. S. Khan, T. Bandyopadhyay and B. Ganguly, *J. Mol. Graph. Model.*, 2012, **34**, 10–17.

17 M. J. Katz, J. E. Mondloch, R. K. Totten, J. K. Park, S. T. Nguyen, O. K. Farha and J. T. Hupp, *Angew. Chemie - Int. Ed.*, 2014, **53**, 497–501.

18 A. M. Plonka, Q. Wang, W. O. Gordon, A. Balboa, D. Troya, W. Guo, C. H. Sharp, S. D. Senanayake, J. R. Morris, C. L. Hill and A. I. Frenkel, *J. Am. Chem. Soc.*, 2017, **139**, 599–602.

19 K. Evans, Z. C. Kennedy, B. W. Arey, J. F. Christ, H. T. Schaef, S. K. Nune and R. L. Erikson, *ACS Appl. Mater. Interfaces*, 2018, **10**, 15112–15121.

20 Y. Wang, L. Li, P. Dai, L. Yan, L. Cao, X. Gu and X. Zhao, *J. Mater. Chem. A*, 2017, **5**, 22372–22379.

21 X. Mu, T. Bertron, C. Dunn, H. Qiao, J. Wu, Z. Zhao, C. Saldana and H. J. Qi, *Mater. Horiz.*, 2017, **4**, 442–449.

22 N. A. Sears, P. S. Dhavalikar and E. M. Cosgriff-Hernandez, *Macromol. Rapid Commun.*, 2016, **37**, 1369–1374.

23 J. Sebastián, S. Manzano, Z. B. Weinstein, A. D. Sadow and I. I. Slowing, *ACS Catal.*, 2017, **7**, 7567–7577.

24 A. J. Wang, T. Paterson, R. Owen, C. Sherborne, J. Dugan, J. M. Li and F. Claeyssens, *Mater. Sci. Eng. C*, 2016, **67**, 51–58.

25 D. K. Patel, A. H. Sakhaei, M. Layani, B. Zhang, Q. Ge and S. Magdassi, *Adv. Mater.*, 2017, **29**, 1–7.

26 H. Furukawa, K. E. Cordova, M. O'Keeffe and O. M. Yaghi, *Science*, 2013, **341**, 974–988.

27 L. M. Pinto, S. Dias and J. Pires, *ACS Appl. Mater. Interfaces*, 2013, **5**, 2360–2363.

28 L. Zhou, X. Zhang and Y. Chen, *Mater. Lett.*, 2017, **197**, 167–170.

29 L. Valenzano, B. Civalleri, S. Chavan, S. Bordiga, M. H. Nilsen, S. Jakobsen, K. P. Lillerud and C. Lamberti, *Chem. Mater.*, 2011, **23**, 1700–1718.

30 F. Vermoortele, R. Ameloot, A. Vimont, C. Serre and D. De Vos, *Chem. Commun.*, 2011, **47**, 1521–1523.

31 G. C. Shearer, S. Chavan, J. Ethiraj, J. G. Vitillo, S. Svelle, U. Olsbye, C. Lamberti, S. Bordiga and K. P. Lillerud, *Chem. Mater.*, 2014, **26**, 4068–4071.

32 J. B. DeCoste, G. W. Peterson, H. Jasuja, T. G. Glover, Y. Huang and K. S. Walton, *J. Mater. Chem. A*, 2013, **1**, 5642–5650.

33 M. C. De Koning, M. Van Grol and T. Breijaert, *Inorg. Chem.*, 2017, **56**, 11804–11809.

34 G. W. Peterson, S.-Y. Moon, G. W. Wagner, M. G. Hall, J. B. Decoste, J. T. Hupp and O. K. Farha, *Inorg. Chem*, 2015, **54**, 9684–9686.

35 A. M. Ploskonka, S. E. Marzen and J. B. DeCoste, *Ind. Eng. Chem. Res.*, 2017, **56**, 1478–1484.

5. 3D Direct-Write printing of Metal-Organic Framework Gels

5.1. Introduction

3D printing relies on the rheological properties of a material to deform, to flow through a nozzle and reform. Typically, these material properties are added by the use of a rheology modifier; such examples include polylactic acid (PLA), polyurethane, and cellulose which display thermoplastic and thermosetting properties and silica, alumina or kaolin clay which display shear-thinning and shear-thickening properties. Many of these materials are very common in 3D printing, such as PLA and various clays, as such they make good matricies for a composite material. Examples of applications include PLA with copper nanoparticles which was used to produce an antibacterial filament while PLA with additional flexibile polymers was used to create an elastic filament. MOF composites have been fabricated in a similar fashion with several different rheology modifiers.

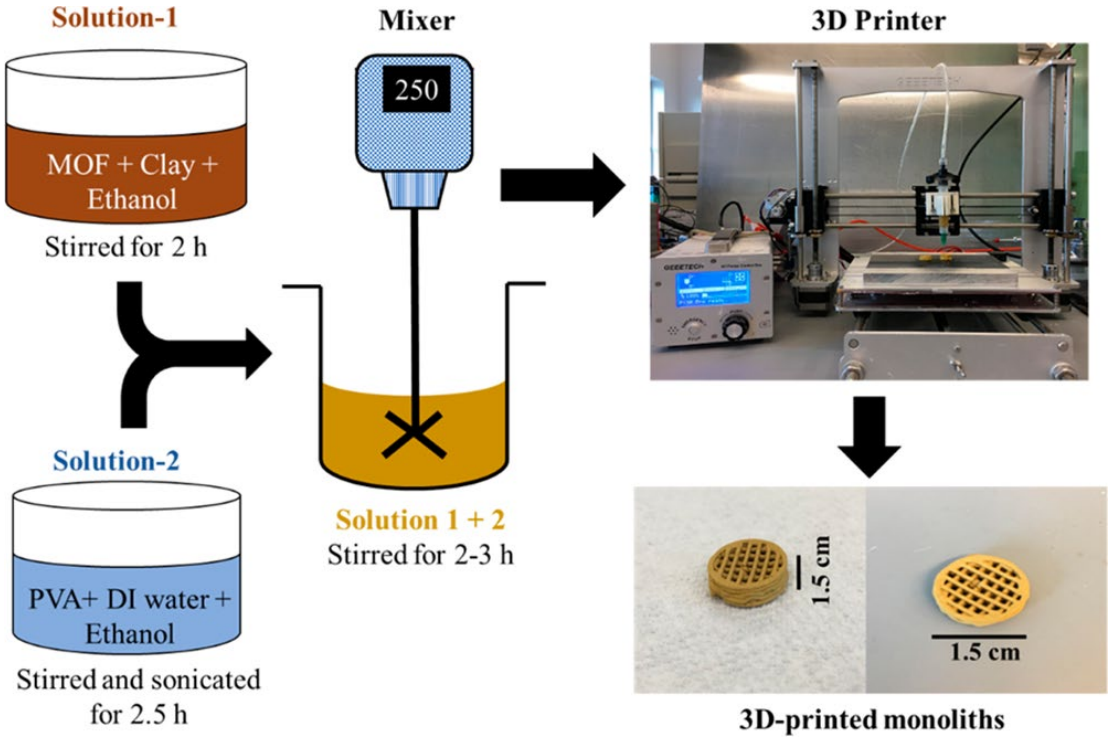

Figure 5.1: Schematic of the method used to create a inorganic-based MOF composite, for 3D printing. Reprinted with permission from Ref. [1] Copyright 2017 American Chemical Society.

Evans *et al.* reported the use of ZIF-8 in ethyl acetate mixed with PLA (an organic rheology modifier) dissolved in trichloromethane before the composite was cast into a thick film producing a MOF composite displaying thermoplastic properties.[2] An inorganic-based MOF composite, shown in Figure 5.1, was created by mixing the MOF with bentonite clay in ethanol before the addition of poly(vinyl alcohol) (PVA) in water and ethanol, before being extruded by direct-write ink 3DP.[1] Current fabrication methods are however time intensive; relying on long mixing times, use of chlorinated solvent and the evaporation of volatile solvents to create the final composite. Also, there is no guarantee with these methods that the MOFs internal porosity is not compromised, reducing the efficiency of the MOF in the desired application. A potential solution would be a material that is both MOF and rheology modifier, negating the need for additional material and reducing fabrication time. This material currently exists and is titled a MOF-gel.

MOF-gels are synthesised by fine tuning the nucleation rate of the MOF crystals. If nucleation is too fast the result is an amorphous metal-organic gel, too slow and the MOF is precipitated from solution. A balance must be struck between a MOF and metal organic gel resulting in a MOF-gel. The MOF-gel displays interesting and useful material properties such as thixotropy while still containing MOF particulates which may have uses in many applications. Work undertaken by Bennett *et al.* has identified a suitable formulation for a UiO-66 MOF-gel that gives a good thixotropic material, tested by the simple means of the inversion of a sample vial.[3] However, the extent of viscoelasticity properties remains unverified for UiO-66 MOF-gel and many others.[4–6] If a MOF-gel was to be used in an application such as 3DP, the extend of the materials ability to flow and reform through a nozzle must be understood to fully exploit the material. A MOF-gel contains nanoparticles of MOFs, which inherently have a large surface area. However, when using the as-synthesised MOF-gel there is no porosity as the MOFs contain unreacted reagents and solvent, to be able to access these nanoparticles a process needs developing to overcome the poor processability of MOFs. This will lead to greater application for the MOF overall.

In this chapter the viscoelastic properties of MOF-gels are investigated, and the method development needed to create a novel MOF-gel composite suitable for the fabrication method of direct-write 3DP.

5.2. Chapter Overview

This chapter introduces MOF-gels - UiO-66, amino-UiO-66 and ZIF-8 and explores their thixotropic properties. The objective of the chapter being to fabricate the MOF-gel to produce a novel composite direct-write ink, with a further demonstration of 3D printability. The novel MOF-gel-based direct-write ink will then be investigated for porosity and use in applications of catalysis and dye adsorption.

5.3. Results and Discussion

A MOF-gel can be defined as a gel-like colloidal suspension of MOF nanoparticles in a solvent matrix.[3] They are the product of a one pot synthesis method, Figure 5.2, involving the use of an excess of metal salt and minimal solvent in a sealed vessel to yield a gel-like material. The synthesis is easily scalable to produce sample from between 5 mL to 300 mL, as shown in Figure 5.3.

Table 5.1 shows a list of reagents for a typical MOF (UiO-66) and MOF-gel synthesis to demonstrate the differences. Traditional solvothermal methods for MOFs typically have an equal (or nearly equal) stoichiometry of metal to ligand to create a solid powder, in an excess of solvent.

Figure 5.2: Autoclaves used for MOF-gel solvothermal synthesis.

Table 5.1: Table of two solvothermal synthesis of a MOF-gel and MOF.

	Zirconyl chloride	**Terephthalic acid**	**N, N - Dimethylformamide**	**Yield**
MOF-gel	3.22 g 18.0 mmol	2.41 g 14.5 mmol	60 mL	White Gel
MOF	2.58 g 14.5 mmol	2.41 g 14.5 mmol	480 mL	White Crystalline powder

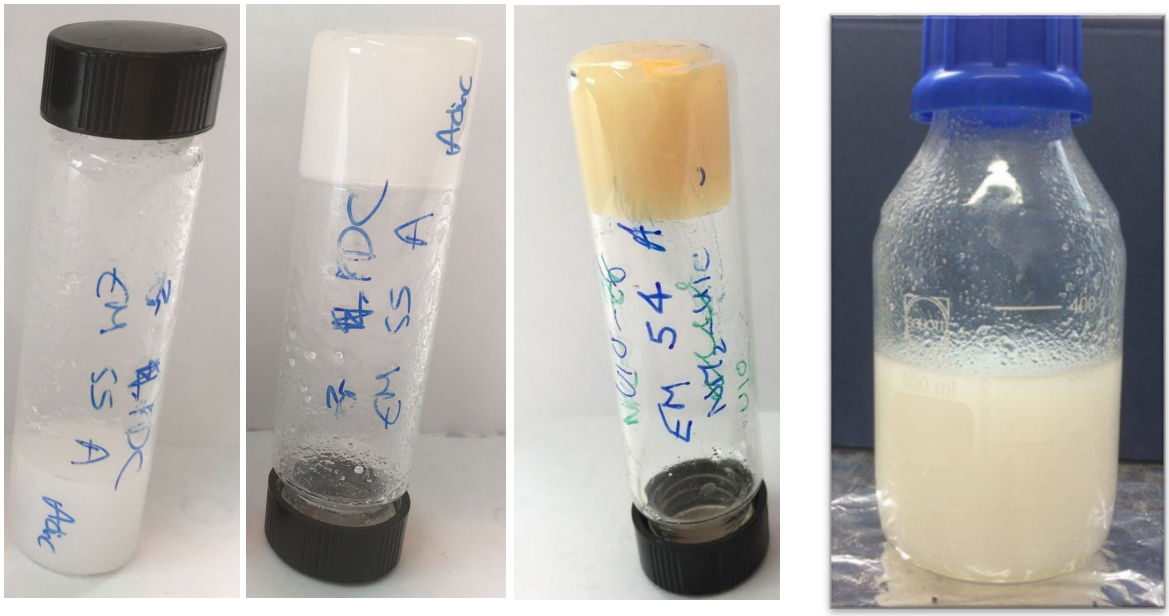

Figure 5.3: MOF-gel after synthesis displaying the thixotropic qualities. From left to right: UiO-66 MOF-gel, inverted UiO-66 MOF-gel, UiO-66-NH_2 MOF-gel, upscaled synthesis of UiO-66 MOF-gel.

The as-synthesised crystalline solid MOF powder is difficult to process and traditionally packed or compressed into shape which hinders processability. To overcome this limitation solid MOF powders can also be mixed with a rheology modifier, extruded and cured into a 3D shape. MOF-gels, however, are not suited to compression or being compacted and instead display thixotropic properties directly from the synthetic pot without the need for a rheology modifier.

When carrying out the synthesis of the MOF-gel, there are physical differences between a MOF-gel and metal organic gel. To confirm if the MOF-gel had been synthesised a series of characterisation methods were carried out to identify if the synthesised gel was either MOF, MOF-gel, or metal organic gel. The characterisation of a MOF-gel over a metal organic gel can be determined by the crystallinity of the sample.

5.3.1. Confirmation of crystalline UiO-66

Following synthesis, PXRD patterns were recorded to confirm the formation of the UiO-66 MOF-gel. Figure 5.4 shows the diffraction patterns for the MOF-gel, and simulated pattern of UiO-66 MOF, from CCDC data file number 4512072.

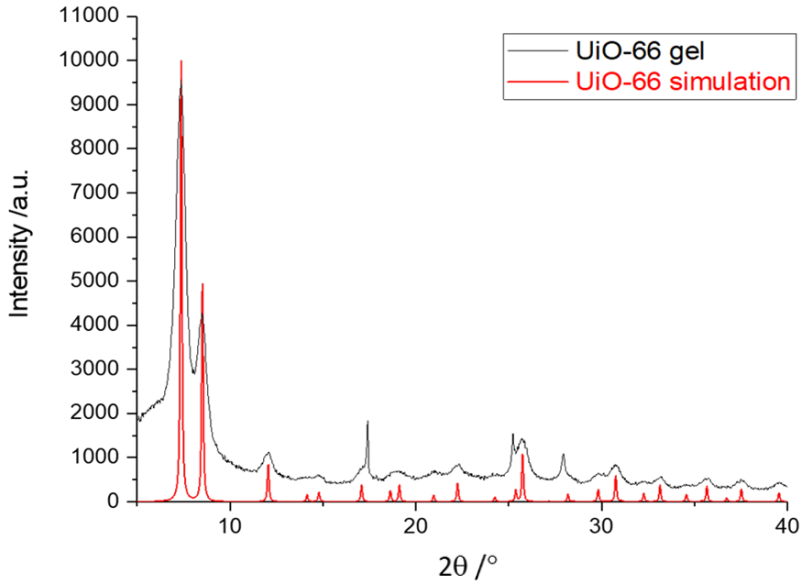

Figure 5.4: PXRD pattern of UiO-66 MOF-gel and UiO-66 simulated pattern.

The resulting PXRD pattern for the UiO-66 MOF-gel shows broad but characteristic diffraction peaks of UiO-66 at 2θ = 7, 8.5, 13 and 17 °. These peaks match with the simulated UiO-66 pattern, however, the peaks for the UiO-66 MOF-gel are broader than the simulated pattern, this almost certainly signifies MOF nanoparticles. This phenomenon is called Scherrer broadening (or particle size broadening) and is caused by incomplete cancellation of x-rays not in phase due to crystallinity being on such a small length scale. If the MOF-gel sample contained longer length scale MOF, the peaks would be sharper and similar to the simulation pattern.

The size of particles was calculated using the Scherrer equation, run within the PXRD software, which displayed a crystalline domain size of 10 to 15 nm. As with previous chapters SEM was used to explore the particle size. The SEM image (Figure 5.5) shows aggregated particulates and ill-defined nanoparticles and as such it is difficult to distinguish the size. A more suitable technique would be transmission electron microscopy (TEM) but it was unavailable at the time.

An interesting fact to consider is that MOF-gel samples must be used within a few days of synthesis otherwise the material properties may differ. This was discovered using a 1-month old MOF-gel sample that was imaged under SEM. The sample showed anisotropic particles that have continued to grow to a micro-scale, shown in Figure 5.5. The larger particulate size could have an impact on the rheology of the material by different interparticle interactions. Consequently, all samples were used in the direct-write ink within a few days of synthesis.

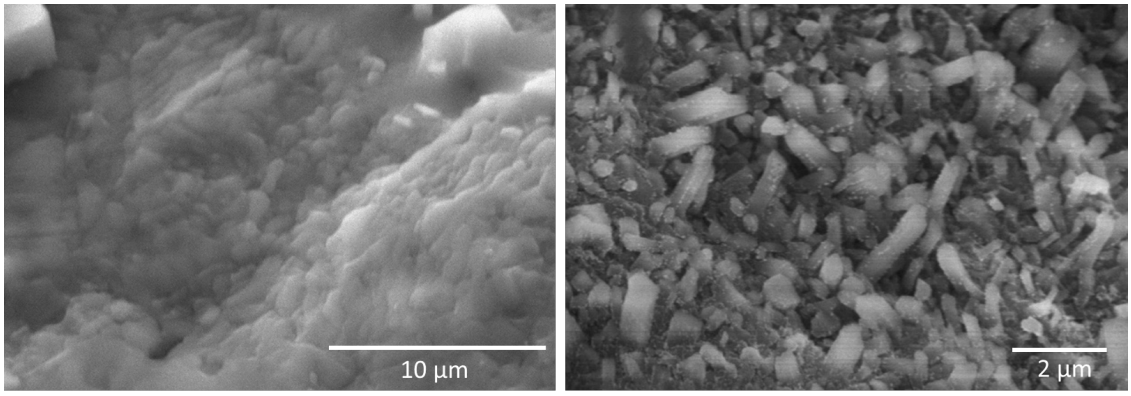

Figure 5.5: SEM image taken by Hitachi TM4000 of MOF-gel after 1 day (left), displaying aggregated and ill-defined nanoparticles and SEM image taken by Cambridge Steroscan - MOF-gel sample after 1 month displaying anisotropic particles (right).

5.3.2. Replacing DMF

DMF is a common solvent in MOF synthesis but is carcinogenic and during MOF synthesis is thermally degraded to dimethylamine and formic acid. Not only are these chemicals toxic to the environment but the methylamine leaves a strong smell and can degrade further to form formaldehyde and ammonia. A solution of MOF-gel was synthesised as described in Section 5.5.1. The as-synthesised UiO-66 MOF-gel (12.84 g) was homogenised with DMF (8 mL) in a centrifuge tube and centrifuged following the procedure in Section 5.5.1. The resulting gel and liquid were collected and measured, this was then repeated seven times and the results are shown in Table 5.2.

Table 5.2: UiO-66 MOF-gel washed multiple times with DMF

UiO-66 MOF-gel	Mass /g	DMF added /mL	Liquid taken after centrifugation /mL
Original	12.84	-	-
1st wash	6.31	8	15
2nd wash	4.91	8	9
3rd wash	3.54	8	8
4th wash	3.05	8	8
5th wash	2.82	8	8
6th wash	2.46	8	8
7th wash	2.20	8	8
Dried Sample	1.78	-	-

The final sample of UiO-66 MOF-gel was placed in a vacuum oven overnight at 90 °C under reduced atmosphere, to remove all solvent. The remaining sample weighed 1.78 g and was assumed to contain excess ligand, metals, intercalated solvent, and MOF. To ascertain the correct quantities TGA should have been undertaken of the sample, however, this investigation went beyond the scope of work.

As can be seen from Table 5.2, the liquid taken after centrifugation did not change after the 3rd wash and also the mass difference between each wash decreased. It was decided that after the 3rd wash a majority of the DMF would have been removed and could now be replaced with a different solvent. Three solvents were trialled and chosen for their availability and lack of high levels of toxicity- acetone, ethanol and isopropyl alcohol. Acetone (5 mL) was added to the washed MOF-

gel and the resulting solution was a gel, that did display thixotropic character. The same was noted with the addition of ethanol. However, when using the MOF-gel it would become fragile, brittle and dry very fast as the solvent evaporated. The final solvent used was isopropyl alcohol, a less volatile solvent. Isopropyl alcohol mixed with UiO-66 MOF-gel presented a thixotropic gel which did not rapidly dry out making it a good substitute to DMF. However, there was insufficient time to follow this up. There were also potentially problematic immiscibility issues, as any chemical introduced to the MOF-gel would have to be miscible with isopropyl alcohol. From this point on there was no washing of MOF-gel and it was used as synthesised with no solvent replacement or washing required because the effect of washing on thixotropy could be examined as part of another body of work.

5.3.3. Thixotropy of UiO-66 MOF-gel

The rheological properties of freshly prepared sample were examined. The MOF-gel in a rudimentary 10 mL sample vial test displayed thixotropic qualities.

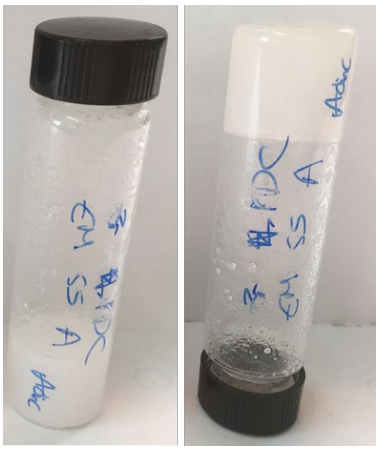

Figure 5.6: Inverted sample vial test of UiO-66 MOF-gel.

The viscosity of UiO-66 MOF-gels was measured as a function of shear rate over time as shown in Figure 5.7. As a shear rate of 50 s^{-1} was applied the UiO-66 MOF-gel had a viscosity of effectively zero. However, as the shear rate decreased to 0.1 s^{-1}, the viscosity sharply increase over a period of 30 seconds to 37 Pa.s. This process was repeated, and the viscosity dropped to zero and then sharply increased s to 20 Pa.s. A third high shear rate was then applied, and the

viscosity of the UiO-66 MOF-gel dropped to zero. The results showed that at a shear rate of 0.1 s^{-1} the viscosity reached 20 Pa.s again.

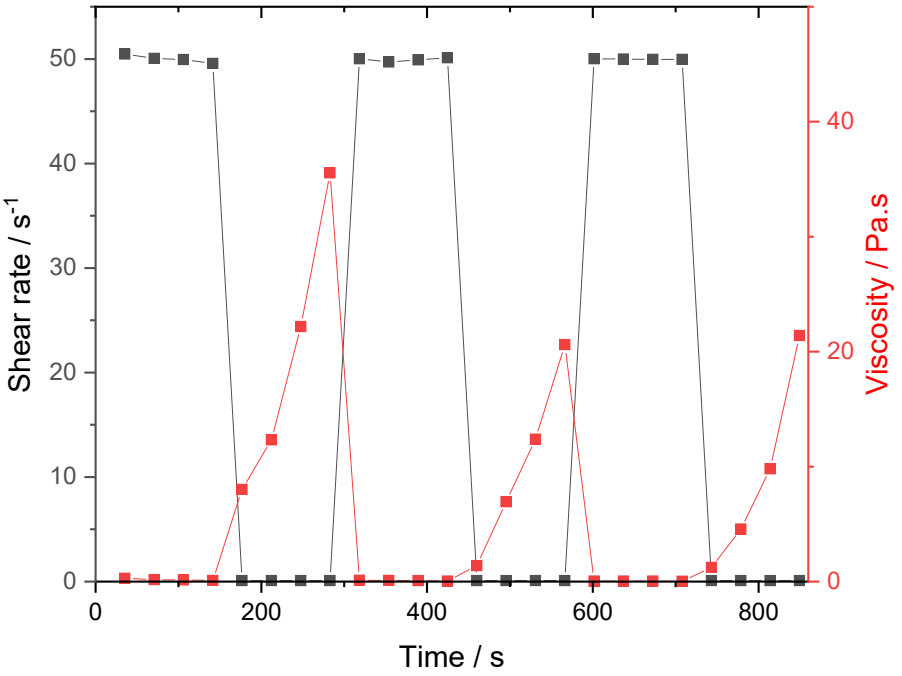

Figure 5.7: Thixotropic results of UiO-66 MOF-gel oscillating shear rate from 0.1 – 50 s^{-1} over time (s), resulting in viscosities ranging from 0 – 40 Pa.s.

After the second shear event the maximum recovered viscosity decreases from 37 to 24 Pa.s. This could be due to the gel network not fully recovering after each shear event, where the intermolecular interactions of the nanoparticles and gel matrix did not have enough time to reform a solid network. When the shear force was applied to this MOF-gel, the viscosity dropped dramatically.

5.3.4. Viscoelasticity of UiO-66 MOF-gel

The shear rheometer is a multifunctional tool. It can measure the reaction of a fluid or gel to shear stress but it can also measure the elastic (storage) and viscous (loss) moduli G′ and G″, respectively. These properties identify the ability of a material to respond to a stress for a viscoelastic fluid under shear. The storage modulus (G′) is the elastic solid like behaviour and the loss modulus (G″) is the viscous response. This determines the ability of the material to hold shape after a deformation event such as extrusion through a nozzle.

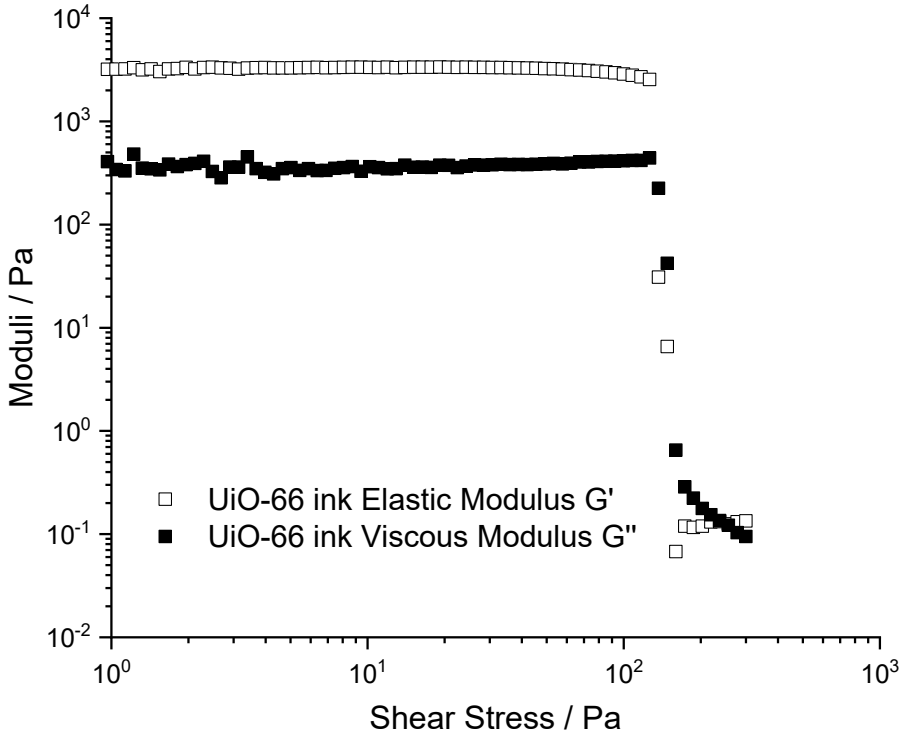

Figure 5.8: log-log UiO-66 MOF-gel storage (elastic) and loss (viscous) moduli, 1-280 Pa.

Extruded material must possess a sufficiently high G′ to maintain the filamentary shape. Thus, when G′ is greater than G″ the shape is maintained after extrusion. Conversely, when a shear stress is applied and G″ is greater, all retention of shape is lost, and the material spreads and wets the plate. The moment when G″ is larger than G′ is where the applied mechanical force is stronger than the interparticle forces, causing the material to yield and flow. The former is desired.

The results displayed in Figure 5.9 show the effect of an increasing shear stress on the UiO-66 MOF-gel. The UiO-66 MOF-gel retained its elastic modulus (G′) to a shear stress of 220 Pa, whereby G′ and G″ dramatically decreased as the gel network collapsed and the MOF-gel acted as a fluid and demonstrated a viscosity moduli of G″= 0.2 Pa. This means that a shear stress of more than 220 Pa was required for deformation and flow of the material. Typically direct-write printers, the mechanical drivers and step-motors, can perform at a maximum shear stress of 320 Pa, and so the UiO-66 MOF-gel was within the limits of a typical 3D printer.[7]

5.3.5. Composition of UiO-66 MOF-gel

It is known that the MOF-gel constituents are UiO-66 nanoparticles in a matrix containing DMF, excess metal salts and terephthalic acid, but the quantity of MOF synthesised in the MOF-gel was unknown. To quantify the amount of UiO-66 in the MOF-gel, two destructive techniques were used: ICP-OES and TGA. TGA demonstrated the breakdown of the MOF-gel relative to the decomposition temperatures of the constituents, while ICP-OES provides information regarding elemental metal quantities.

The results are shown in Figure 5.10 and show the first weight loss step from 30 – 300 °C derived from a combination of many events. This first step included the loss of water and the dehydroxylation of the MOF framework,[8] as well as the loss of DMF, as its boiling point of 153 °C. Any solvent or water intercalated into the MOF will also have contributed to the weight loss before 300 °C. From 300 – 500 °C there was almost no weight lost and the sample was relatively stable, this step consisted of a skeleton framework of zirconium metal nodes and terephthalic acid. From 500 - 600 °C the terephthalic acid linker groups broke down releasing benzene, benzoic acid, and 1,1'-biphenyl as the major decomposition products.[9] The remaining 23.5 % from 600 °C onwards was attributed to ZrO_2 and small amounts of carbonised material remaining in the crucible considered negligible.

The amount of ZrO_2 was 23.5 % where the Zr content was calculated to be 17.4 %, as shown in Table 5.3. The Zr content derived from TGA was used to compared against the Zr content from the ICP-OES analysis. The ICP-OES results were 17.706 % Zr, the results in Table 5.3 offer a comparison of the two techniques. Considering the potential of TGA to leave a carbon soot was not considered, the results are in good agreement and 17 % of the MOF-gel was Zr.

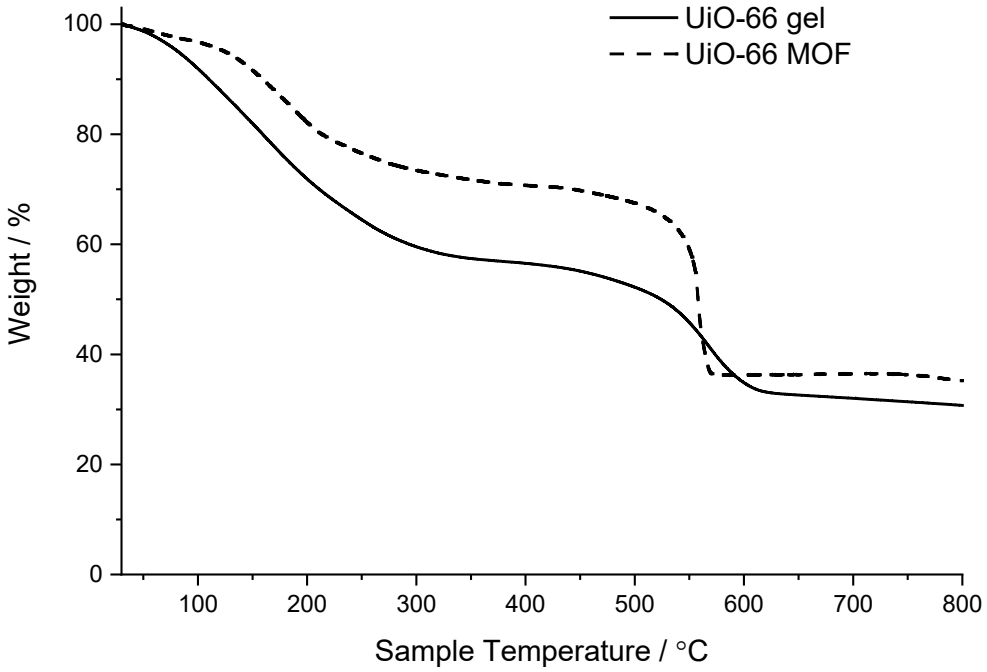

Figure 5.9: TGA results of UiO-66 MOF and UiO-66 MOF-gel, ran under air at 20 ms^{-1}.

Table 5.3: Results from TGA and ICP-OES displaying the percentage of Zr and ZrO_2.

Technique	Zr %	ZrO_2 %
ICP-OES	17.706	-
TGA	17.4	23.5

The matrix was likely to include un-used metal salts and ligand dissolved in the remaining solvent. From the TGA (Figure 5.9) the percentage of solvent was known to be 42 % DMF. However, the amount of unused ligand was unknown and unable to be determined from the TGA. To solve the issue of the unknown composition of the matrix, it was washed three times with fresh DMF of the same volume as the synthesis required. This mitigated the unknown constituents in the matrix replacing them with DMF particles. There has been work done where the solvent has been changed to ethanol, when a quick drying MOF-gel monolith was required, relying on solvent evaporation of a low boiling point solvent. However, for this 3DP direct-write ink, the solvent

was not required to evaporate quickly so another method of setting the MOF-gel was investigated, namely photopolymers.

5.3.6. Formulation of UiO-66 ink

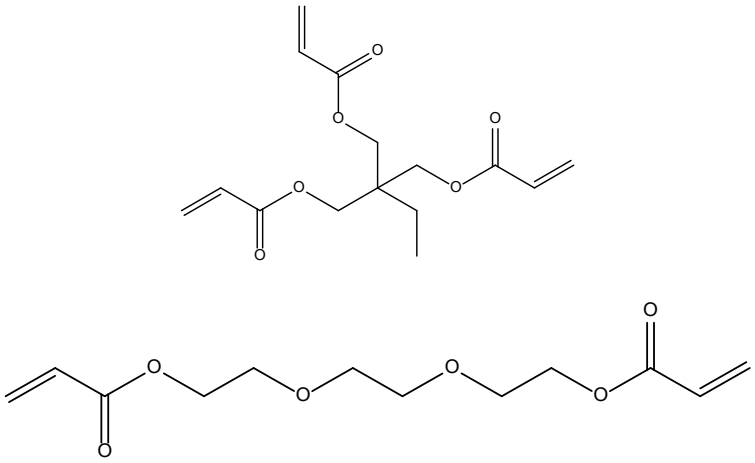

Figure 5.10: Photopolymers used in the formulation of UiO-66 ink: TMPTA (top) and TEGDA (bottom).

The as-synthesised MOF-gel could be extruded through a nozzle and thereby 3D printed but it has no ability to be cured. Other 3D printed materials rely on the rapid cooling of a melted thermoplastic or the rapid solvent evaporation after extrusion to set the material into shape. The traditional materials such as clay and thermoplastics would not be suitable. In this case, a mixture of photopolymers were chosen that were not rheology modifiers, in a bid to show that the MOF-gels can modify the rheology of a 3DP ink. Acrylate-based photopolymers were chosen, as they provide a rapid cure on exposure to UV radiation. The acrylates used were TEGDA and TMPTA, Figure 5.10, chosen because of their previous success in direct-write applications,[10,11] expense, rapid reactivity and they were readily available in the laboratory.

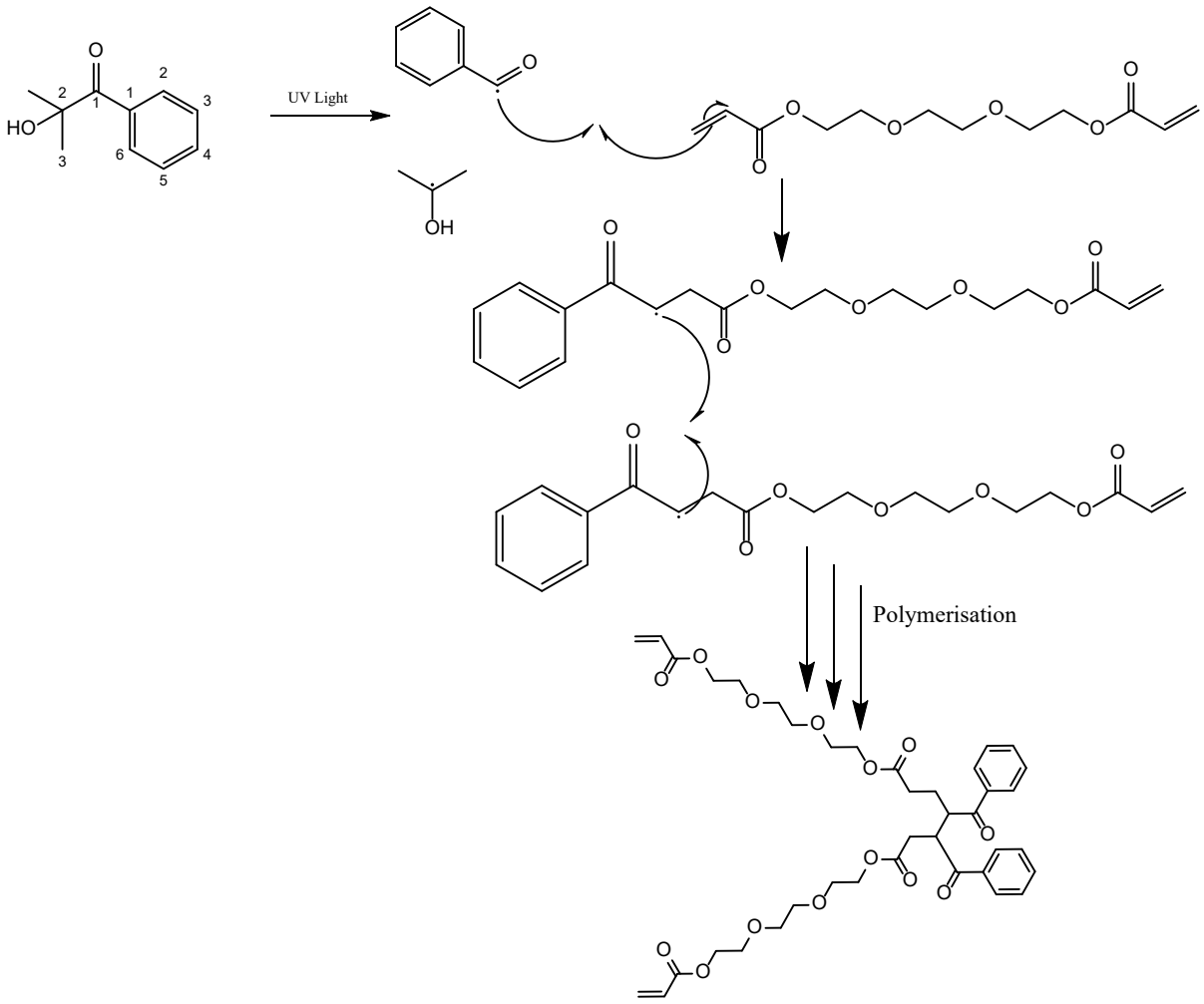

Figure 5.11: 2-hydroxy-2-methylpropiophenone activation by UV light at 365 nm and polymerised with TEGDA.

The photopolymers require a photoinitiator to initiate the free radical polymerisation. The photoinitiator (2-hydroxy-2-methylpropiophenone) was chosen for its reactivity to the 365 nm UV light and availability in the laboratory.[12] It was mixed in a small quantity as outlined in the experimental Section 5.5.1, with TEGDA and TMPTA to produce a direct-write ink. Formulations were trialled to create a formulation with minimum acrylate and maximum MOF-gel. During formulation of the direct-write ink, exploratory testing was carried out, by extruding small amounts of sample from a 5 mL disposable syringe onto tin foil and irradiating them with UV light. Formulations ranged from 10 – 50 % acrylate/photoinitiator blend. The formation that cured the best, was found to be 84 wt.% MOF-gel, 7.5 wt.% TMPTA, 7.5 wt.% TEGDA and 1

wt.% 2-hydroxy-2-methylpropiophenone. Upon exposure to UV radiation, the ink polymerised, as shown in Figure 5.11 demonstrating the photoinitiation and photopolymerisation of 2-hydroxy-2-methylpropiophenone with TEGDA. Further testing of this ink was then undertaken to demonstrate that the ink is thixotropic; it can be 3D printed and that it opens applications of the MOF, overcoming any processability issues.

5.3.7. Properties of UiO-66 ink

The final formulation contained 84 wt.% MOF-gel and should display thixotropy. To demonstrate that the MOF-gel-based direct-write ink was thixotropic, rheometric testing was again undertaken in a similar experiment to the MOF-gel. The test was designed to determine what happened if the ink was stopped in the extruder and restarted

Results shown in Figure 5.12 indicate the initial viscosity of the direct-write ink was 35 Pa.s but rapidly decreased on application of the 50 s^{-1} shear rate. On removal of the shear, the ink did not recover and was limited to 15 Pa.s although a small upward trend did suggest the ink may have slowly regained some viscosity. The test was repeated for 4 runs, with each successive run having a lower viscosity for ink dropping from 15 – 7 Pa.s. The results indicated that the new ink was quicker at regaining its viscosity after a shear event, however the viscosity decreased. The viscosity decrease would be down to the dilution of the MOF-gel, by the addition of additional polymers. From these results the viscosity of the ink decreases with each restart, this implied that the style of 3D printing needed to be continuous. A traditional 3D printing technique stops the flow, moves the printer head, and then start flow again. This therefore limits the designs that might be available. As such, the design chosen for this work was is a cylinder as once the flow of material starts it is not stopped until it is out of material.

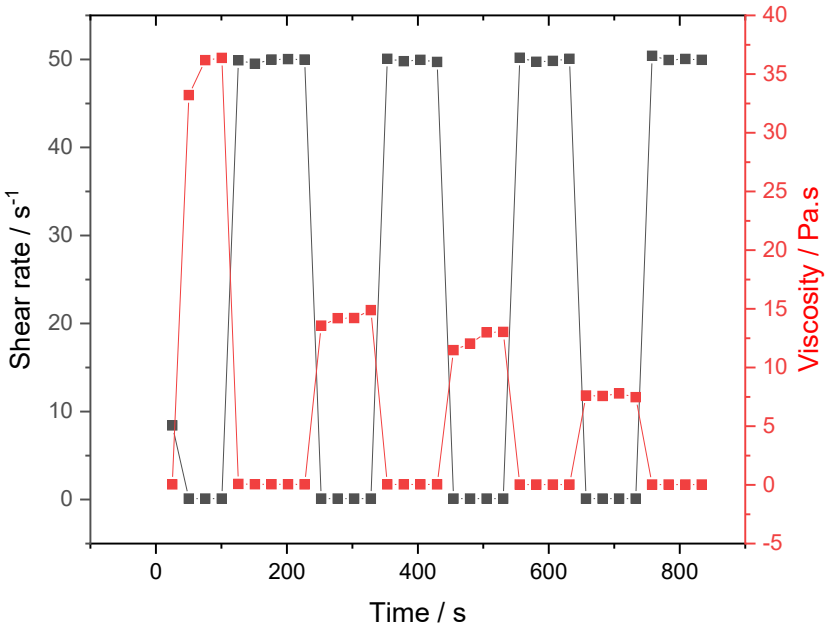

Figure 5.12: Thixotropic results of UiO-66 MOF-gel-based direct-write ink oscillating shear rate from 0.1 – 50 s^{-1} over time (s), resulting in viscosities ranging from 0 – 40 Pa.s.

5.3.8. 3D printing.

The rheological tests showed that the MOF-gel-based direct-write ink was suitable for continuous 3D printing. As such the material was placed into a syringe and covered, to prevent unwanted curing. The ink was then extruded by a K8200 Vellemen printer following the G-code written as given in Section 5.5.6, while the sample was exposed to continuous UV radiation.

The resulting cylinder shape can be seen in Figure 5.13. The cylinder design was hollow consisting of 8 layers continuously printed. The image of the polymerised material did look unpleasing as there was unreacted polymer and DMF causing a slime around the shape. For the first 4 layers, the printer extruded material at the same rate. After these layers, there was less material in the syringe but the same pressure being applied, so the material flowed too quickly causing a bulbous effect, so the print looks larger on the topmost layers. This could be avoided by a reduction in the stepper speed as the print continued to the higher layers, but this was beyond the body of work.

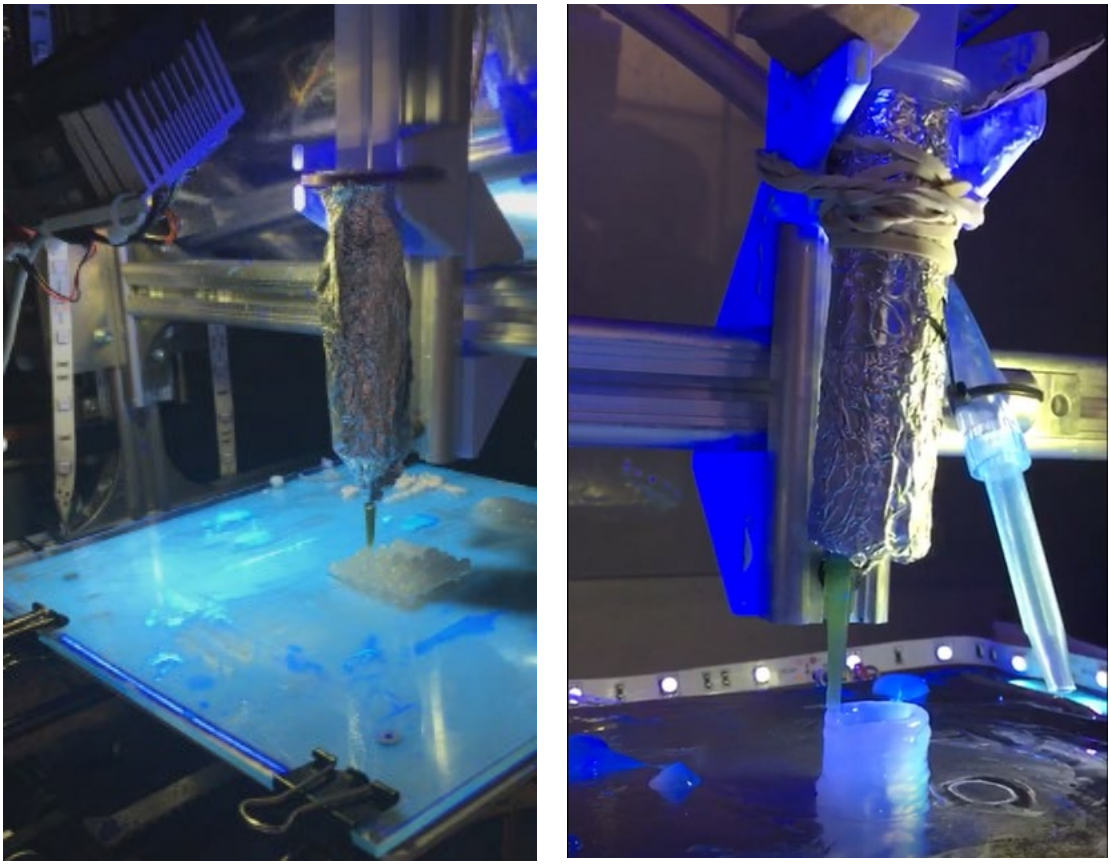

Figure 5.13: 3DP MOF-gel based direct-write ink, the image on the left shows the experimental set up of the Vellemen K8200 including UV light and LED strip lighting around the foil wrapped syringe. The image on the right is a later set up with the addition of gaseous nitrogen to retard oxygen inhibition and a foil base to reflect the UV light. A video is available of the 3DP of the cylinder shape on request.

Although the result may have looked unpleasing, Figure 5.14, they do demonstrate that the UiO-66-gel direct-write ink could be 3D printed. Further testing could be carried out on the formulation to include a more complex mixture of polymers to generate better end-product with more elasticity, faster cure times or smaller resolution.

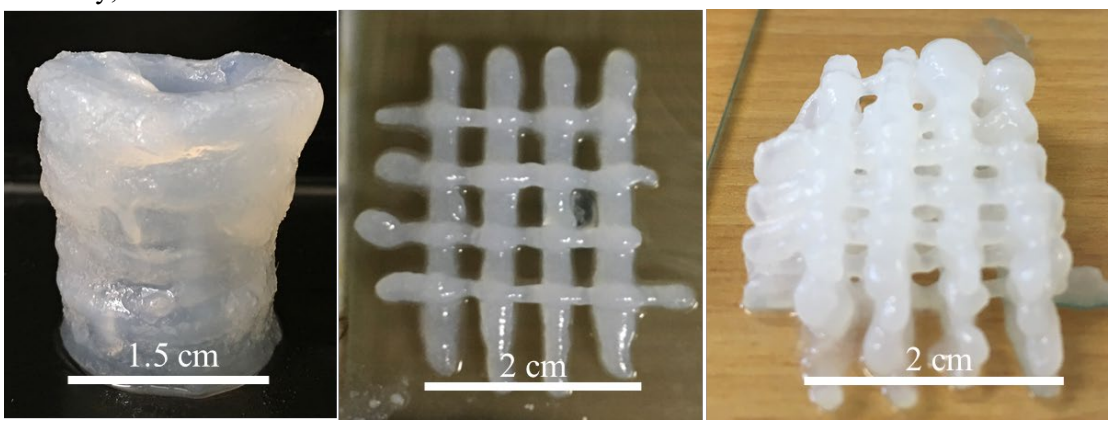

Figure 5.14: 3D printed shapes from the MOF-gel-based direct-write ink.

SEM was used to explore the particle size and environment of the nanoparticles in the polymer. It could be predicted from the previous SEM images of the MOF-gel, that the nanoparticles would not be well defined. The images in Figure 5.15, show a non-porous structure with small and larger aggregates of nanoparticles and polymer scattering the surface.

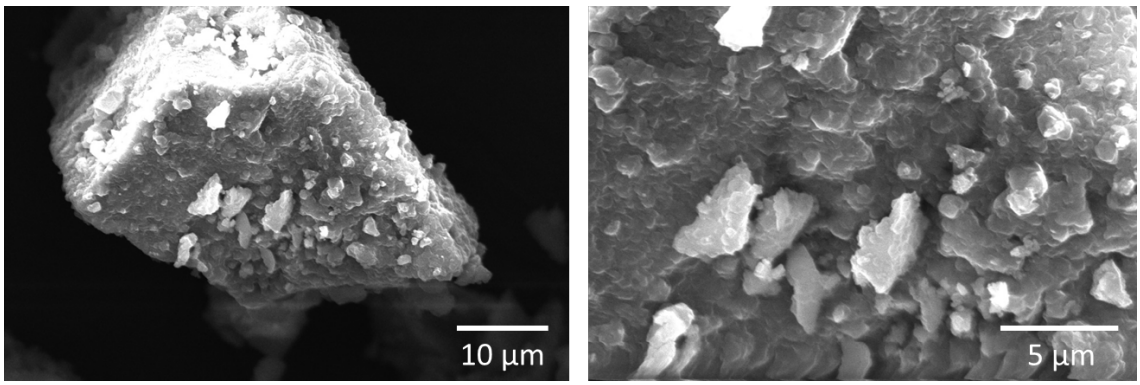

Figure 5.15: SEM images of UiO-66-gel direct-write ink

5.3.9. Thermal Analysis of MOF-gels

The amount of MOF present in the ink theoretically should have been 7.43 %. This was calculated by assuming all Zr and terephthalic acid was used up in the reaction. This could be confirmed experimentally by thermal decomposition of a samples by ICP-OES and TGA data of the polymerised UiO-66 ink. As before, the TGA was performed in air. From the TGA in Figure 5.16, 13.2 % ZrO_2 (9.8 % Zr) remained. The ICP-OES results for the UiO-66 ink was 6.592 % Zr present in the formulation. This correlated with the theoretical amount in the ink and suggests that the TGA has both ZrO_2 and carbonised ash in equal amounts remaining after thermal degradation.

The TGA for the UiO-66 ink followed the trend of the UiO-66 gel, except for one extra weight loss step at 350 – 450 °C, this drop could be the polymer acrylates burning off.

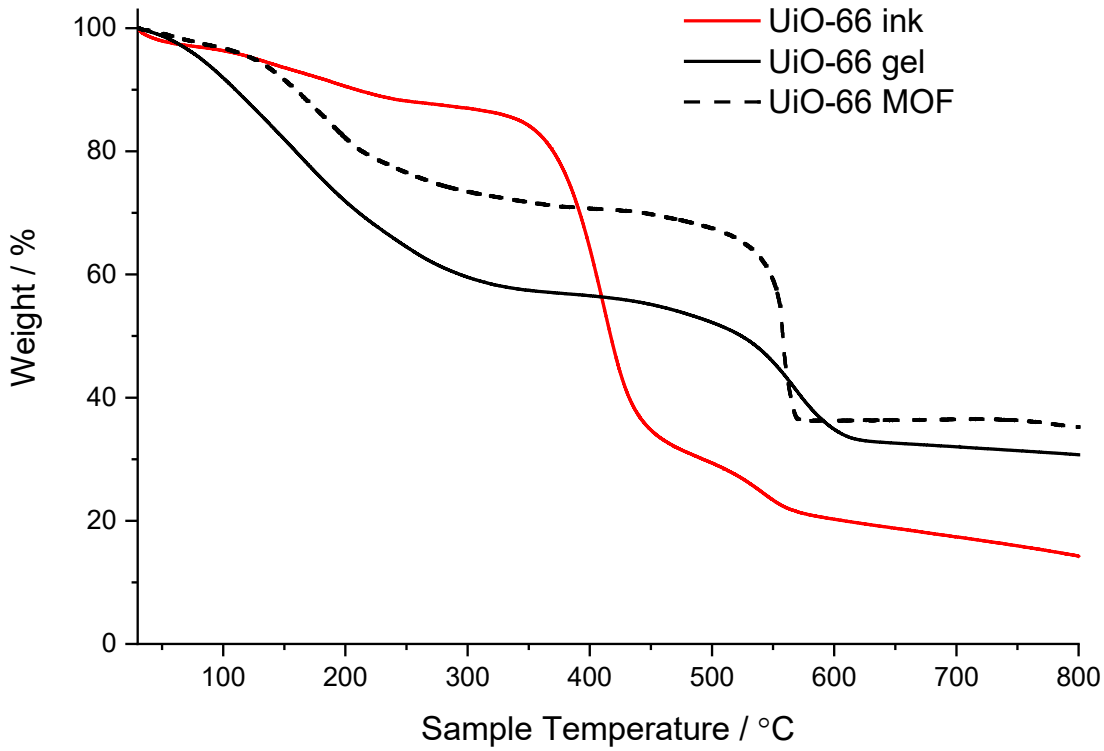

Figure 5.16: TGA results of UiO-66 MOF, UiO-66 MOF-gel and MOF-gel-based ink, ran under air at 20 ms^{-1}.

To investigate if the polymers burnt off at 350 – 450 °C, they were tested individually as shown in Figure 5.17. The samples tested were polymerised samples of TMPTA and TEGDA using the same photointiators used in the ink formulation. Under oxidising conditions, the weight loss profiles of TMPTA and TEGDA showed three weight loss steps. The first step was likely the loss of water from the acrylates, and loss of excess photointiator up to 200 °C. The TMPTA and TEGDA are thermally stable from 300 – 400 °C, with no measurable weight loss observed. A

large weight from 400 – 500 °C, indicated that the bulk of the polymeric network degraded. A smaller weight loss step at 500 – 600 °C could be the remainder of material thermally degrading.

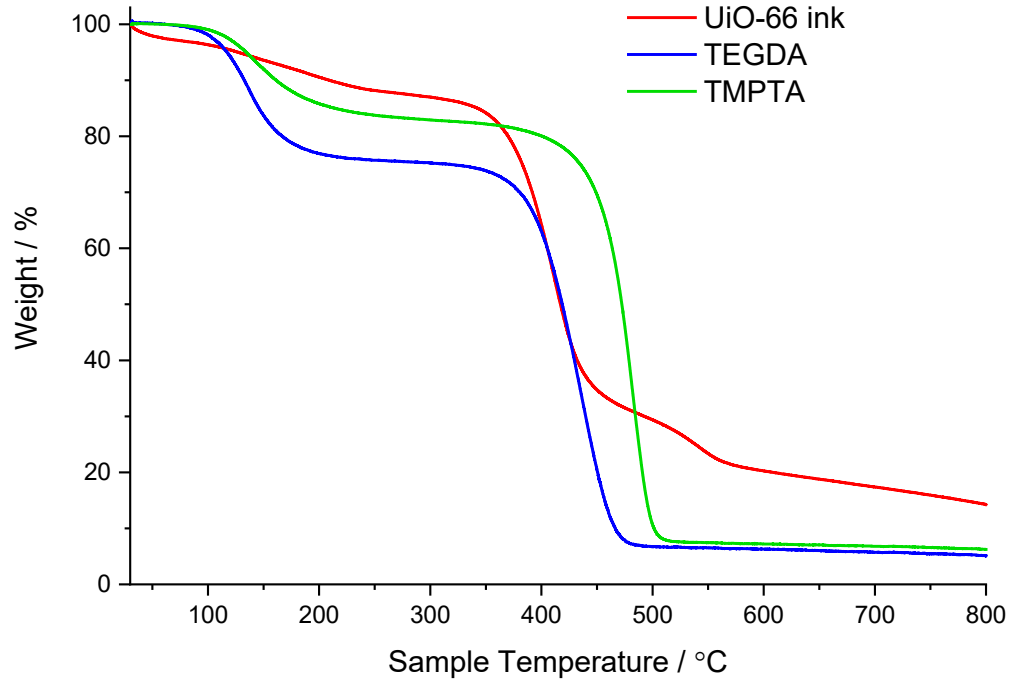

Figure 5.17: TGA results of TMPTA, TEGDA and UiO-66-gel-based direct write ink.

5.3.10. Physical Properties of the direct-write ink

The 3D printed objects created from the MOF-gel-based direct write ink were not brittle or fragile. They could be handled with a pair of tweezers but no special precautions were taken. The samples were also mechanically strong; to demonstrate this a monolithic sample (prepared as in Section 5.5.8) was taken for compression testing.

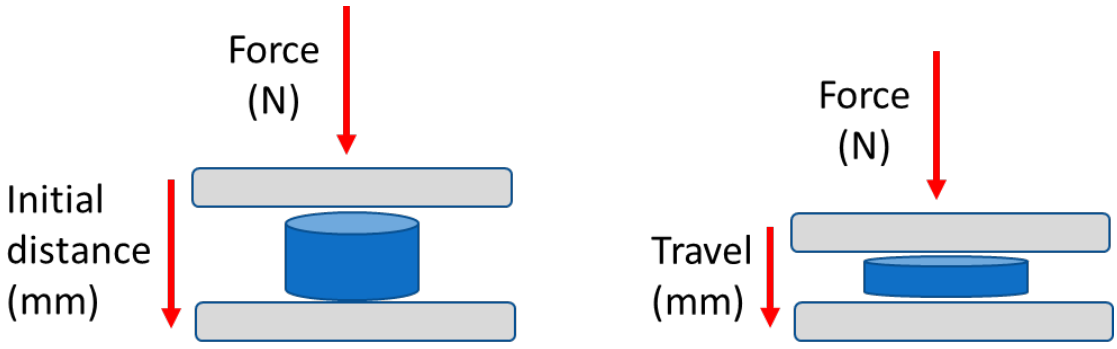

Figure 5.18: Principle of compression testing for UiO-66 polymer sample

Figure 5.18 demonstrates the principle behind compression testing, whereby a sample is placed under a force (N) and displaced by a distance (mm) called travel. The force is maintained until

the sample is broken, which is associated with a significant drop in force. Figure 5.19 shows the results of compression testing, where it can be demonstrated that the sample could withstand a compressive force of 25.2 N with a displacement of 3.5 mm before breaking.

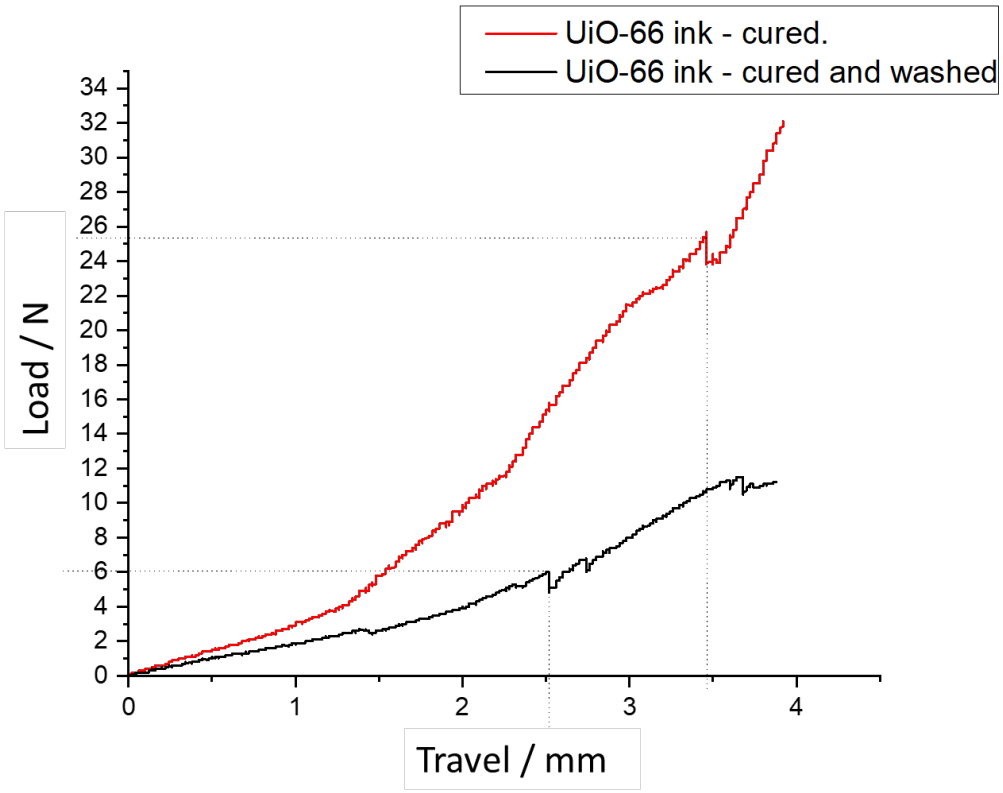

Figure 5.19: Results of mechanical testing of UiO-66 polymer.

However, during testing, a fluid could be seen escaping from the sample. It was postulated that the sample may be, to some extent, porous and holding excess fluid in its pores. The fluid in question would be large amounts of excess DMF, terephthalic acid and uncured acrylate. The sample was retested, after washing with ethanol and then left at room temperature for one hour. The sample broke at a compressive load of 6 N at 2.5 mm displacement. This was dramatically less than the cured sample. It could be considered that the effect of the regents left in the cured sample aided and helped maintain the mechanical stability of the sample. It was also investigated to what extent the washed sample was porous. BET testing was conducted on the washed sample

and a very low surface area of 24 m^2g^{-1} was demonstrated. A typical powdered sample of UiO-66 MOF nanoparticles was around 880 m^2g^{-1}.[13]

5.3.11. Ability to adsorb dye.

With the low surface area of 24 m^2g^{-1} shown by BET testing, it is clear the MOF was not active. The MOF was likely sealed into the polymer. To visualise this lack of absorptivity, the sample was placed into a syringe, and rhodamine dye was placed above as shown in Figure 5.20.

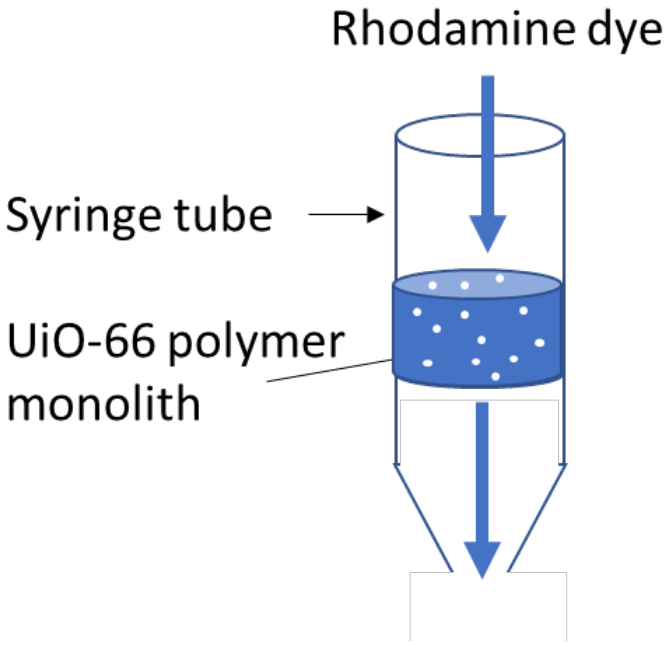

Figure 5.20: Schematic diagram of rhodamine dye flowing through a UiO-66 polymer monolith sample.

The sample measured 2.5 cm by 1 cm. As shown in Figure 5.21, the sample was cut in half and there were patches of pink and white. Areas of pink indicated the uptake of rhodamine dye, while areas of white indicated no uptake. The monolithic sample absorbed the dye around the edges of the sample, or near cracks where the dye could flow through by a capillary effect.

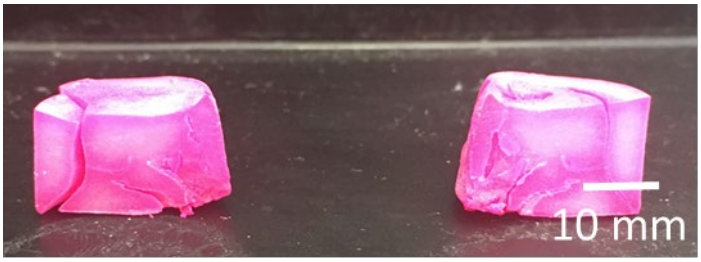

Figure 5.21: UiO-66 polymer monolith after a flow of rhodamine dye, sliced in half.

While the sample in this form may not be porous, as indicated by both BET and adsorption methods, the sample could be activated by heat, to degrade specific polymers, much like the 4DP ink in Chapter 4.

5.3.12. UiO-66-NH_2 MOF-gel

Other MOF-gels were synthesised to demonstrate that a range of MOFs could exhibit and form a MOF-gel and so act as their own rheology modifier. UiO-66-NH_2 MOF-gel, as shown in Figure 5.22 was synthesised as in section 5.5.2 and formed a light brown gel, and on testing in the rheometer showed a viscosity of 74 Pa.s. This result was much higher than the UiO-66-gel and the increased viscosity could be caused by the increased number of hydrogen bonds and so stronger intermolecular forces.

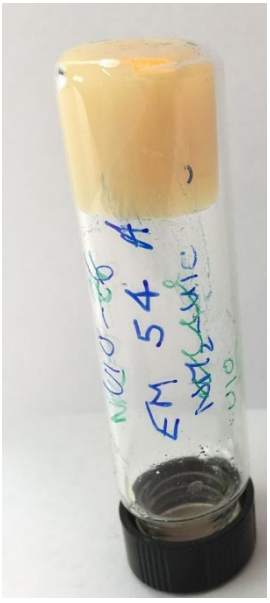

Figure 5.22: UiO-66-NH_2 MOF-gel upturned in a sample vial.

UiO-66-NH_2 MOF-gel was mixed with TMPTA and photointiator, in the same quantities as UiO-66 MOF-gel, Section 5.5.2. However, during the UV curing process, it was noted that the formulation would not cure. It was investigated and found that the free radical polymerisation was being hindered by the presence of the amino group on the terephthalic acid. The amino terephthalic acid absorbs wavelengths from 300 – 400 nm,[14] the UV wavelength used was 365 nm and so any free radical initiation was severely hindered. Another photoinitiator of higher or

lower UV activity could have been chosen, but the UV light source would have to be changed and both alterations were not readily available at the time. Testing on UiO-66-NH_2 MOF-gel ink was not carried any further.

5.3.13. ZIF-8 MOF-gel

Another trialled MOF-gel was ZIF-8. The synthesis of this MOF-gel is different to UiO-66. The synthesis does not require heat, but instead relies on rapid crystallisation of ZIF-8 from a solution contained $Zn(NO)_2.6H_2O$, 2-methylimidazole and triethylamine (Section 5.5.3). The synthesis works by rapid deprotonation of the ligand by triethylamine and the rapid crystallisation of ZIF-8 nanoparticles to create a MOF-gel. Initial testing of the MOF-gel, much like UiO-66 MOF-gel, showed the ability of the material to flow and reform after a shear event. As such the material was tested to show the thixotropic ability. Figure 5.23 displays the result of multiple shear events on the ZIF-8 MOF-gel. The initial viscosity of the material was around 90 Pa.s and after the first shear event of 50 s^{-1} the viscosity becomes effectively zero. On the removal of the shear rate to 0 s^{-1}, the material recover to a viscosity of 70 Pa.s and roughly maintains this viscosity for the next 3 shear events. Unlike UiO-66 MOF-gel, the thixotropic results from ZIF-8 MOF-gel demonstrated this MOF-gels had the ability to retain viscosity after shear events.

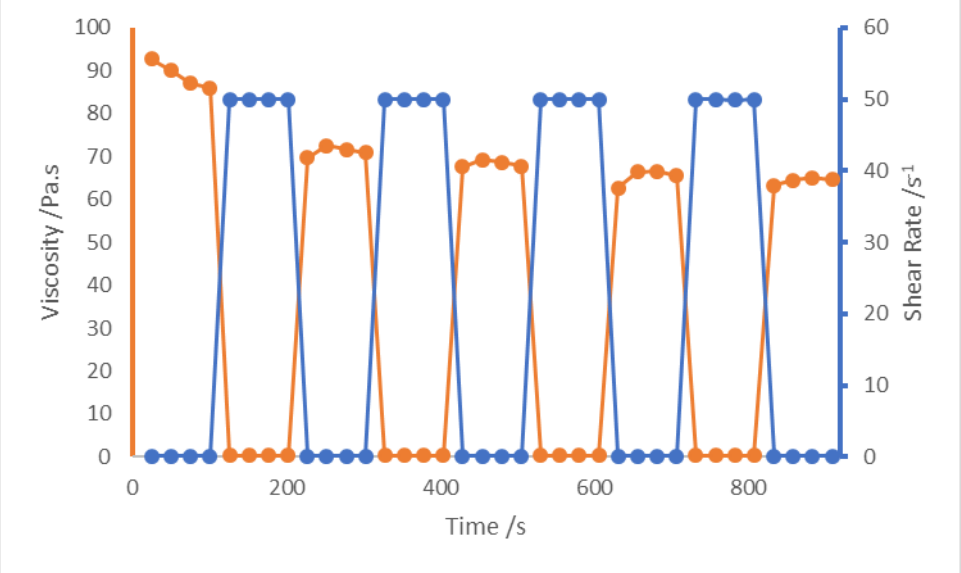

Figure 5.23: Viscosity against shear rate and time to show recovery of ZIF-8 MOF-gel.

5.3.13.1. Replacing DMF

The work in this section was undertaken with the help of Matylde Brisinger.

DMF is a commonly used solvent in MOF synthesis to deprotonate the ligand. Because of the speed of the synthetic reaction of ZIF-8, taking seconds, it was investigated if the DMF solvent could be changed to a different solvent with:

- A lower boiling point – to allow the solvent to evaporate at ambient temperatures, to enhance the solidification of a 3D printed material.
- Green credentials – DMF is not a sustainable chemical and there are other alternatives such as acetone and isopropanol which are cheaper and more abundant.
- No carcinogenic properties – DMF is carcinogenic and its by-products are toxic to the environment.

The aim was to change the DMF to a solvent of similar polarity and lower boiling point, Table 5.4 outlines a list of common solvent, relative polarity, and boiling point.

Table 5.4: List of solvents by increasing polarity and respective boiling points.

Solvent.[15]	**Relative polarity.**[16]	**Boiling Point /°C.** [15]
Chloroform	0.259	61.2
Dichloromethane	0.309	39.8
Acetone	0.355	56.2
DMF	0.386	153
t-butyl alcohol	0.389	82.2
Isopropyl alcohol	0.546	82.4
Methanol	0.762	64.6
Water	1	100

Acetone possesses a lower polarity than DMF and it a cheap, abundant and has a lower boiling point, the solvent has also been reported for the synthesis of ZIF-8.[17] t-butyl alcohol possesses the closest polarity to DMF and a reasonable substitute.

The use of chloroform and dichloromethane is not widely documented in the synthesis of MOFs. However they possess lower boiling points than DMF. This renders them attractive for use in MOF-gels since they will undergo solvent evaporation more readily, which may enhance ink solidification upon extrusion during DW 3DP. Isopropyl alcohol has a high polarity but a relatively lower boiling point. Methanol is a common protic solvent used in the ZIF-8 formulation. The chosen solvents were methanol, isopropyl alcohol and t-butyl alcohol as dichloromethane and chloroform were to be avoided for their high volatility and negative health impact.

Figure 5.24 shows the results of the synthesis using methanol, isopropyl alcohol, and t-butyl alcohol. None of the resulting solutions were highly thixotropic and clear separation of solvent and MOF can be seen from isopropyl alcohol and t-butyl alcohol. However, the sample produced from methanol was the most promising, displaying some ability to be thixotropic with a small amount of sample remaining at the top of the vial when upturned, and with fine tuning could work as an alternative solvent to DMF.

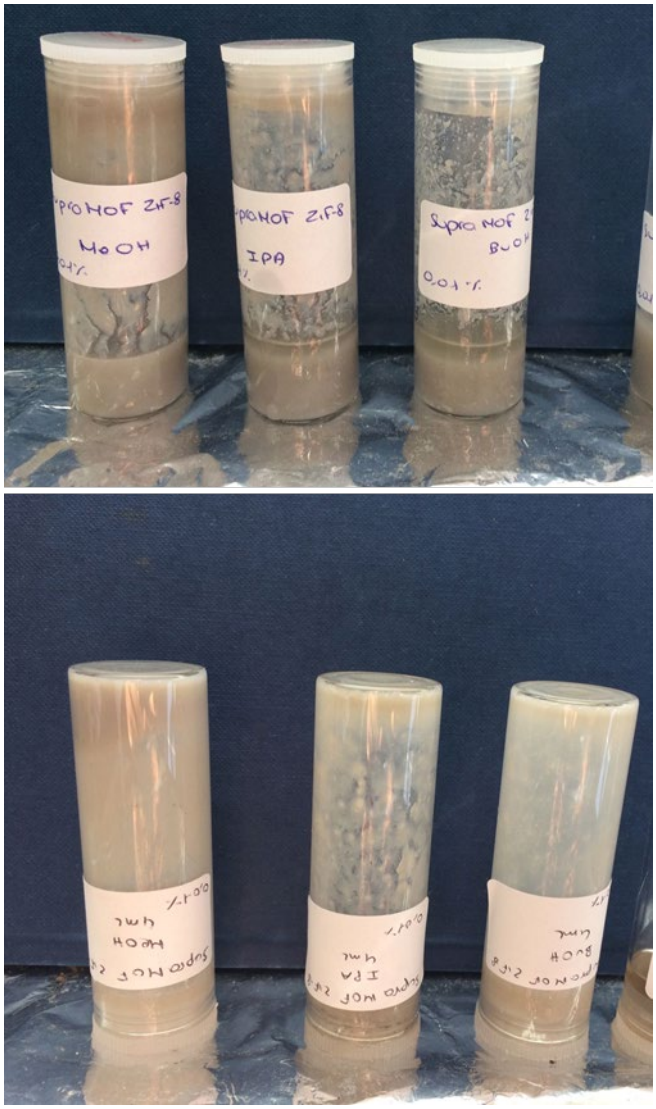

Figure 5.24: Images of ZIF-8 synthesis using different solvents and also upended sample vials to suggest if any display thixotropic qualities.

5.3.13.2. Porosity of ZIF-8 MOF-gel

The MOF-gel, produced with DMF, was tested to see if any active MOF was available in the MOF-gel and would indicate the MOF-gels suitablility to be used for applications that MOFs are currently utilised for.

The ZIF-8 MOF-gel was sent for preliminary BET testing and results returned a surface area of only 19.4 $m^2 g^{-1}$. A literature value for ZIF-8s surface area of 1617 $m^2 g^{-1}$. This implies that the

surface area of ZIF-8 and its intrinsic porosity is blocked and hence not active. The MOF-gel was not tested further after results of the BET indicated a low surface area and lack of porosity.

5.4. Conclusion

The material properties of MOF-gels represent an important step forward in the creation of a MOF-based 3D printable ink that requires no additional rheology modifier. This study confirmed the viscosities of UiO-66, UiO-66-NH_2 and ZIF-8 MOF-gels and that the materials are thixotropic. While efforts were made to replace DMF, it is the best solvent for MOF synthesis and more experimental work is required to tune the synthesis using alternative solvents.

UiO-66 MOF-gel was further studied for its viscoelastic properties. When the MOF-gel was mixed with photopolymers and extruded a 3D printed structure could be created, with the use of UV radiation. The 3D printed structure was sufficiently mechanically stable to be handled without special precautions to avoid fracture. The MOF present in the direct-write ink possessed a low surface area, when analysed by BET and a rudimentary rhodamine adsorption test, the material demonstrated that the MOFs function is blocked by the cured polymer.

5.5. Experimental

5.5.1. Preparation of UiO-66-gel-based ink

Synthesised UiO-66 MOF-gel (84 wt.%) was homogenised with TMPTA (7.5 wt.%), TEGDA (7.5 wt.%) and 2-hydroxy-2-methylpropiophenone (1 wt.%) using an ultra-torrex homogeniser at 1000 rpm for 2 minutes.

5.5.2. Preparation of UiO-66-NH_2 ink

UiO-66-NH_2 MOF-gel was synthesised by creating a solution of $ZrOCl_2 \cdot 8H_2O$ (3.22 g) in DMF (60 mL) in a 500 mL Schott glass bottle. Amino-terephthalic acid (2.62 g) was added and sonicated until all solids had visibly dissolved. The solution was sealed and then placed in a preheated oven at 80 °C for 2 hours then left to cool to room temperature.

Synthesised UiO-66-NH_2 MOF-gel (84 wt.%) was homogenised with TMPTA (15 wt.%) and 2-hydroxy-2-methylpropiophenone (1 wt.%) using an ultra-torrex homogeniser at 1000 rpm for 2 minutes.

5.5.3. Preparation of ZIF-8 MOF-gel

ZIF-8 nanoparticle synthesis as published in the literature by Chaudari & Tan.[18]

$Zn(NO)_2.6H_2O$ was dissolved in methanol (20 mL) and added rapidly to a solution of 2-methyl imidazole (6.86 g), triethylamine (4.90 g) and methanol (22 ml) and shaken in the vessel for 20 seconds.

5.5.4. Rheometry - shear oscillation

The Rheometric tests carried out in Section 5.3.2 were carried out using this programme below and repeated three times.

Table 5.5: Rheometry oscillation testing parameters

Shear rate (s^{-1})	Wait (s)	Integration time (s)
0.1	1	15
0.1	1	15
0.1	1	15
0.1	1	15
50	1	15
50	1	15
50	1	15
50	1	15

5.5.5. 3D Printer

The Vellemen 8200 3D printer was purchased online and then modified with a paste extruder available from the same supplier. A UV light and UV strip lights were added and nitrogen flowed through the system. A video is available of the 3D printing of MOF-gel-based direct write ink.

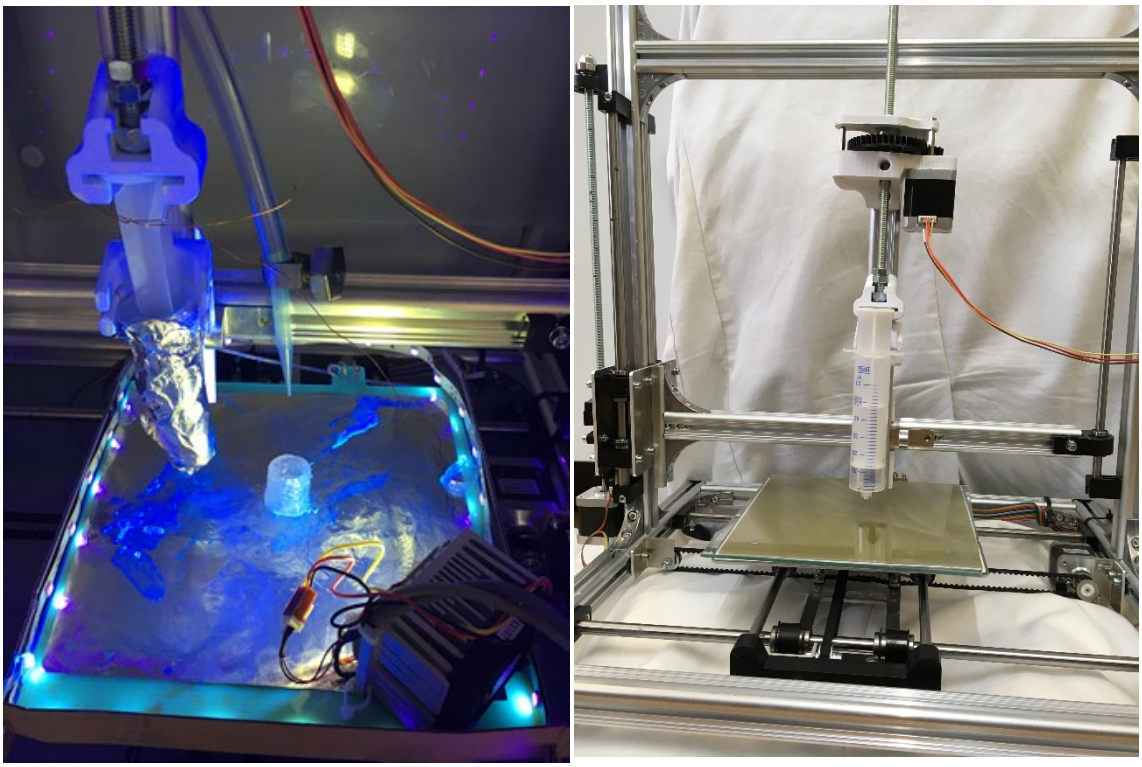

Figure 5.25: Setup for 3DP MOF-gels, showing syringe, printed cylinder and the UV lights. Note- not the position that the UV light is in when printing, it is elevated and 10 cm away. Right – Vellemen K8200 setup with the paste extruder and no lights.

5.5.6. G-Code of Cylinder

```
;Sliced at: {day} {date} {time}
;Basic settings: Layer height: {layer_height} Walls: {wall_thickness} Fill: {fill_densit
;Print time: {print_time}
;Filament used: {filament_amount}m {filament_weight}g
;Filament cost: {filament_cost}
;M190 S{print_bed_temperature} ;Uncomment to add your own bed temperature line
;M109 S{print_temperature} ;Uncomment to add your own temperature line
G21        ;metric values
M82        ;set extruder to absolute mode
T1         ;set Paste extruder #2
M302       ; Allow Cold Extrusion
M92 E3000 ; Set Extruder EEPROM for Paste
G28
G1 F4000 X150 Y180
G92
G92 E0                  ;zero the extruded length
G1 F200 E10             ;extrude 10mm of feed stock
G92 E0                  ;zero the extruded length again
G1 F{travel_speed}
;Put printing message on LCD screen
M117 Printing...
```

```
;LAYER:0
M107
;LAYER:1
G0 F6000 X95.149 Y97.155 Z1.650
;TYPE:WALL-OUTER
G1 F300 X97.155 Y95.149 E0.58516
G1 X99.692 Y93.857 E1.17240
G1 X102.500 Y93.411 E1.75885
G1 X105.309 Y93.857 E2.34551
G1 X107.844 Y95.148 E2.93229
G1 X109.852 Y97.157 E3.51817
G1 X111.143 Y99.692 E4.10496
G1 X111.589 Y102.500 E4.69141
G1 X111.143 Y105.309 E5.27806
G1 X109.852 Y107.843 E5.86466
G1 X107.843 Y109.853 E6.45084
G1 X105.309 Y111.144 E7.03744
G1 X102.500 Y111.589 E7.62406
G1 X99.692 Y111.144 E8.21048
G1 X97.155 Y109.852 E8.79773
G1 X95.149 Y107.845 E9.38303
G1 X93.857 Y105.309 E9.97009
G1 X93.411 Y102.500 E10.55674
G1 X93.857 Y99.692 E11.14319
G1 X95.149 Y97.155 E11.73044
```

```
;LAYER:2
G0 F6000 X95.149 Y97.155 Z3.150
G92 E0
;TYPE:WALL-OUTER
G1 F300 X97.155 Y95.149 E0.58516
G1 X99.692 Y93.857 E1.17240
G1 X102.500 Y93.411 E1.75885
G1 X105.309 Y93.857 E2.34551
G1 X107.844 Y95.148 E2.93229
```

```
;End GCode
M104 S0                     ;extruder heater off
M140 S0                     ;heated bed heater off (if you have it)
M92 E262  ; Reset Extruder EEPROM
G91                                 ;relative positioning
G1 E-1 F300                         ;retract the filament a bit before lifting the nc
G1 Z+0.5 E-5 X-20 Y-20 F{travel_speed} ;move Z up a bit and retract filament even more
M84                         ;steppers off
G90                         ;absolute positioning
;{profile_string}
```

Figure 5.26: G-Code of cylinder shape

5.5.7. Slicing settings for Cura.

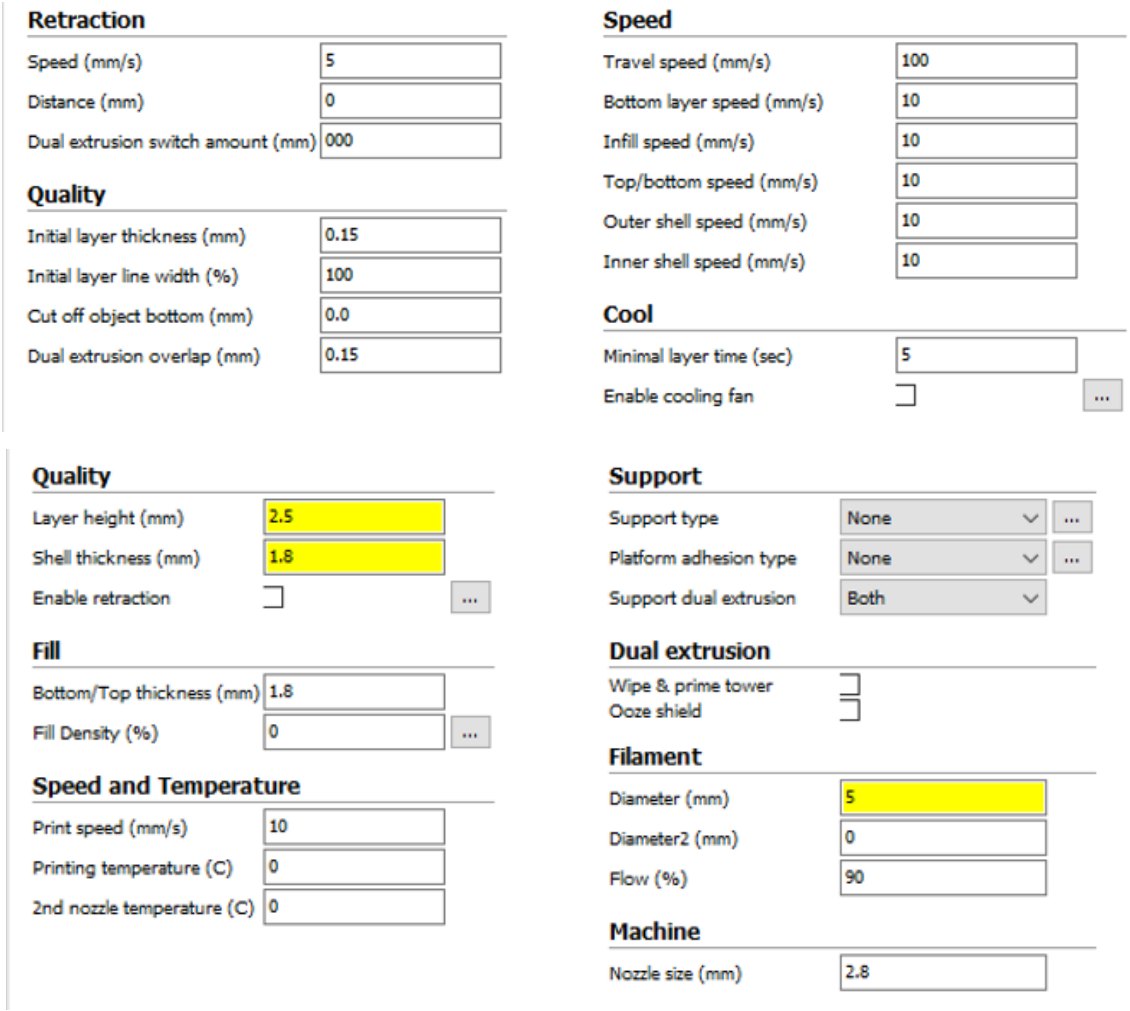

Figure 5.27: Slicing settings for Cura.

5.5.8. Preparation of UiO-66 polymer monolith sample

A syringe (50 mL) was placed upside down and 10 mL of UiO-66 ink was added. The sample was then placed under UV light to cure for 2 minutes.

5.6 References

1 H. Thakkar, S. Eastman, Q. Al-Naddaf, A. A. Rownaghi and F. Rezaei, *ACS Appl. Mater. Interfaces*, 2017, **9**, 35908–35916.

2 K. Evans, Z. C. Kennedy, B. W. Arey, J. F. Christ, H. T. Schaef, S. K. Nune and R. L. Erikson, *ACS Appl. Mater. Interfaces*, 2018, **10**, 15112–15121.

3 B. Bueken, N. Van Velthoven, T. Willhammar, T. Stassin, I. Stassen, D. A. Keen, G. V. Baron, J. F. M. Denayer, R. Ameloot, S. Bals, D. E. De Vos and T. D. Bennett, *Chem. Sci.*, 2017, **8**, 3939–3948.

4 B. M. Connolly, M. Aragones-Anglada, J. Gandara-Loe, N. A. Danaf, D. C. Lamb, J. P. Mehta, D. Vulpe, S. Wuttke, J. Silvestre-Albero, P. Z. Moghadam, A. E. H. Wheatley and D. Fairen-Jimenez, *Nat. Commun.*, 2019, **10**, 1–11.

5 I. K. Shamsudin, I. Idris, A. Abdullah, J. Kim and M. R. Othman, in *AIP Conference Proceedings*, American Institute of Physics Inc., 2019, vol. 2124, p. 020057.

6 L. Liu, J. Zhang, H. Fang, L. Chen and C.-Y. Su, *Chem. - An Asian J.*, 2016, **11**, 2278–2283.

7 G. Siqueira, D. Kokkinis, R. Libanori, M. K. Hausmann, A. S. Gladman, A. Neels, P. Tingaut, T. Zimmermann, J. A. Lewis and A. R. Studart, *Adv. Funct. Mater.*, 2017, **27**, 1–10.

8 L. Valenzano, B. Civalleri, S. Chavan, S. Bordiga, M. H. Nilsen, S. Jakobsen, K. P. Lillerud and C. Lamberti, *Chem. Mater.*, 2011, **23**, 1700–1718.

9 A. B. Elmas Kimyonok and M. Ulutürk, *J. Energ. Mater.*, 2016, **34**, 113–122.

10 A. J. Wang, T. Paterson, R. Owen, C. Sherborne, J. Dugan, J. M. Li and F. Claeyssens, *Mater. Sci. Eng. C*, 2016, **67**, 51–58.

11 S. C. Ligon, R. Liska, J. Stampfl, M. Gurr and R. Mülhaupt, *Chem. Rev.*, 2017, **117**, 10212–10290.

12 X. Kuang, K. Chen, C. K. Dunn, J. Wu, V. C. F. Li and H. J. Qi, *ACS Appl. Mater. Interfaces*, 2018, **10**, 7381–7388.

13 A. M. Ploskonka, S. E. Marzen and J. B. DeCoste, *Ind. Eng. Chem. Res.*, 2017, **56**, 1478–1484.

14 N. Liédana, P. Lozano, A. Galve, C. Téllez and J. Coronas, *J. Mater. Chem. B*, 2014, **2**, 1144–1151.

15 S. Murov, Properties of Solvent Used in Organic Chemistry, http://murov.info/orgsolvents.htm#TABLE 2, (accessed 8 April 2020).

16 C. Reichardt and T. Welton, *Solvents and Solvent Effects in Organic Chemistry*, Wiley-VCH Verlag GmbH & Co. KGaA, Weinheim, 2010.

17 E. L. Bustamante, J. L. Fernández and J. M. Zamaro, *J. Colloid Interface Sci.*, 2014, **424**, 37–43.

18 A. K. Chaudhari and J.-C. Tan, *Chem. Commun.*, 2017, **53**, 8502–8505.

6. Conclusion and Future Work

The foregoing work presented in this thesis has shown various fabrication techniques of novel MOF composites that overcome a MOFs lack of processability by the use and modification of 3DP and time-dependent 3DP. MOFs have a wide range of applications such as carbon capture, separation, and catalysis mainly due to their highly porous and ordered structure, but MOFs are equally hindered by their porosity and struggle to be incorporated into a polymer matrix without drastically loosing function. The work carried out in this thesis involved the use of 3DP technologies to produce novel materials, that could be employed to help tackle a range of applications including climate change and pollution.

Two methods of 3DP were discussed and employed - SLA and direct-write ink. They were chosen as the most common techniques of 3DP available but also most versatile and adaptable. The first technique to be trialled was SLA 3DP, the objective was to produce a composite which displayed alignment of the MOF particulates and to investigate the magnetic alignment of MOFs using iron-based products. The MOFs used in this trial were selected for their anisotropic rod or needle-like shape but also for their ability to function as carbon capture devices - MIL-53(Al), MIL-68(In), MIL-68(Ga) and NU-1000. It was hypothesised that by alignment of these such MOFs when placed into a real-world application, such as flue gas from a high producer of CO_2, they would capture and store CO_2 more efficiently aligned, as opposed to unaligned. It was then investigated to see if anisotropic MOFs could be magnetically aligned. Firstly, two MOFs - MIL-68(In) and MIL-68(Ga) were doped with iron salts during synthesis to investigate if iron could be added to the MOFs architecture. Semi-quantitative analysis of PXRD patterns revealed that by doping with iron the unit cell volume altered, in the case of MIL-68(In) the unit cell volume decreased as In^{3+} was replaced by Fe^{3+} and MIL-68(Ga) saw an increase in unit cell volume. This suggested that iron was present in the MOF and iron was found by ICP-OES. Attempts were trialled to verify this level by SEM-EDX however the MOFs were unstable under the electron beam and were

difficult to image. The MOFs were then tested to establish their magnetic character, all the MOFs with doped iron displayed very weak or limited magnetic mass susceptibility when measured experimentally. However, two samples with highest amount of iron were analysed further to establish the magnetic character by undertaking vibrating sample magnetometer experiments. The experiments showed that the samples displayed diamagnetic character but had extremely low magnetisation results of 0.06 EMU g^{-1}, results of iron oxide nanoparticle in the literature displayed 70 EMU g^{-1}. It was decided not to continue doping iron in the MOF as the magnetic field required to align a sample with such low results would require an electromagnet, which would be both expensive and bulky to use and not within the scope of this work. If a strong enough electromagnet could be sourced and attached to an SLA 3DP then any internal electronics would require shielding from the magnetic field or damage the internal electronics.

The second trial to create a magnetically aligned MOF composite used iron oxide nanoparticles as the source of magnetic character. Instead of being doped into the structure, the iron oxide nanoparticles were adsorbed onto the structure of the MOF by electrostatic adsorption. Three MOFs were trialled, NH_2-MIL-68(In), NH_2-MIL-53(Al) and NU-1000. By altering the pH of the iron oxide nanoparticle solution, the amount of adsorption could be tuned to maximise the extent of iron oxide nanoparticles on the MOF. The result of the adsorption was clearly seen under the TEM and FTIR, ICP-OES and SEM-EDX also confirmed the presence of iron oxide or elemental iron. A phenomenon of MOF 'breathing' was noted on the analysis of MIL-53(Al), as the MOF can expand and contract dependent on the guest molecules- large and bulky DMF being replaced by H_2O reduces the pore volume of the MOF. NH_2-MIL-68(In) did not survive the process of the addition of iron oxide nanoparticles as the MOF was susceptible to acid and would degrade on contact with the iron oxide nanoparticle solution at pH 3.5 or 5.9. Once confirmed that iron oxide was adsorbed onto the surface MOFs NH_2-MIL-53 and NU-1000 they were analysed for their magnetic character and magnetic mass susceptibility. There was correlation between the amount of iron present and the magnetic mass susceptibility of the MOFs, with low amount of iron returning low magnetic susceptibility readings and *vice versa*. NH_2-MIL-53(Al) with iron oxide

nanoparticles was tested in the vibrating sample magnetometer which demonstrated that the sample was diamagnetic with a result of 3 EMU g^{-1}, two orders of magnitude greater than the previous iron-doped samples. Knowing the samples were susceptible to a magnetic field, they were added into a polymer medium and exposed to an applied magnetic field created by two neodymium magnets. The images captured by optical microscopy clearly captured the extent of alignment and show strong alignment to the applied magnetic field. The MOF with iron oxide nanoparticles were mixed with a 3D printable photocurable resin and placed in an SLA 3D Printer to demonstrate the ability to create a composite of aligned MOF, this was successful for MOFs NU-1000 and NH_2-MIL-53(Al). Once the composite was produced it was apparent that the polymer composite containing the MOF offered no porosity and so no flow through of CO_2 would be achieved and carbon capture would not be possible.

While initially the MOFs in chapter 3 were chosen for their carbon capture credentials other applications of orientation were investigated. Taking note from ordered liquid crystals being used in optical devices (LCD TVs), the ordered MOF composite was tested for optical activity. Two samples of NU-1000 MOF composite were produced: aligned and unaligned. By placement of fixed and aligned MOF particulates in a polymer composite, an optical response was seen to linearly polarized UV light. The sample with no alignment produced no response. The optical response was reportedly produced by the alignment of the pyrene rings in the linker group of the MOF NU-1000. It was not trialled on any other MOFs as they did not contain large aromatic systems that produce a clear indication of optical activity when aligned. For further experimentation, it would be suggested to test other pyrene-based MOFs such as SION-8 for optical activity. The idea could be taken one step further, with inspiration again from liquid crystals, and allow dynamic control of the magnetic MOFs to alternate the orientation of the MOFs by adjusting the magnetic field and testing the optical response.

Chapter 4 of the presented the use of direct-write 3DP and the fabrication of a 4D printable MOF composite. The objective was to create a novel composite to tackle pollutants in the environment, in particular persistent organic pollutants (POP) which can damage wildlife, destroy ecosystems and impact on human health. POPs can be organophosphate-based and have been weaponised as deadly nerve agents. The MOF UiO-66 was known for its capability to degrade nerve agents, however its use as a solid powder limited it use in real-world applications and required a fabrication technique where it may be deployed with ease and retain efficiency at nerve agent degradation. This required the development of a formulation suitable for the method of direct-write 3DP.

Firstly, the formulation of the ink must contain high amounts of MOF, to allow maximum catalytic efficiency in the degradation of nerve agent. It was found a formulation of 80% MOF with photocurable resins displayed suitable characteristics for a direct-write 3DP ink by binding all powdered MOF into the resin. Secondly, a direct-write 3DP ink must display thixotropic to allow the material to extrude and flow, as such testing was undertaken to ensure the ink formulated would be thixotropic. This was achieved by the mixing of UiO-66 with photocurable resins alongside UV photoinitiators. The resulting material was investigated for its viscoelastic properties by applying an increasing shear rate to the material and examining the change in viscosity. As shear rate increased, viscosity decreased and subsequently improved after the reduction of shear rate. The material could be successful extruded by direct-write 3DP with the modification of a syringe extruder and UV lights. On extrusion of the material, it would cure instantly under UV light to form a solid material in the desired shape and then partially calcined in an open-air furnace. This material was tested for its ability to catalyse the degradation of nerve agent simulant methyl paraoxon. The 4DP MOF composite showed a half-life of 48 minutes, reaching 80% conversion at 100 minutes. While the composite has a half-life four times less than UiO-66 MOF powder, it was much greater than with no catalyst present. The 4DP MOF composite also displayed high specific surface area of 633 m^2g^{-1} which was greater than current UiO-66 polymer composites.

The ability for the 4DP MOF composite to tackle the nerve agent simulant was good and showed promise, for future testing it would be suggested that other POPs could be tested against the MOF composite and capture the ability of the MOF to catalyse the reaction. For future work on this project, it would be suggested to repeat the catalysis multiple times on the same sample to understand its reusability and efficiency after each use. The fabrication technique developed herein using direct-write 3DP and post-processing in an open-air furnace could be applied to other MOFs with good thermal and mechanical stability, but would be unsuitable for any fragile MOFs. Additionally, it was intended that a 4DP MOF composite fabricated in this way may also be useful for carbon capture, in which it would show great promise not only for its storage ability, but for the mechanical stability of the 4DP MOF composite and its ability to be handled with ease and placed in and out of solution with no requirement to filter out powdered MOF particulates.

The concluding work presented in this body of work included the analysis and development of MOF-gels - UiO-66, UiO-66-NH_2 and ZIF-8 to be used in direct-write 3DP. Current knowledge of the material properties of MOF-gels was under researched and so it was intended here to investigate further into properties such as rheology and understand their thixotropic properties and 3D printability. The benefit of understanding the material properties of the MOF-gel is that for future research into environmental health and tackling CO_2 it may help accelerate the field. The MOF-gels porosity along with catalysis and ability to adsorb aqueous pollutants was investigated and shown to have limited application in the field currently. The MOF-gel formulated for 3DP was not porous enough to allow the flow of gaseous elements through the pores and to the MOFs, blocking the MOF from functioning. Whilst attempts to 3D print were successful there would need to be a revision of the formulation and modification of the 3DP equipment and software to fabricate a more reproducible shape.

The foregoing work has presented contributions to the field by the development of novel and promising methods for processing of new MOF-based materials.

Appendix

Nuclear Magnetic resonance, NMR

NMR experiments carried out by Adam Young.

The percentage hydrolysis at each time point was determined by dividing the $^{31}P\{^{1}H\}$-NMR integral(s) of the signal(s) of the hydrolysis products by the sum of all $^{31}P\{^{1}H\}$ integrals (and multiplying by 100). The time point values were defined as the time of measurement start plus 1.5 minutes (total measurement time per time point was 3 minutes).

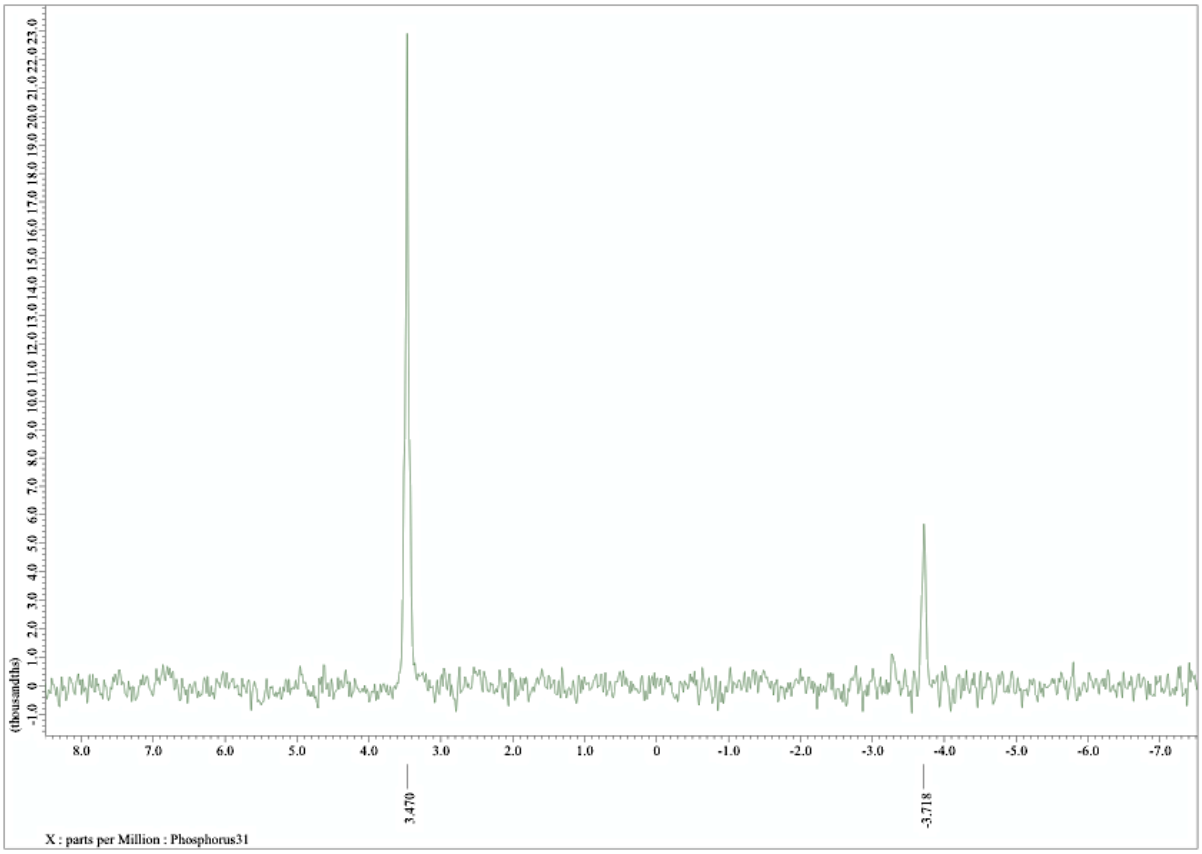

Figure A1: $^{31}P\{^{1}H\}$-NMR spectrum of methyl paraoxon after 200 minutes of catalysis using UiO-66 MOF. The peak at -3.72 ppm is unreacted methyl paraoxon. The peak at 3.47 ppm is the desired hydrolysis product (dimethyl phosphate).

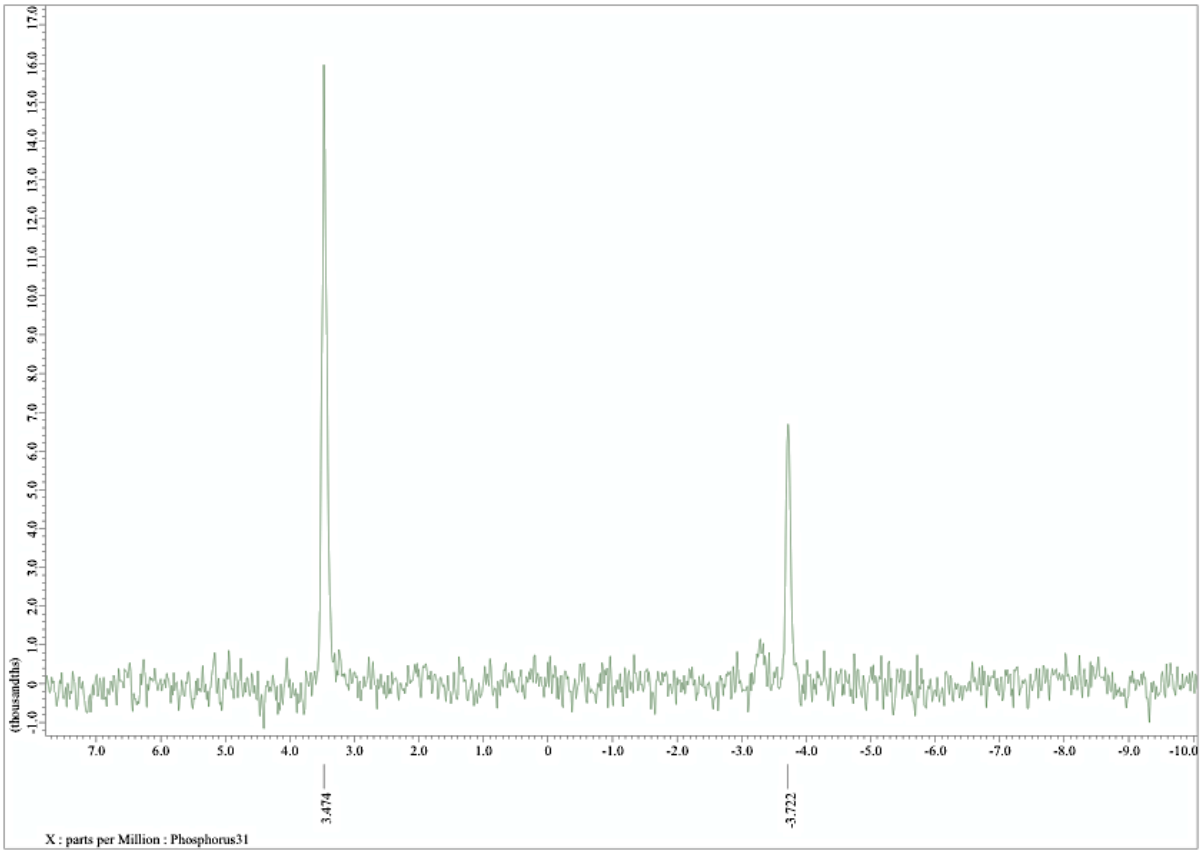

Figure A2:$^{31}P\{^{1}H\}$-NMR spectrum of methyl paraoxon after 200 minutes of catalysis using UiO-66 3D printed composite. The peak at -3.72 ppm is unreacted methyl paraoxon. The peak at 3.47 ppm is the desired hydrolysis product (dimethyl phosphate).

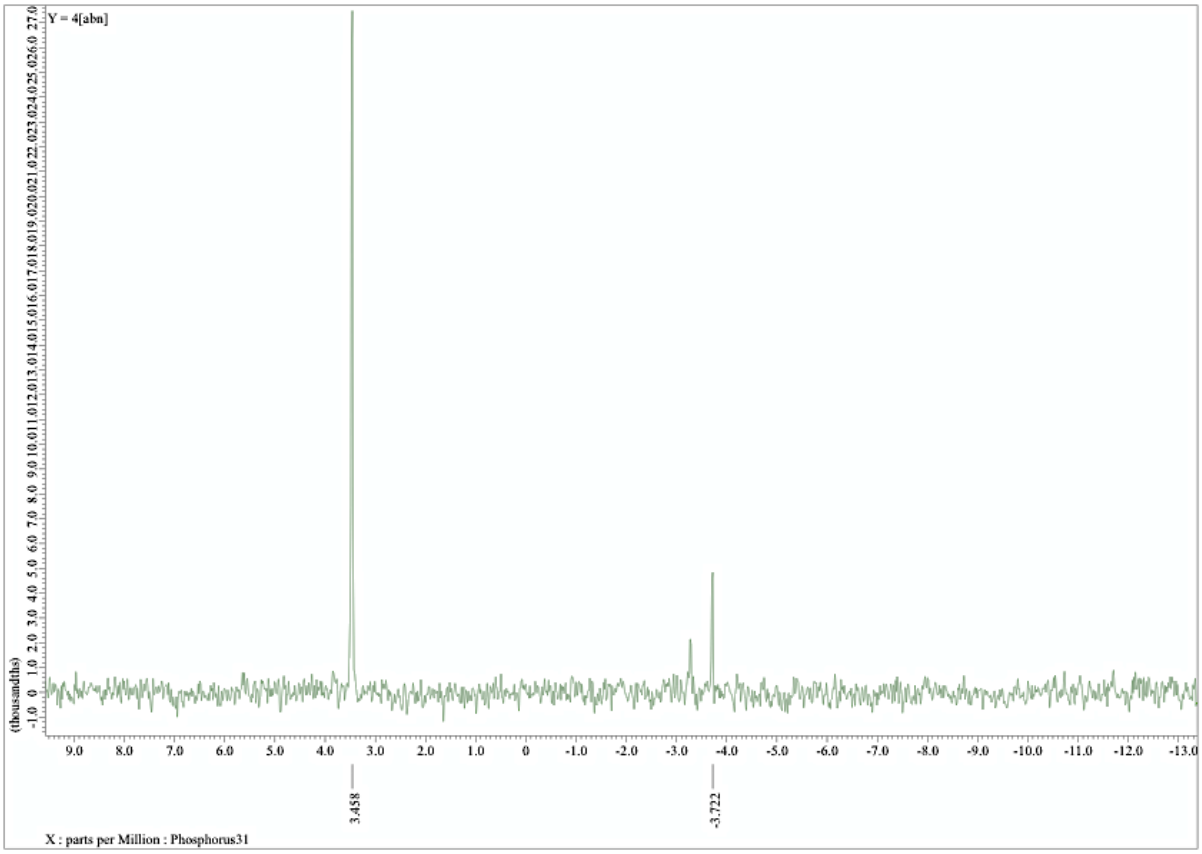

Figure A3: $^{31}P\{^{1}H\}$-NMR spectrum of methyl paraoxon after 360 minutes of hydrolysis catalysis using UiO-66 3D printed composite. The peak at -3.72 ppm is unreacted methyl paraoxon. The peak at 3.46 ppm is the desired hydrolysis product (dimethyl phosphate).

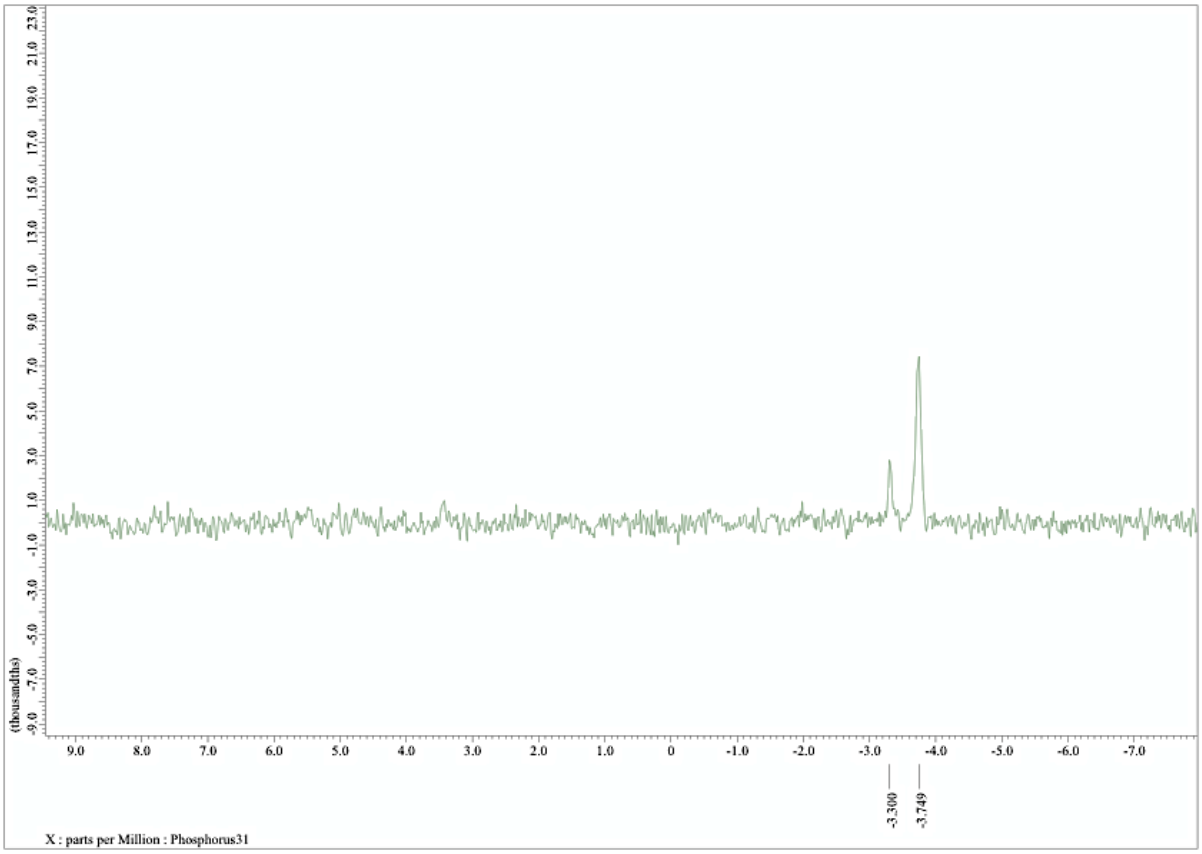

Figure A4: ^{31}P NMR of methyl paraoxon after 200 minutes of self-hydrolysis without any MOF catalyst. The peak at -3.745 ppm is unreacted methyl paraoxon. The peak at 3.30 ppm is a hydrolysed phosphonate compound, methyl 4-nitrophenyl phosphate.[4]